University of Alberta

Optical properties of rare-earth-doped silicon nanocomposites

by

Aaron Christopher Hryciw 

A thesis submitted to the Faculty of Graduate Studies and Research
in partial fulfillment of the requirements for the degree of

Doctor of Philosophy

Department of Physics

Edmonton, Alberta
Spring 2007

Your file Votre référence
ISBN: 978-0-494-29688-2
Our file Notre référence
ISBN: 978-0-494-29688-2

(In the name of Allah the most merciful, the most beneficient)

And on the earth are signs for those who have Faith with certainty.

And also in your own selves. Will you not then see?

(Holy Qur'an, Surah 51, verse 20-21)

This thesis is dedicated to my parents, for their unwavering love and support during all the joys, griefs, defeats, and triumphs I have experienced during my studies. I'm reasonably confident—to at least three standard deviations—in stating that without you, I wouldn't have made it.

Abstract

Silicon-based light-emitting materials show much promise for integrated photonics applications. In particular, nanocrystalline silicon can exhibit efficient visible emission, though the mechanism of luminescence is still the subject of some controversy. This thesis reports on the optical properties and device applications of silicon nanocomposite thin films with varying characteristics: amorphous and crystalline nanoclusters (NCs), both undoped and doped with rare-earth (RE) elements.

Silicon nanocomposite thin films can be prepared by co-evaporation of Si, SiO, and/or SiO_2 followed by annealing to induce phase separation. Such films typically exhibit a broad photoluminescence (PL) band centred between ~600–800 nm. RE-doped *a*-Si-NC films can exhibit relatively sharp emission in the near infrared, with excitation cross-sections on the order of 10^{-16} cm^2 due to the sensitisation effect of the Si NCs—an increase in excitation efficiency by over five orders of magnitude compared with typical values for RE-doped SiO_2. Er^{3+} in particular is important due to its emission at 1.5 μm, corresponding to the wavelength of minimum attenuation in conventional silica optical fibres.

To demonstrate control over the spectral width and centre wavelength of emission for photonic applications, undoped and RE-doped *a*-Si-NC films have been incorporated into optical resonator structures (microcavities) with Ag mirrors. For *a*-Si films, the emission is tunable from 475 to 875 nm, extendable to 1630 nm upon the addition of Er.

It is well known that Si NCs are capable of efficient energy transfer to many of the RE^{3+}

ions; the specific nature of the non-radiative transfer process, however, has not been established with certainty. Efficient nanocluster-mediated excitation has been demonstrated for Nd-, Tb-, Dy-, Er-, Tm-, and Yb-doped a-Si-NC films.

From luminescence modelling of ensembles of a-Si NCs, the observed quenching with increased annealing temperature can be accounted for by assuming a non-radiative defect density of $\sim 10^{20}$ cm^{-3}. The population dynamics of the coupled NC–Er^{3+} system were investigated via a phenomenological rate-equation model for weak optical pumping. A phonon-assisted energy-transfer process is suggested by comparison with experimental time-resolved PL measurements; future work in this area is required to confirm this interpretation.

Preface

This thesis catalogues the evolution of my graduate studies, tracing the somewhat meandering path among the several related projects I have undertaken over the last five years. The progression from one related topic to another is a natural part—if not one of the most important aspects!—of scientific inquiry, so it seems fitting that this final account of my Ph.D. work should mirror it fully. While the topics presented herein range from optical properties of ion-implanted silicon nanocrystals in SiO_2, to fabrication and characterisation of optical resonators based on amorphous Si nanocluster (NC) composites (both intrinsic and doped with rare-earth (RE) elements), to theoretical modelling of luminescence processes in the Si-NC:RE and a-Si-NC systems, the common thread connecting all the projects is that of *nanoscale silicon*.†

This dissertation is of hybrid style, comprising both published and unpublished work; as such, it is divided (unlike Gaul) into four parts:

The first part, consisting of Chap. 1, is the overall introduction to the thesis, providing a general overview and motivation for the work as well as presenting some fundamental ideas regarding the physics of amorphous semiconductors (which are rarely mentioned in conventional condensed matter texts) and the rare-earth elements; a familiarity with crystalline semiconductor theory—at least at a conceptual level—is assumed. While by no means exhaustive, this introduction explains many ideas which are crucial to the discussions in later chapters.

The second part, encompassing Chaps. 2–5, consists of published papers which are largely independent; they may be read as separate articles on related topics in the physics and applications of nanoscale silicon thin films. These chapters are not identical to their respective published versions: some minor modifications have been made in the interest of readability and appropriateness for inclusion within a thesis as opposed to a journal. Chapter 2 is unique in this thesis in that it is the only chapter dealing exclusively with Si nano*crystals* fabricated via ion implantation; all other chapters concern mainly *amorphous* Si NCs, produced via physical vapour deposition.

The third part is composed of Chaps. 6 and 7: as-yet-unpublished work on modelling luminescence and tunnelling processes in ensembles of a-Si NCs, and rate-equation modelling of the Si-NC–Er^{3+} energy transfer process, respectively. The work presented in these chapters indicates the state of inquiry with respect to these two topics at the time of writing; after further investigation, it is intended that they too will be submitted for publication.

†It is therefore obligatory to reference the now-legendary paper by Leigh Canham on efficient luminescence from porous Si as soon as possible.[1] This paper arguably contains the first explicit mention of quantum size effects with respect to emission from silicon, although there are earlier publications (e.g., Refs.[2,3]) which, although unrecognised by the authors, also dealt with nanoscale silicon.

The fourth part comprises the appendices. These are an important part of the thesis, as they provide, in some detail, many of the calculations which had to be omitted from the publications due to length constraints, further explanations of some of the specific models and experimental techniques alluded to in various chapters, and corrections to a number of papers in the literature. As such, the reader who is primarily interested in results may omit the appendices; the reader who wishes to know more about "how it was done" should include them.

A. C. F. H.
Edmonton, Alberta, Canada

Bibliography

[1] L. T. Canham, "Silicon quantum wire array fabrication by electrochemical and chemical dissolution of wafers", *Appl. Phys. Lett.*, vol. 57, no. 10, pp. 1046–1048, 1990.

[2] C. Pickering, M. I. J. Beale, D. J. Robbins, P. J. Pearson, and R. Greef, "Optical studies of the structure of porous silicon films formed in p-type degenerate and non-degenerate silicon", *J. Phys. C*, vol. 17, no. 35, pp. 6535–6552, 1984.

[3] R. Carius, R. Fischer, E. Holzenkampfer, and J. Stuke, "Photoluminescence in the amorphous system SiO_x", *J. Appl. Phys.*, vol. 52, no. 6, pp. 4241–4243, 1981.

Acknowledgement

It may be regarded as an exercise in futility to try to enumerate all the people who have made the time I spent completing my Ph.D. the enjoyable experience that it (mostly) was; however, I do feel compelled to try. First, I must acknowledge my supervisor, Dr. Al Meldrum: a more accessible mentor and advisor I could not have asked for, from my early days doing an Engineering Physics fourth-year project to the present. Our discussion topics ranged from physics to metaphysics, literature, and zymurgy. My thanks go to my office-mates and colleagues, Nicole MacDonald, Florian Lenz, Tom Clement, and Angela Beltaos, for the many hours of talk we shared: bouncing ideas off of each other with respect to our research and coursework helped clear up many a problem, and our less-technical discussions on language, religion, pop culture, philosophy, practical jokes, cooking, music, and visual art "enriched" the graduate studies experience. My special thanks go to Nicole for painting the watercolour for the cover of my *From Water to Ice* string quartet—it mirrored the physics in the music perfectly (thanks also for letting me keep the original!). Thanks to Paul "TEX" Moffatt for keeping my self-esteem in check, for all the mischief you incited and helped me incite (both within the office and without), and for the innumerable lunches we shared, having confirmed each one in increasingly original and ridiculous ways. Thanks to Dave Kachman, for his labour-saving coding skills (that little application got a lot of milage!). I am very grateful to Dr. Mike Brett, who continued to write me about one reference letter per year, even after I was no longer in the ECE department. I would also like to acknowledge my graduate course professors—Drs. Jack Tuszynski, Andrzej Czarnecki, Massimo Boninsegni, Jeremy Sit, Steve Dew, Ray DeCorby, and Richard Marchand—for their expertise and patience in teaching me the more rigorous (and interesting) aspects of physics; special thanks to Ray also for all of our Er-related collaboration and for being the resident photonics guru. Though I haven't taken a course from him since third-year undergrad, Dr. Zbigniew Gortel has always been there throughout my graduate studies as a resource for all things theoretical in condensed matter physics—thanks, Zbyszek, for all the long discussions! I would also like to thank our collaborators at the Chinese University of Hong Kong, Dr. Quan Li and her research group, for all the excellent TEM work they did—perhaps someday we shall meet, and I can thank you personally! The host of wizard technicians deserves a special acknowledgement for being there on a daily basis to solve problems, point out the obvious, and teach me many of the technical skills required in the laboratory: Ken Marsh, Don Mullin, Greg Popowich, and Tony Walford. I also acknowledge generous financial support from NSERC, *i*CORE, Alberta Scholarship Programs, and the University of Alberta. Lastly, I would like to thank my family and my friends (especially Jason Stelck and Tish Prouse) for constant love, prayers, and support, listening to me rant when things got tough, helping me to relax, and reminding me that, if I remember to eat and sleep, things usually work out.

Contents

List of Tables

List of Figures

List of Symbols

Ideally, each symbol used in this thesis would have a unique meaning; in some cases, however, this could not naturally be achieved, due to the historical use of certain symbols for several different purposes. In any event, the correct meaning of a given multiply-defined symbol should be clear from the context in which it is used.

A	1. Absorptivity. 2. Electron affinity.
A_c	Capture area.
a	1. Nanocluster radius. 2. Lattice constant.
a_B	Exciton Bohr radius.
a_j	Probability amplitude of an electron existing on site j.
B	Width of energy band due to atomic interactions.
C_{ij}	Coupling coefficient for transfer of energy from level i to level j.
c	Speed of light in a vacuum. $c = 2.998 \times 10^8$ m/s.
c_d	Contribution to steady-state photoluminescence intensity from NCs containing non-radiative defects.
c_{df}	Contribution to steady-state photoluminescence intensity from NCs which are defect-free.
c_j	Electron annihilation operator.
$c_j^\dagger$	Electron creation operator.
D	Diameter.
$D(x)$	Cumulative probability density.
d	Thin-film thickness.
E	Energy.
E_{av}	Average gap between valence and conduction bands.
$E_{c,v}$	Conduction- or valence-band mobility edge.
E_F	Fermi energy.
E_g	Bandgap or mobility gap.
ΔE_g	Increase of bandgap due to quantum confinement.
E_j	Electron energy at site j.
$E(\mathbf{k})$	Electron energy in a band-structure diagram.
E_o	Tauc optical gap.

E_U	Band-tail Urbach energy.
f_{RF}	RF sputtering frequency.
$g(r)$	Pair correlation function.
h	The Planck constant. $h = 6.626 \times 10^{-34}$ J·s = 4.136×10^{-15} eV·s.
$\hbar$	The Planck constant divided by 2π. $\hbar = 1.055 \times 10^{-34}$ J·s = 6.582×10^{-16} eV·s.
I	Ionisation energy.
$I_{\mathrm{NC}}(h\nu)$	Simulated PL intensity spectrum from an a-Si NC.
$I_{\mathrm{NC_{inh}}}(h\nu)$	Inhomogeneously-broadened simulated PL intensity spectrum from an ensemble of a-Si NCs with a size distribution.
$I(t)$	Light intensity as a function of time.
$I(x)$	Light intensity as a function of distance through an absorbing medium (as used in Beer's Law).
$\mathbf{J}$	Total (spin and orbital) angular momentum operator for an atom.
$\mathbf{k}$	Wavevector.
k	1. Wavenumber (i.e., $k = \lvert\mathbf{k}\rvert$). 2. Extinction coefficient (negative of the imaginary part of the complex index of refraction).
k_B	The Boltzmann constant. $k_B = 1.381 \times 10^{-23}$ J/K = 8.617×10^{-5} eV/K.
$\mathbf{L}$	Orbital angular momentum operator for an atom.
$\mathbf{l}_k$	Orbital angular momentum operator for electron k.
M_j	Molar mass of element j.
m_0	Electron rest mass. $m_0 = 9.11 \times 10^{-31}$ kg.
$m^*_{e,h}$	Electron or hole effective mass.
m_l	Magnetic quantum number.
m_s	Spin quantum number.
N_A	The Avogadro number. $N_A = 6.022 \times 10^{23}$ mol^{-1}.
$N(E)$	Density of states.
N_i	Population of level i.
N_{nr}	Volume non-radiative defect density (cm^{-3}).
N_{snr}	Surface non-radiative defect density (cm^{-2}).
$N(\nu)$, $N(\lambda)$	Complex index of refraction. $N = n - ik$, where n is the index of refraction and k is the extinction coefficient.
n	Index of refraction.
$\mathcal{N}_i$	Population of level i (held constant).
n_{NC}	NC number density.
P	Pressure.
$P(h\nu)$	Probability of electron–hole recombination at energy $h\nu$ in an a-Si NC.
$P(x)$	Probability density function.
p	A probability.

$p_{c,v}(E)$	Probability that the lowest-energy electron (c) or hole (v) state in an a-Si NC is at energy E.
Q	Cavity (resonator) quality factor.
Q_{sca}	Scattering contribution to the extinction efficiency.
Q_{abs}	Absorption contribution to the extinction efficiency.
$\mathbf{R}$	Vector connecting any two lattice points in a crystal.
$R, R(h\nu)$	Reflectivity.
R_0	Characteristic distance for which the probabilities of energy transfer and radiative de-excitation via electric multipole interactions is equal.
R^2	Coefficient of determination.
R_c	Capture radius.
R_t	Radius of an a-Si spherical quantum dot, or the half-width of an a-Si quantum well.
Ry^*	Exciton Rydberg energy.
r	A distance.
r_{ij}	Distance between electrons i and j.
$\mathbf{S}$	Spin angular momentum operator for an atom.
$S(\omega)$	Experimental QFRS spectrum.
$S(\omega;\tau)$	Single-exponential QFRS peak.
$\mathbf{s}_k$	Spin angular momentum operator for electron k.
T	1. Temperature. 2. Transmittivity. 3. Tunnelling barrier transparency.
T_0	Characteristic temperature for temperature quenching of bulk a-Si.
T_b	Boiling point.
T_f	Freezing point.
T_g	Glass transition temperature.
t	Time.
U	Mott correlation energy.
$u_{n\mathbf{k}}(\mathbf{r})$	Bloch envelope.
V	1. Volume. 2. Potential energy barrier height for tunnelling.
V_c	Capture volume.
V_{jk}	Anderson "hopping" matrix element.
$V_{\text{n.n.}}$	Nearest-neighbour hopping matrix element.
$V(\mathbf{r})$	Crystal potential.
v	A velocity.
W	Anderson disorder potential width.
w	A transition rate.
$x_{j_{\text{wt}}}$	Weight fraction of species j in a film.
$x_{j_{\text{at}}}$	Atomic fraction of species j in a film.

$\mathcal{Y}$	Free-space optical admittance. $\mathcal{Y} = 2.6544 \times 10^{-3}$ S.
y	Optical admittance in a medium.
y_L	Luminescence quantum efficiency.
Z	Atomic mass number.
z	First (nearest-neighbour) coordination number.
α	1. Absorption coefficient. 2. Inverse localisation length.
β	1. Stretched-exponential parameter determining the "degree of stretching." 2. Phonon-assisted non-radiative energy transfer probability parameter.
β_T	Coefficient of thermal expansion.
$\epsilon(\nu)$	Complex dielectric constant. $\epsilon(\nu) = \epsilon_1(\nu) + i\epsilon_2(\nu)$.
ϵ_0	Permittivity of free space. $\epsilon_0 = 8.854 \times 10^{-12}$ C^2/Nm^2.
$\epsilon_1(\nu)$	The real part of the dielectric constant.
$\epsilon_2(\nu)$	The imaginary part of the dielectric constant.
η_0	Maximum quantum efficiency of bulk a-Si.
η_j	1. Quantum efficiency of nanocluster j. 2. Population of level j at $t = t_{off}$.
$\eta_{p,s}$	Tilted optical admittance for p- or s-polarised waves.
λ	A wavelength.
λ_0	PL band centre wavelength.
$\Delta\lambda_{\frac{1}{2}}$	PL band full width at half maximum.
μ	1. Population mean. 2. Reduced mass of an electron and a hole.
ν	A frequency.
ν_0	Attempt-to-escape frequency for a carrier in a quantum well.
$\rho(R_t)$	NC radius size distribution.
$\rho(\tau)$	Lifetime distribution.
ρ_x	Mass density of material x.
σ	1. Absorption cross-section. 2. Standard deviation of a distribution.
σ^2	Variance of a distribution.
τ	1. A time constant or lifetime. 2. Molecular rearrangement time.
Φ	Excitation photon flux.
$\|\Phi_j\rangle$	Wavefunction of atomic orbital at atom j.
Ψ	Wavefunction.
$\psi_{n\mathbf{k}}(\mathbf{r})$	Bloch wavefunction.
ω	An angular frequency.

List of Abbreviations and Acronyms

a-	Amorphous.
AOM	Acousto-optic modulator.
APTE	Addition de photons par transfert d'énergie.
BCC	Body-centred cubic.
BPF	Band-pass filter.
c-	Crystalline.
CCD	Charge-coupled device.
CMOS	Complementary metal-oxide-semiconductor.
CRN	Continuous random network.
CVD	Chemical vapour deposition.
CW	Continuous wave.
DBR	Distributed Bragg reflector.
DC	Direct current.
DE	Differential equation.
DOS	Density of states.
ECE	Electrical and computer engineering.
EDFA	Erbium-doped fibre amplifier.
EDWA	Erbium-doped waveguide amplifier.
EELS	Electron energy-loss spectroscopy.
EFTEM	Energy-filtered transmission electron microscopy.
EMPA	Electron microprobe analysis.
ESA	Excited-state absorption.
ESE	Excited-state excitation.
EXAFS	Extended X-ray absorption fine structure.
FCC	Face-centred cubic.
FWHM	Full width at half maximum.
GIF	Gatan image filter.
HCP	Hexagonal close-packed.
HPCVD	High-pressure chemical vapour deposition.
HREM	High-resolution electron microscopy.
IC	Integrated circuit.

IUPAC	International Union of Pure and Applied Chemistry.
LCAO	Linear combination of atomic orbitals.
LED	Light-emitting diode.
LIA	Lock-in amplifier.
LPCVD	Low-pressure chemical vapour deposition.
MC	Monte Carlo.
M↔I	Metal↔insulator.
NC	Nanocluster.
NIR	Near infrared.
OLED	Organic light-emitting diode.
p-	Porous.
PCF	Pair correlation function.
PECVD	Plasma-enhanced chemical vapour deposition.
PL	Photoluminescence.
ppta	Parts per trillion atomic.
PVD	Physical vapour deposition.
QFRS	Quadrature frequency-resolved spectroscopy.
RCM	Random coil network.
RCP	Random close packing.
RDF	Radial distribution function.
RE	Rare earth.
RF	Radio frequency.
RGB	Red-green-blue.
SNR	Signal-to-noise ratio.
SRO	Silicon-rich oxide.
StrExp	Stretched exponential.
TEM	Transmission electron microscopy.
TRS	Time-resolved spectroscopy.
UV	Ultraviolet.
YAG	Yttrium aluminium garnet ($Y_3Al_5O_{12}$).
ZBLAN	A glass containing Zr, Ba, La, Al, and Na fluorides.

CHAPTER 1

Exposition: Light from silicon, amorphous semiconductors, and rare-earth-doped photonic materials

1.1 Coaxing light from silicon

Silicon is easily the most technologically-important material on Earth.† Capable of being purified to electrically-active impurity levels of only a few tens of ppta,[2] crystalline Si serves as the foundation of the entire integrated microelectronics industry, while current fabrication processes for photovoltaic devices rely on the amorphous form of the element. Silicon's relative abundance, the mature state of its processing technologies, the controlled manner in which its electrical properties may be modified, and its benign chemistry make it the material of choice for electronic applications.

The growth of integrated circuits (ICs) has been exponential since the industry's infancy in the early 1960s, prompting Gordon Moore, co-founder of Intel, to formulate his famous observation in 1965 that the complexity of ICs (usually taken as commensurate to the number of transistors on a chip) would double every year;[3] this empirical rule is now generally known as *Moore's Law*. In 1975, the doubling period was revised by Moore to two years, and has been a standard which the microelectronics industry has endeavoured to meet ever since. This is, however, becoming more and more of a struggle. Projections of Moore's Law suggest component densities of over 10^9 transistors per chip by 2010,[4] and already, interconnect issues such as latency, cross-talk, noise, and power dissipation are becoming limiting factors in device performance and speed, foreboding the demise of conventional microelectronics.[5] As a means of overcoming such copper-interconnect bottlenecks, there is now a strong research thrust to develop *optical* interconnect technologies, exploiting the wide bandwidth offered by optical as opposed to electrical signals, though the degree of electrical–optical integration (i.e., board-to-board, chip-to-chip, or potentially even intra-chip) is still in its nascency.[6] However, since silicon is the material platform upon which microelectronics is founded, a truly monolithically-integrated opto-electronic system (if it is to take advantage of well-established IC processing techniques) requires a silicon-based light-emitter. It is therefore a challenge that bulk crystalline silicon possesses a very low luminescence efficiency.

†One is tempted to say "in Earth" as well: silicon is the second most abundant element in the earth's crust (~27.7%).[1]

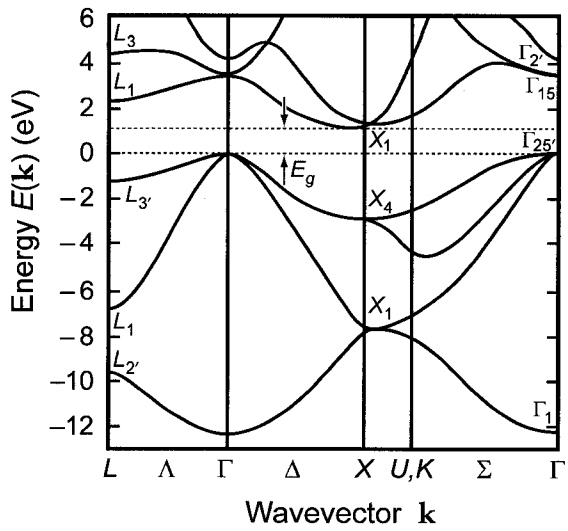

Fig. 1.1: Theoretical band structure of crystalline silicon, calculated with semiempirical pseudopotentials, after Ref.[10]. $E_g \approx 1.17$ eV corresponds to the electronic bandgap. Note the mismatch in wave vector for the positions of the valence band maximum (occurring at Γ) and the conduction band minumum (occurring at X), indicating the indirect-gap nature of Si.

Bulk c-Si is an indirect-gap semiconductor, in which the extrema of the valence and conduction bands occur at different wavenumbers k (see Fig. 1.1). As such, the "optical" bandgap, characterised by vertical interband transitions, occurs at a higher energy than the minimum energy required to form an electron–hole pair (the "electronic" bandgap, E_g). Crystal momentum conservation therefore dictates that optical absorption is a phonon-assisted process; the onset is weak with respect to direct-gap semiconductors because of the low probability associated with the many-particle nature of the transition.[7] Furthermore, the intrinsic radiative decay lifetimes from indirect-gap semiconductors are very long ($\tau_r \approx 1$ ms to 1 s) compared to the competing rates for non-radiative transitions such as the Auger effect (e.g., $\tau_A \approx 10$ ns in bulk Si)[8] or recombination through defects,[9] resulting in a negligible luminescence quantum yield.[7] This low internal quantum efficiency, defined as the number of photons emitted per electron–hole pair excited, essentially precludes the fabrication of useful light-emitting devices from bulk Si if the emission is based on recombination across the fundamental bandgap.

However, since 1984, it has been known that the luminescence efficiency in porous silicon (p-Si), produced by partial electrochemical dissolution of Si wafers in hydrofluoric acid, is modified drastically from that of bulk c-Si.[11] Such p-Si films are characterised by nanoscale dot- or needlelike c-Si grains surrounded by SiO_2, and yield intense photoluminescence (PL) in the visible (typically in the 600–800-nm range). This was first recognised as a quantum confinement effect by Canham in 1990:[12] when the size of the p-Si crystallites becomes sufficiently small, the confining effect of the finite crystallite size increases the effective bandgap.

Quantum confinement in semiconductor nanocrystals may be briefly sketched as follows.[7] The hydrogen-like state of a bound electron-hole pair, or *exciton*, is characterised for a given crystalline material by its *exciton Bohr radius*,

$$a_B = \frac{\epsilon\hbar^2}{\mu e} = \epsilon\frac{m_0}{\mu} \times 0.53 \text{ Å}$$

and its *exciton Rydberg energy*,

$$Ry^* = \frac{e^2}{2\epsilon a_B} = \frac{\mu e^4}{2\epsilon^2\hbar^2} = \frac{\mu}{m_0}\frac{1}{\epsilon^2} \times 13.6 \text{ eV}$$

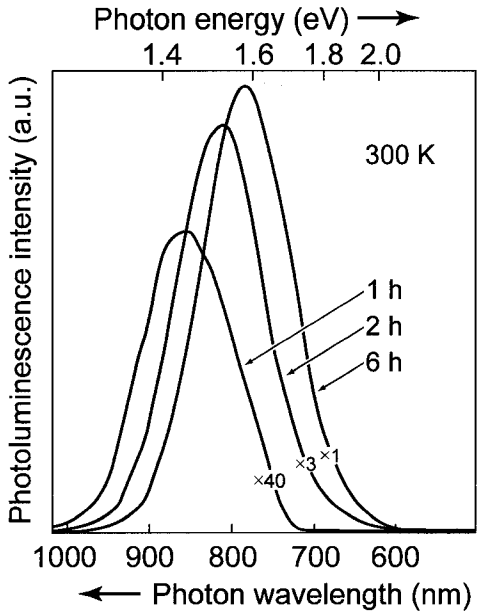

Fig. 1.2: Room-temperature photoluminescence spectra of anodised porous silicon after immersion in 40% aqueous HF for the times indicated. The blueshift with increasing etching time, with concomitant increase in porosity and decrease in mean crystallite size, is taken as evidence for quantum confinement. Excitation was 200 mW (unfocused) at 514 nm. (After Ref. [12])

where $\mu = (m_e^{*-1} + m_h^{*-1})^{-1}$ is the reduced mass of the electron-hole pair, ϵ is the dielectric constant of the crystal, m_0 is the rest mass of an electron, and m_e^* and m_h^* are the effective masses of an electron and hole, respectively, in the crystal. Quantum confinement occurs when the characteristic size of the nanostructure becomes comparable to or smaller than the exciton Bohr radius.

In the *effective mass approximation*, the effective masses of the carriers are considered to be the same as in a bulk crystal;[7] two confinement regimes exist, depending on the nanocrystal size. For a spherical crystalline of radius a, weak confinement occurs when a is a few times larger than a_B. In this regime, the bandgap is enlarged with respect to the bulk crystal by an amount

$$\Delta E_g = \frac{\hbar^2 \pi^2}{2\mu a^2} = \left(\frac{\pi a_B}{a}\right)^2 Ry^* \tag{1.1}$$

A similar expression may be derived for the strong confinement limit, in which $a \ll a_B$:

$$\Delta E_g = \frac{\hbar^2 \pi^2}{2\mu a^2} - 1.786 \frac{e^2}{\epsilon a} \tag{1.2}$$

where the second term describes a small decrease in energy due to the effective Coulomb interaction between a strongly-confined electron and hole. In both confinement regimes, the additive shift with respect to E_g scales roughly as $1/a^2$.

For c-Si, $a_B \approx 4.3$ nm, allowing for relatively easy fabrication of nanoscale Si structures which exhibit quantum confinement effects. Porous Si of suitably high porosity generally exhibits a broad PL band peaking between ~1.55 and 2.15 eV, blueshifted significantly from the 1.12-eV bandgap of bulk c-Si. This emission is very efficient compared to bulk Si (as high as 10%),[13] being easily visible to the unaided eye for moderate excitation powers. The results of Canham,[12] which typify p-Si emission, are illustrated in Fig. 1.2.

With the proof-of-principle for efficient luminescence from nanostructured Si demonstrated by p-Si, the case for a silicon-based light emitter began to look somewhat "brighter."

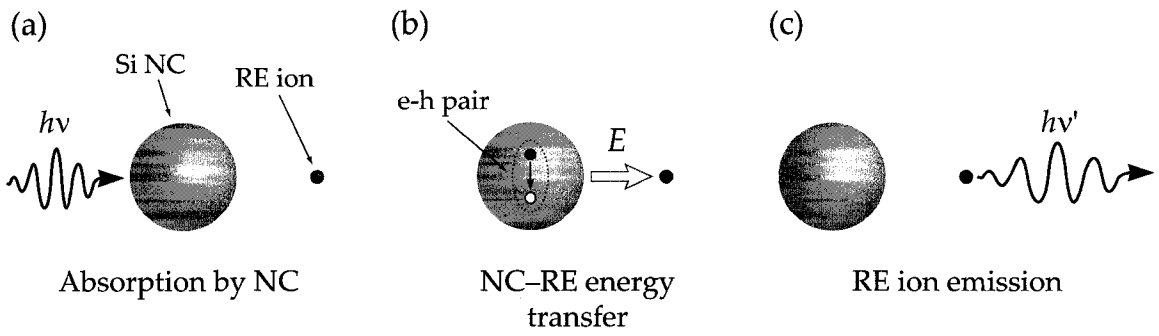

Fig. 1.3: Schematic of the sensitisation of RE ions by Si NCs. In (a), an incident photon within a broad band of possible energies is absorbed by the NC, exciting an electron-hole pair. The e-h pair recombines non-radiatively in (b), transferring its energy to the RE ion, which emits at its own characteristic energies in (c). The effective excitation cross-section of RE ions in close proximity to Si NCs can be orders of magnitude greater than the intrinsic absorption cross-section of the RE. For example, $\sigma_{eff}^{Er^{3+}} \approx 10^{-16}$ cm^2 for erbium and Si NCs in silica, compared to $\sigma^{Er^{3+}} \approx 10^{-21}$ cm^2 for Er-doped SiO_2.[32]

However, porous silicon's fragility and susceptibility to environmental effects (such as oxidation) limit its practical utility in a viable photonic device. Several other methods of fabricating Si nanocrystals have since been developed, with varying suitability for device applications: aerosol procedures involving pyrolysis of silane (SiH_4),[14,15] laser ablation of bulk Si,[16,17] deep-UV lithography and reactive ion etching of Si wafers,[18] chemical synthesis involving inverse micelles[19] or arrested precipitation,[20] and thermal precipitation of nanoclusters (NCs) via phase separation of silicon-rich oxides. For this last class of techniques, the silicon suboxides may be prepared by various means, including ion implantation,[21,22] plasma-enhanced chemical vapour deposition (PECVD),[23,24] co-evaporation of Si, SiO, and/or SiO_2,[25,26] and sputtering.[27,28]

While the phase-separation technique can produce robust, well-passivated nanocrystals protected by a surrounding silica matrix, the temperatures required to crystallise the nanoclusters is generally on the order of 1000 °C or higher. This poses a significant obstacle to integration of silicon-nanocrystal-based light-emitting components on conventional complementary metal-oxide-semiconductor (CMOS) microelectronics platforms, since the maximum post-process annealing temperature for CMOS wafers is on the order of 500 °C.[29] More recently, however, it has come to light that *amorphous* silicon nanoclusters, which can be prepared by phase separation, but requiring much lower annealing temperatures than their crystalline counterparts (300–800 °C), can also exhibit luminescence in the visible and near infrared (NIR), with intensities comparable to that of *c*-Si NCs.[26,30,31] As in the crystalline case, the PL is blueshifted with respect to the bulk material, and possesses a much higher quantum efficiency. It is this class of materials, viz. *a*-Si NCs, with which the majority of this thesis is concerned.

Another important characteristic of Si NCs is their ability to act as sensitisers of rare-earth (RE) ions, notably the lanthanides, which exhibit relatively sharp emission in the visible and NIR. When a RE-doped host material also contains Si nanoparticles, the excitation cross-section of the ions can be increased by five orders of magnitude compared to the case when NCs are absent (Fig. 1.3). This NC-mediated excitation path also takes advantage of the broad absorption band intrinsic to ensembles of Si NCs as opposed to direct optical pumping of RE ions, in which absorption only occurs in sharp bands corresponding to allowed electronic transitions. For *c*-Si NCs, this fact has been well known for

over 12 years;[33,34] recently, a-Si NCs have also been shown to sensitise RE emission with comparable efficiency.[31,35] Since many of the radiative transitions in RE ions correspond to technologically-important wavelengths, rare-earth doping represents a powerful method of extending the versatility of Si-NC-based light-emitting materials. As such, three of the chapters of this thesis are devoted to RE-doped a-Si NC films.

Spurred on by the promise of monolithically-integrated opto-electronics, several different approaches toward achieving efficient light emission from a Si-based material platform are currently under investigation. The use of quantum confinement in c-Si quantum wells, wires, and dots (both intrinsic and doped with rare earths) is being considered for LED and solid-state laser applications (e.g., see Refs.[36–38] and references contained therein). Another approach, which achieves quantum confinement effects in bulk Si wafers via dislocation engineering (essentially providing local spatial confinement of injected carriers through an appropriately-designed array of dislocation loops), shows much promise as an effective means of producing near-infrared LEDs using wholly CMOS-compatible processes.[39] An exciting recent development is the first demonstration of an electrically-pumped laser using AlGaInAs quantum wells grown on a silicon-on-insulator wafer.[40] As a hybrid III–V/Si technology, this device integrates a natural photonic material system with the mature fabrication processes available for silicon. Ultimately, each of the approaches discussed in this section have the same technological goal: raising photonics to the same level of ubiquity currently enjoyed by microelectronics.

By means of general introduction to the work presented herein, the remainder of this chapter addresses two broad topics which are fundamental to the discussions contained in the ensuing chapters: basic physical concepts regarding (1) amorphous materials, and (2) rare-earth elements.

1.2 Fundamental concepts of amorphous semiconductors

If one were to form a definition of solid-state physics based on the topics covered in the vast majority of solid-state and condensed matter texts, one would inevitably come to the conclusion that "solid-state" was tantamount to "crystalline." This is largely due to the fact that the periodicity and symmetry of the atomic lattice intrinsic to crystals provides a wealth of mathematical tools (e.g., reciprocal space, Bloch states) which facilitate quantitative descriptions of the crystalline material properties. *Amorphous* materials, on the other hand, generally receive only a passing mention in most condensed matter books, often in connection with a remark such as "...the lack of a periodic array of ions...has left the subject of amorphous solids in [a] primitive state compared with the highly developed theory of crystalline solids."[41] While it may be conceded that the complexity of amorphous solids hinders their inclusion in introductory solid-state texts, such materials form a fascinating—and increasingly technologically-important—branch of condensed matter physics. While a detailed survey of amorphous solid theory is far beyond the scope of this section, it is the hope that the following brief précis of important physical principles of amorphous materials will help to redress the aforementioned deficiency in traditional condensed matter physics pedagogy.†

†The reader is referred to the texts by Zallen,[42] Elliott,[43] and Mott and Davis[44] for a much more detailed description of the subject than is possible here.

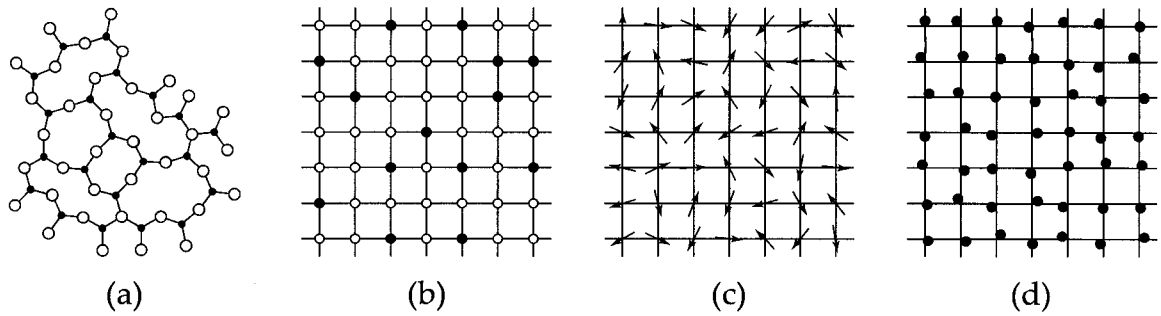

Fig. 1.4: Principal types of disorder found in solids: (a) Topological disorder (long-range order absent), (b) Substitutional disorder (randomness in atom identity on a periodic lattice), (c) Spin disorder (randomness in spin orientation on a periodic lattice), (d) Vibrational disorder (randomness in instantaneous deviation from equilibrium position on a periodic lattice). (After Ref.[43].)

1.2.1 Amorphous solids: definitions and types of disorder

All amorphous solids are characterised by structural *randomness* or *disorder*, though by itself, this is an insufficient definition, since structural disorder can manifest itself in several ways; topological (geometric), substitutional (compositional), spin (magnetic), and vibrational disorder are the principal forms.[43] The latter three, however, are forms of randomness which may be present even if the underlying lattice of atomic sites is perfectly periodic. In an alloy such as brass, although the material structure is a face-centred cubic crystal (for low zinc concentrations), the Zn and Cu atoms substitute for each other randomly in the lattice (Fig. 1.4b). Substituting zinc for manganese produces the magnetic alloy Cu–Mn, which, for dilute solutions, has the property of possessing random spin orientations at each atomic site, though the crystallinity of the lattice itself is unaffected (Fig. 1.4c).[†] Furthermore, all atoms in solids—crystalline or amorphous—exhibit vibrational disorder about their equilibrium positions, if only due to zero-point motion (Fig. 1.4d). Topological disorder, however, occurs when translational periodicity is destroyed completely: the long-range order typified by crystals is entirely absent (Fig. 1.4a). It is this lack of long-range order which provides the definition for "amorphous;" it also led to the rather disheartening opening to Zachariasen's classic 1932 paper: "It must be frankly admitted that we know practically nothing about the atomic arrangement in glasses."[45] Experimentally, amorphous materials are easily recognised by the absence of sharp Bragg spots or rings in diffraction experiments, in favour of diffuse annuli (see, e.g., Fig. 4.1b). Note, however, that the definition of amorphicity does not rule out the possibility of *short*-range order, a property of many covalently-bonded glasses.

The vocabulary concerning amorphous materials is far from standardised, with varying definitions in the literature for terms such as "amorphous," "non-crystalline," "glassy," and "vitreous." For the purposes of this discussion, we will follow Elliott's terminology,[43] treating *amorphous* and *non-crystalline* as synonyms referring to any materials lacking long range order, reserving *glassy* and *vitreous* for amorphous materials exhibiting a glass transition. Also, *lattice* will be taken to denote the set of equilibrium positions for atoms in a solid, free from any connotation of long-range order (as distinct from a Bravais lattice); in this sense it may be used equally to refer to the atomic positions of amorphous as well as crystalline materials.

[†]Such a material is generally referred to as a *spin glass*.

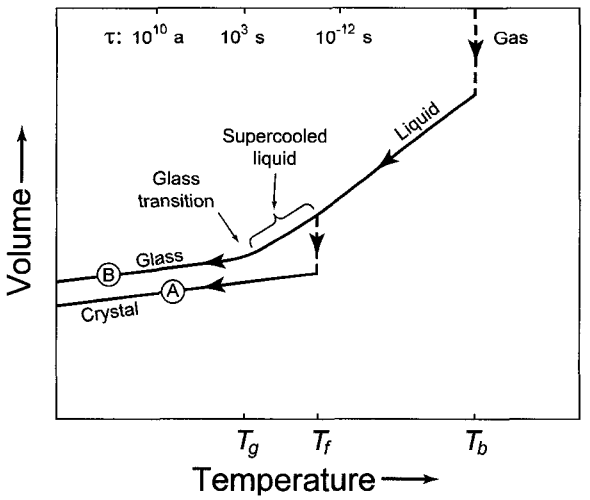

Fig. 1.5: Schematic $V(T)$ diagram indicating the cooling paths resulting in crystalline (path A) and amorphous (path B) solids. T_g, T_f, and T_b refer to the material's glass transition, freezing, and boiling temperatures, respectively. As an example, for SiO_2, these temperatures correspond to ~1175 °C , ~1650 °C , and 2230 °C . Also shown are order-of-magnitude values for typical molecular relaxation times, τ. (After Ref.[42])

Preparation of amorphous materials

The transitions from gas to liquid to solid phase due to cooling are familiar processes: an ensemble of initially isolated, uncorrelated gas atoms gradually lose kinetic energy, condensing into a liquid of well-defined volume at the material's boiling point, T_b, and increasing its density in a continuous fashion until a liquid→solid transition occurs. After solidification, the material's volume V continues to decrease slowly, governed by its coefficient of thermal expansion, $\beta_T = \frac{1}{V}\left(\frac{\partial V}{\partial T}\right)_P$, and remaining finite as $T \to 0$. A typical process may be described by the $V(T)$ plot shown in Fig. 1.5.

The solidification process, however, may follow one of two general paths in V–T space. It may experience a discontinuity in V at the material's freezing point, T_f (path A in Fig. 1.5), yielding a crystalline solid, or it may solidify continuously (path B), characterised by a smooth shift to a shallower slope around the glass transition temperature, T_g, yielding an amorphous solid. Note that β_T for both the crystalline and amorphous cases is similar after solidification. Which of the two paths the material follows depends on the rate of cooling.

The relevant timescale to which the cooling rate must be compared is the material's average molecular relaxation time, τ. $1/\tau$ may be regarded as the rate at which the molecular configuration of the material may respond at a given temperature. As shown by the approximate typical values on the top axis of Fig. 1.5, τ changes dramatically with temperature: from the picosecond regime near the freezing point to the age of the universe at a temperature significantly lower than the glass transition temperature (e.g., $T_g - 50$ K), a range of some thirty orders of magnitude! Below T_g, the timescale of molecular rearrangement therefore quickly exceeds the timescale of any conceivable experiment, and the atomic structure becomes frozen into the lattice (crystalline or amorphous) of well-defined equilibrium positions. Thus, for an amorphous material to result, the temperature range between T_f and T_g must be traversed quickly enough to bypass the nucleation and growth process required for crystallisation.

In this way, it may be seen that the historical assumption that only certain materials (the so-called "glass-forming solids" such as oxide glasses and organic polymers) could be prepared in amorphous form is erroneous: it is simply a matter of being able to cool a given material "fast enough and far enough"[46] below T_g. The requisite minimum cooling rate, however, varies enormously between materials: for the Pyrex (silicate) glass forming the

200-inch mirror of the Hale telescope at the Palomar Observatory, an eight-month cooling period (corresponding to $\dot{T} \approx 3 \times 10^{-5}$ Ks^{-1}) was adequate; for many metallic glasses, $\dot{T} \gtrsim 10^{6}$ Ks^{-1} is necessary.[42]

Several different methods exist by which amorphous solids may be prepared; however, great variation in cooling rates restrict the applicability of each method for a given material. The main techniques are as follows:

1. **Melt quenching** techniques are the oldest methods of preparing amorphous solids: the ancient Phonecians were adept at making silicate glasses as early as 3000 BC. For materials with high glass-forming tendency such as oxide glasses, which require only a slow cooling rate, such a quenching process can be as simple as turning off the furnace in which the melt was produced. Moderately fast quenching may be effected by plunging a sealed ampoule filled with a charge of the melt into a liquid bath with a high thermal conductivity and latent heat of vaporisation.[43]

   Melt spinning is a type of quenching capable of producing ribbons or wires of amorphous metals, which can require very fast cooling rates. For these techniques, a cooled, rapidly-rotating "chill-block," typically of copper, is put in intimate contact with molten metal, either by propelling a jet of the melt onto the disc, or by lowering the disc to touch the surface of a melt reservoir. Such techniques can achieve cooling rates in excess of 10^{6} Ks^{-1}.[42,43] A summary of cooling rates typical of quenching processes is given in Table 1.1.

2. **Physical vapour deposition** (evaporation, sputtering) is the most versatile approach, capable of producing amorphous thin films of materials with even the lowest glass-forming tendency, such as metals. For evaporation, the source material is heated to its melting or sublimation point in a high-vacuum chamber (typical base pressure of a few μTorr); the resulting flux of vaporised material then condenses on a substrate positioned within the line-of-sight of the source.[†] The heating usually takes place by placing the source material in a refractory metal "boat" through which a large DC current is passed, or by bombarding it with a high-energy beam of electrons. The substrate may also be heated or cooled if necessary: for Ga and Bi, the substrate must be maintained at liquid-He temperatures to prevent crystallisation.

   The major disadvantage of evaporation is the difficulty in controlling the composition of the resulting thin films, especially when depositing compounds which have a tendency toward differential evaporation (i.e., the species with higher vapour pressure evaporates first, leading to a film rich in that species and changing the composition of the source material with time). One method of circumventing this difficulty is to employ *flash evaporation*, in which the source material, as a fine powder, is continuously dropped onto a heated filament or boat at very high temperature, vaporising the material completely.

   Sputtering involves bombarding a source target with ions (typically Ar) from a low-pressure plasma, dislodging atoms (or clusters thereof) from the surface, and depositing them as a thin film on a substrate. The pressures used in sputtering are usually significantly higher (~1–10 mTorr) than in evaporation. The Ar^{+} ions are attracted to the target either by applying a negative voltage (in the case of conducting

[†]For a pressure of 7.5×10^{-6} Torr, the mean free path of gas molecules is on the order of 6.6 m (greatly exceeding typical source–substrate distances), causing most evaporated species to reach the substrate via a straight-line, collision-free trajectory.[47]

targets), or an RF field (in the case of insulating targets; usually, $f_{RF} = 13.56$ MHz). Variations to this process include introducing a gas such as O_2 into the chamber to react with the flux from the target (reactive sputtering), using multiple targets, or using a target which is a conglomerate of several materials.[48]

All of the work discussed in subsequent chapters of this thesis concerns thin films produced by thermal or electron-beam evaporation.

3. **Chemical vapour deposition** (CVD) techniques rely on the reaction of process gas(es) to form the desired products, which are then adsorbed on the substrate as a thin film; there are numerous methods by which this process may be implemented. In plasma-enhanced CVD (PECVD), also known as glow discharge decomposition, a plasma of the reactants is produced by application of an RF field by inductive or (now more typically) capacitive coupling. Glow discharge decomposition of silane (SiH_4) by the reaction $SiH_{4\,(g)} \rightarrow Si_{\,(s)} + 2H_{2\,(s)}$ has been the preferred method of preparing hydrogenated amorphous silicon (a-Si:H) since first demostrated by Chittick *et. al* in 1969.[49,50] These films may also be heavily doped by adding phosphine (PH_3) or diborane (B_2H_6) to the chamber, producing n- and p-type a-Si:H, respectively. Some of the many other variations on the basic process CVD include using high or low pressure (HPCVD, LPCVD), high or low temperatures of the substrate and/or the chamber walls, and photo-inducing the reaction using a laser.[48] CVD processes generally do not suffer from the line-of-sight deposition requirement found in PVD, and can result in a much more uniform coating of the substrate.

Method	Cooling rate $\dot{T}$ (Ks^{-1})
Annealing	
large telescope mirror	10^{-5}
"optical" glass	3×10^{-4}
"ordinary" glass	10^{-3}–10^{-2}
Air quenching	1–10
Liquid quenching	10^{2}–10^{3}
Melt spinning	10^{6}–10^{8}
Evaporation, sputtering	$\sim 10^{9}$

Table 1.1: Cooling rates of typical melt quenching methods (after Ref.[43]). Although PVD processes do not strictly involve quenching of a *melt*, an estimate of the cooling rate is included for comparison with conventional quenching techniques; the very high value for $\dot{T}$ is indicative of the ease of producing amorphous materials by this method.

There are numerous other methods by which it is possible to fabricate amorphous materials, including gel desiccation, electrolytic deposition, laser glazing, chemical precipitation, reaction amorphisation, irradiation (neutron, electron, ion), shock-wave transformation, and shear amorphisation.[42,43] The first three classes of techniques enumerated above, however, are the most important in terms of practical production.

Structure of amorphous solids

As stated earlier, the defining structural characteristic of an amorphous material, that which differentiates it from crystallinity, is its lack of long-range order. This is not to say, however, that the atomic positions are completely uncorrelated. On the contrary, atoms in an amorphous solids are *not* randomly distributed in space, as they are in a dilute gas. Fig. 1.6 schematises the arrangement of atoms (at a given moment in time) for a crystal, amorphous solid, and an ideal gas. In both the crystalline and amorphous cases, the lattice

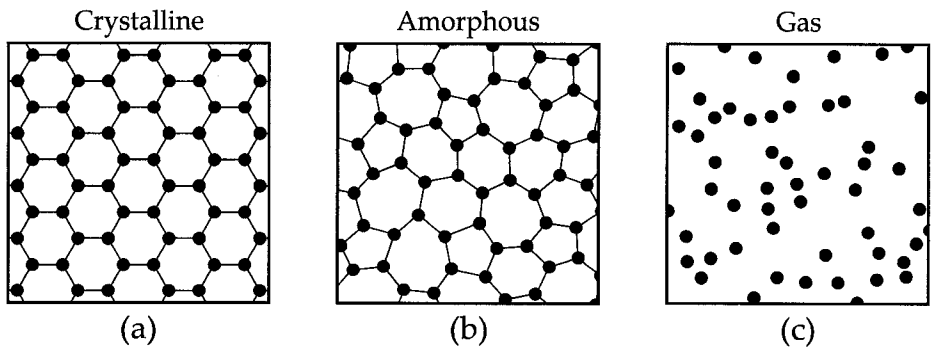

Fig. 1.6: Schematic of atomic positions in: (a) a crystal, (b) an amorphous solid, and (c) a dilute gas at a given moment in time (after Ref.[42]).

is marked by a high degree of local correlation with respect to similarity in bonding. Neglecting vibrational motion, for a perfect crystal, the bond lengths and angles are *exactly* equal, whereas for an amorphous solid, while *nearly* equal, there exists a statistical distribution in these quantities. This gradual loss of order as one progresses from short to long range may be elucidated with the help of a plot of the *pair correlation function* (PCF), $g(r)$, for the three cases shown schematically in Fig. 1.6.

$g(r)\ dr$ is the probability that the centres of two particles may be found separated within the distance range r and $r + dr$, normalised to the particle density. Also commonly encountered is a form of PCF which is not normalised to the particle density, generally referred to as the *radial distribution function* (RDF). For simplicity, we may visualise atoms as hard spheres of diameter D. In a gas (Fig. 1.7c), the only restriction on the interparticle spacing is that there may be no overlap, causing $g(r) \rightarrow 0$ for $r < D$; otherwise, the particle positions are uncorrelated, resulting in uniform probability ($g(r) = 1$). At the other extreme, $g(r)$ of a perfect crystal (Fig. 1.7a) is characterised by sharp (δ-function) peaks, corresponding to the positions of the nearest neighbours, next-nearest neighbours, and so on. In general, the spacing of these δ-functions decreases with increasing r. A typical amorphous solid (Fig. 1.7b) possesses qualities of both of these foregoing cases: the short-range order manifests itself by broadened peaks for small values of r, corresponding to the *average* positions of the first few nearest-neighbours; for large values of r, however, the absence of long-range order results in a uniform probability, causing $g(r) \rightarrow 1$, as in the gas case. Experimentally, $g(r)$ may be obtained via a spatial inverse Fourier transform of diffraction patterns.[42]

A second quantity by which we may partially characterise the structure of amorphous solids is the *first coordination number*, z, defined as the number of nearest neighbours. This single number provides much information on the short-range order and bonding of the solid. A low coordination number ($z \leq 4$) generally indicates the predominance of directional covalent bonding, producing a structure which is not close packed: $z = 1$ and $z = 2$ imply a *disconnected* lattice with units consisting of diatomic molecules and closed rings or extended linear chains, respectively, relatively weakly bound together; $z = 4$ implies a tetrahedral structure, such as found in Si and Ge. Conversely, a close-packed structure usually connotes the existence of non-directional ionic, metallic, or van der Waals bonding, resulting in a high coordination number ($z = 8$ for BCC, $z = 12$ for FCC and HCP). An experimental value for z may be extracted by integrating over the first peak in a RDF.

Strictly speaking, given the distribution in interparticle spacing, the true coordination

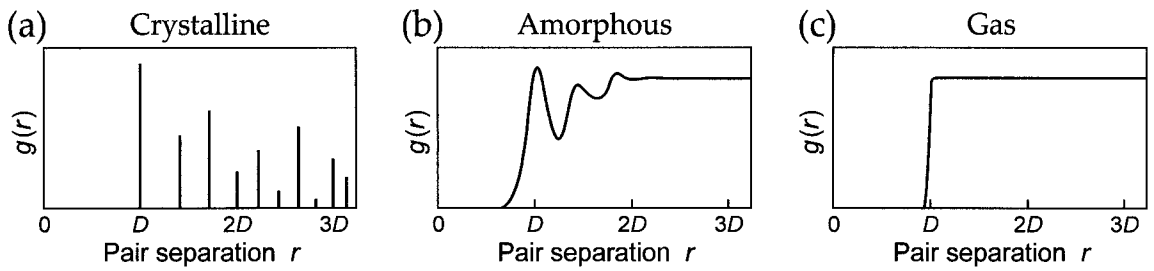

Fig. 1.7: Sketch of normalised pair correlation functions for a perfect crystal (close-packed FCC), amorphous solid, and gas, assuming hard sphere particles of diameter D.

number for each atom in an amorphous solid is unity, but this does not in general presuppose the existence of diatomic molecules in a glass, as in the case of crystalline hydrogen.[42] This may be seen by considering that for a solid consisting of atoms which have paired off into molecules, any atom a which has a nearest neighbour b is itself the nearest neighbour to atom b. For a general amorphous solid, however, atom a may have b as its nearest neighbour, whereas the nearest neighbour of b is c; this is the case whenever a, b, and c form the vertices of a scalene triangle with $\overline{ac} > \overline{ab} > \overline{bc}$. However, this point turns out to be moot when considering real crystals and amorphous materials: the experimental width of the first RDF peak *is nearly the same* in both forms of a given substance,[42] since vibrational disorder contributes to the peak width even in crystals. This remarkable similarity indicates that similar bonding characteristics dominate the short-range structure in both the amorphous and crystalline forms of the same material.

There are three major models for the overall structure of amorphous solids, supported by such experimental characterisation techniques as diffraction (neutron, electron, X-ray) and extended X-ray-absorption fine structure (EXAFS): *continuous random networks* (CRN),[45] *random close packing* (RCP),[51] and *random coil models* (RCM).[52] CRN structures are characteristic of most covalent glasses, such as silica, a-Si, and the chalcogenide glasses. The schematic of an amorphous solid shown in Fig. 1.6b is a representation of a CRN for a $z = 3$ material such as vitreous carbon; its crystalline counterpart, graphite, is represented by the honeycomb lattice in Fig. 1.6a. While both of these ideal structures are threefold coordinated, have nearly constant bond lengths, and do not contain any dangling bonds, in the amorphous case, a distribution in the bond angles causes the breakdown in long-range order.

Simple metallic glasses, on the other hand, typically exhibit random close packing due to their isotropic bonding.[†] Such a structure may be realised macroscopically by allowing ball bearings to settle in a container with irregular walls (planar walls promote the formation of a periodic lattice), and corresponds to a local energy minimum in terms of the configuration. As might be expected from the $V(T)$ curves in Fig. 1.5, the packing fraction of RCP structures is less than that of FCC or HCP lattices: 0.637 vs. 0.7405 for the crystalline case. However, each sphere is secured in its position by (usually) six nearest neighbours, preventing a smooth transition to crystallinity by continuous densification. An illustration of a RCP cluster is shown in Fig. 1.8, constructed via a potential energy minimisation procedure.

The random coil model is arguably the most commonly-encountered form of amorphous solid in modern everyday life, as it comprises the structure of plastics: glasses con-

[†]Other names for random close packing include *dense random packing* and *Bernal structure*.[42]

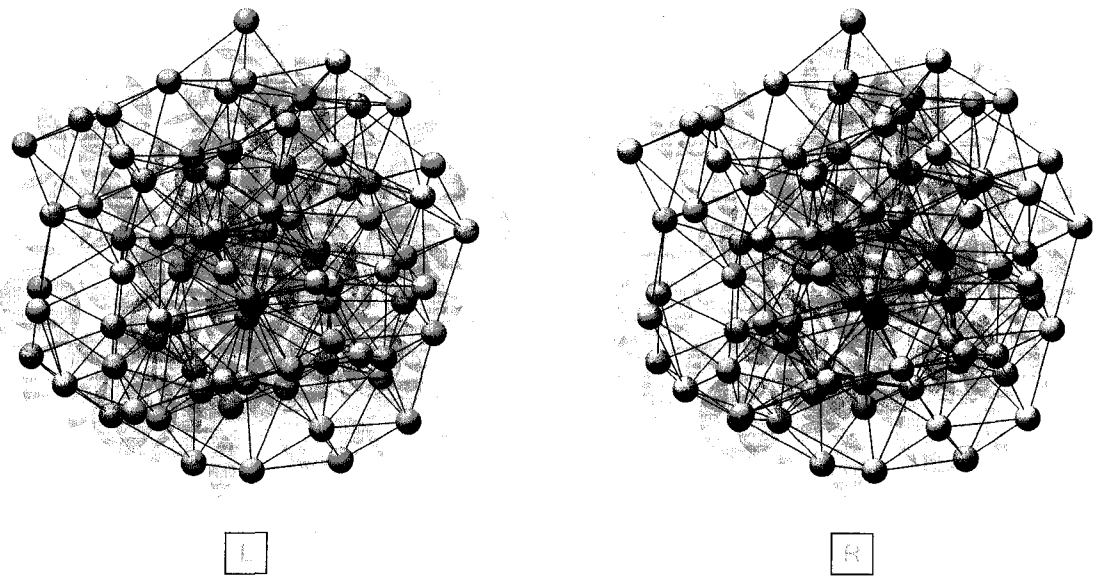

Fig. 1.8: An 84-atom random-close-packed cluster (stereo pair). For this model, implemented using MATLAB, 84 spheres (of diameter D) with an initial random position distribution were allowed to relax via potential energy minimisation (pairwise Lennard-Jones potential). For clarity, the atoms are plotted as solid spheres with diameter $0.3D$; the full extent of the space occupied by each atom is shown by the transparent shells. Atoms are shown bonded to their neighbours if their separation is less than $1.3D$.

sisting of 1D-network long polymerised chains of organic molecules. In this model, the configuration of each strand of polymer is equivalent to a self-avoiding 3D random walk.[52] In such an organic glass, each chain typically permeates a spherical region of space with a characteristic radius of approximately 30 nm, as demonstrated by neutron scattering experiments.[42] This radius has been observed to be proportional to the square root of the number of monomer units in the chain, a signature of the structure's random-walk origin.

Since the main amorphous materials considered in the forthcoming chapters are amorphous silicon, silica, and silicon suboxide (i.e., SiO_x, with $x < 2$), the most relevant of the aforementioned structures to this thesis is the CRN model. In particular, for a-Si, we shall see that the short-range order dictated by the nature of the Si–Si bonds has some surprising consequences—at least to a condensed matter physicist who has been brought up on crystalline solid theory. The disorder inherent in the distribution of bond characteristics, on the other hand, leads (somewhat more expectedly) to some electronic properties which differ considerably from crystalline Si.

So far in this discussion we have been considering "perfect," defect-free amorphous solids. The concept of a defect in an amorphous solid, however, is necessarily different than in a crystalline material, since the former has no unique idealised structure with which to compare the atomic positions. In a crystal, any atoms which are out of place with respect to the relevant periodic lattice are considered defects; the two simplest examples are vacancies and interstitials (Fig. 1.9a). Contrast this with the situation in an amorphous solid, where the only (short-range) structural characteristic is the coordination number, z. As such, we may define the elementary defect in an amorphous material as a *coordination* defect, in which the bonding of a the defect atom results in a different z. The simplest case is that of an isolated dangling bond (Fig. 1.9b). If we consider a $z = 4$ crystal structure such as that of c-Si (diamond), we see that a single vacancy results in *four* dan-

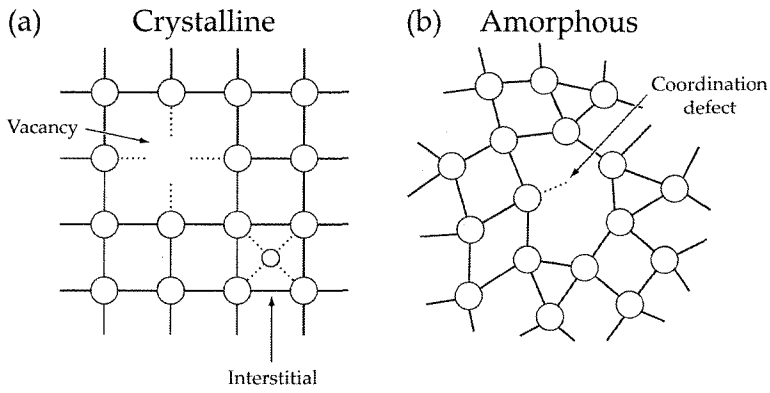

Fig. 1.9: Schematic of elementary defects in crystalline and amorphous solids. The preferred coordination for atoms in both structures is $z = 4$. Note that the disorder in the amorphous solid permits the formation of an isolated dangling bond, whereas in the crystalline case, this is not allowed (minimum of four dangling bonds). (After Ref.[50])

gling bonds; isolated dangling bonds are not permitted in a crystal, whereas the disorder in the CRN structure allows such a possibility. The density of defects within an amorphous semiconductor can have a profound effect on the material's electrical characteristics. A further discussion of bond defects in amorphous semiconductors will be included in the next section.

1.2.2 Electronic and optical properties

We now turn to the electronic and optical properties of amorphous materials; we will concentrate on amorphous semiconductors in general and a-Si in particular, as they bear the most relevance to this thesis.

Local order and bonding

Figure 1.10 is a plot of reflectivity for bulk Ge in liquid, crystalline, and amorphous form, in the energy range corresponding to electronic excitations (ultraviolet). The clear qualitative difference between the long-wavelength behaviour of the liquid and and solid phases is indicative of the distinct electronic natures of the materials: $Ge_{(l)}$, with $R(h\nu) \rightarrow 1$ as $h\nu \rightarrow 0$, is a metal, whereas $R(0) \approx 0.36$ for both c- and a-Ge, which are semiconductors. A contrasting case is that of selenium, which is unique among the elements in that it is semiconducting in all three forms.[53†] This difference can be explained by Ioffe's rule, which predicts the fundamental electronic character of a material (metal, semiconductor, insulator) in terms of z.[55] The strong covalent bonding in crystalline Se yields a structure composed of long helical chains (triclinic, most stable) or Se_8 rings (monoclinic, metastable); for both crystalline phases, $z = 2$. The triclinic polymer structure persists relatively unchanged upon melting, and while the particular molecular arrangement in a-Se varies with preparation technique, in all cases the nearest-neighbour distance, bond angles, and twofold coordination remains nearly the same as in the crystal and liquid, maintaining the semiconducting nature of Se regardless of its phase.[53] In Ge, however, the coordination of the solid phases ($z = 4$) shifts to $z \approx 8$ in the liquid, changing the material from a semiconductor to a metal. These two examples illustrate the predominance of short-range order on the overall electronic properties of a material.

The covalent bonding in tetragonally-coordinated materials such as Si and Ge may be illustrated with the help of a molecular orbital diagram, as shown in Fig. 1.11. In the usual

†$Se_{(l)}$ is a semiconductor near its melting point of ~217 °C; at temperatures higher than ~1100 °C it becomes metallic.[54]

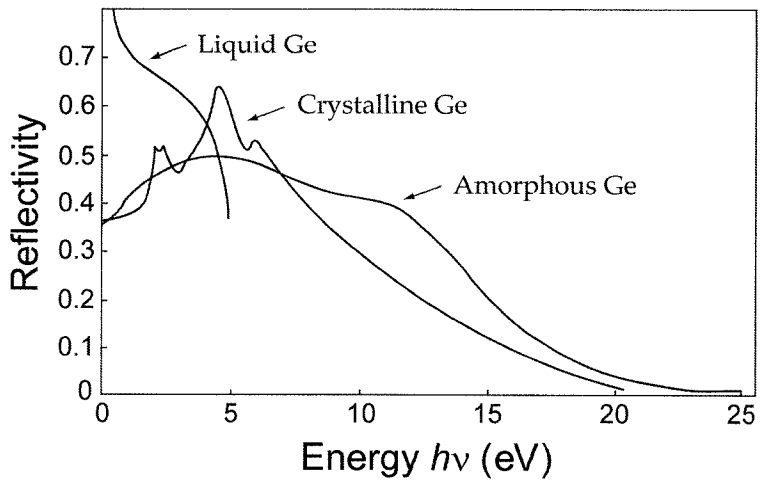

Fig. 1.10: Reflectivity of liquid, crystalline, and amorphous Ge in the energy range corresponding to electronic transitions. (After Ref.[56])

sort of gedanken experiement, we can imagine "building" a Si solid (either crystalline or amorphous) by bringing together initially isolated Si atoms from infinity. The electron configuration of an isolated Si atom is [Ne]$3s^2 3p^2$; the ten core electrons do not participate in bonding. The "first stage" in the bonding process is the hybridisation of the orbitals: mixing of the two $3s$ and $3p$ states to yield four equivalent sp^3 orbitals, at an energy cost of $\sim$6 eV.[42] When four other similarly-hybridised Si atoms are made to surround the first atom in tetragonal coordination, the overlap of the sp^3 orbitals between nearest-neighbour atoms along the Si–Si bond axes results in the formation of bonding and antibonding orbitals, the splitting between which is $\sim$5 eV. Upon the formation of covalent bonds, the initial 6-eV energy cost is more than compensated for, each bond reducing the energy by 2.5 eV, to yield a net change of -4 eV per atom.

The bonding configuration which minimises energy varies from element to element. For instance, in Se, with a valency of six ([Ar]$3d^{10}4s^2 4p^4$), no hybridisation occurs: four electrons fill the $4s$ states and two of the $4p$ states, leaving the remaining two $4p$ electrons to form a *lone pair*. The lone-pair and $4s$ electrons to not contribute to bonding. As such, the coordination of Se is two. The predicted coordination number for an atom in a solid may be found using Mott's "8-N" rule[57]

$$z = \begin{cases} 8 - N & \text{for } N \geq 4 \\ N & \text{for } N < 4 \end{cases} \tag{1.3}$$

where N is the number of valence electrons for the isolated atom. Eq. (1.3) codifies the general rule for covalent bonding: maximise the number of electron pairs in bonding orbitals, with the remainder in non-bonding states; antibonding orbitals remain empty.

In a solid consisting of many atoms, interactions between the bonds broaden the bonding and antibonding states into bands of finite width; these are the valence and conduction bands, characterised by their respective densities of states $N(E)$, also sketched in Fig. 1.11. The quantity E_{av} shown in the figure is the average gap between the two bands, with the minimum separation corresponding to the bandgap E_g. It is important to note that the above description makes no mention of whether the material is amorphous or crystalline. As such, the main qualitative features of the density of states functions are the same in both cases. Indeed, the values for E_g and E_{av} are nearly the same in c- and a-Si: $\sim$1 eV and

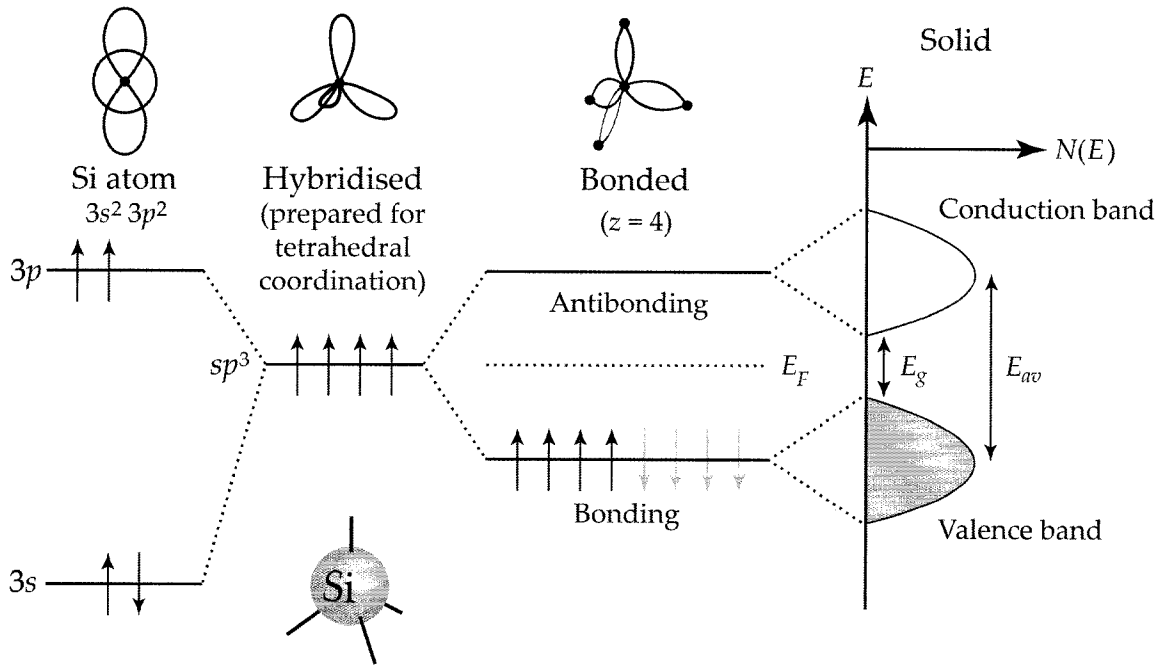

Fig. 1.11: Schematic of the bonding configuration for Si, resulting in tetrahedral coordination. At right is a sketch of the density of states function, $N(E)$, resulting from the bonding and interactions between bonds. Note that this situation is substantially the same in both the crystalline and amorphous cases. The bandgap E_g, average gap E_{av}, and Fermi energy E_F are also shown. (After Refs.[50] and[42].)

~5 eV, respectively.[42†] In both cases, for intrinsic (undoped) materials, the Fermi energy E_F lies mid-gap.

Bandgap and density of states

It is perhaps surprising to those accustomed to crystalline solid theory that an amorphous solid should exhibit any sort of bandgap at all, since the existence of forbidden energy regions in a crystal is intimately connected with its periodicity. This periodicity is accounted for in the Hamiltonian by the crystal potential $V(\mathbf{r})$, which approximates the average potential experienced by an electron due to interactions with *all* of the nuclei and other electrons in the solid; it has the property that, for all vectors $\mathbf{R}$ connecting points in the lattice, $V(\mathbf{r}+\mathbf{R}) = V(\mathbf{r})$. By Bloch's theorem, the solutions to the Schrödinger equation for electrons subjected to such a potential can be written as the product of a plane wave and a function sharing the periodicity of the lattice:[41]

$$\psi_{n\mathbf{k}}(\mathbf{r}) = e^{i\mathbf{k}\cdot\mathbf{r}} u_{n\mathbf{k}}(\mathbf{r}) \tag{1.4}$$

where the *Bloch envelope* $u_{n\mathbf{k}}(\mathbf{r})$ possesses the same translational invariance as $V(\mathbf{r})$, viz. $u_{n\mathbf{k}}(\mathbf{r}+\mathbf{R}) = u_{n\mathbf{k}}(\mathbf{r})$. As such, the allowed values of the electron wavevectors $\mathbf{k}$ are contingent upon the symmetry (and long-range order) of the crystal lattice.

A convenient representation of the allowed electron energies in a crystal is a band structure diagram of E as a function of $\mathbf{k}$, illustrated for a 1D weak periodic potential in Fig. 1.12. The opening up of energy gaps at wavevectors corresponding to the edges of the Brillouin

†In *hydrogenated* amorphous silicon, however, the optical bandgap is higher, generally lying in the 1.7–1.9 eV range.[50]

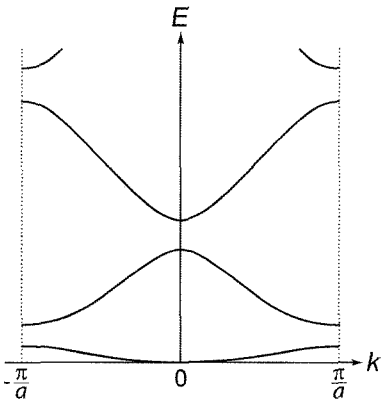

Fig. 1.12: Reduced zone scheme representation of the band structure for a 1D linear lattice of atoms. (After Ref.[41])

zone (e.g., $k = \pm\frac{\pi}{a}$ for a 1D chain of atoms with lattice constant a) may be thought of as the result of destructive interference of Bragg-reflected Bloch waves off the lattice planes.[43] However, no such $E(\mathbf{k})$ band structure representation exists for amorphous materials: not possessing a periodic lattice, the electrons cannot be described by Bloch waves. As such, the elegant Bloch construction in conventional crystal theory cannot justify the existence of an energy gap in amorphous materials. This is refuted rather strongly by the fact that common silica window glass is transparent throughout the visible range, indicating that an energy gap of at least ~3 eV must exist.

The existence of a bandgap in amorphous solids was put on a firmer theoretical footing with a "proof-of-existence" theorem by Weaire and Thorpe, for tetrahedrally-bonded semiconductors such Si and Ge.[58,59] In their model, they considered only the short-range order due to bonding, using a tight-binding Hamiltonian with interactions V_1 and V_2 corresponding to interactions between sp^3 orbitals on the same atom and on nearest-neighbour atoms, respectively:

$$H = V_1 \sum_{\substack{i \\ j \neq j'}} |\Phi_{ij}\rangle \langle \Phi_{ij'}| + V_2 \sum_{\substack{i \neq i' \\ j}} |\Phi_{ij}\rangle \langle \Phi_{i'j}| \tag{1.5}$$

In this equation, the wavefunctions $|\Phi_{ij}\rangle$ are the hybridised sp^3 orbitals as sketched in Fig. 1.11. Such a Hamiltonian is clearly applicable to both the crystalline and amorphous cases, since it contains no reference to long-range order. It was shown by Weaire and Thorpe that for $|V_2| > 2|V_1|$, there is no overlap between the valence band (constructed from binding orbitals) and conduction band (constructed from antibonding orbitals), yielding a bandgap of $E_g \geq 2|V_2 - V_1|$.[43] As such, although it cannot be represented in an $E(\mathbf{k})$ diagram as in the crystalline case, a bandgap can exist in an amorphous solid as well.

A concept which *is* shared by both crystals and amorphous solids is that of the density of states (DOS) $N(E)$, shown in schematic form for a typical amorphous semiconductor such as a-Si in Fig. 1.13. The DOS for the familiar parabolic bands in the crystalline case is indicated by the dotted lines, characterised by abrupt edges. The effect of topological disorder in the amorphous lattice is to broaden these sharp edges into an exponential distribution of states trailing off into the gap, the so-called *band tails*. Empirically, the band-tail DOS for either band may be written as[9]

$$N(E) = N_0 e^{E/E_0} \qquad \text{for } E \leq 0 \tag{1.6}$$

where E is understood to be zero at the mobility edge E_c (E_v), and negative below (above) this energy, as shown in Fig. 1.13, N_0 is the DOS at the mobility edge, and E_0 is an empiri-

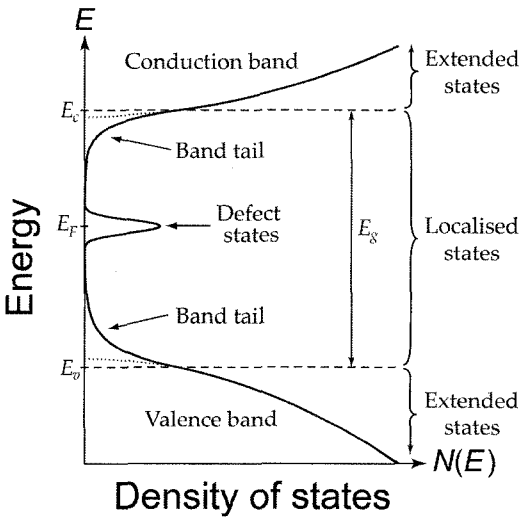

Fig. 1.13: Schematic density of states for a typical amorphous semiconductor. E_v and E_c are the mobility edges for the valence and conduction bands, respectively, with $E_g = E_c - E_v$ defining the mobility gap. Departures from the ideal CRN structure such as coordination defects manifest themselves as deep-gap defect states. The abrupt band edges corresponding to the crystalline case are shown as dotted lines.

cal parameter relating to the breadth of the tail. What exactly is meant by the *mobility edges* E_c and E_v is considered in the next section; we see from Fig. 1.13 that they roughly correspond to the band edges in the crystalline case. In a "perfect" amorphous solid with no defects, the entire DOS would comprise the contributions from the bands and the band tails. However, any deviation from the ideal CRN structure—such as coordination defects—introduces a distribution of states deep within the gap. This narrow band of defect states has the effect of pinning the Fermi level near mid-gap, although this does *not* therefore result in metallic behaviour, since such defect states are *localised* and do not contribute to conduction.[43] Since $N(E)$ is not zero between the mobility edges (as it is between bands in a crystal), but merely small, it is customary to refer to this region as a *pseudogap*.

Electron localisation↔delocalisation transitions

Band theory for crystalline materials treats electrons as independent, assigning them to the set of Bloch states characterised by a wavevector $\mathbf{k}$ and integer band index n according to Fermi-Dirac statistics. In this theory, a crystal comprising N unit cells can fill each band with a maximum of $2N$ electrons (due to spin degeneracy); the filling of the bands—partial or complete—determines the basic electronic nature of the material, that is, whether it is an insulator or a metal at zero temperature. We consider the $T = 0$ case for simplicity in this discussion, since it has the benefit of providing a sharp boundary (at the Fermi energy E_F) between occupied and unoccupied states. A metal contains partially-filled bands, E_F lying within a band, whereas an insulator has E_F within a gap separating the valence (full) and conduction (empty) bands. For materials with an even number of electrons per unit cell, capable of filling an integral number of bands, a slight change in temperature or pressure can shift the band structure such that a transition from metal to insulator (M↔I) occurs, removing an overlap between the bands which had formerly resulted in conduction; such a situation occurs for ytterbium.[42] It is important to note that the electrons are still characterised by *extended* Bloch states, irrespective of whether the material is metallic or insulating. In amorphous semiconductors, however, a M↔I transition occurs via an entirely different mechanism: a transition in the nature of the electron wavefunctions from

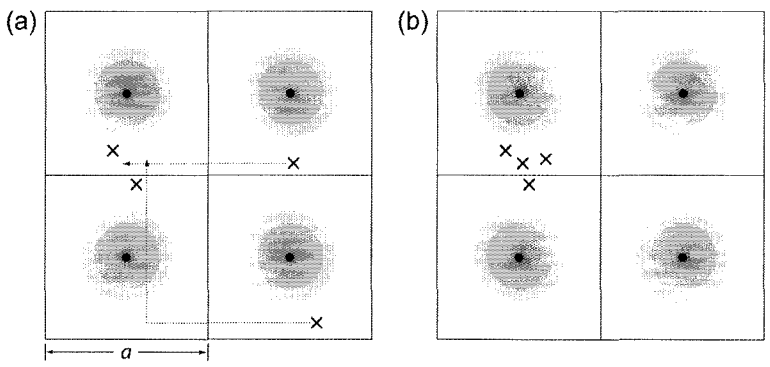

Fig. 1.14: A schematic of two degenerate electron configurations with respect to band theory, which is unable to distinguish energy differences due to translations of electrons by integer numbers of the lattice vectors, shown here as a for a square lattice. Each valence elctron is represented by a $\times$; core electrons are shown as the shaded circles around the solid nuclei. The inter-electron Coulomb energy $\frac{e^2}{4\pi\epsilon_0 r_{ij}}$ is not accounted for in one-electron band theory. (After Ref.[42].)

extended to *localised* states. Such a phenomenon is called the *Anderson transition.*†

A rigorous treatment of Anderson localisation is somewhat of a mathematical *tour de force,* and beyond the scope of this introduction. We shall therefore make the segue into the Anderson transition from another M↔I transition which is conceptually easier to understand, viz. the *Mott transition.*[61] These two phenomena are similar in the sense that they are both M↔I transitions which illustrate the breakdown of independent-electron theory in solids.

We begin by considering a crystal of an alkali metal such as sodium, which has a single valence electron; the structure of Na is BCC, with a lattice constant of ~4.3 Å. Independent-electron band theory predicts one-electron solutions consisting of Bloch waves, each electron existing in an extended state throughout the lattice. Since there is only a single electron per unit cell with which to occupy the highest band, the material is a metal, as this band is only half-filled (N out of a possible $2N$ states are occupied). Altering the lattice constant slightly would result in a modest adjustment of the band energies, but the overall picture would remain the same. However, let us now suppose that, maintaining the periodicity of the crystal, we shift the lattice constant to some large (macroscopic) value, such as 1 m. From the standpoint of Bloch theory, nothing qualitative has changed: the material would still be a metal. This is, of course, absurd, as we would merely have a collection of *isolated* atoms, each with one filled $3s$ orbital; the periodicity of their arrangement would be immaterial. Transferring an electron from one widely-separated atom to another would increase the energy of the system by an amount $I - A$, where I is the ionisation energy and A the electron affinity of the atom. For Na, $I \approx 5.14$ eV and $A \approx 0.55$ eV, yielding ~4.6 eV per electron transferred.

The reason why band theory fails in this context is because, as a one-electron theory, it does not consider the possibility of *correlations* in electron motion which could reduce the overall energy of the configuration. This is illustrated in Fig. 1.14: the energy of both configurations would be the same in band theory, since the $V(\mathbf{r})$ is an estimate of the *average* potential experienced by a single electron. Although the configuration of Fig. 1.14b clearly has a higher energy, the extra Coulomb repulsion between the clustered electrons is not considered. For a given solid, the *correlation energy* is this overestimation of the ground-state energy as calculated by band theory due to its disregard of electron interactions. In certain cases—such as that of NiS_2—the correlation energy causes a material, which ought to be metallic according to band theory, to have an insulating ground state.

The criterion for the formation of such *Mott insulators* may be sketched as follows.[42]

†Incidentally, it was P. W. Anderson who coined the phrase "condensed matter physics," when he renamed his research group in 1967.[60]

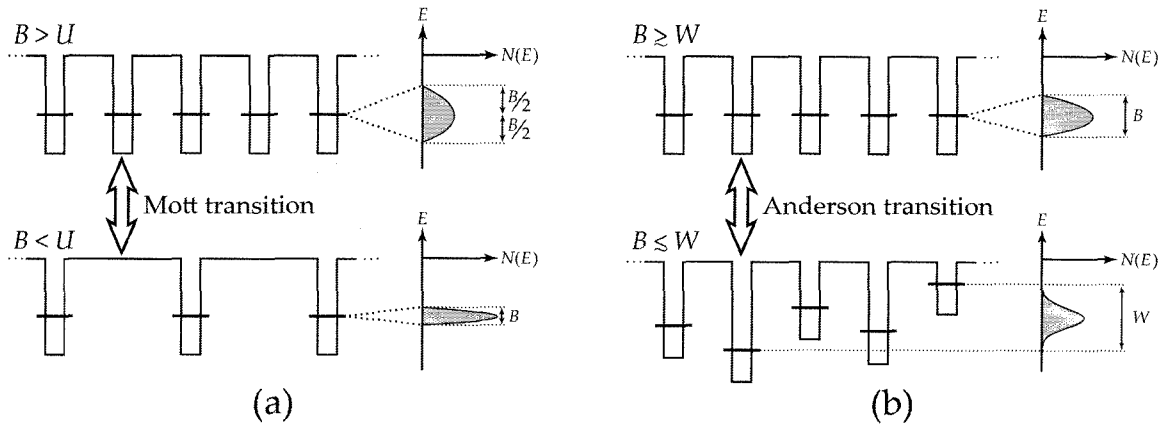

Fig. 1.15: Schematic illustrations of the Mott (a) and Anderson (b) M↔I transitions due to electron localisation. In both cases, the bandwidth of the orbital interactions is B, centred about the sharp ground-state energy of the isolated atoms, which is represented by the horizontal lines. In (a), if the lattice spacing in a metal is increased such that B becomes less than the correlation energy U, the material becomes a Mott insulator. For the Anderson transition shown in (b), all electrons become localised if the width of the random potential W greatly exceeds B (if $\frac{W}{B} \gtrsim 3$). (After Ref.[42].)

We represent the atoms in the crystal by a 1D linear array of identical potential wells, the valence electrons of which would reside in identical bound states for isolated wells. In the solid, however, interactions broaden these ground states into a band of width B, centred about the energy of the isolated case (Fig. 1.15a, top). The half-filling of the highest band therefore results in an average valence electron energy of approximately $-B/4$ with respect to the free atom ground state; the cohesion in solid metals is due to this *delocalisation*-induced lowering in energy. Since such a reduction in kinetic energy by smoothing of interfering wavefunctions requires overlap between the orbitals of neighbouring atoms to be effective, B is a function of the lattice constant a, tending to zero as $a \to \infty$. As mentioned before, there exists a correlation cost associated with doubly-occupying an atom, which we will call U ($U \approx 4.6$ eV for the atomic limit in Na). This is the result of the Coulomb repulsion between two electrons located on the same site, which raises the energy of the "second" electron. By the independent-electron nature of Bloch theory, the probability for an electron to occupy each site is equal, yielding probabilities of $\frac{1}{4}$, $\frac{1}{2}$, and $\frac{1}{4}$ for zero, one, and two electrons on a given atom, respectively. As such, the average potential-energy cost due to correlation is $U/4$ per electron. If this exceeds the reduction in energy due to delocalisation ($\sim B/4$), the material will be a Mott insulator. Thus, we may write the condition for correlation-induced localisation simply as

$$U > B \qquad \text{(Mott localisation).} \tag{1.7}$$

To summarise, for a large enough lattice spacing, the potential-energy cost of correlation wins out over the savings in kinetic energy due to delocalisation.

Bypassing the mathematical details of Anderson localisation, we may first consider it in analogy to the Mott transition just described. In the Anderson model,[62] the topological disorder of the amorphous solid enters in the form of *random site energies*: the energy E_j of site j is a stochastic variable, distributed according to a probability distribution with a characteristic width of W. This is shown schematically in Fig. 1.15b as a distribution of well depths with corresponding ground-state energies. W represents the maximum range of potential energies an electron could encounter in the solid, as a result of the variability

of atomic environments. The criterion for localisation, as shown by Anderson, is then embodied by the ratio W/B, the so-called *disorder parameter*: for W/B greater than a critical value on the order unity, *all* the valence band states become localised.

We may provide the barest précis of the model as follows.[42,62] We consider a lattice (disordered *or* periodic) of sites j described by the following Hamiltonian:

$$H = \sum_j E_j c_j^\dagger c_j + \sum_{j \neq k} V_{jk} c_j^\dagger c_k \tag{1.8}$$

where E_j is the energy of an electron occupying site j, V_{jk} is the interaction matrix element allowing an electron to "hop" from site k to site j, and $c_j^\dagger$ and c_j are the electron creation and annihilation operators for site j. For simplicity, we use a linear combination of atomic orbitals (LCAO) expansion for the electron wave function in terms of the atomic orbitals $|\Phi_j\rangle$ centred about each site j: $\psi = \sum_j a_j |\Phi_j\rangle$. We assume ψ is an eigenfunction of Eq. (1.8), satisfying $H\psi = E\psi$, to obtain

$$Ea_j = E_j a_j + \sum_{j \neq k} V_{jk} a_k \tag{1.9}$$

The probability amplitude a_j that an electron is on site j therefore has a time dependence governed by

$$i\hbar \frac{da_j}{dt} = E_j a_j + \sum_{j \neq k} V_{jk} a_k \tag{1.10}$$

Anderson's procedure was to initially place an electron in $|\Phi_n\rangle$, that is, $a_n(0) = 1$, and investigate $a_n(t)$ as $t \to \infty$. If, in this limit, a_n remains finite, the wavefunction decaying rapidly with distance away from n, we say that such an electron is localised at site n (Fig. 1.16c).

It is usually instructive, when the general solution to a problem is particularly difficult, to look at some limiting cases; we do so here, using a 1D linear chain of atoms for simplicity. Noting that the effect of disorder is contained primarily in the stochastic nature of E_j, we lose nothing essential by adapting Eq. (1.9) to the simpler case of a periodic lattice. We further simplify the situation by only allowing nearest-neighbour hopping, viz. $V_{jk} = V_{\text{n.n.}}$ for the z possibilities of transfer to an adjacent atom, and zero otherwise:

$$Ea_k = E_k a_k + V_{\text{n.n.}} \sum_{\delta=1}^{z} a_{k+\delta} \tag{1.11}$$

where now, out of forethought, we use k as the site index.

The limiting case of $W = 0$ (i.e., all E_k equal) corresponds to the crystalline phase. For a 1D linear chain, $z = 2$; we therefore set all $E_k = 0$ to obtain

$$Ea_k = V_{\text{n.n.}}(a_{k-1} + a_{k+1}) \tag{1.12}$$

By Bloch theory, we assume a plane-wave solution of the form $a_k = a_0 e^{ik\phi}$, substituting into Eq. (1.12) to yield $E = 2V_{\text{n.n.}} \cos\phi$. As such, $E \in [-2V_{\text{n.n.}}, 2V_{\text{n.n.}}]$, and the bandwidth for the $z = 2$ case is $B = 4V_{\text{n.n.}}$. It can be shown that for higher dimensions,[42]

$$B = 2zV_{\text{n.n.}} \tag{1.13}$$

This expression for B therefore corresponds to the bandwidth sketched in the top portion of Fig. 1.15b, that is, the characteristic kinetic-energy term due to delocalisation.

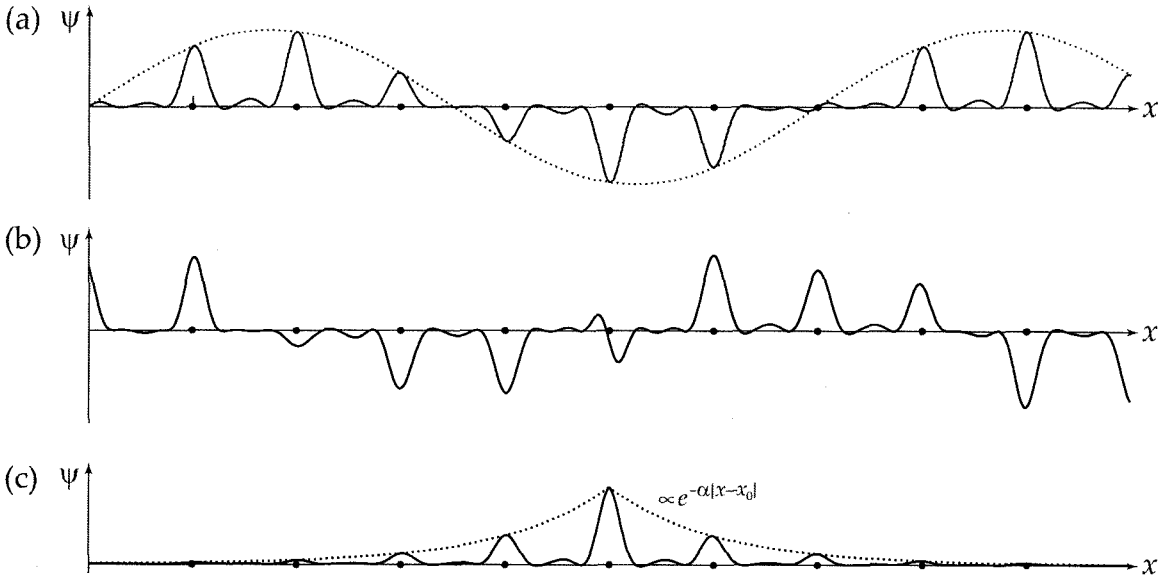

Fig. 1.16: Comparison of schematic wavefunction amplitudes for (a) extended states in a crystal, (b) extended states in an amorphous solid, and (c) localised states in an amorphous solid. The disorder inherent in amorphous materials causes frequent scattering of electrons between Bloch states, causing the extended state wavefunctions to lose phase coherence within a few lattice constants (b). A strongly-localised electron has a wavefunction whose envelope decays rapidly ($\propto e^{-\alpha|x-x_0|}$) with distance from the localisation site at x_0 (c); α is the inverse localisation length. (After Ref.[50])

The opposite limit, that of complete localisation, results if we turn off the hopping mechanism, viz. setting $V_{\text{n.n.}} = 0$. Electrons then remain in the orbital $|\Phi_j\rangle$ in which they are initially placed, yielding $E = E_j$ and $a_k = \delta_{jk}$, where δ_{jk} is the Kronecker delta.

To estimate the critical value of W/B resulting in localisation without delving into the minutiæ of Anderson's involved analysis, we can consider it in a heuristic treatment of non-degenerate perturbation theory, starting in the limit of complete localisation ($W/B \gg 1$), and considering $V_{\text{n.n.}}$ as a small perturbation. By first-order perturbation theory, the electron orbitals on adjacent atoms j and k are mixed with an amplitude on the order of $V_{\text{n.n.}}/(E_j - E_k)$, with higher-order terms corresponding roughly to powers of this expression.[42] For simplicity, we assume that E_j is at the centre of the energy distribution, of width W, with the energies E_k of the z nearest neighbours spaced uniformly across the band at intervals of W/z. The dominant contribution to $V_{\text{n.n.}}/(E_j - E_k)$ results from the smallest value of $|E_j - E_k|$, which, in this present case, would be $W/2z$ (for z odd). We therefore require, for the perturbation series to converge, that

$$\frac{2zV_{\text{n.n.}}}{W} < 1 \tag{1.14}$$

Since $B = 2zV_{\text{n.n.}}$ by Eq. (1.13), we return to the approximate condition for Anderson localisation, namely $W > B$.

A more detailed analysis reveals that the actual critical value of W/B for complete localisation is approximately 3.[50] Since $B \approx 5$ eV in typical amorphous semiconductors such as a-Si:H, this criterion is *not* met. However, it was later recognised by Mott[57] (among others) that even if the disorder potential is not sufficient to localise *all* electrons, localisation can still occur for states in the low-energy tails of the bands. The energies marking the boundary between the localised states in the band tails and the extended states in the

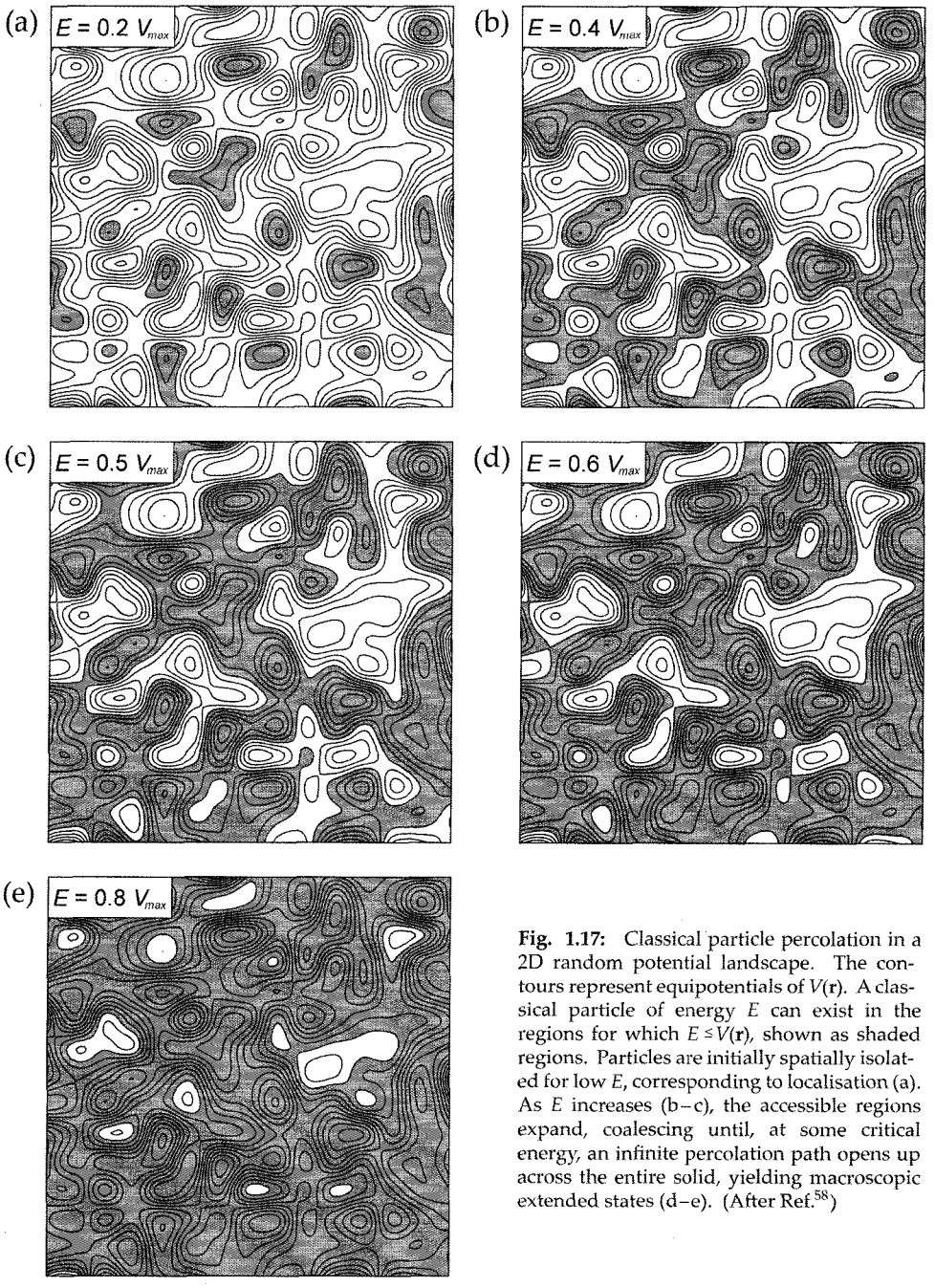

Fig. 1.17: Classical particle percolation in a 2D random potential landscape. The contours represent equipotentials of $V(\mathbf{r})$. A classical particle of energy E can exist in the regions for which $E \leq V(\mathbf{r})$, shown as shaded regions. Particles are initially spatially isolated for low E, corresponding to localisation (a). As E increases (b–c), the accessible regions expand, coalescing until, at some critical energy, an infinite percolation path opens up across the entire solid, yielding macroscopic extended states (d–e). (After Ref.[58])

valence and conduction bands are therefore called the *mobility edges*, shown as E_v and E_c in Fig. 1.13. An Anderson transition therefore results when the Fermi level is pushed through a mobility edge, due to changes in such parameters as composition, pressure, or an external electric field.[42]

There exists an intuitive analogy to the classical limit of the Anderson transition within the context of percolation theory.[63] We envision an amorphous solid as a potential landscape characterised by random (but smooth) fluctuations between $V(\mathbf{r}) = 0$ and $V(\mathbf{r}) = V_{\text{max}}$, as illustrated in 2D by the contour maps in Fig. 1.17. The motion of a classical particle of energy E is restricted to regions of space where $E \leq V(\mathbf{r})$ (shaded regions in

Fig. 1.17). At low E, all electrons are localised (Fig. 1.17a). As E increases, the accessible regions of space expand, gradually linking together until, at a critical value of E, which we denote E_c ($E_c \approx V_{\max}/2$ in this case), a percolation path opens up across the entire structure, such that the accessible region is now infinite in extent. The crossing from below this critical energy to above it corresponds to a localisation→delocalisation transition. It must be emphasised that this analogy is for the classical limit only: quantum-mechanical particles such as electrons are capable of tunnelling through thin classically-forbidden barriers. Also, the coexistence of localised and extended states at the same energy (for $E \gtrsim E_c$) is not permitted by quantum mechanics: such degenerate states would mix. Thus, in a real amorphous semiconductor, the extended and localised states are sharply divided at the mobility edges. For the *a*-Si NC films discussed in this thesis, it is Anderson localisation, rather than Mott localisation, which is responsible for the existence of localised states in the band tails.

1.2.3 Optical absorption in amorphous semiconductors

We conclude our survey of the key physical concepts of amorphous semiconductors with a short discussion on their optical properties. Measuring the response of a material to light as a function of frequency ν (or wavelength λ or energy $h\nu$, equivalently) is one of the most basic experimental approaches to investigate electronic and vibrational characteristics of condensed matter. The optical properties embodied in such a response are important both in providing valuable information as to the basic nature of the material, as well as being relevant to technological applications of amorphous solids such as waveguiding structures and photovoltaic devices. In this section, we will restrict our discussion to the energy range corresponding to electronic excitations, viz. from energies on the order of the bandgap to some tens of eV higher.

In general, two functions are required to describe the total spectral response, providing information both about its phase and its amplitude. Typically, the real and imaginary parts of the complex dielectric constant, $\epsilon(\nu) = \epsilon_1(\nu) + i\epsilon_2(\nu)$, or of the complex index of refraction, $N(\nu) = n(\nu) - ik(\nu)$, are used for this purpose; these two quantities are related via $N^2(\nu) = \epsilon(\nu)$.[42†] These functions are typically probed by absorption and reflectivity measurements, although, for a weakly-absorbing thin film on a transparent thick substrate, the optical constants $n(\nu)$ and $k(\nu)$, as well as the film thickness d, can be obtained from a single *transmission* measurement (see Appendix B.1.2). In principle, $N(\nu)$ may be measured experimentally in a reflectivity measurement: for normal incidence, the complex reflectance coefficient is given by $R(\nu)^{1/2}e^{i\theta} = \frac{N-1}{N+1}$, where $R(\nu)$ is the reflectivity (the ratio of reflected vs. incident *intensity*). In an absorbing medium, the light intensity $I(x)$ decays exponentially via Beer's Law: $I(x) = I(0)e^{-\alpha(\nu)x}$, where $\alpha(\nu)$ is the absorption coefficient, in units of inverse length (typically specified in cm^{-1}), and x is the optical path length in the material.[‡] In the vicinity of a material's absorption edge, $\alpha(\nu) \approx (2\pi\nu/nc)\epsilon_2$, where c is the speed of light in a vacuum. As such, $\epsilon_2(\nu)$ is often used as a dimensionless representation of absorption.[42]

[†]Regarding the names of the optical constants composing $N(\nu)$, $n(\nu)$ is referred to, somewhat awkwardly, as the (real) index of refraction, and $k(\nu)$ is the extinction coefficient (not to be confused with the wavenumber k!).

[‡]Adding to the semantic confusion is the fact that $\alpha(\nu)$ is also sometimes called the extinction coefficient. We shall not do so here, reserving that name for the quantity k which forms the negative imaginary part of the complex index of refraction. α and k are related via $\alpha = 4\pi k/\lambda$.

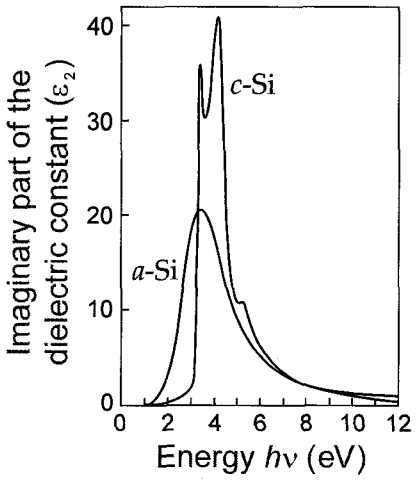

Fig. 1.18: A comparison of the strength of electronic transitions in c- and a-Si, here represented by the real part the dielectric constant, $\epsilon_2(h\nu)$. Although the bandgaps of both materials are ~1 eV, c-Si, as an indirect-gap semiconductor, is weakly absorbing until ~3 eV, at which point vertical transitions become possible. In contrast, a-Si, with no such restriction in **k**-space, exhibits significant absorption in the 1–3-eV range. (After Ref.[64].)

In crystalline semiconductors, the periodicity of the lattice places severe restrictions on the nature of absorption processes: only those transitions which conserve the wavevector **k** are allowed.† Non-vertical transitions on an $E(\mathbf{k})$ diagram can only occur by second-order processes: the deficit in momentum must be supplied by the creation or annihilation of phonons; such processes are much weaker—by orders of magnitude—than direct, first-order ("vertical") processes.[42] These limitations on **k** are the cause of the sharp features characteristic of crystalline reflectivity spectra, as illustrated in Fig. 1.10.

In amorphous semiconductors, however, the strong scattering caused by the structural disorder effects such a large uncertainty in **k** that the wavevector is no longer a good quantum number. As such, transitions can occur efficiently if the overlap of states in *real* space is sufficient,[50] causing the fine structure present in the absorption spectra of crystals to be absent for amorphous semiconductors. This relaxation of momentum-conservation rules also makes the distinction between direct and indirect bandgaps meaningless, as exemplified by silicon in Fig. 1.18. In both its amorphous and crystalline forms, the bandgap of Si is on the order of 1 eV. For a-Si, this energy corresponds to the mobility gap, whereas for c-Si, this is the minimum gap between valence and conduction bands (as shown in Fig. 1.1, these extrema occur at different values of **k**). Also from Fig. 1.1, it is seen that the minimum energy for vertical transitions is on the order of 3 eV; the restrictions on **k** therefore prevent significant absorption in c-Si between ~1 and ~3 eV. From the standpoint of solar-cell technology, this poses a problem, since the majority of solar radiation lies in this range. Contrariwise, interband electronic transitions in a-Si are allowed for all energies exceeding the mobility gap, greatly increasing its absorption in the 1–3-eV range with respect to the crystalline case. The high absorption coefficient ($> 10^5$ cm^{-1}) of a-Si is such that a thin (~1-μm) film is capable of absorbing the majority of solar radiation; for this reason, it is the material of choice for conventional large-scale solar-cell applications.[65]

Interband transitions in amorphous semiconductors often yield an upper absorption edge ($\alpha \gtrsim 10^4$ cm^{-1}) which may be described by a relation proposed by Tauc:[56]

$$\alpha h\nu \propto (h\nu - E_o)^2 \tag{1.15}$$

†To be precise, this is not *strictly* true: the absorption of a photon with momentum $\hbar\mathbf{q}$ *does* change the wavevector **k** of a Bloch electron by **q**; however, since typical values of $|\mathbf{q}|$ are in the 10^5 cm^{-1} regime, compared to ~10^8 cm^{-1} for $|\mathbf{k}|$ at the Brillouin zone edge, such transitions are essentially "vertical" on an $E(\mathbf{k})$ diagram.[41]

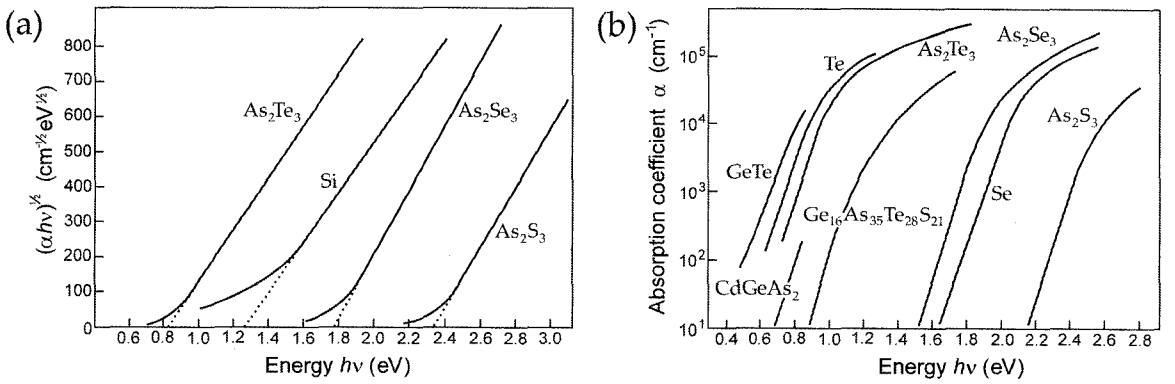

Fig. 1.19: Optical absorption edges for amorphous materials exhibiting (a) Tauc and (b) Urbach edges. In (a), the dashed lines indicate the extrapolation from the linear region used to obtain the optical gap E_o. In (b), the slope of the linear region can be used to extract the Urbach energy E_U. (After Ref.[44])

where E_o is the *optical gap* of the material, corresponding to the difference between the extrapolated extended state edges (the ends of the dotted curves in Fig. 1.13); as such, it is rather an underestimate of the mobility gap E_g. A *Tauc plot* of $(\alpha h\nu)^{1/2}$ vs. $h\nu$ yields E_o via an extrapolation of the linear portion of the graph (Fig. 1.19a). Since both band–band and tail–band transitions can contribute to α in the absorption regime used for Tauc plots, however, the value of E_o obtained using this technique may not represent the true value of the optical gap, although it is useful for tracking changes in the bandgap due to changes in parameters such as temperature or pressure.[43]

The lower absorption edge of amorphous semiconductors is typically characterised by an exponential energy dependence:[44]

$$\alpha \propto e^{h\nu/E_U} \tag{1.16}$$

where the *Urbach energy* E_U describes the slope of the band tails. For most amorphous semiconductors (excluding a-Ge and a-Si, however), E_U ≈10–25 eV, and is constant at room temperature.[43] It is tempting to attribute this behaviour to the fact that the band tail DOS functions are exponential with energy (i.e., $N(E) \propto \exp[E/2E_U]$). However, the remarkable similarity in values of E_U for a wide variety of amorphous semiconductors seems to bear against this interpretation (see Fig. 1.19b). Furthermore, many *crystalline* materials also exhibit Urbach edges, albeit with a somewhat more pronounced temperature dependence).[43†] One possible explanation[67] is that variations in local internal electric fields, due to even the small amount of disorder found in crystals, are sufficient to create wide, deep potential troughs into which the electrons bound in excitons can tunnel, the steady-state wavefunction amplitude being exponentially small in the vicinity of the hole. A Gaussian distribution in these microfield strengths would then yield an Urbach edge comparable to experimental observations.

The foregoing discussion of amorphous semiconductor physics has brought to light several important characteristics of the classes of materials discussed in the majority of this thesis, viz. amorphous silicon and silicon oxide glasses. At this point in the introduction,

†Urbach's original paper[66] commented on the near-constancy of E_U for crystalline AgBr, AgCl, Ge, TiO_2 and CdS: E_U was within a factor of two of k_BT for all of these materials, where T is the temperature and k_B is Boltzmann's constant.

however, we now turn to a second topic of relevance: materials doped with rare-earth elements.

1.3 Rare-earth-doped photonic materials

The lanthanides comprising atomic numbers 58 (Ce) through 70 (Yb) are important elements in photonic materials,† finding applications in fibre and waveguide optical amplifiers,[69–71] solid-state lasers,[71–73] novel display technologies,[74] and optical data storage,[75] among others. Even today, despite the efforts of the International Union of Pure and Applied Chemistry (IUPAC), these elements are still commonly referred to by their historical "rare earth" (RE) moniker, originating from the (erroneous) initial perception that they were much less abundant in the Earth's crust than more familiar metals such as lead or gold.[68‡] In this section, we introduce some of the key characteristics of (and notation for) the electronic structure of trivalent RE ions, illustrating how their unique qualities have been exploited in a variety of photonic applications.

1.3.1 Electronic configuration

The rare-earth elements mentioned above share a common feature with respect to their electronic configurations: a partially-filled $4f$ shell, relatively well-shielded from external electric fields by $5s^2$ and $5p^6$ electrons (see Table 1.2). Because of this shielding, the energy levels of the (usually trivalent) RE ions in solids are largely host-independent. As such, since the $4f$ electrons are essentially not involved in chemical bonding, an understanding of optical absorption and emission from RE^{3+} ions due to intra-$4f$ transitions may be approached principally in terms of the theory of *atomic* spectroscopy.[77] Such intra-$4f$ transitions are parity forbidden, but become weakly allowed due to the state-mixing effect of crystal-field interactions.[78] A detailed account of the electronic energy level structure of the RE^{3+} series was published by G. H. Dieke *et al.* in 1968;[79] these results are summarised most conveniently in so-called "Dieke diagrams," as shown in Fig. 1.20, which has since become an invaluable tool for all researchers of materials doped with rare earths. The levels of free RE ions are sharp; in a solid, however, each level is split into a manifold of sublevels (*crystal-field splitting*), which, due to thermal broadening, forms a band which is nearly continuous.[80]

The *term symbol* notation used to label the RE^{3+} ion energy levels in Table 1.2 and Fig. 1.20 warrants some explanation. Such notation is used for atomic states of multi-electron atoms described by the LS (or Russell-Saunders) coupling scheme, in which spin–orbit interactions are small relative to Coulomb interactions between electrons.[77] In this scheme, the orbital (**L**) and spin (**S**) contributions to the total angular momentum are obtained by summing the relevant momenta of each electron independently. That is, for a free

†For this discussion, we shall adopt a rather broad definition of *photonics*, allowing it to refer to any technology in which the photon plays an analogous role to the electron in *electronics*. Such a definition includes light generation and detection, communications, and optical computing applications.[68]

‡Because they are often present in relative abundance in the same ores containing the lanthanides listed above and/or possess many chemical properties similar to those elements, lanthanum (La, Z=57), yttrium (Y, Z=39), and scandium (Sc, Z=21) are sometimes included as rare earths.[76]

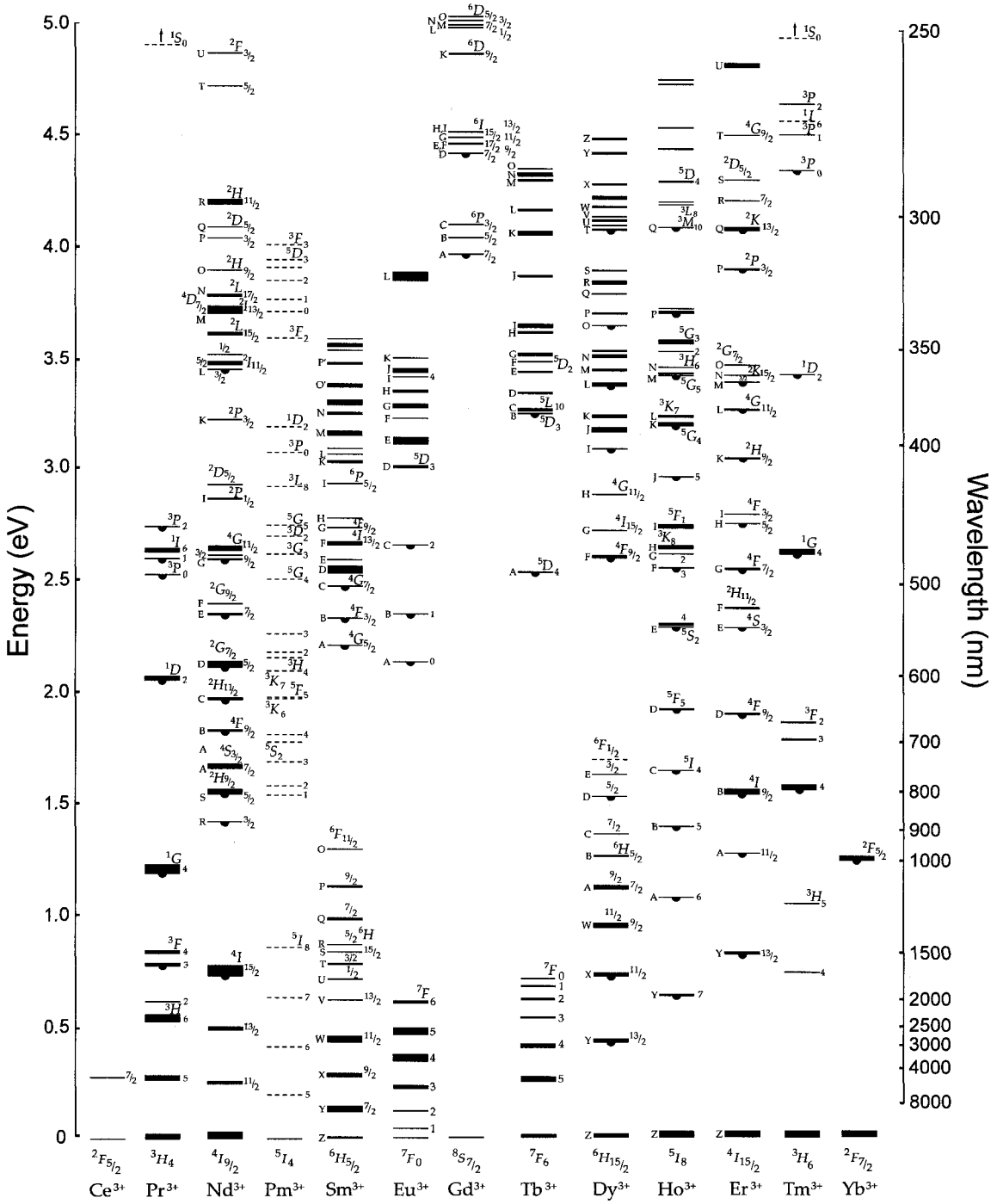

Fig. 1.20: "Dieke" diagram of energy level structure for trivalent rare earth ions (cerium through ytterbium) in a crystalline $LaCl_3$ host. The crystal-field splitting of each level is indicated by the thickness of the line, and a hanging semicircle denotes a radiative transition (in $LaCl_3$) from that level to the ground state. Dashed lines indicate estimates from less complete data. (After Ref.[79])

Table 1.2: Energy configurations and ground state term symbols for trivalent rare earth ions. (After Ref.[77])

Atomic number	Chemical symbol	Element	RE^{3+} electronic configuration	RE^{3+} ground state term symbol
57	La	Lanthanum	$4f^0$	$^1S_0$
58	Ce	Cerium	$4f^1$	$^2F_{5/2}$
59	Pr	Praseodymium	$4f^2$	$^3H_4$
60	Nd	Neodymium	$4f^3$	$^4I_{9/2}$
61	Pm	Promethium	$4f^4$	$^5I_4$
62	Sm	Samarium	$4f^5$	$^6H_{5/2}$
63	Eu	Europium	$4f^6$	$^7F_0$
64	Gd	Gadolinium	$4f^7$	$^8S_{7/2}$
65	Tb	Terbium	$4f^8$	$^7F_6$
66	Dy	Dysprosium	$4f^9$	$^6H_{15/2}$
67	Ho	Holmium	$4f^{10}$	$^5I_8$
68	Er	Erbium	$4f^{11}$	$^4I_{15/2}$
69	Tm	Thulium	$4f^{12}$	$^3H_6$
70	Yb	Ytterbium	$4f^{13}$	$^2F_{7/2}$
71	Lu	Lutetium	$4f^{14}$	$^1S_0$

ion with N electrons, the total orbital and spin angular momentum operators are given by

$$\mathbf{L} = \sum_{k=1}^{N} \boldsymbol{l}_k \tag{1.17}$$

and

$$\mathbf{S} = \sum_{k=1}^{N} \boldsymbol{s}_k \tag{1.18}$$

where $\boldsymbol{l}_k$ and $\boldsymbol{s}_k$ are the orbital and spin operators of the kth electron. The total angular momentum operator, $\mathbf{J}$, is then given by

$$\mathbf{J} = \mathbf{L} + \mathbf{S} \tag{1.19}$$

The electronic state of the ion are frequently summarised by the term symbol of the form $^{2S+1}L_J$, where S and J are labelled with their numerical values, and L is labelled with a capital letter: $L = 0, 1, 2, 3, 4, 5, \ldots$ are denoted by S, P, D, F, G, H, $\ldots$ (alphabetically thereafter, with J omitted), respectively.

The ground-state electronic configuration, and associated term symbol, may be determined by the use of *Hund's rules*, one formulation of which is as follows (paraphrased from Refs.[41,81]):

1. The configuration with the greatest total spin S, consistent with the Pauli exclusion principle, has the lowest energy.

2. The configuration with the greatest total orbital angular momentum L, consistent with the Pauli exclusion principle and Rule 1, has the lowest energy.

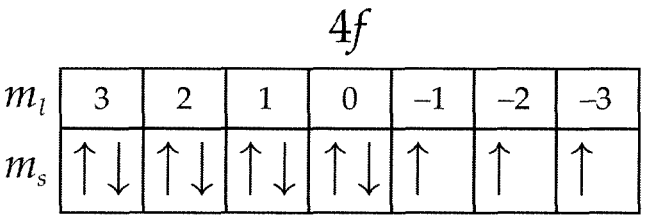

Fig. 1.21: Lowest-energy electron configuration for $4f^{11}$, using Hund's first two rules. ↑ (↓) represents an electron with $m_s = +\frac{1}{2}$ $(-\frac{1}{2})$.

3. The value of the total angular momentum J resulting in the lowest energy will be $|L - S|$ if the subshell is less than half-filled, and $L + S$ if the subshell is more than half-filled.

It is illustrative to work out an example; we now do so for the ground state of Er^{3+}, which has 65 electrons given by the configuration [Xe]$4f^{11}$. We need only consider the partially-filled $4f$ shell, since the filled $5s$ and $5p$ shells do not contribute any net angular momentum. By Hund's first and second rules, we begin filling the 14 available $4f$ states by assigning seven electrons with maximum spin (i.e., $m_s = +\frac{1}{2}$) to the different m_l states; by the Pauli exclusion principle, the remaining four electrons must have $m_s = -\frac{1}{2}$, which we assign to the highest m_l states. This situation is shown in Fig. 1.21, where ↑ represents a spin $+\frac{1}{2}$ electron and ↓ represents a spin $-\frac{1}{2}$ electron. The total spin of the configuration is the sum of the m_s values for the unpaired electrons: $S = \frac{3}{2}$. Similarly, the total orbital angular momentum is $3+3+2+2+1+1+0+0-1-2-3 = 6$, which is specified by the letter I. Since the shell is more than half filled, $J = L + S = 6 + \frac{3}{2} = \frac{15}{2}$ by Hund's third law, yielding a term symbol for the ground state of Er^{3+} of $^4I_{15/2}$, in agreement with Table 1.2. We will now discuss some of the many energy-transfer processes by which intra-$4f$ transitions in RE^{3+} ions may be excited.

1.3.2 Energy transfer processes

Direct optical excitation of RE ions in glassy hosts is a relatively weak process (compare absorption cross-sections of $\sigma \approx 10^{-21}$ cm^2 for Er^{3+} in SiO_2 with $\sigma \approx 4 \times 10^{-16}$ cm^2 for rhodamine 6G in ethanol[82]). However, the process of indirect RE excitation, that is, via energy transfer from another species (such as a Si NC or another RE ion), can be much more efficient. In such cases, the energy is said to be transferred from a *sensitiser* (or *donor*) to an *activator* (or *acceptor*).[83] For isolated ions, transitions occurring during optical absorption and luminescence are (to within energies of the order k_BT) of the Stokes type, in which emitted photons have lower energies than those which were absorbed. *Interacting* RE ions, however, are capable of anti-Stokes behaviour due to sensitiser–activator coupling effects, resulting in the upconversion of luminescence from the NIR to the visible or UV regions of the spectrum.[84]

Several such energy transfer processes are known to exist, which may be broadly divided into those in which the activators are initially in their ground states, and those in which they are initially excited; these are illustrated in Fig. 1.22. Unfortunately, there exists a great deal of inconsistency in the literature with respect to the naming of these mechanisms. We will therefore discuss the circumstances in which each process in Fig. 1.22 may occur, indicating the various names by which they have been known, and clarifying, for the purposes of this thesis, the nomenclature we shall use.

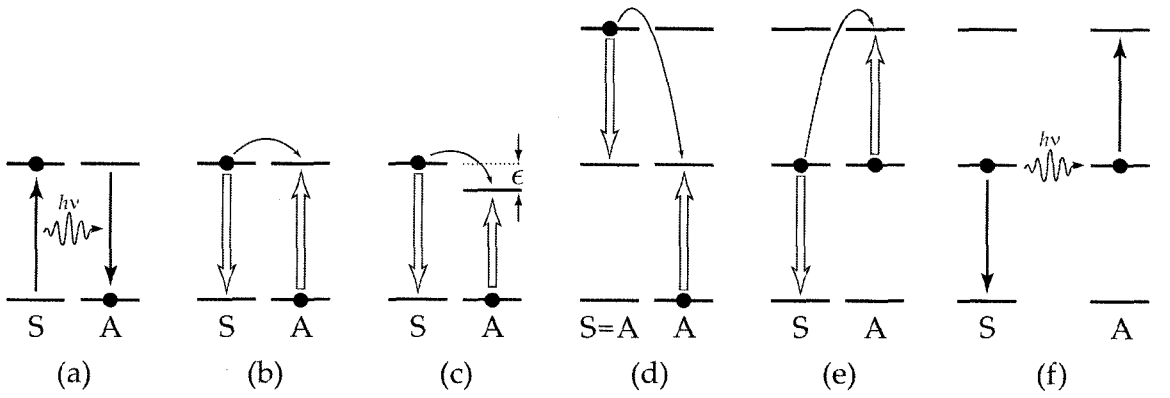

Fig. 1.22: Energy transfer processes between a sensitiser (S) and an activator (A). Hollow arrows denote a non-radiative transition due to an interaction (electrostatic, magnetostatic, exchange) between S and A. Resonant radiative transfer processes are of type (a): radiative recombination of S and subsequent absorption of the photon by A. In (b), the process is non-radiative (e.g. electric multipole interactions). Situation (c) is the non-resonant case of (b): the difference in energy ϵ is compensated for by the creation or annihilation of phonons. In (d), two identical ions interact, both relaxing to excited states. Both S and A are initially excited in (e); the recombination of S pushes A into a higher excited state. In (f), an initially-excited A absorbs a photon resulting from the radiative recombination of S. (After Ref.[84])

A simple resonant, radiative process between two species is of the type shown in Fig. 1.22a. The activator A, initially in its ground state, absorbs a real photon (resonant with one of its transitions) which resulted from the radiative recombination of the sensitiser S. In such a case, the origin of the photon (i.e., whether from S or from some other source) is incidental; as such, the efficiency of this process is governed simply by the absorption cross-section of A.[†] The probability of such a transfer between an S and an A separated by a distance R is therefore given by[84]

$$p_{SA} = \frac{\sigma_A}{4\pi R^2}\frac{1}{\tau_S}\int g_S(\nu)g_A(\nu)\,d\nu \tag{1.20}$$

where σ_A is the integrated absorption cross-section of the activator, τ_S is the radiative lifetime of the sensitiser, $g_S(\nu)$ is the emission spectrum of S, and $g_A(\nu)$ is the absorption spectrum of A. Note the $1/R^2$ dependence of this probability.

In (b), as in (a), the de-excitation of S results in the excitation of A, but in this case, *no* real photon is emitted. Instead, this non-radiative energy transfer is effected by electrostatic, magnetostatic, or exchange interactions between S and A. With respect to electrostatic interactions, the dipole–dipole case was first examined by Förster; as such, transitions of this sort are often referred to as *Förster transfer.*[85] The theory of this mechanism was later extended to multipole and exchange interactions by Dexter.[86] Experimentally, situation (a) can be differentiated from (b) in three ways.[83] First, in (a), since the absorption (by activators) of photons emitted from sensitisers is dependent on the photon path length within the medium, the activator emission intensity is a function of the size and shape of the specimen; in particular, as the specimen volume increases, the luminescence yield does likewise. In (b), since the probability of transfer is short-range, the emission intensity of the activators is independent of volume. Second, depending on the spectral overlap between $g_S(\nu)$ and $g_A(\nu)$, the observed shape of the emission spectrum from the sensitisers

[†]Here we are considering the probability of radiative transfer from a single sensitiser to a single activator; for a real specimen containing many sensitisers and activators, the overall efficiency of the process would also be dependent on the specimen size and shape.

will change with activator concentration if the excitation transfer is of the radiative type; for processes of type (b), the spectral shape of S emission remains unchanged. Third, in (b), the non-radiative transfer from S to A constitutes a competitive de-excitation pathway with respect to the sensitisers' intrinsic radiative de-excitation, shortening the observed luminescence lifetime of S increasingly as the concentration of A (n_A) is itself increased; in (a), the radiative recombination occurs as usual, unaffected by the presence of A, yielding τ_S independent of n_A.

For electric multipole interactions of the type described by Dexter,[86] the transfer probability may be written in the form

$$p_{SA} = \frac{1}{\tau_S}\left(\frac{R_0}{R}\right)^S \tag{1.21}$$

where R_0 is the characteristic distance for which the probabilities of energy transfer and radiative de-excitation are equal, and the value of S depends on the nature of the multipole interaction: for dipole–dipole interactions, $S = 6$; for dipole–quadrupole, $S = 8$; for quadrupole–quadrupole, $S = 10$.

Because it depends on the overlap between the relevant S and A electron wavefunctions, the probability for transfer due to electron exchange effects (sometimes referred to as *Dexter transfer*) decays exponentially with S–A separation:

$$p_{SA} \propto e^{-R/R_c} \tag{1.22}$$

where R_c is a parameter related to the wavefunctions of S and A. This mechanism is therefore very weak unless S and A are extremely closely spaced.[86]

For all of the non-radiative energy transfer processes (Fig. 1.22b–e), the identity of the dominant mechanism (i.e., electrostatic, magnetostatic, exchange) depends on the nature of the transition (forbidden or allowed) and the S–A spacing.

If S and A are identical RE ions, processes of the type sketched in Fig. 1.22b result in the diffusion of energy throughout the ensemble. In this context, the process is often called *energy migration* or *pair-induced quenching*,[69] since it becomes increasingly likely that a non-radiative quenching centre will be encountered as migration becomes more effective. The name of this process is sometimes also called *cross-relaxation*, although this term unfortunately is also used to refer to a variety of other energy transfers between identical ions; as such, we will reserve this term for a specific situation, as explained later.†

The situation shown in Fig. 1.22c is similar to that of Fig. 1.22b, except that there is now an energy mismatch ϵ between the S and A transitions. For RE ions in host solids, such a process becomes allowed via interactions with phonons: the discrepancy in energy is compensated for by the creation or annihilation of phonons; the former situation is illustrated in Fig. 1.22c. Small energy mismatches on the order of 100 meV can be accommodated by one or two phonons with energies near $k_B\Theta_D$, where Θ_D is the Debye temperature of the solid.[84] For multiphonon-assisted transfer, the probability has been shown to exhibit an exponential dependence on the energy mismatch:[88] $p_{SA} \propto e^{-\beta\epsilon}$, where β is related to the non-radiative decay parameters and the phonon occupation number.[84] As a function of temperature, the transfer rate may therefore be written in the form

$$w_{SA}(T) = w_{SA}(0)\left\{1 - \exp\left[-\hbar\omega/k_BT\right]\right\}^{-N} \tag{1.23}$$

†For a discussion on such semantic difficulties relating to nomenclature, the reader is referred to Chap. 8 of Ref.[87].

for a N-phonon process, where $\hbar\omega$ is the energy of the dominant phonon contributing to the transfer and $w_{SA}(0)$ is the zero-temperature transfer rate.[88]

Interactions within ensembles of the same RE ion (i.e., the sensitiser and acceptor ions are identical) of the general type shown in Fig. 1.22d are often referred to as *cross-relaxation* processes.[84,89] According to some authors,[89] the defining characteristic of cross-relaxation is that the final configuration, after the transfer, involves both ions being in an excited state (i.e., a downconversion process); this is the definition which will be used in this thesis. As alluded to above, however, "cross-relaxation" is often treated rather more casually: it has also been used to describe energy transfers of type (b)[84] and (e);[69,90] we will not do so here.

Processes described schematically by Fig. 1.22e have been given different names, depending on the identities of S and A. For S and A identical, it is frequently called *cooperative upconversion*; such a mechanism is responsible for the red/NIR and green emission commonly observed from Er-doped waveguide structures pumped at 1.48 μm.[69,91] In such cases, if resonant with respect to the spacings between the higher energy levels, two adjacent excited ions may interact, one de-exciting and transferring its energy to the second to excite it further; the second ion may then de-excite radiatively to its ground state, yielding a photon of higher energy than the pump photons (an anti-Stokes process). Referring to Fig. 1.20, it may be seen that the $^4I_{13/2} \rightarrow ^4I_{15/2}$ transition energy is very close to that of the $^4I_{13/2} \rightarrow ^4I_{11/2}$ transition, allowing upconversion from 1.53 μm to ~800 nm. Similarly, two Er^{3+} ions excited to the $^4I_{11/2}$ state may couple to yield upconverted ~540-nm emission from $^2H_{11/2} \rightarrow ^4I_{15/2}$ and $^4S_{3/2} \rightarrow ^4I_{15/2}$ transitions. Auzel[84] prefers to call this process the *APTE effect*, from the French *addition de photons par transfert d'énergie*; not surprisingly, perhaps, it has also been called cross-relaxation.[69,90] In this thesis, *cooperative upconversion* will be used.

If S and A are *not* the same species, the non-radiative process shown in in Fig. 1.22e is sometimes called *excited-state absorption* (ESA); such is the terminology of Kenyon and coworkers when describing re-excitation of Er^{3+} from $^4I_{13/2}$ to $^2H_{11/2}$ and $^2S_{3/2}$ via transfer from Si NCs emitting in their ~800-nm band.[92,93] However, "absorption" tends to recall the absorption of real photons, rather than a non-radiative electric multipole or exchange interaction. As such, we will reserve *excited-state absorption* for processes of type (f), regardless of the origin of the photon incident on A,[84] and refer to those of type (e), in which S and A are different, as *excited-state excitation* (ESE).[94]

The foregoing energy-transfer processes are known to be active in many glass systems doped with RE ions, though there can be a great deal of difficulty in determining the details of which mechanism is principally responsible for the observed RE emission.[†] This has not, however, prevented the development of several technologically-important applications exploiting the properties of rare earths, a few examples of which we will use to conclude this section.

1.3.3 Applications

From the 1940s until quite recently, the primary commercial application employing the unique electronic characteristics of the rare earths were the production of strong permanent magnets: the partially-filled $4f$ shells of the lanthanides cause them to have magnetic

[†]During Symposium C of the 2005 European Materials Research Society (E-MRS) Spring Meeting, devoted to rare-earth-doped photonic materials, the discussion regarding the mechanism of energy transfer from Si NCs to RE ions was once rather colourfully referred to as a "theological debate."

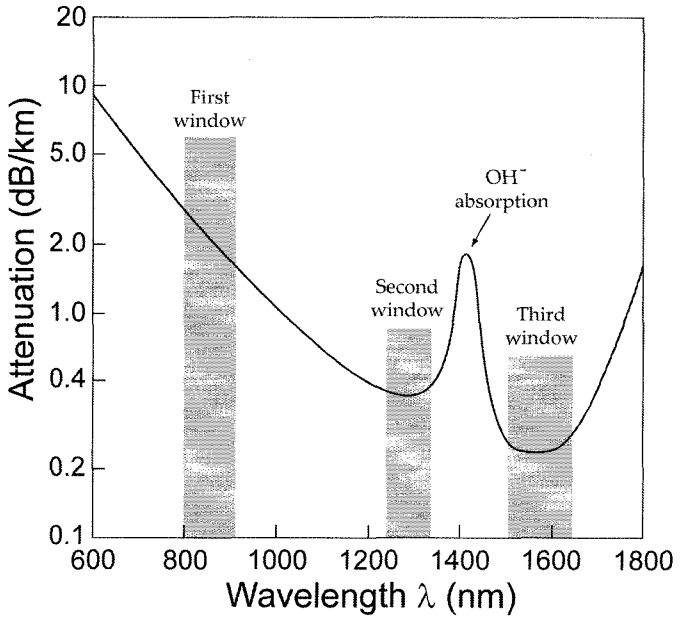

Fig. 1.23: Loss spectrum of conventional silica optical fibres, indicating the three transparency windows at 800 nm, 1.3 μm, and 1.5 μm. While the locations of the second and third windows is obvious from this graph, forming local and global minima, respectively, on either side of an absorption peak at ~1.4 μm due to OH^- ions, the definition of the first window is not; it indicates the position of a local minimum (of ~4.0 dB/km) which existed in the fibres used in the early optical networks of the 1970s. (After Ref.[80].)

moments which are among the highest of all the elements.[68] However, as increasing bandwidth requirements for communications systems have incited intense worldwide research interest in photonic materials, it is the *optical* properties of rare-earth ions which have now come to the forefront.[95] We will therefore provide a brief list of some of the more important applications.

Optical amplifiers

The main wavelength range used in modern long-haul optical communication networks is centred about ~1.5 μm, the so-called third transparency window for minimum signal attenuation in conventional silica optical fibres (see Fig. 1.23). To maintain a detectable signal intensity, amplification is required for optical fibres exceeding ~80 km in length. In early fibre networks (1980s), such amplification was achieved using optical–electrical–optical transducers called repeaters: the incoming (weak) optical signal was detected, converted to an electrical signal, amplified electronically, and converted back into an optical signal.[71] All-optical amplifier technology made its advent in the late 1980s, permitting the amplification of several wavelength division multiplexed channels within the same fibre. Most notable among such optical amplifiers are erbium-doped fibre amplifiers (EDFAs), taking advantage of the $^4I_{13/2} \rightarrow {}^4I_{15/2}$ transition in Er^{3+} which peaks in intensity near 1540 nm. In commercial systems, the population inversion required for amplification is effected by a laser diode pump at 980 nm (exciting to the $^4I_{11/2}$ level) and/or 1480 nm (exciting to the upper region of the $^4I_{13/2}$ manifold). The amplification regions of industrial EDFAs are quite long (typically ~20–50 m)[71] due to the weak coupling of the Er^{3+} ions with light; much research effort has been spent on developing compact, robust Er-doped *waveguide* amplifiers (EDWAs) for integrated photonics,[69,70,91,96,97] some using Si NCs as sensitisers. As yet, however, no commercially-viable Si-NC:Er EDWA devices have been fabricated, though it has been demonstrated that such devices should in principle be possible.[70]

Table 1.3: Typical intra-$4f$ transitions used in RE-doped solid-state lasers.[72,99]

RE ion	Transition	Wavelength
Pr^{3+}	$^3P_{0,1} \rightarrow {}^3H_4$	490 nm
	$^3P_{0,1} \rightarrow {}^3H_5$	520 nm
	$^3P_{0,1} \rightarrow {}^3F_2, {}^3H_6$	630 nm
	$^1G_4 \rightarrow {}^3H_5$	1.3 μm
Nd^{3+}	$^2P_{3/2} \rightarrow {}^4I_{9/2}$	381 nm
	$^4F_{3/2} \rightarrow {}^4I_{9/2}$	870–950 nm
	$^4F_{3/2} \rightarrow {}^4I_{11/2}$	1.05–1.12 μm
	$^4F_{3/2} \rightarrow {}^4I_{13/2}$	1.3–1.4 μm
	$^4F_{3/2} \rightarrow {}^4I_{15/2}$	1.74–2.13 μm
Er^{3+}	$^2H_{11/2}, {}^4S_{3/2} \rightarrow {}^4I_{15/2}$	550 nm
	$^2H_{11/2}, {}^4S_{3/2} \rightarrow {}^4I_{13/2}$	850 nm
	$^4I_{13/2} \rightarrow {}^4I_{15/2}$	1.53–1.60 μm
Tm^{3+}	$^1G_4 \rightarrow {}^3H_6$	460 nm
	$^1G_4 \rightarrow {}^3F_4$	650 nm
	$^1G_4 \rightarrow {}^3H_5$	790 nm
	$^3F_4 \rightarrow {}^3H_6$	1.9 μm
Yb^{3+}	$^2F_{5/2} \rightarrow {}^2F_{7/2}$	980 nm

Solid-state lasers

There are many solid-state laser materials which rely on rare-earth element transitions, some of which—such as the ubiquitous Nd:YAG system (yttrium aluminum garnet: $Y_3Al_5O_{12}$) emitting at 1064 nm—are now well-established technologies.[72] Fibre lasers doped with Tm (typical operating wavelength of 1.9 μm) or Yb and/or Er (980 nm or 1.5 μm) are also commercially available, with output powers exceeding 100 watts not uncommon.[†] There is also interest in RE-based lasers emitting in the UV-visible, a more difficult spectral range in which to achieve efficient lasing.[72] Examples of the the more important RE-doped systems used for such visible lasers are Pr-, Tm-, Er-doped, $YLiF_4$ crystals and fluorozirconate (ZBLAN) glass fibres (with or without Yb codoping); for UV emission, Nd-doped ZBLAN fibre lasers have been demonstrated at room temperature.[98] Table 1.3 summarises some of the laser wavelengths possible due to intra-$4f$ transitions in trivalent RE ions.

Probes of material properties

Apart from being useful dopants for the above-mentioned photonic applications, the lanthanides—especially erbium—can also serve as sensitive probes of a variety of material properties.[100] Er and Pr can be used to track the point-defect density in a-Si via segregation and trapping experiments; in a similar fashion, Er and Ho can track and modify the segregation of O in the same host material. The concentration of OH^- (an insidious quenching centre in silica fibres and waveguides) can be probed by looking at the lifetime of the 1.5-μm PL from Er-doped silica, since the energy of the $^4I_{13/2} \rightarrow {}^4I_{15/2}$ transition is resonant with a vibrational stretching mode of OH^-. A similar quenching effect on the lifetime of this transition can also be used to track radiation damage, the radiation-induced

[†]See, for example, the fibre lasers offered by IPG Photonics (www.ipgphotonics.com).

defects constituting a competitive non-radiative de-excitation pathway. Although the relative spacing of the energy levels in the lanthanides is relatively host independent, the crystal-field splitting of the levels can vary rather significantly due to changes in the ion's local environment. As such, the spectral width and shape of the RE PL can serve as a probe of the short-range order of the host matrix. For example, the PL from Er^{3+} in single crystals is characterised by sharp peaks, as opposed to the smoother, broadened emission typical in amorphous hosts. Furthermore, quantitative structural data for the host can be obtained from EXAFS measurements on Er. While most RE-based material property characterisation experiments have been performed using Er,[†] the commonality of the filled $5s$ and $5p$ outer shells make similar measurements possible, in principle, for most of the rare earths.

1.4 Conclusion

The optical properties of silicon nanocomposites doped with RE ions are interesting both in terms of fundamental physics and technological applications. In this chapter, we have introduced some basic concepts pertaining to amorphous semiconductors and the rare earths which are important in the context of the remainder of the thesis. Having done so, we now bring this exposition to a close, and present to the reader several developmental episodes on the subject of RE-doped Si nanocomposites. These six ensuing chapters will explain several semi-independent, yet related, aspects of this versatile nanostructured material system, with further elaboration and details of calculations being found in the Appendices.

Bibliography

[1] F. K. Lutgens and E. J. Tarbuck, *Essentials of geology*, Prentice Hall, Harlow, England, ninth edition, 2005, ISBN: 0-131-49749-9, p. 44.

[2] H. Dawson and R. Flagella, "Polycrystalline silicon capable of yielding long lifetime single crystalline silicon", *U.S. Patent 4921026*, 1990.

[3] G. Moore, "Cramming more components onto integrated circuits", *Electronics*, 19 April 1965.

[4] G. T. Reed and A. P. Knights, *Silicon photonics: an introduction*, John Wiley and Sons, Ltd., Chichester, England, 2004, ISBN: 0-470-87034-6.

[5] R. H. Havemann and J. A. Hutchby, "High-performance interconnects: an integration overview", *Proc. IEEE*, vol. 89, no. 5, pp. 586–601, 2001.

[6] N. Savage, "Linking with light", *IEEE Spectrum*, vol. 39, no. 8, pp. 32–36, 2001.

[7] S. V. Gaponenko, *Optical properties of semiconductor nanocrystals*, Cambridge University Press, Cambridge, 1998, ISBN: 0-521-58241-5.

[8] I. Mihalcescu, J. C. Vial, A. Bsiesy, F. Muller, R. Romestain, E. Martin, C. Delerue, M. Lannoo, and G. Allan, "Saturation and voltage quenching of porous-silicon luminescence and the importance of the Auger effect", *Phys. Rev. B*, vol. 51, no. 24, pp. 17605–17613, 1995.

[9] J. I. Pankove, *Optical processes in semiconductors*, Dover, Mineola, 1971, ISBN: 0-486-60275-3.

[†] See the rather hyperbolically-titled article "Erbium as a probe of everything?" by A. Polman.[100]

[10] J. R. Chelikowsky and M. L. Cohen, "Nonlocal pseudopotential calculations for the electronic structure of eleven diamond and zinc-blende semiconductors", *Phys. Rev. B*, vol. 14, no. 2, pp. 556–582, 1976.

[11] C. Pickering, M. I. J. Beale, D. J. Robbins, P. J. Pearson, and R. Greef, "Optical studies of the structure of porous silicon films formed in p-type degenerate and non-degenerate silicon", *J. Phys. C*, vol. 17, no. 35, pp. 6535–6552, 1984.

[12] L. T. Canham, "Silicon quantum wire array fabrication by electrochemical and chemical dissolution of wafers", *Appl. Phys. Lett.*, vol. 57, no. 10, pp. 1046–1048, 1990.

[13] D. Kovalev, H. Heckler, G. Polisski, and F. Koch, "Optical properties of Si nanocrystals", *Physica Stat. Sol. B*, vol. 215, no. 2, pp. 871–932, 1999.

[14] K. A. Littau, P. J. Szajowski, A. J. Muller, A. R. Kortan, and L. E. Brus, "A luminescent silicon nanocrystal colloid via a high-temperature aerosol reaction", *J. Phys. Chem.*, vol. 97, no. 6, pp. 1224–1230, 1993.

[15] D. Amans, S. Callard, A. Gagnaire, J. Joseph, G. Ledoux, and F. Huisken, "Ellipsometric study of silicon nanocrystal optical constants", *J. Appl. Phys.*, vol. 93, no. 7, pp. 4173–4179, 2003.

[16] L. Patrone, D. Nelson, V. I. Safarov, M. Sentis, W. Marine, and S. Giorgio, "Photoluminescence of silicon nanoclusters with reduced size dispersion produced by laser ablation", *J. Appl. Phys.*, vol. 87, no. 8, pp. 3829–3837, 2000.

[17] K. Watanabe, K. Sawada, M. Koshiba, M. Fujii, and S. Hayashi, "Photoluminescence decay-dynamics of Si nanoparticles prepared by pulsed laser ablation", *Appl. Surf. Sci.*, vol. 197, pp. 635–638, 2002.

[18] A. G. Nassiopoulos, S. Grigoropoulos, D. Papadimitriou, and E. Gogolides, "Light emission from silicon nanostructures produced by conventional lithographic and reactive ion etching techniques", *Physica Stat. Sol. B*, vol. 190, no. 1, pp. 91–95, 1995.

[19] J. P. Wilcoxon, G. A. Samara, and P. N. Provencio, "Optical and electronic properties of Si nanoclusters synthesized in inverse micelles", *Phys. Rev. B*, vol. 60, no. 4, pp. 2704–2714, 1999.

[20] D. S. English, L. E. Pell, Z. H. Yu, P. F. Barbara, and B. A. Korgel, "Size tunable visible luminescence from individual organic monolayer stabilized silicon nanocrystal quantum dots", *Nano Lett.*, vol. 2, no. 7, pp. 681–685, 2002.

[21] E. Neufeld, S. Wang, R. Apetz, C. Buchal, R. Carius, C. W. White, and D. K. Thomas, "Effect of annealing and H_2 passivation on the photoluminescence of Si nanocrystals in SiO_2", *Thin Solid Films*, vol. 294, no. 1–2, pp. 238–241, 1997.

[22] A. Hryciw, A. Meldrum, K. S. Buchanan, and C. W. White, "Effects of particle size and excitation spectrum on the photoluminescence of silicon nanocrystals formed by ion implantation", *Nucl. Instr. Meth. B*, vol. 222, no. 3–4, pp. 469–476, 2004.

[23] Z. Y. Wang, J. Li, X. F. Huang, L. Wang, J. Xu, and K. J. Chen, "Patterned structures of silicon nanocrystals prepared by laser annealing", *Solid State Commun.*, vol. 117, no. 6, pp. 383–386, 2001.

[24] A. J. Kenyon, P. F. Trwoga, C. W. Pitt, and G. Rehm, "Luminescence efficiency measurements of silicon nanoclusters", *Appl. Phys. Lett.*, vol. 73, no. 4, pp. 523–525, 1998.

[25] H. Rinnert and M. Vergnat, "Influence of the temperature on the photoluminescence of silicon clusters embedded in a silicon oxide matrix", *Physica E*, vol. 16, no. 3–4, pp. 382–387, 2003.

[26] A. Meldrum, A. Hryciw, A. N. MacDonald, C. Blois, K. Marsh, J. Wang, and Q. Li, "Photoluminescence in the silicon-oxygen system", *J. Vac. Sci. Tech. A*, vol. 24, no. 3, pp. 713–717, 2006.

[27] S. Charvet, R. Madelon, and R. Rizk, "Structural, ellipsometry and photoluminescence spectroscopy studies of silicon nanograins embedded in a silica matrix", *Solid-State Electr.*, vol. 45, no. 8, pp. 1505–1511, 2001.

[28] J. U. Schmidt and B. Schmidt, "Investigation of Si nanocluster formation in sputter-deposited silicon sub-oxides for nanocluster memory structures", *Mater. Sci. Eng. B*, vol. 101, no. 1–3, pp. 28–33, 2003.

[29] S. Sedky, A. Witvrouw, H. Bender, and K. Baert, "Experimental determination of the maximum post-process annealing temperature for standard CMOS wafers", *IEEE Trans. Electr. Dev.*, vol. 48, no. 2, pp. 377–385, 2001.

[30] Y. Kanemitsu, "Efficient light emission from crystalline and amorphous silicon nanostructures", *J. Luminesc.*, vol. 100, no. 1–4, pp. 209–217, 2002.

[31] N. M. Park, T. Y. Kim, S. H. Kim, G. Y. Sung, K. S. Cho, J. H. Shin, B. H. Kim, S. J. Park, J. K. Lee, and M. Nastasi, "Luminescence of Er-doped amorphous silicon quantum dots", *Thin Solid Films*, vol. 475, no. 1–2, pp. 231–234, 2005.

[32] F. Priolo, G. Franzò, D. Pacifici, V. Vinciguerra, F. Iacona, and A. Irrera, "Role of the energy transfer in the optical properties of undoped and Er-doped interacting Si nanocrystals", *J. Appl. Phys.*, vol. 89, no. 1, pp. 264–272, 2001.

[33] A. J. Kenyon, P. F. Trwoga, M. Federighi, and C. W. Pitt, "Optical properties of PECVD erbium-doped silicon-rich silica: evidence for energy transfer between silicon microclusters and erbium ions", *J. Phys. Cond. Mat.*, vol. 6, no. 21, pp. L319–L324, 1994.

[34] M. Fujii, M. Yoshida, Y. Kanzawa, S. Hayashi, and K. Yamamoto, "1.54 μm photoluminescence of Er^{3+} doped into SiO_2 films containing Si nanocrystals: Evidence for energy transfer from Si nanocrystals to Er^{3+}", *Appl. Phys. Lett.*, vol. 71, no. 9, pp. 1198–1200, 1997.

[35] A. Meldrum, A. Hryciw, A. N. MacDonald, C. Blois, T. Clement, R. DeCorby, J. Wang, and Quan Li, "Interaction between rare-earth ions and amorphous silicon nanoclusters produced at low processing temperatures", *J. Luminesc.*, vol. 121, pp. 199–203, 2006.

[36] A. Irrera, F. Iacona, I. Crupi, C. D. Presti, G. Franzò, C. Bongiorno, D. Sanfilippo, G. Di Stefano, A. Piana, P. G. Fallica, A. Canino, and F. Priolo, "Electroluminescence and transport properties in amorphous silicon nanostructures", *Nanotechnology*, vol. 17, no. 5, pp. 1428–1436, 2006.

[37] L. Pavesi, S. Gaponenko, and L. Dal Negro, Eds., *Towards the first silicon laser*, vol. 93 of *NATO Science Series II*, Kluwer Academic Publishers, Norwell, Massachusetts, 2003, ISBN: 1-402-01193-8.

[38] P. M. Fauchet, "Progress toward nanoscale silicon light emitters", *IEEE J. Sel. Top. Quant. Electr.*, vol. 4, no. 6, pp. 1020–1028, 1998.

[39] Wai Lek Ng, M. A. Lourenco, R. M. Gwilliam, S. Ledain, G. Shao, and K. P. Homewood, "An efficient room-temperature silicon-based light-emitting diode", vol. 410, no. 6825, pp. 192–194, 2001.

[40] A. W. Fang, H. Park, O. Cohen, R. Jones, M. J. Paniccia, and J. E. Bowers, "Electrically pumped hybrid AlGaInAs-silicon evanescent laser", *Opt. Expr.*, vol. 14, no. 20, pp. 9203–9210, 2006.

[41] N. W. Ashcroft and N. D. Mermin, *Solid state physics*, Holt Rhinehart, New York, 1976, ISBN: 0-03-083993-9.

[42] R. Zallen, *The physics of amorphous solids*, John Wiley and Sons, Inc., New York, 1983, ISBN: 0-471-01968-2.

[43] S. R. Elliott, *Physics of amorphous materials*, Longman Group Limited, London, 1983, ISBN: 0-582-44636-8.

[44] N. F. Mott and E. A. Davis, *Electronic processes in non-crystalline materials*, Oxford University Press, London, 1971, ISBN: 0-198-51259-7.

[45] W. H. Zachariasen, "The atomic arrangement in glass", *J. Amer. Chem. Soc.*, vol. 54, pp. 3841–3851, 1932.

[46] D. Turnbull, "Under what conditions can a glass be formed?", *Contemp. Phys.*, vol. 10, no. 5, pp. 473–488, 1969.

[47] J. F. O'Hanlon, *A user's guide to vacuum technology*, John Wiley and Sons, Inc., Hoboken, New Jersey, third edition, 2003, ISBN: 0-471-27052-0, p. 15.

[48] M. Ohring, *Materials science of thin films: deposition and structure*, Academic Press, San Diego, second edition, 2002, ISBN: 0-12-524975-6.

[49] R. C. Chittick, J. H. Alexander, and H. F. Sterling, "Preparation and properties of amorphous silicon", *J. Electrochem. Soc.*, vol. 116, no. 1, pp. 77–81, 1969.

[50] R. A. Street, *Hydrogenated amorphous silicon*, Cambridge University Press, Cambridge, 1991, ISBN: 0-521-37156-2.

[51] P. Chaudhari and D. Turnbull, "Structure and properties of metallic glasses", *Science*, vol. 199, no. 4324, pp. 11–21, 1978.

[52] P. J. Flory, "Spatial configuration of macromolecular chains", *Science*, vol. 188, no. 4195, pp. 1268–1276, 1975.

[53] F. Greuter, "Electronic surface properties of a liquid semiconductor: selenium", *J. Phys. C*, vol. 18, no. 12, pp. 2527–2537, 1985.

[54] H. Ikemoto, I. Yamamoto, and H. Endo, "The optical properties of liquid chalcogens", *J. Non-Cryst. Sol.*, vol. 156, pp. 732–735, 1993.

[55] A. F. Ioffe and A. R. Regel, "Non-crystalline, amorphous, and liquid electronic semiconductors", in *Progress in Semiconductors, vol. 4*, A. F. Gibson, Ed., pp. 237–291. John Wiley and Sons, Inc., New York, 1960.

[56] J. Tauc, "Optical properties of amorphous semiconductors", in *Amorphous and liquid semiconductors*, J. Tauc, Ed., pp. 159–220. Plenum Publishing Company Ltd, New York, 1974, ISBN: 0-306-30777-4.

[57] N. F. Mott, "Conduction in non-crystalline materials. III. Localized states in a pseudogap and near extremities of conduction and valence bands", *Philos. Mag.*, vol. 19, no. 160, pp. 835–852, 1969.

[58] D. Weaire, "Existence of a gap in the electronic density of states of a tetrahedrally bonded solid of arbitrary structure", *Phys. Rev. Lett.*, vol. 26, no. 25, pp. 1541–1543, 1971.

[59] M. F. Thorpe and D. Weaire, "Electronic density of states of amorphous Si and Ge", *Phys. Rev. Lett.*, vol. 27, no. 23, pp. 1581–1584, 1971.

[60] http://en.wikipedia.org/wiki/Condensed_matter_physics.

[61] N. F. Mott, "The basis of the electron theory of metals, with special reference to the transition metals", *Proc. Phys. Soc. London A*, vol. 62, no. 355, pp. 416–422, 1949.

[62] P. W. Anderson, "Absence of diffusion in certain random lattices", *Phys. Rev.*, vol. 109, no. 5, pp. 1492–1505, 1958.

[63] R. Zallen and H. Scher, "Percolation on a continuum and localization-delocalization transition in amorphous semiconductors", *Phys. Rev. B*, vol. 4, no. 12, pp. 4471–4479, 1971.

[64] D. T. Pierce and W. E. Spicer, "Electronic structure of amorphous Si from photoemission and optical studies", *Phys. Rev. B*, vol. 5, no. 8, pp. 3017–3029, 1972.

[65] A. Catalano, "Solar cells made of amorphous and microcrystalline semiconductors", in *Amorphous and microcrystalline semiconductor devices: optoelctronic devices*, J. Kanicki, Ed., pp. 9–75. Artech House, Inc., Norwood, Massachusetts, 1991, ISBN: 0-89006-490-3.

[66] F. Urbach, "The long-wavelength edge of photographic sensitivity and of the electronic absorption of solids", *Phys. Rev.*, vol. 92, no. 5, pp. 1324–1324, 1953.

[67] J. D. Dow and D. Redfield, "Electroabsorption in semiconductors: the excitonic absorption edge", *Phys. Rev. B*, vol. 1, no. 8, pp. 3358–3371, 1970.

[68] A. J. Steckl and Zavada J. M., "Photonic applications of rare-earth-doped materials", *MRS Bull.*, vol. 24, no. 9, pp. 16–17, 1999.

[69] G. N. van den Hoven, E. Snoeks, A. Polman, C. van Dam, J. W. M. van Uffelen, and M. K. Smit, "Up-conversion in Er-implanted Al_2O_3 waveguides", *J. Appl. Phys.*, vol. 79, no. 3, pp. 1258–1266, 1996.

[70] P. G. Kik and A. Polman, "Towards an Er-doped Si nanocrystal sensitized waveguide laser – the thin line between gain and loss", in *Towards the first silicon laser*, L. Pavesi, S. Gaponenko, and L. Dal Negro, Eds., vol. 93 of *NATO Science Series II*, pp. 383–400. Kluwer Academic Publishers, Norwell, Massachusetts, 2003, ISBN: 1-402-01193-8.

[71] M. Dejneka and B. Samson, "Rare-earth-doped fibers for telecommunications applications", *MRS Bull.*, vol. 24, no. 9, pp. 39–45, 1999.

[72] R. Moncorgé, L. D. Merkle, and B. Zandi, "UV-visible lasers based on rare-earth ions", *MRS Bull.*, vol. 24, no. 9, pp. 21–26, 1999.

[73] T. Gregorkiewicz and J. M. Langer, "Lasing in rare-earth-doped semiconductors: hopes and facts", *MRS Bull.*, vol. 24, no. 9, pp. 27–31, 1999.

[74] J. Ballata, J. S. Lewis, III, and P. Holloway, "Display applications of rare-earth-doped materials", *MRS Bull.*, vol. 24, no. 9, pp. 51–56, 1999.

[75] E. S. Maniloff, A. E. Johnson, and T. W. Mossberg, "Spectral data storage using rare-earth-doped crystals", *MRS Bull.*, vol. 24, no. 9, pp. 46–50, 1999.

[76] R. C. Weast, *CRC Handbook of Chemistry and Physics*, The Chemical Rubber Company, Cleveland, Ohio, 50th edition, 1969.

[77] G. Liu, "Electronic energy level structure", in *Spectroscopic properties of rare earths in optical materials*, G. Liu and B. Jacquier, Eds., pp. 1–94. Springer, Berlin, 2005, ISBN: 3-540-23886-7.

[78] M. F. Reid, "Transition intensities", in *Spectroscopic properties of rare earths in optical materials*, G. Liu and B. Jacquier, Eds., pp. 95–129. Springer, Berlin, 2005, ISBN: 3-540-23886-7.

[79] G. H. Dieke, *Spectra and energy levels of rare earth ions in crystals*, Interscience Publishers, 1968, ISBN: 0-470-21390-6.

[80] G. Keiser, *Optical fiber communications*, McGraw-Hill, Boston, third edition, 2000, ISBN: 0-07-232101-6.

[81] D. C. Harris and M. D. Bertolucci, *Symmetry and spectroscopy: an introduction to vibrational and electronic spectroscopy*, Dover Publications, Inc., New York, 1989, ISBN: 0-486-66144-X.

[82] S. Li and C. Y. She, "Two-photon absorption cross-section measurements in common laser dyes at 1.06 μm", *Opt. Acta*, vol. 29, no. 3, pp. 281–287, 1982.

[83] T. Förster, "10th Spiers Memorial Lecture: Transfer mechanisms of electronic excitation", *Discuss. Faraday Soc.*, vol. 27, no. 7, pp. 7–17, 1959.

[84] F. Auzel, "Up-conversion in RE-doped solids", in *Spectroscopic properties of rare earths in optical materials*, G. Liu and B. Jacquier, Eds., pp. 265–319. Springer, Berlin, 2005, ISBN: 3-540-23886-7.

[85] T. Förster, "Zwischenmolekulare Energiewanderung und Fluoreszenz", *Annalen der Physik*, vol. 2, no. 1–2, pp. 55–75, 1948.

[86] D. L. Dexter, "A theory of sensitized luminescence in solids", *J. Chem. Phys.*, vol. 21, no. 5, pp. 836–850, 1953.

[87] L. Carroll, *Through the looking-glass and what Alice found there*, Henry Altemus Publishing, Philadelphia, 1899.

[88] N. Yamada, S. Shionoya, and T. Kushida, "Phonon-assisted energy transfer between trivalent rare-earth ions", *J. Phys. Soc. Japan*, vol. 32, no. 6, pp. 1577–1586, 1972.

[89] L. J. Richardson, C. E. Bonner, J. Lewis, G. B. Loutts, W. J. Rodriguez, and B. M. Walsh, "Temperature dependence on the cross-relaxation rates in Tm^{3+} doped strontium fluorapatite", *J. Luminesc.*, vol. 109, no. 3–4, pp. 129–133, 2004.

[90] B. Srinivasan, E. Poppe, J. Tafoya, and R. K. Jain, "High-power (400 mW) diode-pumped 2.7 μm Er:ZBLAN fibre lasers using enhanced Er–Er cross-relaxation processes", *Electr. Lett.*, vol. 35, no. 16, pp. 1338–1340, 1999.

[91] A. Polman, "Erbium implanted thin film photonic materials", *J. Appl. Phys.*, vol. 82, no. 1, pp. 1–39, 1997.

[92] W. H. Loh and A. J. Kenyon, "Excited state absorption in the Si nanocluster-Er material system", *IEEE Phot. Tech. Lett.*, vol. 18, no. 1, pp. 289–291.

[93] C. J. Oton, W. H. Loh, and A. J. Kenyon, "Er^{3+} excited state absorption and the low fraction of nanocluster-excitable Er^{3+} in SiO_x", *Appl. Phys. Lett.*, vol. 89, no. 3, pp. Art. no. 031116, 2006.

[94] D. Pacifici, G. Franzò, F. Priolo, F. Iacona, and L. Dal Negro, "Modeling and perspectives of the Si nanocrystals–Er interaction for optical amplification", *Phys. Rev. B*, vol. 67, no. 24, Art. no. 245301, 2003.

[95] *MRS. Bull.*, vol. 24, no. 9, September 1999.

[96] H. S. Han, S. Y. Seo, J. H. Shin, and N. Park, "Coefficient determination related to optical gain in erbium-doped silicon-rich silicon oxide waveguide amplifier", *Appl. Phys. Lett.*, vol. 81, no. 20, pp. 3720–3722, 2002.

[97] P. G. Kik and A. Polman, "Gain limiting processes in Er-doped Si nanocrystal waveguides in SiO_2", *J. Appl. Phys.*, vol. 91, no. 1, pp. 534–536, 2002.

[98] D. S. Funk, J. W. Carlson, and J. G. Eden, "Ultraviolet (381 nm), room temperature laser in neodymium-doped fluorozirconate fibre", *Electr. Lett.*, vol. 30, no. 22, pp. 1859–1860, 1994.

[99] J. T. Verdeyen, *Laser Electronics*, Prentice Hall, Upper Saddle River, New Jersey, third edition, 1995, ISBN: 0-137-0666-6, p. 149.

[100] A. Polman, "Erbium as a probe of everything?", *Physica B*, vol. 300, no. 1–4, pp. 78–90, 2001.

CHAPTER 2

Effects of particle size and excitation spectrum on the photoluminescence of silicon nanocrystals formed by ion implantation[†]

2.1 Introduction

This chapter summarises the first project, initiated and completed in 2002, which involved the optical characterisation of Si nanocrystals in silica fabricated via ion implantation. Up to this point, nearly all of the work on nanoscale silicon had concentrated on crystalline nanostructures, since it had not yet been recognised that luminescent *amorphous* nanoclusters could be produced using the same phase separation technique, but without the high annealing temperatures required for crystallisation. As well as providing an historical context for this thesis, describing the behaviour of c-Si NCs and the controversy associated with the PL mechanism, the work presented in this chapter ultimately leads to the projects discussed in all ensuing chapters, which focus on a-Si NCs.

There are now more than 3900 citations to the discovery of PL caused by quantum confinement in porous silicon, as reported 16 years ago.[2] Numerous methods have been developed to form silicon nanocrystals, and the optical properties of these materials have attracted considerable research interest. Ion implantation is a widely used and effective method for forming luminescent Si nanocrystals embedded in an optically transparent matrix such as fused quartz.[3] Despite the indirect bandgap and correspondingly slow carrier recombination, optical gain comparable to that obtained in direct-gap semiconductors has been reported in ion-implanted specimens,[4] although the difficulty in reproducing these results has called the validity of this report into question.[5] Ion implantation can be used to dope Si nanocrystal composites with erbium to produce intense emission at 1.5 μm, suggesting possible applications as fibre amplifiers,[6,7] as indictated in §1.3.3. Er-implanted silicon nanocrystal composites have also been embedded within distributed Bragg reflectors to produce highly directional and spectrally-narrow emission,[8,9] and electroluminescent device structures using Si nanocrystals show attractive characteristics in comparison to porous silicon, including increased carrier injection, robustness, and stability.[10]

Silicon nanocrystals formed by implantation and annealing of fused silica emit at peak wavelengths ranging from 700 to 900 nm. Many authors favour a "pure" quantum con-

[†] A version of this chapter has been published.[1]

finement model in which the emission is due to bandgap recombination.[11–15] Accordingly, the emission energy should depend directly on nanocrystal size, and recent work has proposed a direct relationship between particle size and emission wavelength.[16] However, other work is inconsistent with this model, but instead attributes the luminescence to surface traps (e.g. Ref.[17]). The broad red PL band is proposed to arise from carrier trapping and recombination at surface Si=O bonds[18,19] that produce stable states in the gap.[20] The silicon dangling bond appears to be the main non-radiative recombination site, as determined by electron spin resonance measurements.[21]

In addition to the conflicting models, some of the experimental results are also contradictory. For example, some authors have recently reported considerably longer radiative lifetimes for larger particles,[16,22] while others find that the lifetime is shorter for samples with a higher silicon concentration.[23,24] Some authors report a linear dependence of the PL intensity on the excitation power,[14,25] while others find an approach toward saturation.[20] Some of these differences may be due to the effects of excitation spectrum (pump power and wavelength), and some to non-radiative decay channels that can affect the measured PL lifetimes. Clearly, for modelling the mechanism(s) of emission, it is vital to perform the experiments with a high degree of care and precision. The objectives of the present work were, therefore, (1) to determine the effects of particle size on the absorption and emission spectra and on the PL lifetimes, (2) to investigate the effects of excitation spectrum on the photoluminescence of silicon nanocrystals formed by ion implantation in a careful and systematic fashion, (3) to determine which of the physical models is most consistent with the comprehensive data set, and (4) to examine the implications for device structures.

2.2 Experimental

Two optical-grade fused quartz wafers were implanted at room temperature with silicon ions. Specimen A was implanted at energies of 35, 70 and 135 keV to fluences of 1.7×10^{16}, 3.0×10^{16} and 7.5×10^{16} ions/cm^2, respectively. Specimen B was implanted at the same energies, but the fluences were increased to 3.2×10^{16}, 5.6×10^{16} and 1.5×10^{17} ions/cm^2. The specimens were annealed at 1100 °C for 1 h in flowing 90% Ar+10% H_2 to induce precipitation of silicon nanocrystals with good luminescence efficiency.[26] Transmission electron microscopy (TEM) was done on a 200 kV LaB_6 instrument, using specimens prepared by standard cross-sectional methods. Continuous wave (CW) PL experiments were performed using an Ar^+ ion laser at wavelengths of either 488 or 514 nm, or a HeCd laser operated at 325 or 442 nm. The spectra were collected with a fibre-optic charge-coupled device (CCD) spectrometer whose sensitivity was normalised with respect to a blackbody light source. Absorption measurements were taken using a deuterium-tungsten lamp interfaced to the same spectrometer system. A diode-pumped solid-state laser emitting ~10 ns pulses at 349 nm was used for PL lifetime measurements.

2.3 Results

The average diameter of the silicon nanocrystals was smaller in specimen A (~1.5 nm, $\sigma = 0.4$ nm) than in specimen B (~2.4 nm, $\sigma = 1.1$ nm). Because the smallest silicon nanocrystals show poor bright-field contrast and can be difficult to detect when embedded in SiO_2, there may be more nanocrystals smaller than 1 nm than appear in the images or histograms (Fig. 2.1). Despite the fact that the cross-section for specimen B was of higher

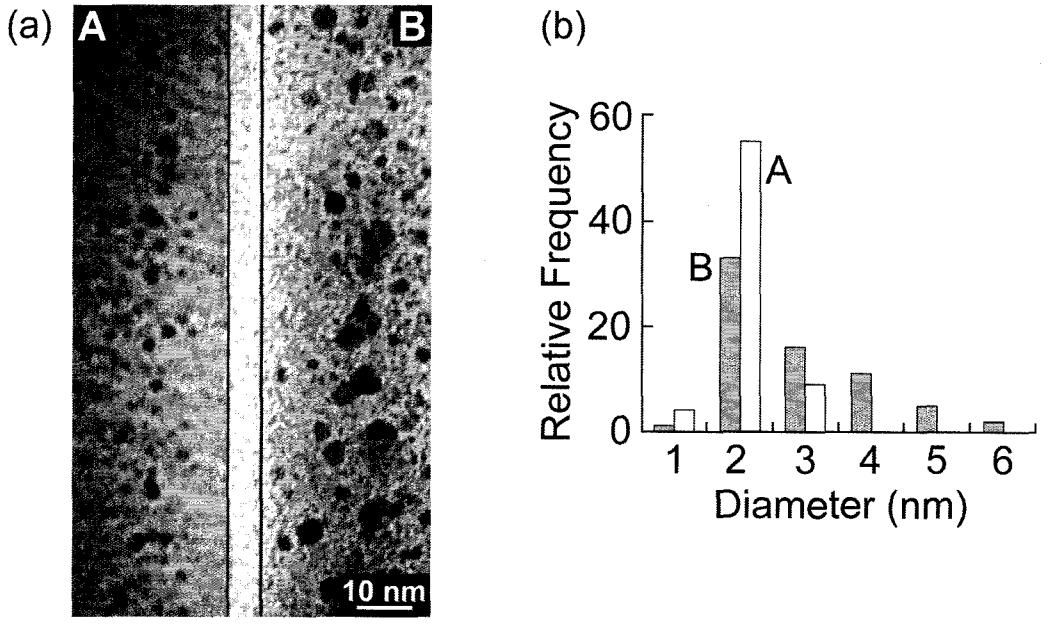

Fig. 2.1: Cross-sectional TEM images of specimens A and B (a) and Si nanocrystal size distribution histograms (b). The TEM images are defocused in order to highlight contrast between the nanocrystals and the SiO_2 matrix. The dark vertical lines mark the specimen surfaces.

quality (the examined area was thinner, as determined visually and by current measurements on the TEM screen), there is a considerable amount of particle overlap through the specimen thickness. This is consistent with previous work that indicated that higher implanted ion fluences produce larger particles as well as a smaller interparticle spacing.[27]

For both specimens, the absorbance spectrum is nearly featureless between 400 and 1000 nm (Fig. 2.2). Specimen A shows a small increase in absorbance with decreasing wavelength between 700 and 370 nm, beyond which the absorbance increases more rapidly. The absorbance spectrum for specimen B shows similar characteristics, except that the region of rapidly increasing absorbance starts at ~420 nm. For both samples, the peak of the photoluminescence occurs in the near infrared and is shifted by approximately 2 eV with respect to the strong absorption. Both the absorption and peak photoluminescence occur at slightly higher energies in specimen A, which has the smaller particles. The peak PL emission intensity was greater for specimen A, despite the lower implanted ion fluence. In these experiments, care was taken to ensure that the excitation and measurement conditions were as similar as possible for both specimens.

The effect of pump power was investigated by varying the incident power on specimen B between 5 and 16 mW (corresponding to photon fluxes of $\sim 6\times10^{19}$ to 2×10^{20} photons/cm^{2}s). As the power increased, the emission peak blueshifted from 827 to 811 nm (Fig. 2.3). Even larger shiftshave been observed when using a higher-power laser to excite the sample. The effect of pump wavelength on specimen B was investigated by measuring the PL spectra using 325-, 442-, 488- and 514-nm excitation wavelengths. All other experimental variables were kept constant and care was taken to use excitation fluxes for the different wavelengths that were as similar as possible. Although the overall PL intensity was higher at shorter pump wavelengths, there was no consistent shift in the PL spectrum over the range of excitation wavelengths used (Fig. 2.4). Finally, a slightly shorter luminescence lifetime was observed for specimen B (Fig. 2.5). Measurements taken

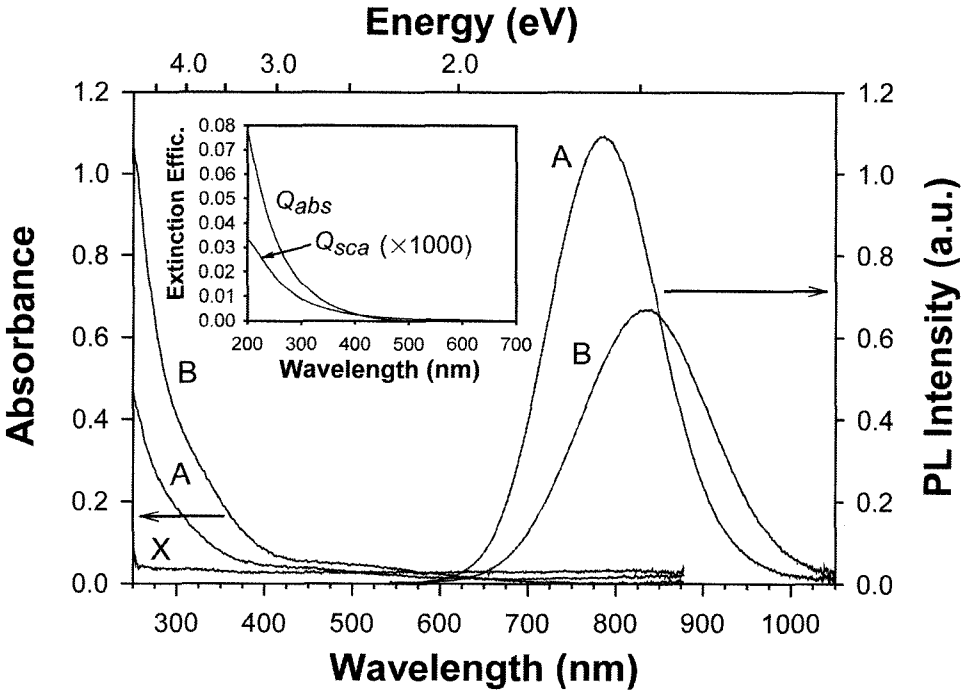

Fig. 2.2: Absorbance and PL spectra for specimens A and B. The PL spectra were taken using 127 mW of 488+514 nm laser. The reference absorption spectrum marked with the X is for a blank fused quartz wafer. **Inset:** absorption and scattering efficiencies, Q_{abs} and Q_{sca}, respectively, calculated using Mie theory for particles 3 nm in diameter.

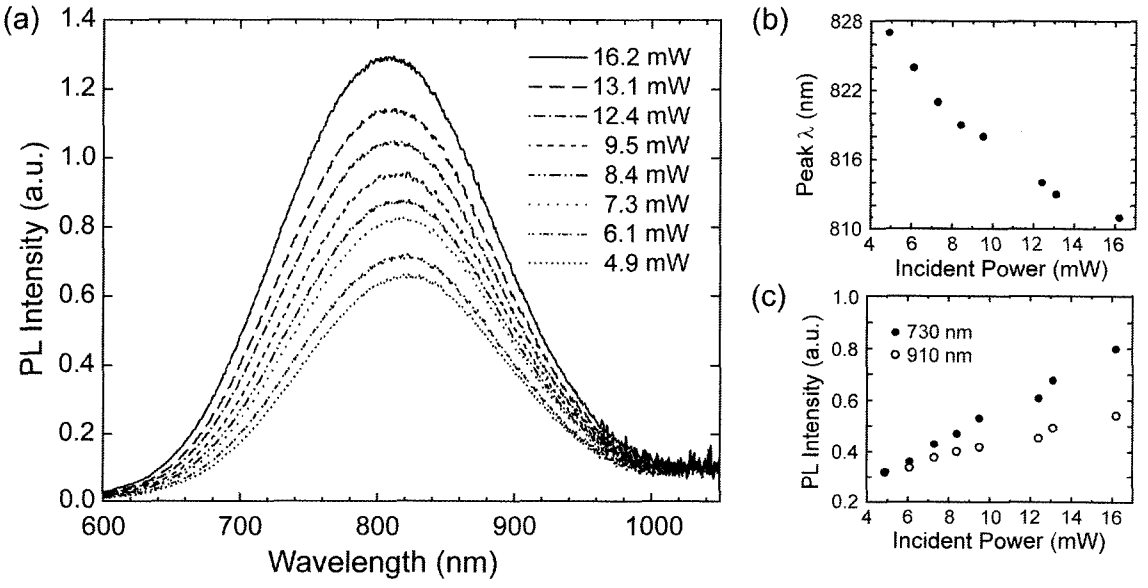

Fig. 2.3: (a) PL spectra for specimen A, taken with different incident laser powers. The 325 nm line of a HeCd laser was focused through a plano-convex lens onto the specimen and a set of neutral density filters was used to obtain different pump powers. (b) Variation of the peak wavelength with pump power. (c) Intensity as a function of pump power at wavelengths of 730 and 910 nm.

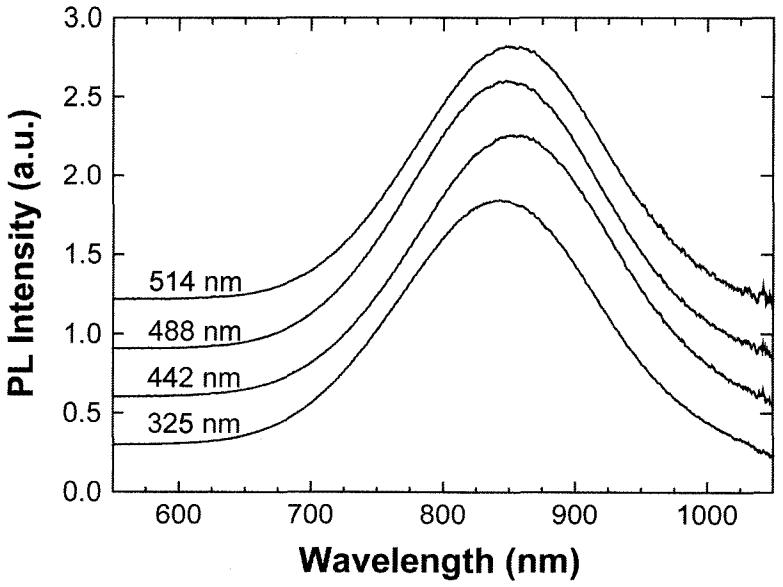

Fig. 2.4: Photoluminescence spectra for specimen B, taken with different pump wavelengths (325, 442, 488 and 514 nm). For clarity, the data are normalised in intensity and are arbitrarily shifted on the vertical axis. All spectra were taken using a pump power of 20 ± 0.5 mW ($\sim 9 \times 10^{17}$ to $\sim 1.4 \times 10^{18}$ photons/cm^{2}s) except for the 442-nm excitation, which was at 18 mW ($\sim 1.1 \times 10^{18}$ photons/cm^{2}s). The slight differences in the spectra are most likely due to these unavoidable variations in excitation power.

of different energy bands (selected using a variable bandpass filter) showed that the luminescence decay was faster on the short-wavelength side of the overall emission peak (Fig. 2.5, inset).

2.4 Discussion

In exact terms, the results plotted in Fig. 2.2 are actually extinction spectra, in which the effects of absorption and scattering (as well as interference due to the modified refractive index of the implanted layer[28]) are superimposed. To distinguish between the two main sources, the absorption and scattering contributions to the extinction efficiency (Q_{abs} and Q_{sca}, respectively) were calculated using Mie theory[29] with the recently-measured optical constants for silicon nanocrystals of comparable size.[30] For the wavelength region of interest, it was found that Q_{abs} was significantly greater than Q_{sca} (Fig. 2.2, inset), which justifies the assumption that the extinction spectra in Fig. 2.2 are effectively absorbance spectra.

2.4.1 Effect of pump power

The photoluminescence peak position is sensitive to the pump photon flux. As the flux on the specimen increases, there is a clear blueshift in the luminescence. The effect is strong enough to be observable even at pump photon fluxes as low as 10^{18} photons/cm^{2}s. A slight (2 nm) shift in the peak position occurs on going from 10 to 20 mW even for an unfocused beam (beam area of ~ 4 mm^2), and the effect is especially pronounced when using a lens to focus the incident light (Fig. 2.3). This spectral blueshift is due to the more rapid decay dynamics on the short wavelength side of the peak (Fig. 2.5, inset). As the power is increased, the slower decay dynamics on the red side of the peak cause a more rapid approach to saturation and, as a result, the PL peak shifts toward shorter wavelengths. This interpretation is in agreement with recent results on porous silicon (e.g. Refs.[14,16,24,31]), and the effect can explain the spectral blueshift at higher pump power.

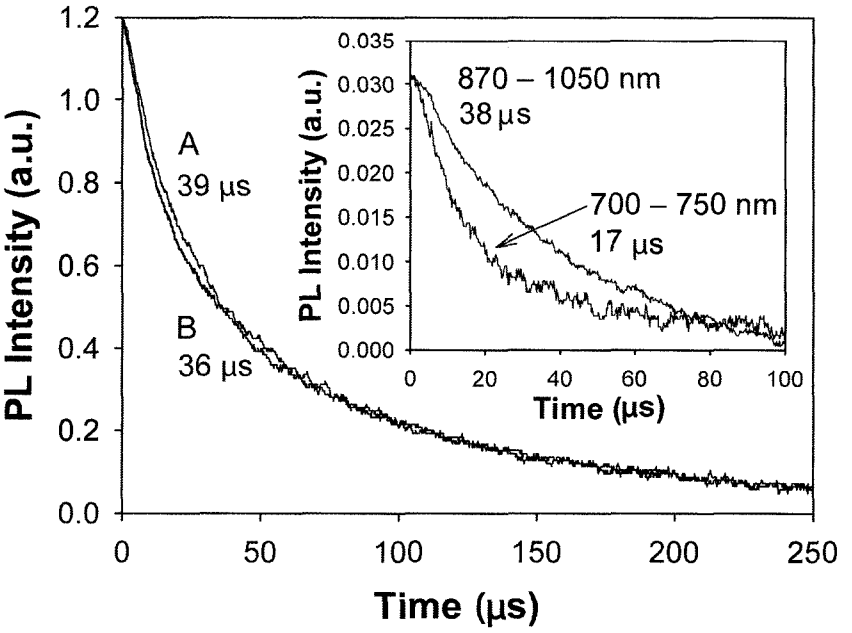

Fig. 2.5: PL decay curves for the two specimens taken over the full emission spectrum. The inset shows decay curves for specimen B taken using a variable bandpass filter that transmitted light between 700 and 750 nm, or between 870 and 1050 nm (these boundaries indicate approximate 1% transmission level through the filter). The decays were fit to stretched exponentials and the resulting lifetimes are shown next to the curves.

It is tempting to attribute the power-dependent blueshift of the luminescence to more rapid dynamics in smaller particles, as has been done in the literature (e.g. see Refs.[14,31]). However, Fig. 2.5 does not show this relationship between particle size and luminescence decay dynamics in specimens A and B. On the other hand, models have been proposed more than 10 years ago[32] in which the stretched exponential behaviour of PL decay is due to tunnelling of electrons into the surrounding matrix, followed by non-radiative recombination. In such models, the lifetime is dominated by non-radiative relaxation such that $\tau \approx \tau_{nr}$. Using the WKB approximation,[32] the transparency of the oxide barrier through which tunnelling can occur increases exponentially with the luminescence energy. Since the lifetime is inversely proportional to the transparency, higher-energy transitions have shorter lifetimes. The observed stretched exponential decay may then be explained as the result of a distribution in the energies and the corresponding lifetimes of the non-radiative transitions.

2.4.2 Effect of particle size

The effects of nanocrystal size can be investigated by comparing specimens with differently-sized particles, or by tuning the excitation energy on a single sample. Both of these methods were employed here. In comparing the two specimens, the absorption energies are at least roughly consistent with models of quantum confinement, which suggest bandgap energies of approximately 2.5 eV for particles of 2.4 nm diameter and ~3.5 eV for a diameter of 1.5 nm (e.g. Refs.[33,34]). However, the extremely large shift between the absorption and emission energies is not consistent with a pure quantum confinement model for the photoluminescence. Smaller Stokes shifts (on the order of 100 meV) can be due to Coulomb and exchange interactions, but such a large shift can-

not be easily explained by these mechanisms. The fact that specimen A, which contains smaller particles, emits at slightly higher energies could be interpreted as being due to quantum confinement, but alternate explanations do exist. It has recently been shown that tunnelling between nanocrystals can be a major contributor to the overall PL behaviour for specimens in which the interparticle spacing is small,[35] as is the case for the densely-packed *c*-Si-NC ensembles present in the specimens considered in this chapter (see Table C.1). Also, it has been suggested that such effects can be due to band-bending when nanocrystals are closely separated by a thin insulating layer.[3] These models imply the importance of interparticle *proximity* in addition to size; the experimental results discussed above are consistent with this interpretation. The nanoparticles in specimen B are closer together (see Fig. 2.1); therefore, qualitatively, tunnelling and/or band-bending effects are more pronounced and can result in lower emission energy.

The decay curves (Fig. 2.5) for both samples fit well to a stretched exponential, given by the expression

$$I(t) = I_0 e^{-(t/\tau)^\beta} \tag{2.1}$$

where I_0 is the initial intensity, τ is the characteristic decay lifetime and β is a parameter indicating the "degree of stretching" ($\beta = 1$ for a single exponential); a further discussion of stretched exponential relaxation is given in §A.4. Nonlinear least-squares regression for β, τ, and I_0 yields lifetimes of $\sim$39 and 36 μs for specimens A and B, respectively, with $\beta \approx 0.7$. The quantum confinement model predicts faster dynamics for smaller particles,[36] due to greater overlap of carrier wave functions and the possible transition to direct-gap behaviour.[20] In the specimens considered in this chapter, however, the sample with the *larger* particles (B) has a slightly greater decay rate. The measurement was repeated several times and cannot be classified as a "deviation."[16] Samples with larger nanocrystals generally have smaller interparticle distances,[37] as observed in Fig. 2.1. Since the tunnelling rate increases as the oxide barrier width between neighbouring particles decreases, the non-radiative rate should be greater for samples with larger mean nanocrystal radii due to their closer spacing. This results in shorter PL lifetimes for the larger (i.e. more closely-spaced) particles.[32]

Particle size effects can be investigated in the same sample by tuning the wavelength across the absorption band. Longer pump wavelengths only excite the larger particles and, in the pure quantum confinement model, this would result in a redshifted emission. For these specimens, there was no consistent shift in the photoluminescence spectrum as a result of pumping over a range of wavelengths from 325 nm to 514 nm. The most noticeable effect is on the intensity of the emission: it is stronger for shorter wavelength excitation. In these experiments, the pumping conditions were made as similar as possible for each wavelength. Since the power of the HeCd laser is controllable only by using external filters, the 442-nm power could not be matched exactly (18.0$\pm$0.5 mW, compared to 20.0$\pm$0.5 mW for all the other lines); as a result, the 442-nm PL spectrum is slightly redshifted with respect to the others. Also, the spot size for the two lasers was not identical. Nevertheless, the results confirm that there is little (if any) direct dependence of the emission spectrum on particle size, contrary to frequent assumptions in the literature.

Furthermore, models incorporating the sub-gap state predict that the recombination energy scales with the bandgap energy.[19] Instead, since there is no obvious dependence of the luminescence wavelength on particle size (Fig. 2.4), the results suggest that the emission energy of a single nanocrystal is homogeneously broadened. This homogeneous broadening has, in fact, been reported for lithographically-prepared silicon nanopillars.[38]

A single point on a bandgap versus particle size diagram may therefore be only a rough representation of the emission energy for a single nanoparticle. Finally, it is to be noted that many investigations use the 488-nm line of an Ar laser to excite the PL, but this can generally only excite a small fraction of the largest particles, as the absorbance at this wavelength is low. Fortunately, the results show that this selective excitation has little if any effect on the resulting PL spectrum.

2.4.3 Device implications

Light-emitting diodes (LEDs), lasers, and other devices based on emission from silicon nanocrystals have been proposed (e.g. Refs.[9,39,40]). Patterned arrays of luminescent nanocrystals may find applications in field emission displays,[41] multicoloured LEDs, or multichannel chemical sensors.[42] These applications will require spatial control over the emitting centres and an ability to tune the emission wavelength. Silicon nanocrystals produced by ion implantation should be bright and durable enough to be patterned into two-dimensionally organised light-emitting arrays.

The problem of achieving in-plane patterning of nanoclusters fabricated via ion implantation has been addressed by Buchanan *et al.*[†] Originally used in the context of magnetic (Fe–Pt) NCs, the technique uses conventional deep-UV lithography to pattern an array of holes in a 760-nm-thick molybdenum mask on a fused quartz substrate. Subsequent ion implantation and removal of the mask by chemical etching yields a specimen with the implanted species arranged in a patterned array. This method was used to effect spatial control over Si NCs to demonstrate their applicability for display technologies.

A Mo-masked fused silica substrate (as explained above) was implanted under identical conditions to those used for specimen A (see §2.2). After mask removal, the sample was annealed for 1 h at 1100 °C in flowing Ar+10% H_2. A PL image taken with a laser scanning confocal microscope (488 nm excitation) is shown in Fig. 2.6; the figure clearly demonstrates that the nanocrystals have been patterned into an array of ~1-μm spots. These results are, to the authors' knowledge, the first example of in-plane two-dimensional patterning of luminescent nanocrystals produced by ion implantation.

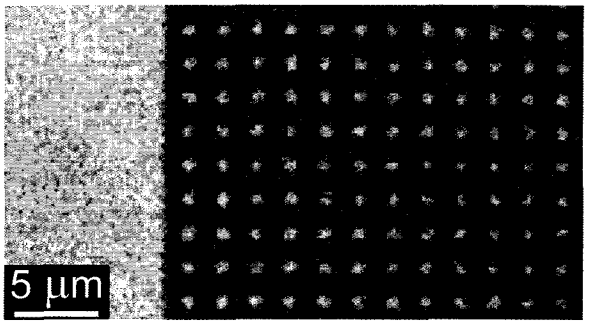

Fig. 2.6: Fluorescence image showing an array of implanted spots (white) containing silicon nanocrystals (right side of image), and a blanket implant (left side of image). The emission spectrum from the implanted regions was similar to that for specimen A. Each implanted spot is slightly less than 1 μm wide and therefore contains many nanocrystals.

Producing multiple-colour arrays will require more complicated procedures, but the results show that controlling the size of the particles will not produce useful variations in the emission spectrum. Instead, doping or chemical modification of the nanocrystals should lead more readily to multicolour emission. Silicon nanocrystals doped with oxygen and nitrogen can potentially produce blue or violet light,[44] helium-irradiated Si quantum dots have been reported to produce a blue emission,[45] Si_3N_4 can emit in the green and

[†]See Ref.[43] and references contained therein.

blue,[46] nanocrystalline SiC offers a broad-wavelength white emission[47] and rare-earth-doped silicon nanocrystal composites emit sharp lines in the near infrared.[6] All of these colours may be achievable through multiple-implantation protocols, but the results show that they cannot be readily achieved by nanocrystal size control alone.

2.5 Conclusion

This chapter presents a systematic investigation of the photoluminescence from *c*-Si NCs embedded in SiO_2 via ion implantation. The measurements show that the PL spectrum is sensitive to excitation power due to the more rapid recombination dynamics at shorter wavelengths, but the spectrum is insensitive to pump wavelength. This is consistent with a sub-gap luminescent centre as the origin of the PL, as opposed to recombination across the quantum-confined bandgap. The PL decay is a stretched exponential, with a slightly shorter lifetime for the specimen with the larger particles. There is a Stokes shift of more than 2 eV between the emitting and absorbing states, and both are blueshifted in the specimen with the smaller particles. The absorption spectra and average particle size are consistent with theoretical estimates of the quantum-confined bandgap energy.[33,34] However, the slight blueshift in the PL spectrum in samples with smaller particles (as observed in Fig. 2.2) has led some authors to assume a pure quantum confinement model, with isolated NCs), to explain the photoluminescence. The experimental results presented in this chapter do not support this explanation, since the PL decay rate is not faster for the smaller particles, as has been frequently observed in well-passivated semiconductor nanocrystals (e.g. Ref.[48]), and there is no dependence of the emission spectrum on the pump wavelength. In short, effects related more to the spacing between particles rather than to their size, such as inter-NC tunnelling within densely-packed ensembles,[35] or recombination of a quantum-confined exciton at a sub-gap radiative trap site or luminescent centre that is not directly dependent on particle size, but may depend on a nanocrystal's immediate environment,[3] best describe these experimental results. This has ramifications when designing a light-emitting device using Si nanocrystals, since effectively tuning the emission colour will be achieved by means other than controlling the average particle size. It has been demonstrated that it is possible to realise good spatial control of nanocrystals produced by ion implantation using conventional photolithography; this technique has been used to fabricate arrays of nanocrystal-containing pixels.

Bibliography

[1] A. Hryciw, A. Meldrum, K. S. Buchanan, and C. W. White, "Effects of particle size and excitation spectrum on the photoluminescence of silicon nanocrystals formed by ion implantation", *Nucl. Instr. Meth. B*, vol. 222, no. 3–4, pp. 469–476, 2004.

[2] L. T. Canham, "Silicon quantum wire array fabrication by electrochemical and chemical dissolution of wafers", *Appl. Phys. Lett.*, vol. 57, no. 10, pp. 1046–1048, 1990.

[3] T. Shimizu-Iwayama, T. Hama, D. E. Hole, and I. W. Boyd, "Characteristic photoluminescence properties of Si nanocrystals in SiO_2 fabricated by ion implantation and annealing", *Solid-State Electr.*, vol. 45, no. 8, pp. 1487–1494, 2001.

[4] L. Pavesi, L. Dal Negro, C. Mazzoleni, G. Franzò, and F. Priolo, "Optical gain in silicon nanocrystals", *Nature*, vol. 408, no. 6811, pp. 440–444, 2000.

[5] P. M. Fauchet, J. Ruan, H. Chen, L. Pavesi, L. Dal Negro, M. Cazzaneli, R. G. Elliman, N. Smith, M. Samoc, and B. Luther-Davies, "Optical gain in different silicon nanocrystal systems", *Opt. Mater.*, vol. 27, no. 5, pp. 745–749, 2005.

[6] G. Franzò, V. Vinciguerra, and F. Priolo, "The excitation mechanism of rare-earth ions in silicon nanocrystals", *Appl. Phys. A*, vol. 69, no. 1, pp. 3–12, 1999.

[7] M. Fujii, M. Yoshida, Y. Kanzawa, S. Hayashi, and K. Yamamoto, "1.54 μm photoluminescence of Er^{3+} doped into SiO_2 films containing Si nanocrystals: Evidence for energy transfer from Si nanocrystals to Er^{3+}", *Appl. Phys. Lett.*, vol. 71, no. 9, pp. 1198–1200, 1997.

[8] F. Iacona, G. Franzò, E. C. Moreira, D. Pacifici, A. Irrera, and F. Priolo, "Luminescence properties of Si nanocrystals embedded in optical microcavities", *Mater. Sci. Eng. C*, vol. 19, no. 1–2, pp. 377–381, 2002.

[9] S. Chan and P. M. Fauchet, "Silicon microcavity light emitting devices", *Opt. Mater.*, vol. 17, no. 1–2, pp. 31–34, 2001.

[10] N. Lalic and J. Linnros, "Light emitting diode structure based on Si nanocrystals formed by implantation into thermal oxide", *J. Luminesc.*, vol. 80, no. 1–4, pp. 263–267, 1999.

[11] E. Neufeld, S. Wang, R. Apetz, C. Buchal, R. Carius, C. W. White, and D. K. Thomas, "Effect of annealing and H_2 passivation on the photoluminescence of Si nanocrystals in SiO_2", *Thin Solid Films*, vol. 294, no. 1–2, pp. 238–241, 1997.

[12] P. Mutti, G. Ghislotti, S. Bertoni, L. Bonoldi, G. F. Cerofolini, L. Meda, E. Grilli, and M. Guzzi, "Room-temperature visible luminescence from silicon nanocrystals in silicon implanted SiO_2 layers", *Appl. Phys. Lett.*, vol. 66, no. 7, pp. 851–853, 1995.

[13] M. L. Brongersma, P. G. Kik, A. Polman, K. S. Min, and H. A. Atwater, "Size-dependent electron-hole exchange interaction in Si nanocrystals", *Appl. Phys. Lett.*, vol. 76, no. 3, pp. 351–353, 2000.

[14] V. Vinciguerra, G. Franzò, F. Priolo, F. Iacona, and C. Spinella, "Quantum confinement and recombination dynamics in silicon nanocrystals embedded in Si/SiO_2 superlattices", *J. Appl. Phys.*, vol. 87, no. 11, pp. 8165–8173, 2000.

[15] J. Valenta, J. Dian, K. Luterová, P. Knápek, I. Pelant, M. Nikl, D. Muller, J. J. Grob, J. L. Rehspringer, and B. Hönerlage, "Temperature behaviour of optical properties of Si^+-implanted SiO_2", *Euro. Phys. J. D*, vol. 8, no. 3, pp. 395–398, 2000.

[16] C. Garcia, B. Garrido, P. Pellegrino, R. Ferre, J. A. Moreno, J. R. Morante, L. Pavesi, and M. Cazzanelli, "Size dependence of lifetime and absorption cross section of Si nanocrystals embedded in SiO_2", *Appl. Phys. Lett.*, vol. 82, no. 10, pp. 1595–1597, 2003.

[17] K. S. Zhuravlev, A. M. Gilinsky, and A. Y. Kobitsky, "Mechanism of photoluminescence of Si nanocrystals fabricated in a SiO_2 matrix", *Appl. Phys. Lett.*, vol. 73, no. 20, pp. 2962–2964, 1998.

[18] G. Allan, C. Delerue, and M. Lannoo, "Nature of luminescent surface states of semiconductor nanocrystallites", *Phys. Rev. Lett.*, vol. 76, no. 16, pp. 2961–2964, 1996.

[19] I. Vasiliev, J. R. Chelikowsky, and R. M. Martin, "Surface oxidation effects on the optical properties of silicon nanocrystals", *Phys. Rev. B*, vol. 65, no. 12, Art. no. 121302, 2002.

[20] D. Kovalev, J. Diener, H. Heckler, G. Polisski, N. Künzner, and F. Koch, "Optical absorption cross sections of Si nanocrystals", *Phys. Rev. B*, vol. 61, no. 7, pp. 4485–4487, 2000.

[21] M. López, B. Garrido, C. Garcia, P. Pellegrino, A. Pérez-Rodríguez, J. R. Morante, C. Bonafos, M. Carrada, and A. Claverie, "Elucidation of the surface passivation role on the photoluminescence emission yield of silicon nanocrystals embedded in SiO_2", *Appl. Phys. Lett.*, vol. 80, no. 9, pp. 1637–1639, 2002.

[22] C. Garcia, B. Garrido, P. Pellegrino, R. Ferre, J. A. Moreno, L. Pavesi, M. Cazzanelli, and J. R. Morante, "Absorption cross-sections and lifetimes as a function of size in Si nanocrystals embedded in SiO_2", *Physica E*, vol. 16, no. 3–4, pp. 429–433, 2003.

[23] F. Priolo, G. Franzò, D. Pacifici, V. Vinciguerra, F. Iacona, and A. Irrera, "Role of the energy transfer in the optical properties of undoped and Er-doped interacting Si nanocrystals", *J. Appl. Phys.*, vol. 89, no. 1, pp. 264–272, 2001.

[24] J. Linnros, N. Lalic, A. Galeckas, and V. Grivickas, "Analysis of the stretched exponential photoluminescence decay from nanometer-sized silicon crystals in SiO_2", *J. Appl. Phys.*, vol. 86, no. 11, pp. 6128–6134, 1999.

[25] A. J. Kenyon, C. E. Chryssou, C. W. Pitt, T. Shimizu-Iwayama, D. E. Hole, N. Sharma, and C. J. Humphreys, "Luminescence from erbium-doped silicon nanocrystals in silica: Excitation mechanisms", *J. Appl. Phys.*, vol. 91, no. 1, pp. 367–374, 2002.

[26] S. P. Withrow, C. W. White, A. Meldrum, J. D. Budai, D. M. Hembree, and J. C. Barbour, "Effects of hydrogen in the annealing environment on photoluminescence from Si nanoparticles in SiO_2", *J. Appl. Phys.*, vol. 86, no. 1, pp. 396–401, 1999.

[27] T. Shimizu-Iwayama, D. E. Hole, and I. W. Boyd, "Mechanism of photoluminescence of Si nanocrystals in SiO_2 fabricated by ion implantation: the role of interactions of nanocrystals and oxygen", *J. Phys. Cond. Mat.*, vol. 11, no. 34, pp. 6595–6604, 1999.

[28] R. G. Elliman, M. J. Lederer, and B. Luther-Davies, "Optical absorption measurements of silica containing Si nanocrystals produced by ion implantation and thermal annealing", *Appl. Phys. Lett.*, vol. 80, no. 8, pp. 1325–1327, 2002.

[29] J. R. Heath, J. J. Shiang, and A. P. Alivisatos, "Germanium quantum dots: optical properties and synthesis", *J. Chem. Phys.*, vol. 101, no. 2, pp. 1607–1615, 1994.

[30] D. Amans, S. Callard, A. Gagnaire, J. Joseph, G. Ledoux, and F. Huisken, "Ellipsometric study of silicon nanocrystal optical constants", *J. Appl. Phys.*, vol. 93, no. 7, pp. 4173–4179, 2003.

[31] M. Koós, I. Pócsik, and É. B. Vázsonyi, "Experimental proof for nanoparticle origin of photoluminescence in porous silicon layers", *Appl. Phys. Lett.*, vol. 62, no. 15, pp. 1797–1799, 1993.

[32] J. C. Vial, A. Bsiesy, F. Gaspard, R. Hérino, M. Ligeon, F. Muller, R. Romestain, and R. M. Macfarlane, "Mechanisms of visible-light emission from electrooxidized porous silicon", *Phys. Rev. B*, vol. 45, no. 24, pp. 14171–14176, 1992.

[33] S. Öğüt, J. R. Chelikowsky, and S. G. Louie, "Quantum confinement and optical gaps in Si nanocrystals", *Phys. Rev. Lett.*, vol. 79, no. 9, pp. 1770–1773, 1997.

[34] N. A. Hill and K. B. Whaley, "A theoretical study of light emission from nanoscale silicon", *J. Electr. Mater.*, vol. 25, no. 2, pp. 269–285, 1996.

[35] R. Lockwood, A. Hryciw, and A. Meldrum, "Nonresonant carrier tunneling in arrays of silicon nanocrystals", *Appl. Phys. Lett.*, vol. 89, Art. no. 263112, 2006.

[36] J. P. Wilcoxon, G. A. Samara, and P. N. Provencio, "Optical and electronic properties of Si nanoclusters synthesized in inverse micelles", *Phys. Rev. B*, vol. 60, no. 4, pp. 2704–2714, 1999.

[37] T. Müller, K. H. Heinig, and W. Möller, "Size and location control of Si nanocrystals at ion beam synthesis in thin SiO_2 films", *Appl. Phys. Lett.*, vol. 81, no. 16, pp. 3049–3051, 2002.

[38] J. Valenta, R. Juhasz, and J. Linnros, "Photoluminescence spectroscopy of single silicon quantum dots", *Appl. Phys. Lett.*, vol. 80, no. 6, pp. 1070–1072, 2002.

[39] P. M. Fauchet, "Progress toward nanoscale silicon light emitters", *IEEE J. Sel. Top. Quant. Electr.*, vol. 4, no. 6, pp. 1020–1028, 1998.

[40] J. De La Torre, A. Souifi, A. Poncet, C. Busseret, M. Lemiti, G. Bremond, G. Guillot, O. Gonzalez, B. Garrido, J. R. Morante, and C. Bonafos, "Optical properties of silicon nanocrystal LEDs", *Physica E*, vol. 16, no. 3–4, pp. 326–330, 2003.

[41] C. C. Chen, C. P. Yet, H. N. Wang, and C. Y. Chao, "Self-assembly of monolayers of cadmium selenide nanocrystals with dual color emission", *Langmuir*, vol. 15, no. 20, pp. 6845–6850, 1999.

[42] T. Vossmeyer, S. Jia, E. Delonno, M. R. Diehl, S. H. Kim, X. Peng, A. P. Alivisatos, and J. R. Heath, "Combinatorial approaches toward patterning nanocrystals", *J. Appl. Phys.*, vol. 84, no. 7, pp. 3664–3670, 1998.

[43] K. S. Buchanan, *Ultrafast magnetic relaxation in nanocomposite materials*, PhD thesis, Department of Physics, University of Alberta, June 2004.

[44] M. Modreanu, M. Gartner, N. Tomozeiu, J. Seekamp, and P. Cosmin, "Investigation on optical and microstructural properties of photoluminescent LPCVD SiO_xN_y thin films", *Opt. Mater.*, vol. 17, no. 1–2, pp. 145–148, 2001.

[45] G. A. Kachurin, M. O. Ruault, A. K. Gutakovsky, O. Kaïtasov, S. G. Yanovskaya, K. S. Zhuravlev, and H. Bernas, "Light particle irradiation effects in Si nanocrystals", *Nucl. Instr. Meth. B*, vol. 147, no. 1-4, pp. 356–360, 1999.

[46] C. M. Mo, L. D. Zhang, C. Y. Xie, and T. Wang, "Luminescence of nanometer-sized amorphous silicon nitride solids", *J. Appl. Phys.*, vol. 73, no. 10, pp. 5185–5188, 1993.

[47] Y. P. Guo, J. C. Zheng, A. T. S. Wee, C. H. A. Huan, K. Li, J. S. Pan, Z. C. Feng, and S. J. Chua, "Photoluminescence studies of SiC nanocrystals embedded in a SiO_2 matrix", *Chem. Phys. Lett.*, vol. 339, no. 5–6, pp. 319–322, 2001.

[48] V. I. Klimov, A. A. Mikhailovsky, D. W. McBranch, C. A. Leatherdale, and M. G. Bawendi, "Quantization of multiparticle Auger rates in semiconductor quantum dots", *Science*, vol. 287, no. 5455, pp. 1011–1013, 2000.

CHAPTER 3

Tunable luminescence from a silicon-rich oxide microresonator †

Wavelength tunability is a key aspect for light-emitting materials, and is one of the critical properties driving research on semiconductor quantum dots[2] and organic microcavity devices.[3] Narrow and well-defined emission spectra are important with respect to the development of optical displays, optical amplifiers, light-emitting diodes, and tunable quantum dot lasers.[4] As discussed in §1.1, silicon-based light emitters in particular represent a key technology that may challenge the bottlenecks currently facing the microelectronics industry.[5] In the previous chapter, however, it was seen that widely-tunable and spectrally-narrow "quantum-dot-like" emission from *c*-Si NCs has remained problematic: the details of the emission process from ensembles of Si NCs cannot be simply explained—as in the case of direct-gap CdSe quantum dots, for example—by pure quantum confinement arguments for isolated NCs. Instead, NC interactions such as carrier tunnelling may play an important role in determining the PL behaviour.

In this chapter, it is demonstrated that silicon-rich oxide films containing *amorphous* Si NCs can be processed at temperatures compatible with silicon microelectronics, while at the same time, the emission wavelength can be tuned throughout the entire visible spectrum and extended to the fibre-optic transparency windows in the NIR. This approach covers most of the 0.4 to 1.6 μm wavelength range needed for silicon-based photonics,[5] produces the widest spectral tunability achieved for any single material, and presents an attractive silicon-based alternative to quantum dot or microcavity organic light-emitting materials for photonic applications.

As discussed in previous chapters, silicon nanocrystal composites are currently the focus of the intense international research efforts that may foreshadow the "optical age of silicon."[6] These efforts are driven by potential photonic applications of silicon-based materials in light-emitting diodes (see, for example, the work of Valenta *et al.*[7]), nanocrystal lasers,[8,9] and erbium-doped waveguide amplifiers (see, for example, the work of Franzò *et al.*[10]). As such, silicon nanocrystal composites have potential for use as light-emitters and optical amplifiers in next-generation optical interconnects.[5]

It was seen in Chap. 2 that *c*-Si NCs in SiO_2 typically exhibit a broad luminescence band centred in the NIR, with a PL quantum efficiency several orders of magnitude higher than that of bulk silicon.[11] When placed within a distributed Bragg reflector (DBR) structure, the emission can be intensified and spectrally narrowed,[12,13] although it is still within the

† A version of this chapter has been published.[1]

700–900 nm range characteristic of the natural emission. This type of fine wavelength control is of recognised importance with respect to luminescent devices.[9] A simpler microcavity consisting of a bottom dielectric stack and a top silver mirror was recently used for a silicon nanocomposite,[14] but wavelength tunability was not demonstrated and the optical modes were relatively broad.

One of the main drawbacks with respect to device integration is the high processing temperature (generally on the order of 1000 °C) required to form luminescent silicon nanoparticles via phase separation of a material with excess atomic silicon. Such high temperatures are incompatible with CMOS technology[15] and, from the point of view of DBRs, make the fabrication of devices based on these materials more difficult, since at least one set of dielectric layers must be exposed to high temperatures during the crystallisation of the nanoparticles. Alternative lower-temperature routes are being explored: for example, recent work demonstrated the fabrication of DBR microcavities in which the nanocrystals were prepared by laser pyrolysis, rather than phase separation.[16] Nevertheless, these devices did not exhibit wide wavelength tunability. Additionally, there is currently widespread interest in microcavity organic light-emitting devices (OLEDs) that do not require high synthesis temperatures.[3,17–19] However, there exist difficulties associated with the lifetimes and reliability of these devices.[20] Furthermore, for red-green-blue (RGB) pixels, several different chemically-compatible materials must be used, thereby complicating the fabrication process.

Although not investigated as widely as silicon nanocrystals formed at high temperatures in SiO_2, a-Si NCs formed from silicon-rich oxide (SRO) films can exhibit spectrally-broad luminescence at considerably lower processing temperatures.[21] This broad visible-to-NIR PL has been variously attributed to band-tail recombination,[22,23] structural defects[24–26] and the presence of ring- or chain-like bonding arrangements.[27,28] However, direct TEM evidence of the existence of nanoscale amorphous Si particles in SRO films annealed at low temperatures, as will be discussed in Chaps. 4 and 5, lends weight to the a-Si-NC theory for the origin of the PL; modelling the luminescence from ensembles of a-Si NCs is the focus of Chap. 6. With respect to light-emitting devices, the broad and intense luminescence spectrum suggests a method of forming tunable, luminescent, SRO-based microcavities using an extremely simple fabrication process that can, in principle, permit colour control throughout the entire visible spectrum and into the near infrared. The material is durable, compatible with microelectronics architectures, and can be synthesised by a variety of straightforward thin-film techniques.

Fabry–Pérot microcavity resonators were grown by sequential electron-beam evaporation of Ag and SiO. A thick (200-nm) silver mirror was first deposited by electron-beam evaporation onto a clean fused-quartz wafer. A layer of SRO was deposited on top of the silver film via thermal evaporation of silicon monoxide. A thin silver mirror was then deposited to form the output coupler, followed by a 20-nm-thick SiO_2 oxidation barrier; silver was selected as the mirror material because of its high reflectivity throughout the visible and NIR spectrum, and its good transmittance at 325 nm (this is the wavelength of the pump laser used for photoluminescence measurements). The specimen was subsequently removed from the evaporation system and was annealed at a temperature of 500 °C in an atmosphere of 95% N_2+5% H_2. The SRO synthesis procedure is similar to that used for preparing silicon nanocrystals,[29] except that thermal processing was done at 500 °C instead of at 1000 °C or higher. A gradient specimen, M, was prepared by holding the substrate off-axis with respect to the source. The Er-doped samples, E1–E4, were prepared by simultaneous thermal evaporation of SiO and electron-beam evaporation of

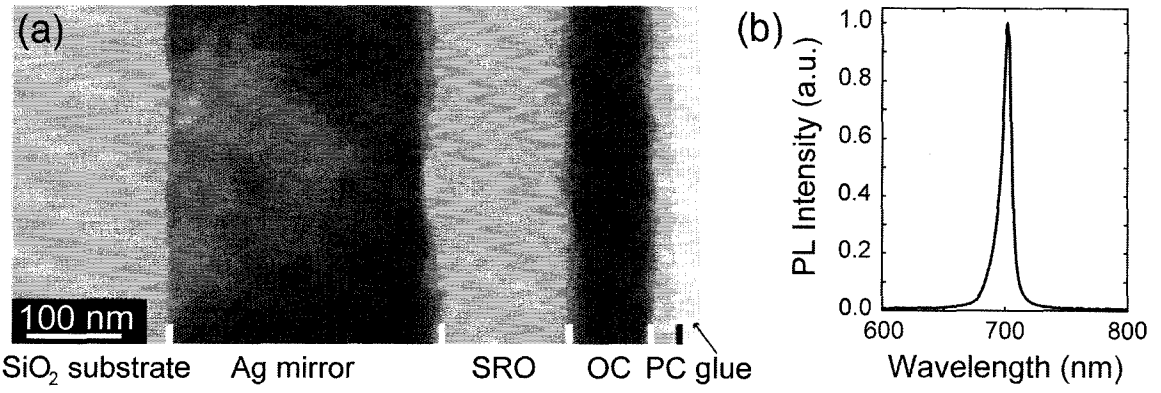

Fig. 3.1: (a) Cross-sectional TEM image of a representative microcavity structure. This sample consists of the SiO_2 substrate, a thick silver mirror, an SRO active layer, an output coupler (OC), and a protective coating (PC). The glue layer is due to the TEM specimen preparation. (b) Luminescence spectrum from the specimen shown in (a).

Er_2O_3 in an approximately 25:1 ratio. Reflection and PL experiments were conducted using a fibre-optic CCD spectrometer system. For the PL experiments, the excitation source was the 325-nm line of a HeCd laser (incident power ~15 mW), and for all measurements, the CCD response was normalised with respect to a standard blackbody radiator. A TEM image of one of the resulting microcavities is shown in Fig. 3.1a. The active SRO layer was featureless at this resolution and fully amorphous; the silver mirrors were polycrystalline. Also visible is the 20-nm-thick protective oxidation barrier that was deposited on the top surface of the specimen.

The resonant optical modes were apparent in the reflection and photoluminescence spectra (Fig. 3.2). The modes depend on the refractive index and thickness of each of the layers and on the optical phase change upon reflection at the SRO-Ag interfaces. Characteristic matrix calculations for an assembly of thin films were used to model the resonant modes and determine the active layer thickness required for the desired wavelengths (see §C.1 for details of these calculations). With increasing mirror thickness, the calculated modes became sharper and shifted to slightly shorter wavelengths, consistent with the experimental results for these structures (Fig. 3.2b). The reflectance modes were slightly broader in the model than in the experiment, suggesting that the output couplers are somewhat thicker than determined by the crystal monitor during deposition.† The cavity quality factor Q is a measure of the sharpness of the resonance, and depends on the lossiness of the resonator. It is defined as[30]

$$Q = \frac{\lambda_0}{\Delta\lambda_{\frac{1}{2}}} \tag{3.1}$$

where λ_0 is the peak wavelength and $\Delta\lambda_{\frac{1}{2}}$ is the full width at half-maximum (FWHM) for the resonance peak. Since it quantifies loss from the cavity, Q depends on the total reflectivity and therefore on the thickness of the output-coupling mirror; it ranged from 17 for the thinnest output coupler to a value of 68 for the thickest ones.

The SRO emitted a broad PL spectrum that extended throughout the visible spectrum

†This was in fact confirmed by TEM, except that the micrographs showed that the output couplers were even *thicker* than suggested by the model. One possible explanation is the significant variation in the optical constants of silver as obtained from different sources. See, for example, *Handbook of Chemistry and Physics*, 76th ed. (Ed: D.R. Lide), CRC Press, Boca Raton, **1995** and *Handbook of Optical Constants of Solids* (Ed: E. Palik), Academic Press, Inc., New York, **1991**. Error in the refractive indices could potentially account for the observed discrepancy in the measured and calculated thickness of the output-coupling mirrors.

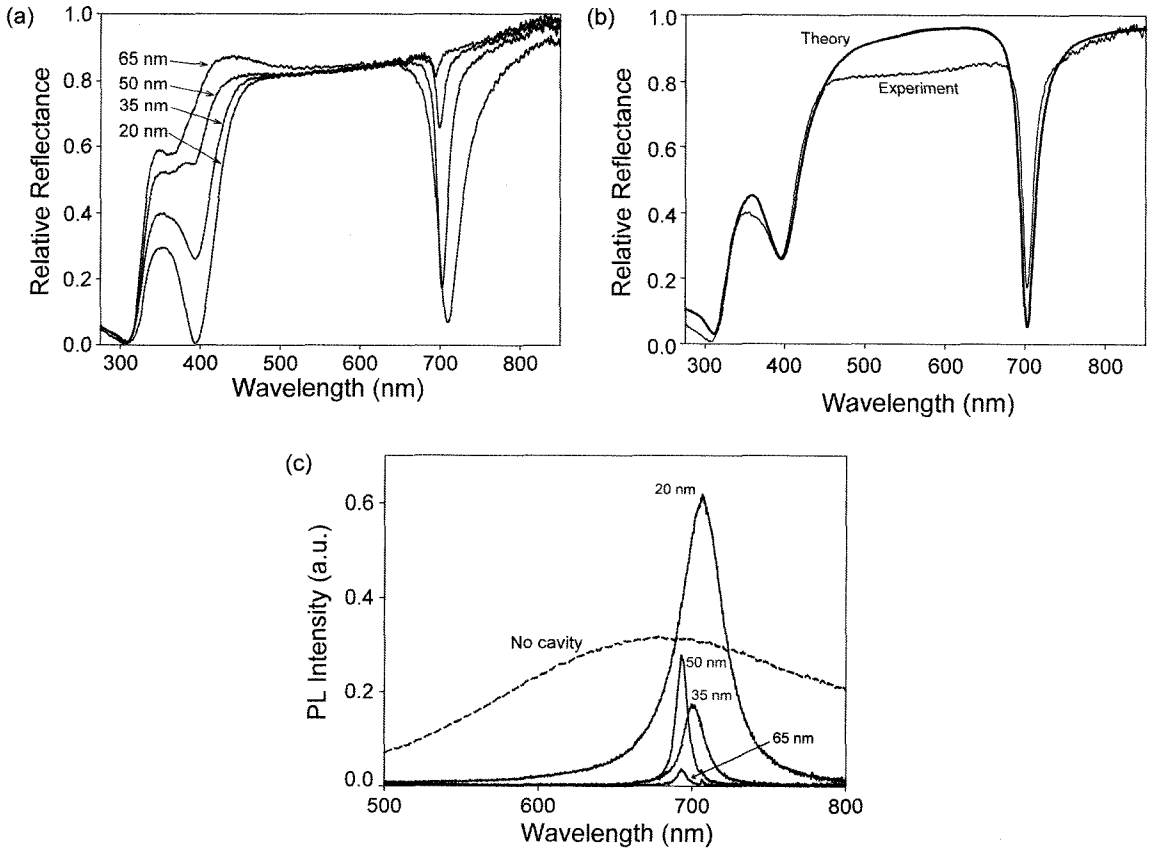

Fig. 3.2: (a) Relative reflection spectra from 120-nm-thick SRO cavities with 20, 35, 50, and 65-nm-thick Ag output couplers. (b) A comparison between the experimental and theoretical reflectance for the cavity with the 35-nm output coupler. (c) Luminescence spectra from the same four microcavities (solid lines) and a bare 120-nm layer of SRO (dotted line).

and tails off in the blue region (Fig. 3.2c). The most intense PL was obtained after processing at 500 °C, a temperature compatible with standard CMOS fabrication.[15] Temperatures as low as 400 °C also produced visible luminescence, and could in principle be used, although the intensity was lower. This type of broadband emission makes the realisation of microcavity emitters especially easy and tunable across a remarkably wide spectral range.

In the presence of the microcavities, the PL spectrum was strongly narrowed (Fig. 3.2c). The intensity at the peak wavelength depends on the quality factor and on the transmission of the output-coupling mirror. With metal mirrors, there is a trade-off between the mirror reflectivity and transmission. The spectra in Fig. 3.2c were collected normal to the surface; at higher angles, however, the intensity decreased and shifted to shorter wavelengths, consistent with models for Fabry-Pérot resonators.[31]

By varying the thickness of the active layer, the light emission may be tuned from 475 to 875 nm. To the author's knowledge, this is currently a record spread for the cavity modes of any single luminescent material. To demonstrate this point, a graded specimen was fabricated in which the thickness of the SRO layer varied uniformly across a single two-inch Si wafer. In this way, any desired first-order resonant wavelength between 475 and 875 nm was obtained simply by moving the pump beam across the specimen (Fig. 3.3). Additional (non-graded) specimens were prepared in which the resonant emission wavelength ranged up to 1 μm, although for such thick active layers, higher-

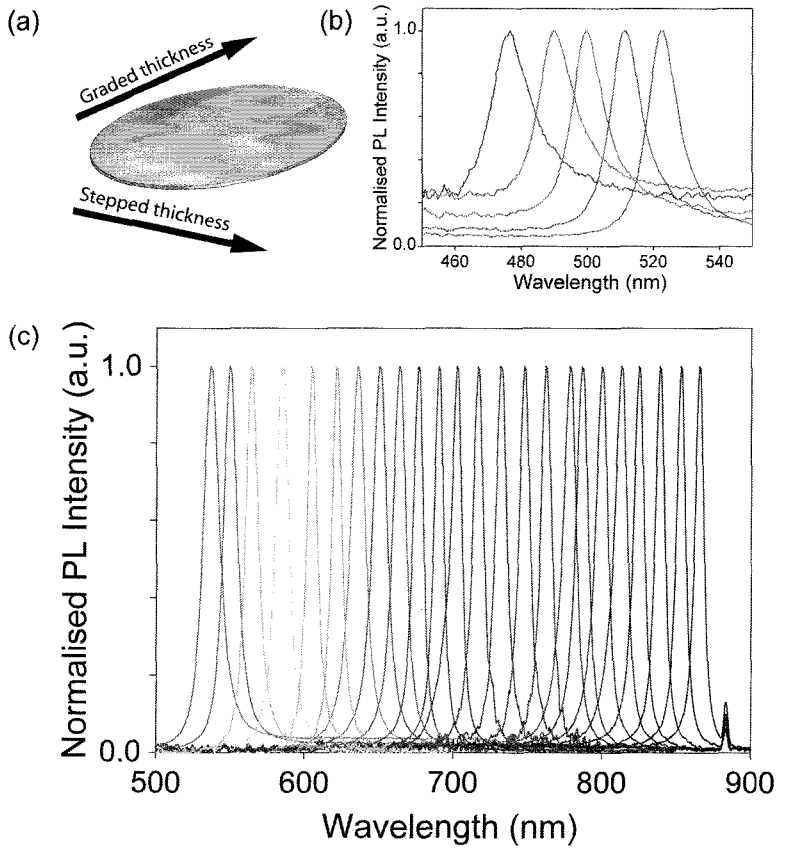

Fig. 3.3: (a) Schematic representation of a variable-thickness microcavity structure. The active layer thickness is smoothly graded in one direction and stepped in another in order to achieve the full colour range. (b) and (c) show luminescence spectra representing the range achievable in the SRO graded samples. The data were obtained from different spectrometers and are normalised for direct spectral comparison, but the blue emitters were the weakest. Any desired peak wavelength between 475 and 875 nm can be selected depending on the location on this specimen, which effectively emits a "rainbow" of fluorescent colours. In (b), the sideband extending toward longer wavelengths is due to the greater luminescence intensity in that spectral region and illustrates the practical short-wavelength limit of these undoped SRO microcavities.

order interference became an issue. The luminescence was readily visible to the unaided eye, and although the intensity was greatest between ~600 and 750 nm, even the weaker 480-nm wavelength blue luminescence is easily observable and was readily captured by an inexpensive digital camera (Fig. 3.4). Therefore, this approach permits the fabrication of wavelength-selectable emitters based on a *single* material whose processing is straightforward and simple. In comparison to these results, a relatively broadband OLED material such as tris(8-hydroxyquinoline)aluminum can be tuned to emit between 500 and 625 nm.[32] The spectral range exhibited by the SRO microcavities (475 to 875 nm), therefore, represents the current record tunability for any single material.

In addition, this microcavity enhancement can easily be extended to the third fibre-optic transparency window at 1.5 μm by lightly doping the SRO with erbium. Fig. 3.5 shows the PL spectra from Er-doped SRO. The resonant wavelength was tuned from 1480

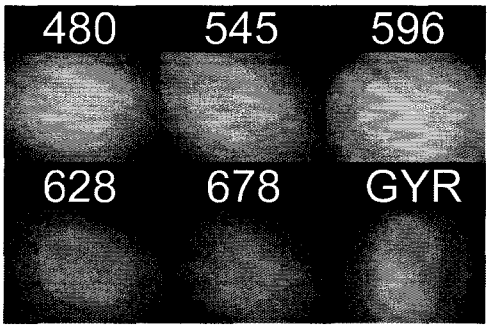

Fig. 3.4: Luminescence images from a variety of SRO microcavities, obtained with an inexpensive digital camera. The resonant wavelengths (in nanometres) are listed above each image. Each spot is approximately 1 mm in diameter. The blue emission corresponded to a second-order mode. The bottom right image shows a graded "rainbow" silicon oxide microcavity, in which the SRO thickness was smallest on the left (green), intermediate in the centre (yellow), and greatest on the right (red). These images illustrate that the fluorescence is readily observed under ambient conditions and exhibits excellent wavelength control.

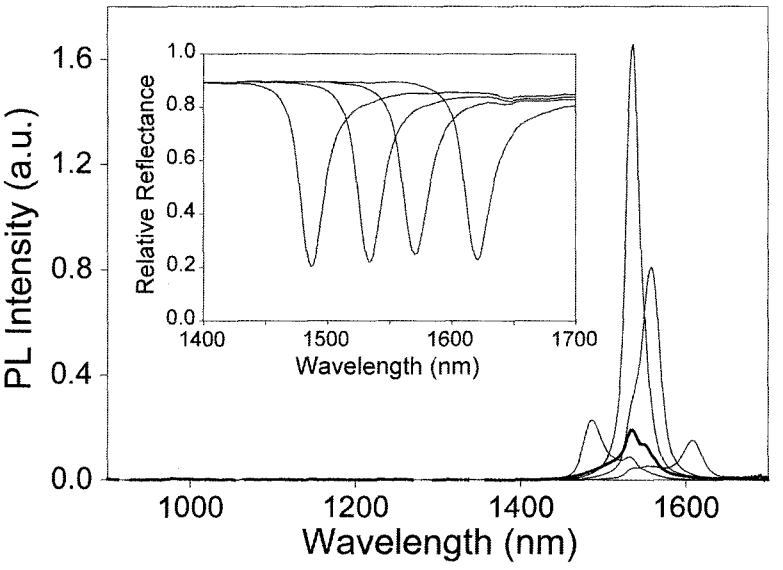

Fig. 3.5: PL spectra of erbium-doped SRO. The thick black line is for a 145-nm-thick bare film, and the thinner lines are for the same material sandwiched between silver mirrors (see Table 3.1). By varying the thickness of the active material, the emission peak was tuned between 1490 and 1610 nm. Relative reflection data for the four cavities are shown on an expanded scale in the inset.

Table 3.1: Active SRO layer thickness and calculated reflectance resonance wavelengths for the samples whose spectra are shown in Fig. 3.3 (M) and Fig. 3.5 (E1-4). The most intense resonant mode for each sample is shown in the last column. The effective "optical thickness" for the SRO layer was calculated using the optical constants of bulk SiO.

Sample	High reflector thickness (Ag) [nm]	Optical thickness (SRO) [nm]	Output coupler thickness (Ag) [nm]	1^{st}-order resonance [nm]
M†	200	67–182	50	variable
E1	200	333	20	1487
E2	200	348	20	1538
E3	200	353	20	1556
E4	200	372	20	1626

†The active layer in this sample was prepared using a deposition process that produces a thickness gradient, so that the desired resonant wavelength can be obtained simply by moving the pump beam laterally across the specimen (See Fig. 3.3).

to 1630 nm, although the strongest emission was obtained at 1535 nm. In comparison to Er-doped SiO_2[33] or Er-doped Si nanocrystals[34] within DBR structures, the synthesis procedure presented here is experimentally much simpler and can readily lend itself to electrical pumping techniques. The properties of such Er-doped a-Si-NC microcavity structures will be discussed in more detail in the following chapter.

There are several advantages and limitations associated with these metal microcavity resonators. An important limitation in the development of, for example, SRO-based lasing devices is the relatively low finesse of the metallic microcavities. Dielectric stacks can have a reflectivity over 99.5%, whereas in the case of metals, the reflectivity is limited by a non-zero extinction coefficient. As an example, the maximum reflectivity of a SiO–Ag interface is ~96% at 800 nm. These factors present an inherent limitation on the Q of the optical modes. In addition, the emission intensity depends on the resonant wavelength and is weakest in the blue, due to the low intrinsic luminescence intensity in that spectral region. Therefore, additional procedures may be necessary to obtain blue luminescence of comparable intensity with the red, orange, and yellow emission.

On the other hand, for devices such as LEDs and optical displays, metal mirrors can

naturally double as electrodes, and, in fact, SRO has been demonstrated to show attractive electroluminescent properties.[35] The low annealing temperatures are compatible with conventional microelectronics fabrication processes, suggesting the possibility of light-emitting resonators built directly on a silicon chip.[15] In addition, the synthesis method requires only three or four separate layers as compared to 20 or more for high-quality DBRs. Despite the experimental simplicity, these SRO-based microcavities demonstrate a remarkable emission wavelength spread from 475 to 875 nm (extended to 1630 nm when doped with Er), as compared to any previous material. Therefore, this approach covers most of the wavelength range between 0.4 and 1.6 μm as required for photonic applications.[5] OLED structures developed for colour display applications routinely incorporate metal mirrors, although without the range of wavelength tunability demonstrated here. To conclude, silicon-rich oxide microcavities can emit almost any colour in the visible spectrum, suggesting that the "optical age of silicon"[6] may indeed be a colourful one.

Bibliography

[1] A. Hryciw, J. Laforge, C. Blois, M. Glover, and A. Meldrum, "Tunable luminescence from a silicon-rich oxide microresonator", *Adv. Mater.*, vol. 17, no. 7, pp. 845–849, 2005.

[2] A. P. Alivisatos, "Semiconductor clusters, nanocrystals, and quantum dots", *Science*, vol. 271, no. 5251, pp. 933–937, 1996.

[3] S. Tokito, T. Tsutsui, and Y. Taga, "Microcavity organic light-emitting diodes for strongly directed pure red, green, and blue emissions", *J. Appl. Phys.*, vol. 86, no. 5, pp. 2407–2411, 1999.

[4] V. I. Klimov, A. A. Mikhailovsky, S. Xu, A. Malko, J. A. Hollingsworth, C. A. Leatherdale, H. J. Eisler, and M. G. Bawendi, "Optical gain and stimulated emission in nanocrystal quantum dots", *Science*, vol. 290, no. 5490, pp. 314–317, 2000.

[5] D. J. Lockwood and L. Pavesi, "Silicon fundamentals for photonics applications", *Top. Appl. Phys.*, vol. 94, pp. 1–50, 2004.

[6] G. T. Reed, "Device physics: The optical age of silicon", *Nature*, vol. 427, no. 6975, pp. 595–596, 2004.

[7] J. Valenta, N. Lalic, and J. Linnros, "Electroluminescence microscopy and spectroscopy of silicon nanocrystals in thin SiO_2 layers", *Opt. Mater.*, vol. 17, no. 1–2, pp. 45–50, 2001.

[8] L. Pavesi, L. Dal Negro, C. Mazzoleni, G. Franzò, and F. Priolo, "Optical gain in silicon nanocrystals", *Nature*, vol. 408, no. 6811, pp. 440–444, 2000.

[9] L. Pavesi, "A review of the various efforts to a silicon laser", *Proc. SPIE*, vol. 4997, pp. 206–220, 2003.

[10] G. Franzò, S. Coffa, F. Priolo, and C. Spinella, "Mechanism and performance of forward and reverse bias electroluminescence at 1.54 μm from Er-doped Si diodes", *J. Appl. Phys.*, vol. 81, no. 6, pp. 2784–2793, 1997.

[11] A. J. Kenyon, P. F. Trwoga, C. W. Pitt, and G. Rehm, "Luminescence efficiency measurements of silicon nanoclusters", *Appl. Phys. Lett.*, vol. 73, no. 4, pp. 523–525, 1998.

[12] F. Iacona, G. Franzò, E. C. Moreira, D. Pacifici, A. Irrera, and F. Priolo, "Luminescence properties of Si nanocrystals embedded in optical microcavities", *Mater. Sci. Eng. C*, vol. 19, no. 1–2, pp. 377–381, 2002.

[13] F. Iacona, G. Franzò, E. C. Moreira, and F. Priolo, "Silicon nanocrystals and Er^{3+} ions in an optical microcavity", *J. Appl. Phys.*, vol. 89, no. 12, pp. 8354–8356, 2001.

[14] T. Ichinohe, D. Kenmochi, H. Morisaki, S. Masaki, and K. Kawasaki, "Si doped SiO_2 glass light emitter within an optical cavity fabricated by ion beam sputter-deposition", *Thin Solid Films*, vol. 377, pp. 87–91, 2000.

[15] S. Sedky, A. Witvrouw, H. Bender, and K. Baert, "Experimental determination of the maximum post-process annealing temperature for standard CMOS wafers", *IEEE Trans. Electr. Dev.*, vol. 48, no. 2, pp. 377–385, 2001.

[16] D. Amans, S. Callard, A. Gagnaire, J. Joseph, F. Huisken, and G. Ledoux, "Spectral and spatial narrowing of the emission of silicon nanocrystals in a microcavity", *J. Appl. Phys.*, vol. 95, no. 9, pp. 5010–5013, 2004.

[17] B. Y. Jung, N. Y. Kim, C. Lee, C. K. Hwangbo, and C. Seoul, "Control of resonant wavelength from organic light-emitting materials by use of a Fabry-Perot microcavity structure", *Appl. Opt.*, vol. 41, no. 16, pp. 3312–3318, 2002.

[18] H. Becker, S. E. Burns, N. Tessler, and R. H. Friend, "Role of optical properties of metallic mirrors in microcavity structures", *J. Appl. Phys.*, vol. 81, no. 6, pp. 2825–2829, 1997.

[19] J. M. Zhao, F. Y. Ma, X. Y. Liu, Y. Liu, G. Q. Chu, Y. Q. Ning, and L. J. Wang, "Three-colour single-mode electroluminescence from Alq_3 tuned by microcavities", *Chinese Phys. Lett.*, vol. 19, no. 10, pp. 1447–1449, 2002.

[20] O. Nuyken, E. Bacher, T. Braig, R. Fáber, F. Mielke, M. Rojahn, V. Wiederhirn, K. Meerholz, and D. Möller, "Crosslinkable hole- and electron-transport materials for application in organic light emitting devices (OLEDs)", *Designed Monomers and Polymers*, vol. 5, no. 2–3, pp. 195–210, 2002.

[21] T. Okada and E. Ohta, "Visible photoluminescence from evaporated SiO_x thin films", *Japanese J. Appl. Phys., Part 1*, vol. 41, no. 11A, pp. 6413–6416, 2002.

[22] R. Carius, R. Fischer, E. Holzenkampfer, and J. Stuke, "Photoluminescence in the amorphous system SiO_x", *J. Appl. Phys.*, vol. 52, no. 6, pp. 4241–4243, 1981.

[23] R. B. Wehrspohn, M. Zhu, and C. Godet, "Visible photoluminescence and its mechanisms from a-SiO_x:H films with different stoichiometry", *J. Luminesc.*, vol. 80, no. 1–4, pp. 449–453, 1998.

[24] J. Y. Jeong, S. Im, M. S. Oh, H. B. Kim, K. H. Chae, C. N. Whang, and J. H. Song, "Defect versus nanocrystal luminescence emitted from room temperature and hot-implanted SiO_2 layers", *J. Luminesc.*, vol. 80, no. 1-4, pp. 285–289, 1998.

[25] Y. Kanzawa, S. Hayashi, and K. Yamamoto, "Raman spectroscopy of Si-rich SiO_2 films: Possibility of Si cluster formation", *J. Phys. Cond. Mat.*, vol. 8, no. 26, pp. 4823–4835, 1996.

[26] Y. C. Fang, L. Y. Li, Y. Y. Zhao, L. J. Qi, W. Q. Li, Z. J. Zhang, and M. Lu, "Photoluminescence of SiO_x thin films after annealing at various temperatures", *Chinese Phys. Lett.*, vol. 20, no. 11, pp. 2042–2044, 2003.

[27] L. X. Yi, J. Heitmann, R. Scholz, and M. Zacharias, "Si rings, Si clusters, and Si nanocrystals—different states of ultrathin SiO_x layers", *Appl. Phys. Lett.*, vol. 81, no. 22, pp. 4248–4250, 2002.

[28] M. Zacharias, J. Heitmann, R. Scholz, U. Kahler, M. Schmidt, and J. Blasing, "Size-controlled highly luminescent silicon nanocrystals: A SiO/SiO_2 superlattice approach", *Appl. Phys. Lett.*, vol. 80, no. 4, pp. 661–663, 2002.

[29] M. Glover and A. Meldrum, "Effect of 'buffer layers' on the optical properties of silicon nanocrystal superlattices", *Opt. Mater.*, vol. 27, no. 5, pp. 977–982, 2005.

[30] J. T. Verdeyen, *Laser Electronics*, Prentice Hall, Upper Saddle River, New Jersey, third edition, 1995, ISBN: 0-137-0666-6, p. 149.

[31] A. B. Djurišić and A. D. Rakić, "Organic microcavity light-emitting diodes with metal mirrors: dependence of the emission wavelength on the viewing angle", *Appl. Opt.*, vol. 41, no. 36, pp. 7650–7656, 2002.

[32] A. Dodabalapur, L. J. Rothberg, T. M. Miller, and E. W. Kwock, "Microcavity effects in organic semiconductors", *Appl. Phys. Lett.*, vol. 64, no. 19, pp. 2486–2488, 1994.

[33] E. F. Schubert, A. M. Vredenberg, N. E. J. Hunt, Y. H. Wong, P. C. Becker, J. M. Poate, D. C. Jacobson, L. C. Feldman, and G. J. Zydzik, "Giant enhancement of luminescence intensity in Er-doped Si/SiO_2 resonant cavities", *Appl. Phys. Lett.*, vol. 61, no. 12, pp. 1381–1383, 1992.

[34] D. Pacifici, A. Irrera, G. Franzò, M. Miritello, F. Iacona, and F. Priolo, "Erbium-doped Si nanocrystals: optical properties and electroluminescent devices", *Physica E*, vol. 16, no. 3–4, pp. 331–340, 2003.

[35] M. Sopinskyy and V. Khomchenko, "Electroluminescence in SiO_x films and SiO_x-film-based systems", *Curr. Opin. Sol. State Mater. Sci.*, vol. 7, no. 2, pp. 97–109, 2003.

CHAPTER 4

Photoluminescence from Er-doped silicon oxide microcavities†

4.1 Introduction

In the previous chapter, it was demonstrated that the broad intrinsic emission from *a*-Si nanocomposites can be narrowed and tuned when incorporated into simple planar microcavity structures with metal mirrors. This was also shown to be the case when the NC films have been doped with erbium, in which the 1.54 μm emission band from the $^4I_{13/2} \rightarrow {}^4I_{15/2}$ intra-4*f* transition can be similarly controlled. As mentioned in §1.1, while Er-doped SiO_2 suffers from ion clustering effects and a low excitation cross-section, co-doping with Si nanoparticles can increase the effective 1.54 μm excitation efficiency by as much as two orders of magnitude.[2] Thus, Er-doped Si nanocomposites comprise a potentially attractive class of materials for application in optical waveguide amplifiers.

Most recent studies of Er-doped Si nanocomposites have relied on thermal processing on the order of 1000 °C or more to induce phase separation in silicon-rich oxides to produce nanocrystals surrounded by a SiO_2 matrix (e.g., Refs.[3–5]). As discussed in previous chapters, while high-quality, well-passivated nanocrystals may thus be produced,[6] such high annealing temperatures pose a significant barrier to the monolithic integration of *c*-Si-NC:Er-based photonic components with CMOS driving circuitry for opto-electronic applications.[7] Low-temperature methods of producing Er-doped Si nanocomposites with comparable luminescent properties are therefore of practical interest. For example, erbium-doped semi-insulating crystalline and amorphous Si (SIPOS),[8,9] and silicon monoxide[10] can exhibit intense 1.54 μm emission after annealing at temperatures on the order of 400–600 °C. Relatively recently, the optical properties of such Er-doped silicon-rich oxides have received renewed interest (e.g., Refs.[11–13]).

In this chapter, an investigation of the PL from Er-doped SiO produced via standard thin-film deposition techniques is presented. The dependence of the 1.54-μm emission mechanism on the microstructure of the SiO:Er, the specimen annealing temperature, and the Er concentration is also examined. To further illustrate the value of this low-temperature anneal, the *a*-Si-NC:Er films have been incorporated into planar Fabry-Pérot microcavities with metal mirrors, as in the previous chapter. The resonant wavelength of these cavities is tunable across the entire 1.54 μm Er^{3+} emission band simply by varying the SiO:Er layer thickness.

† A version of this chapter has been published.[1]

4.2 Experimental

Five 150-nm-thick films of silicon oxide with varying Er doping concentrations were deposited under high vacuum on high-purity SiO_2 substrates via co-evaporation of SiO and Er_2O_3 at a base pressure of $\sim 1.5 \times 10^{-4}$ Pa. The silicon monoxide was thermally evaporated using a baffled-box source, whereas electron-beam evaporation was used for the erbium oxide. The samples were subsequently annealed for 1 h in flowing N_2, Ar, or forming gas (95% N_2 + 5% H_2), at temperatures ranging from 300 to 1000 °C.

Electron microprobe analysis (EMPA) was employed to obtain compositional analyses of the films, using SiO_2 and $ErPO_4$ as standards (Smithsonian), and a beam energy of 3 kV. The structural composition of the films was determined using TEM and energy-filtered imaging.

Steady-state PL spectra were collected with a fibre-optic system and analysed with InGaAs and Si CCD spectrometers, using the 325-nm line of a HeCd laser or the 476-nm line of an argon ion laser for continuous wave excitation. The spectral response of the spectroscopy system was corrected by normalising to a standard blackbody radiator. PL lifetime measurements were obtained using a thermoelectrically-cooled amplified InGaAs photodiode connected to a digital storage oscilloscope. The 476 nm laser beam was chopped using an acousto-optic modulator at a frequency of 10 Hz, with 20 mW of power incident on the specimen during excitation over a circular spot ~0.6 mm in radius. PL collected by optical fibres was passed through a 1550-nm band-pass filter before detection by the InGaAs photodiode; the system response time was ~20 μs.

The planar Fabry-Pérot microcavities were fabricated on Si or SiO_2 substrates using the thin film deposition system mentioned above. A 200-nm-thick layer of Ag was deposited via electron-beam evaporation to form a high-reflectivity bottom mirror, followed by a SiO:Er layer. On one sample, a variation in thickness in the SiO:Er layer was achieved by off-axis thermal evaporation of the SiO. A thin layer of Ag was then deposited to form the output coupler. Finally, a ~20 nm layer of SiO_2 was deposited as an oxidation barrier. The general structure of these microcavities is the same as that presented in the TEM micrograph of Fig. 3.1a.

4.3 Results and discussion

4.3.1 Compositional analysis of SiO:Er films

The microstructure of the SiO films was investigated using TEM techniques, including high-resolution electron microscopy (HREM), selected area electron diffraction, and energy-filtered TEM (EFTEM). The results illustrated in Fig. 4.1 are for an undoped SiO film annealed at 500 °C in forming gas for 1 h. The HREM image and diffraction pattern shown in Fig. 4.1a and b, respectively, confirm that the SiO (when annealed at such low temperatures) is fully amorphous with a cluster/matrix combination. As a comparison, TEM analyses of films annealed at 900 °C or higher indicate the presence of *crystalline* nanoparticles.[14] The presence of amorphous Si clusters is further confirmed by Fig. 4.1c, obtained by superposing the silicon (red) and oxygen (blue) EFTEM images of the SiO film. The mean diameter of these Si-rich clusters is 2–3 nm.

The chemical composition of the Er-doped SiO films (determined by EMPA) is summarised in Table 4.1. The films are nearly stoichiometric SiO, but are slightly oxygen-rich, most likely due to the decomposition of Er_2O_3 and/or the SiO during evaporation.

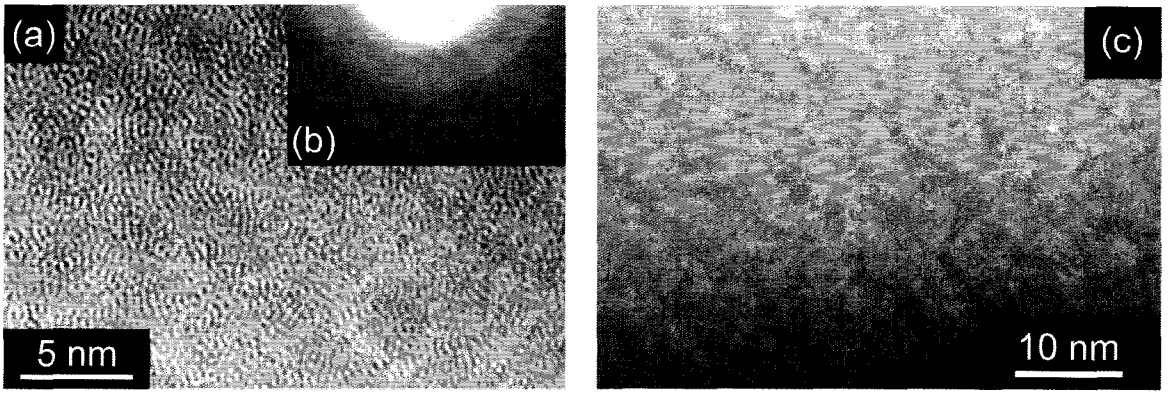

Fig. 4.1: TEM analysis of an SiO film annealed for 1 h at 500 °C in forming gas: (a) HREM image, (b) diffraction pattern of Si cluster, (c) EELS elemental map (red: Si, blue: O)

The abundance of oxygen in the films is important from the perspective of the 1.54 μm PL intensity, as the formation of Er–O complexes produces a defect level in the Si band wherein trapped excitons may efficiently couple their recombination energy to Er^{3+} ions via dipole–dipole coupling (Förster transfer) or an Auger process.[12] Such complexes also reduce the mobility and thus the segregation of Er, which can lessen concentration quenching effects.[13]

4.3.2 The effect of annealing

To determine the effect of the annealing process gas on the Er^{3+} PL, three ~0.20-at.%-Er films were annealed for 1 h at 500 °C in flowing N_2, Ar, and forming gas (Fig. 4.2). A factor of ~10 increase in peak intensity for 325-nm excitation is observed after annealing in either Ar or N_2, which has been attributed to a relaxation from O_h to C_{4v} in the symmetry of the sixfold coordination of O around Er, required to optically activate the Er^{3+}.[15] The crystal-field splitting resulting from C_{4v} symmetry is sufficient to allow the parity-forbidden $^4I_{13/2} \rightarrow {}^4I_{15/2}$ transition which produces the 1.54-μm PL. Annealing in forming gas (95% N_2+5% H_2), however, provides an increase in intensity of ~20 times with respect to the as-deposited film. The ability of hydrogen to reduce alternative non-radiative recombination channels on Si nanoparticle surfaces is well documented.[6] This increase in PL intensity with hydrogenation is consistent with results for Er-doped SiO_2 films with high excess silicon content.[16] Forming gas was therefore used for all subsequent anneals to maximise the Er^{3+} PL.

The inset of Fig. 4.2 shows the dependence of the Er^{3+} PL peak intensity on annealing temperature for Sample C. The increase in intensity up to a maximum after 500 °C annealing has been attributed to a reduction of defects such as dangling bonds, which could act

Table 4.1: Compositional analysis of SiO:Er films obtained using EMPA. All data are normalised to 100%.

Sample	Si (at.%)	O (at.%)	Er (at.%)
A	49.6±0.1	50.4±0.3	0.04±0.02
B	49.4±0.2	50.5±0.3	0.09±0.02
C	49.4±0.3	50.3±0.5	0.20±0.02
D	48.3±0.4	50.3±0.5	1.37±0.02
E	47.4±0.4	50.2±0.3	2.46±0.02

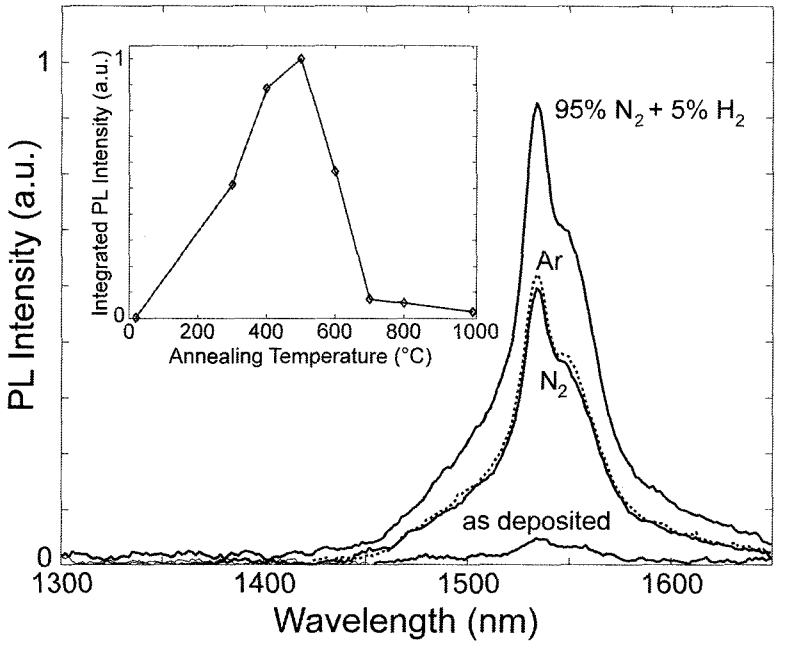

Fig. 4.2: Dependence of Er^{3+} emission on annealing process gas for a 0.20-at.%-Er film annealed for 1 h at 500 °C. Excitation is ~40 mW of the 325-nm line of an HeCd laser. **Inset:** integrated Er^{3+} PL intensity for a 0.20-at.%-Er film annealed in forming gas as a function of annealing temperature.

as Er^{3+} non-radiative recombination centres.[10,17] Upon further increasing the annealing temperature, the intensity decreases; oxygen out-diffusion and Er precipitation or recrystallisation are possible reasons for this behaviour.[17]

4.3.3 The effect of Er concentration

Fig. 4.3 illustrates the PL dependence on the Er concentration for SiO:Er films annealed in forming gas at 500 °C for 1 h. Three PL bands were emitted by the films: the intense Er^{3+}-related band centred at 1535 nm (Fig. 4.3a), a much weaker band at 980 nm (due to the $^4I_{11/2} \rightarrow {}^4I_{15/2}$ Er^{3+} transition), and a broad band extending from ~450 to 950 nm, centred at ~675 nm (Fig. 4.3b). We attribute the visible/near-infrared emission to the presence of the amorphous Si nanoparticles, as confirmed by TEM; this emission is typical of silicon-rich oxide films, and consistent with the studies of films containing crystalline[5,16] or amorphous[18] nanoclusters.

Upon increasing the Er concentration by a factor of ~4.3 (from 0.04 to 0.20 at.%), the integrated intensity of the 1535 nm PL peak increases by a factor of ~3.7; concurrently, the integrated visible peak decreases by a factor of ~3. As the PL was excited at a wavelength which was not resonant with an Er^{3+} transition (325 nm), this behaviour is consistent with the transfer of energy from excitons created in the amorphous Si nanoparticles to the Er^{3+} ions. Auger excitation of Er^{3+} to the $^4I_{13/2}$ level by exciton recombination in the nanoclusters is often cited[5,19] as the excitation mechanism in Er-doped Si nanocrystals; defect-mediated Auger excitation[20,21] as well as resonant tail-to-tail Förster transfer[20] has also been proposed for Er^{3+} excitation in *a*-Si. In the so-called "strong coupling" model,[22] a nanoparticle becomes "dark" (i.e., unable to emit its characteristic visible/NIR PL) once coupled to a neighbouring Er^{3+} ion, given a sufficiently fast energy transfer process.

Further evidence of an efficient coupling mechanism is presented by the nearly complete quenching of the visible PL upon increasing the Er concentration from 0.20 to 2.46 at.%. Concurrently, the 1.54 μm PL peak decreases only by a factor of ~2.5. This decrease in 1.54 μm PL for large Er concentrations may be attributed to clustering or con-

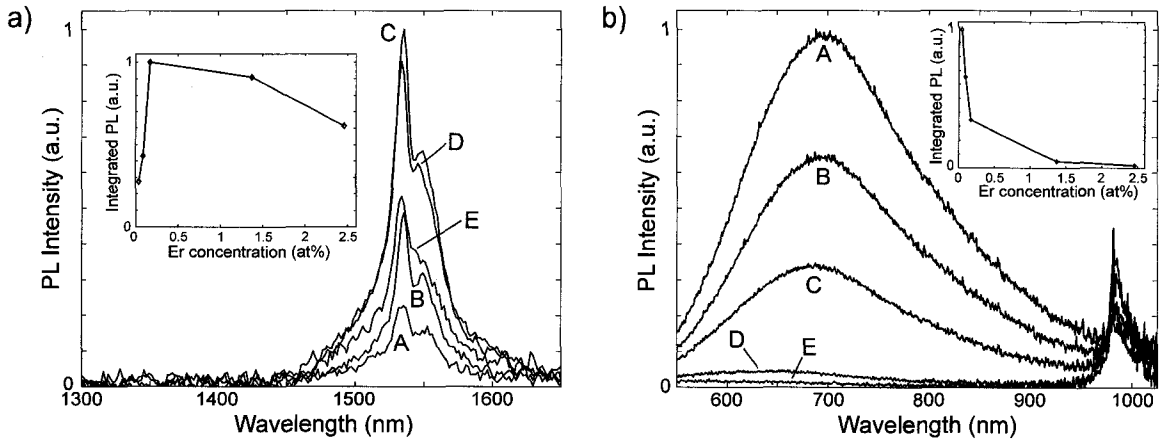

Fig. 4.3: Photoluminescence spectra of Samples A–E with integrated intensities vs. Er concentration shown in insets (~40 mW of 325 nm excitation): (a) 1.54 μm Er^{3+} emission, (b) visible Si nanocluster emission. The small peak centred at 980 nm is due to the $^4I_{11/2} \rightarrow {}^4I_{15/2}$ transition in Er^{3+}, and was not included in the integrated intensity plot.

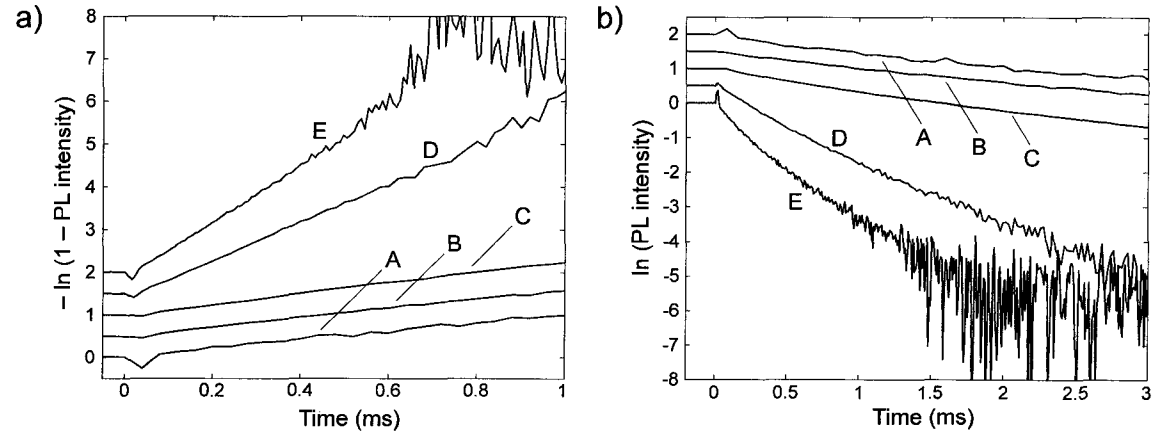

Fig. 4.4: PL dynamics curves for Samples A–E, using 476-nm excitation. For clarity, the curves are normalised to their peak values and vertically offset: (a) PL rise curves, (b) PL decay curves.

centration quenching effects. Further evidence of the coupling between amorphous nanoclusters and Er^{3+} ions is obtained from the excitation cross-sections.

4.3.4 PL dynamics

Values for an effective excitation cross-section for the Er^{3+} ions may be determined by considering the 1.54-μm PL dynamics. For a simple two-level system, the $1/e$ rise time (τ_r) and decay time (τ_d) are related to the excitation rate by the expression $R = \tau_r^{-1} - \tau_d^{-1}$.[23] 1.54-$\mu$m PL rise and decay measurements for specimens A–E are shown in Fig. 4.4, with rise and decay times ranging from ~0.2 to ~1.1 ms and ~0.3 to ~2.5 ms, respectively. The reduction in τ_d by approximately 30% upon increasing the Er concentration from 0.04 to 0.20 at.% is evidence of concentration quenching, which may partly account for the increase in the integrated 1.54-μm band intensity by only a factor of 3.7 for a concomitant increase in Er concentration of 4.3 (inset of Fig. 4.3a).

From the excitation rate, we may obtain an effective Er^{3+} excitation cross-section, incorporating the energy transfer from the Si nanoclusters as well as non-radiative transi-

Table 4.2: Effective Er^{3+} PL dynamics and excitation cross-section results for Samples A–E

Sample	Decay time τ_d ±0.04 (ms)	Rise time τ_r ±0.02 (ms)	Excitation rate, R (1/s)	Effective excitation cross-section, $\sigma_{eff}^{Er^{3+}}$ ($\times 10^{-16}$ cm^2)
A	2.33	1.10	479	1.1±0.3
B	2.43	0.99	594	1.4±0.3
C	1.70	0.84	596	1.4±0.3
D	0.43	0.25	1666	3.9±0.9
E	0.25	0.17	1669	3.9±0.9

tions, using $R = \sigma_{eff}^{Er^{3+}} \times \Phi_{phot}$. The excitation photon flux of $\sim 4 \times 10^{18}$ cm^{-2}s^{-1} yields $\sigma_{eff}^{Er^{3+}} \approx 10^{-16}$ cm^2, similar to reported values for Er-doped nanocrystalline Si (e.g. Ref.[24]), and several orders of magnitude larger than the direct Er^{3+} optical absorption cross-section on the order of 10^{-21} cm^2. The calculated values for $\sigma_{eff}^{Er^{3+}}$ are summarised in Table 4.2. Due to the non-zero system response time, these values represent a lower limit for $\sigma_{eff}^{Er^{3+}}$. These large cross-sections indicate that, as sensitisers of Er^{3+}, the amorphous Si nanoclusters are as effective as silicon nanocrystals. Since the amorphous clusters are formed by low-temperature annealing of SiO, they offer much greater compatibility with CMOS fabrication processes. A more detailed investigation of the NC–Er^{3+} system PL dynamics is the subject of Chap. 7.

4.3.5 Characterisation of microcavities

To demonstrate the use of SiO:Er for photonics applications, we constructed simple trial devices consisting of Fabry-Pérot planar microcavities with Ag mirrors. The Er concentration in the active layer is ~0.20 at.%, and the specimens were annealed at 500 °C in flowing N_2/H_2 for 1 h. Cavity A has a 50-nm-thick output coupler and a graded-thickness SiO:Er layer, resulting in a smooth tuning of the resonant wavelength across the ~7.5-cm length of the substrate; Cavity B has a ~50-nm-thick output coupler mirror, and is tuned to the peak Er^{3+} emission at 1535 nm. Reflectance and transmission spectra for these structures were modelled using a characteristic matrix method for an ensemble of thin films (see §C.1).

As illustrated in Fig. 4.5, the emission from Cavity A may be tuned across the entire Er^{3+} band (~1480–1610 nm) by exciting different positions along the substrate; only fifteen representative emission peaks are shown in the figure for clarity. For the cavity thickness resonant with the peak emission at 1535 nm, the full-width at half-maximum (FWHM) is ~17 nm.

For PL collected normal to the surface of Cavity B, the FWHM of the emission is 19.3 nm. The cavity quality factor may be calculated from Eq. (3.1); however, one must take into account the spectral shape of the underlying Er^{3+} PL band when determining the linewidth. For a planar cavity, the intensity transmission coefficient is given by[25]

$$T(\vartheta) = \frac{(1-R_1)(1-R_2)}{(1-\sqrt{R_1R_2})^2 + 4\sqrt{R_1R_2}\sin^2\vartheta} \tag{4.1}$$

where R_1 and R_2 are the intensity reflection coefficients of the top and bottom mirrors, respectively, and ϑ is the optical length of the cavity. For metal mirrors, a phase shift is

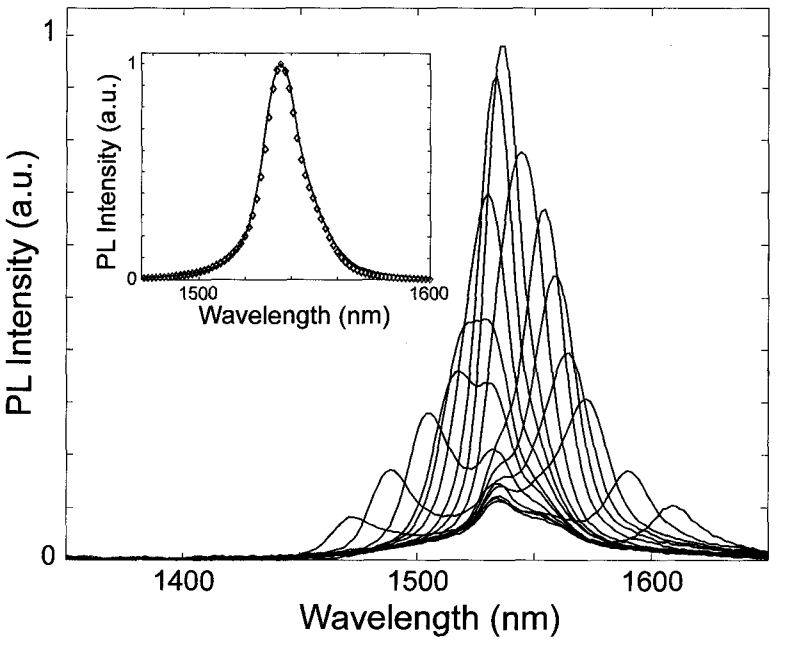

Fig. 4.5: Tunable emission from Cavity A (graded SiO:Er layer thickness). Excitation was ~40 mW at 325 nm. **Inset:** PL collected normally from Cavity B (solid line), and the resulting fit of the product of Eq. (4.1) and the no-cavity Er^{3+} PL (open symbols).

introduced upon each reflection, yielding $\vartheta = 2\pi dn/\lambda + (\phi_1 + \phi_2)/2$, where d is the physical thickness of the cavity and ϕ_i are the phase shifts at the mirrors. For Cavity B, R_2 may be taken as the maximum value for reflection at a SiO–Ag interface, as the bottom mirror is several times thicker than the skin depth at 1535 nm ($R_2 = 0.962$); the value of R_1, however, is subject to greater uncertainty due to the SiO_2 coating of the top mirror. Fitting the product of Eq. (4.1) and the no-cavity PL to the cavity emission (inset Fig. 4.5) returns values of $d = 362$ nm and $R_1 = 0.940$. The resulting transmission coefficient function has a FWHM of 26.2 nm, yielding a cavity quality factor of $Q \approx 59$. Although this is lower than the quality factors of microcavities using distributed Bragg reflectors (DBRs) as mirrors, the fabrication technique using metal mirrors is much simpler; also, a wide range of tunability is possible simply by adjusting the SiO:Er layer thickness, without adjusting any mirror parameters. These strongly-emitting microcavity structures, fabricated using straightforward, low-temperature processing techniques, are made possible by the large effective excitation cross-section and broadband sensitisation of Er^{3+} in the material described. As such, these results illustrate some important practical advantages associated with the use of *amorphous* silicon nanoclusters as erbium sensitisers.

4.4 Conclusions

Er-doped silicon nanocomposite thin films fabricated by co-evaporation of SiO and Er_2O_3 have been optimised for 1.54-μm emission with respect to Er concentration, annealing temperature, and process gas. A 0.20-at.%-Er film annealed at 500 °C for 1 h in forming gas exhibited the most intense Er^{3+} emission, compatible with standard CMOS fabrication. This makes SiO:Er a candidate for monolithically-integrated opto-electronic applications. TEM analysis indicated the presence of amorphous Si nanoclusters 2–3 nm in diameter surrounded by a SiO_x matrix. From PL lifetime measurements, the effective excitation cross-section of the Er^{3+} was found to be $\sim 2\times10^{-16}$ cm^2, similar to that of crystalline Si nanoparticles. To demonstrate the use of SiO:Er in photonics applications, planar Fabry-

Pérot microcavities with metal mirrors were constructed. The resonant wavelength is tunable across the entire 1.54-μm emission band by varying the SiO:Er layer thickness. A cavity resonant at the Er^{3+} peak of 1535 nm was found to exhibit a quality factor of $\sim$59. The control over the directionality and spectral shape of the emission afforded by such simple device structures suggests the potential of using SiO:Er as a material for integrated photonics.

Bibliography

[1] A. Hryciw, C. Blois, A. Meldrum, T. Clement, R. DeCorby, and Q. Li, "Photoluminescence from Er-doped silicon oxide microcavities", *Opt. Mater.*, vol. 28, no. 6–7, pp. 873–878, 2006.

[2] F. Iacona, G. Franzò, E. C. Moreira, and F. Priolo, "Silicon nanocrystals and Er^{3+} ions in an optical microcavity", *J. Appl. Phys.*, vol. 89, no. 12, pp. 8354–8356, 2001.

[3] P. G. Kik and A. Polman, "Exciton-erbium interactions in Si nanocrystal-doped SiO_2", *J. Appl. Phys.*, vol. 88, no. 4, pp. 1992–1998, 2000.

[4] J. H. Shin, J.-H. Jhe, S. Y. Seo, Y. H. Ha, and D. W. Moon, "Er-carrier interaction and its effects on the Er^{3+} luminescence of erbium-doped Si/SiO_2 superlattices", *Appl. Phys. Lett.*, vol. 76, no. 24, pp. 3567–3569, 2000.

[5] M. Fujii, M. Yoshida, Y. Kanzawa, S. Hayashi, and K. Yamamoto, "1.54 μm photoluminescence of Er^{3+} doped into SiO_2 films containing Si nanocrystals: Evidence for energy transfer from Si nanocrystals to Er^{3+}", *Appl. Phys. Lett.*, vol. 71, no. 9, pp. 1198–1200, 1997.

[6] S. P. Withrow, C. W. White, A. Meldrum, J. D. Budai, D. M. Hembree, and J. C. Barbour, "Effects of hydrogen in the annealing environment on photoluminescence from Si nanoparticles in SiO_2", *J. Appl. Phys.*, vol. 86, no. 1, pp. 396–401, 1999.

[7] S. Sedky, A. Witvrouw, H. Bender, and K. Baert, "Experimental determination of the maximum post-process annealing temperature for standard CMOS wafers", *IEEE Trans. Electr. Dev.*, vol. 48, no. 2, pp. 377–385, 2001.

[8] S. Lombardo, S. U. Campisano, G. N. van den Hoven, A. Cacciato, and A. Polman, "Room-temperature luminescence from Er-implanted semi-insulating polycrystalline silicon", *Appl. Phys. Lett.*, vol. 63, no. 14, pp. 1942–1944, 1993.

[9] G. N. van den Hoven, J. H. Shin, A. Polman, S. Lombardo, and S. U. Campisano, "Erbium in oxygen-doped silicon: Optical excitation", *J. Appl. Phys.*, vol. 78, no. 4, pp. 2642–2650, 1995.

[10] S. W. Roberts, G. J. Parker, and M. Hempstead, "The photoluminescence of erbium-doped silicon monoxide", *Opt. Mater.*, vol. 6, no. 1–2, pp. 99–102, 1996.

[11] Y. H. Ha, S. Kim, D. W. Moon, J.-H. Jhe, and J. H. Shin, "Er^{3+} photoluminescence properties of erbium-doped Si/SiO_2 superlattices with subnanometer thin Si layers", *Appl. Phys. Lett.*, vol. 79, no. 3, pp. 287–289, 2001.

[12] M. Schmidt, J. Heitmann, R. Scholz, and M. Zacharias, "Bright luminescence from erbium doped nc-Si/SiO_2 superlattices", *J. Non-Cryst. Sol.*, vol. 299, pp. 678–682, 2002.

[13] J. S. Ha, G. Y. Sung, S. Lee, Y. R. Jang, K. H. Yoo, C. H. Bae, J. S. Jeon, S. H. Nam, and S. M. Park, "The effects of ambient oxygen pressure on the 1.54 μm photoluminescence of Er-doped silicon-rich silicon oxide films grown by laser ablation of a Si plus Er target", *Appl. Phys. A*, vol. 79, no. 4–6, pp. 1485–1488, 2004.

[14] M. Glover and A. Meldrum, "Effect of 'buffer layers' on the optical properties of silicon nanocrystal superlattices", *Opt. Mater.*, vol. 27, no. 5, pp. 977–982, 2005.

[15] M. Ishii, T. Ishikawa, T. Ueki, S. Komuro, T. Morikawa, Y. Aoyagi, and H. Oyanagi, "The optically active center and its activation process in Er-doped Si thin film produced by laser ablation", *J. Appl. Phys.*, vol. 85, no. 8, pp. 4024–4031, 1999.

[16] J. H. Shin, S.-Y. Seo, and S.-J. Lee, "Effect of hydrogenation on room-temperature 1.54 μm Er^{3+} photoluminescent properties of erbium-doped silicon-rich silicon oxide", *Appl. Phys. Lett.*, vol. 73, no. 25, pp. 3647–3649, 1998.

[17] J. S. Ha, C. H. Bae, S. H. Nam, S. M. Park, Y. R. Jang, K. H. Yoo, and K. Park, "Er^{3+} photoluminescence from Er-doped amorphous SiO_x films prepared by pulsed laser deposition at room temperature: The effects of oxygen concentration", *Appl. Phys. Lett.*, vol. 82, no. 20, pp. 3436–3438, 2003.

[18] H. Rinnert, M. Vergnat, G. Marchal, and A. Burneau, "Strong visible photoluminescence in amorphous SiO_x and SiO_x:H thin films prepared by thermal evaporation of SiO powder", *J. Luminesc.*, vol. 80, no. 1–4, pp. 445–448, 1998.

[19] A. J. Kenyon, P. F. Trwoga, M. Federighi, and C. W. Pitt, "Optical properties of PECVD erbium-doped silicon-rich silica: evidence for energy transfer between silicon microclusters and erbium ions", *J. Phys. Cond. Mat.*, vol. 6, no. 21, pp. L319–L324, 1994.

[20] A. Janotta, M. Schmidt, R. Janssen, M. Stutzmann, and C. Buchal, "Photoluminescence of Er^{3+}-implanted amorphous hydrogenated silicon suboxides", *Phys. Rev. B*, vol. 68, no. 16, Art. no. 165207, 2003.

[21] I. N. Yassievich, M. S. Bresler, and O. B. Gusev, "Defect-related Auger excitation of erbium ions in amorphous silicon", *J. Phys. Cond. Mat.*, vol. 9, no. 43, pp. 9415–9425, 1997.

[22] P. G. Kik, M. L. Brongersma, and A. Polman, "Strong exciton-erbium coupling in Si nanocrystal-doped SiO_2", *Appl. Phys. Lett.*, vol. 76, no. 17, pp. 2325–2327, 2000.

[23] P. G. Kik and A. Polman, "Towards an Er-doped Si nanocrystal sensitized waveguide laser – the thin line between gain and loss", in *Towards the first silicon laser*, L. Pavesi, S. Gaponenko, and L. Dal Negro, Eds., vol. 93 of *NATO Science Series II*, pp. 383–400. Kluwer Academic Publishers, Norwell, Massachusetts, 2003, ISBN: 1-402-01193-8.

[24] F. Priolo, G. Franzò, D. Pacifici, V. Vinciguerra, F. Iacona, and A. Irrera, "Role of the energy transfer in the optical properties of undoped and Er-doped interacting Si nanocrystals", *J. Appl. Phys.*, vol. 89, no. 1, pp. 264–272, 2001.

[25] J. T. Verdeyen, *Laser Electronics*, Prentice Hall, Upper Saddle River, New Jersey, third edition, 1995, ISBN: 0-137-0666-6, p. 149.

CHAPTER 5

Interaction between rare-earth ions and amorphous silicon nanoclusters produced at low processing temperatures†

5.1 Introduction

The ability of Si NCs—amorphous as well as crystalline—to sensitise the emission from Er^{3+} has led to widespread investigation of this class of materials for potential photonic applications, as discussed in the previous chapter. There have also been a few reports on silicon nanocomposites doped with neodymium[2–4] and ytterbium,[5] and at least two similar papers on silicon nanocrystals doped with Er, Nd, Yb, and Tb, although the work focused on erbium.[6,7] Investigations of the properties of silicon nanocomposites doped with rare earths other than erbium are few; however, they can be important for several reasons. First, the silicon-nanocrystal-to-rare-earth transfer mechanism in erbium-doped silicon nanocomposites is still much debated. Since the individual rare-earth ions have different $4f$-shell energy levels that overlap to varying degrees with the silicon nanocluster absorption and PL spectra, it may be possible to provide evidence on the interaction mechanism. Second, many of the infrared emission wavelengths are of technical importance (see, for example, §1.3 and Ref.[8]).

As mentioned previously, one of the outstanding difficulties with using silicon nanocrystalline composites for optical applications is the high thermal processing temperature required to optimise the luminescence, where temperatures in excess of 1000 °C are common. With respect to LED-like electroluminescent devices, such high temperatures can make electrical contacts and back-reflector layers particularly difficult to fabricate. In Chap. 4, it was shown that efficient Er^{3+} emission at 1.5 μm was possible from a-Si-NC films processed at temperatures compatible with standard CMOS processing;[9] the extension of this sensitisation effect to other RE elements will now be considered.

Using high-resolution energy-filtered TEM, it was recently shown that SiO films annealed between temperatures of 400 and 800 °C contain a three-phase mixture of Si, SiO, and SiO_2.[10] The silicon is present in the form of amorphous clusters ranging in mean radius from ~1.0 to 1.5 nm, depending on the processing conditions. The objective of the work presented in this chapter was to dope these amorphous silicon nanocomposites with the rare-earth elements Nd, Tb, Dy, Er, Tm, and Yb to investigate the possible energy

† A version of this chapter has been accepted for publication.[1]

transfer mechanisms, and evaluate the ability of these amorphous nanoclusters to sensitise luminescent transitions in the rare-earth elements in general. In order to demonstrate low-temperature fabrication at temperatures compatible with CMOS processing, the discussion will focus on materials for which the annealing temperature is 500 °C or lower.

5.2 Experimental

Specimens were prepared by co-evaporation of SiO and either the rare-earth metal or rare-earth oxide. The 200-nm-thick films were deposited onto fused quartz wafers, and the composition of the films was tracked *in situ* by two separate rate monitors. In all cases the molar concentration of the rare earth was less than 1%, as estimated from the rate monitors. In the case of Er and Nd, the compositional data was checked by EMPA using a 3-kV beam and standard correction techniques. For Nd, Er, and Yb, the rare-earth concentrations were varied to determine the composition producing the most intense emission. Specimens were annealed in 95% N_2+5% H_2 (forming gas) at 400 or 500 °C for 1 h, as hydrogen is known to increase the PL intensity due to the passivation of non-radiative traps on nanocluster surfaces.[11,12] PL spectroscopy was conducted using the 325-nm line of a HeCd laser as the excitation source (spot size ~4 mm^2, ~15 mW power), and a CCD spectrometer whose spectral response was normalised with a standard blackbody radiation source. Electron microscopy was performed on undoped samples using an FEI ST20 field emission TEM equipped with a Gatan Image Filter (GIF).

5.3 Results and Discussion

The microstructure of the SiO films annealed at 400 °C is shown in Fig. 5.1a-c. These images, taken with the silicon L edge (a) or oxygen K edge (b) centred on the GIF entrance slit clearly show the inhomogeneous nature of the films. The Si is segregated into clusters having a mean diameter of 2.4 nm (σ = 0.3 nm) and 2.8 nm (σ = 0.5 nm) for the specimens annealed at 400 and 500 °C, respectively. There is a broad PL peak centred at 640 nm (700 nm) for specimens annealed at 400 °C (500 °C) that shares many characteristics with amorphous silicon band-tail emission. First, for both samples, this PL peak was characterised by non-exponential dynamics: in time-resolved spectroscopy, a fast decay is observed over a few microseconds, as well as a much longer one with a characteristic time of several hundred microseconds (Fig. 5.2). This is similar to the case for amorphous silicon, which is generally reported to have two or three lifetime components ranging from ~1 μs to as much as 1 ms.[13,14] As reported recently,[15] the temperature dependence of the integrated intensity of this peak increased by a factor of 5 to 6 on going from 300 to 77 K (inset to Fig. 5.2); this behaviour is also consistent with investigations of amorphous silicon films[16] and amorphous porous silicon.[17] A more detailed investigation of the PL dynamics and quenching behaviour is given in Chap. 7.

Having established that the PL has many characteristics similar to amorphous silicon, a preliminary attempt was made to model the spectrum, assuming that the PL originates from amorphous silicon nanoparticles. The technique used was that of Estes and Moddel,[18] who extended work done by Dunstan and Boulitrop[19] by considering the density of states for both localised and extended states in bulk a-Si. In the derivation of this model, quantum confinement effects are ignored, as they are unlikely to be observed in a-Si unless the particle diameter is smaller than ~1 nm, which is the approximate spatial extent of the

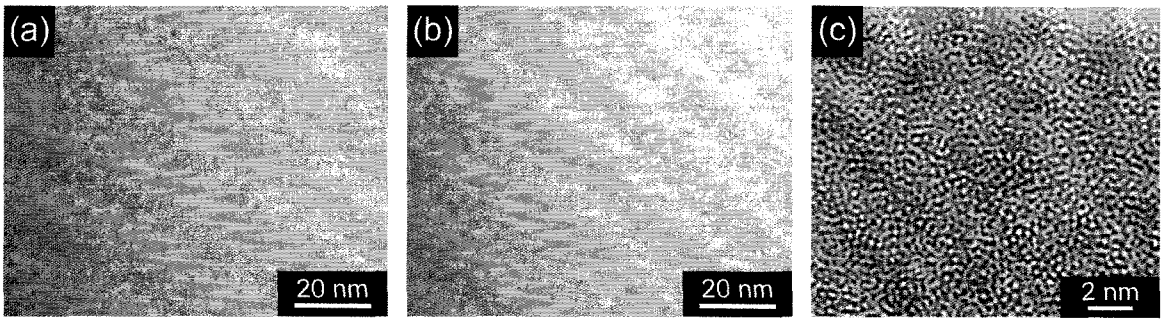

Fig. 5.1: Energy-filtered TEM images of SiO annealed at 400 °C, with the slit centred on the silicon L line (a) and the oxygen K line (b). Image (c) is a high-resolution micrograph in which the silicon clusters appear dark on a lighter background.

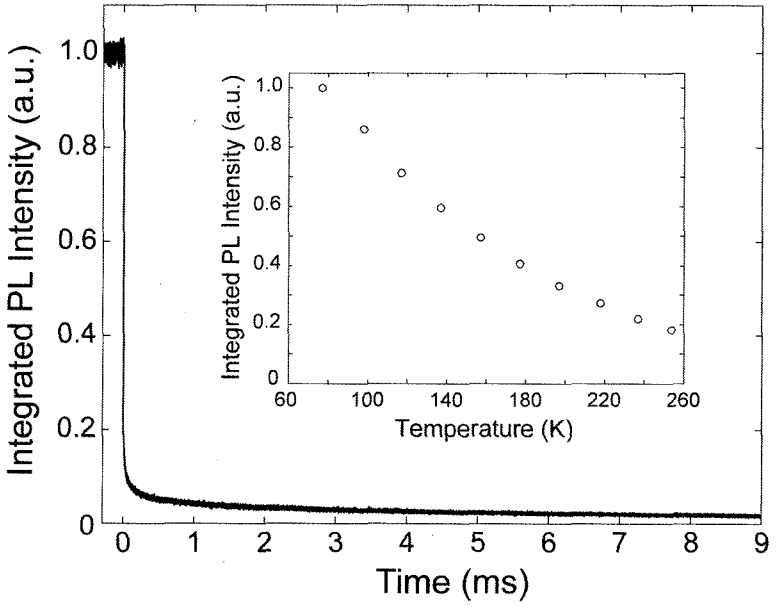

Fig. 5.2: Time-resolved PL decay curve from an SiO film annealed at 500 °C; note the strongly non-exponential dynamics. Excitation was 0.75 mW at 476 nm square-wave-modulated at 9.5 Hz. **Inset:** Integrated PL intensity as a function of specimen temperature.

carrier wave functions in localised band tail states.[20†] Instead, the effect of particle size to limit the availability of non-radiative traps and deep tail states for radiative recombination by purely geometrical means. The photoluminescence spectrum $I(h\nu)$ can be obtained from

$$I(h\nu) = \frac{4h\nu}{R_t^3} \int_0^{R_t} r^2 \eta_i(r) P(h\nu, r)\, \mathrm{d}r \tag{5.1}$$

where $P(h\nu, r)$ is the probability distribution function for conduction and valence band tail states in a given nanocluster corresponding to an emitted photon of energy $h\nu$, η_i is the radiative quantum efficiency as a function of the non-radiative capture volume and the surface capture area, R_t is the cluster radius, and the integration variable r represents the position of the capture sphere within the cluster (details on the derivation of this model are provided in Chap. 6 and Ref.[18]).

[†]This is indeed an oversimplification of the density of states for nanoscale a-Si—the density of states above the mobility gap should be affected by quantum confinement for NCs of comparable size to the extended carrier wavefunctions—but it should only have a small effect on the resultant PL spectrum if carriers excited into extended states rapidly thermalise down into energy states lying deep in the band tails.

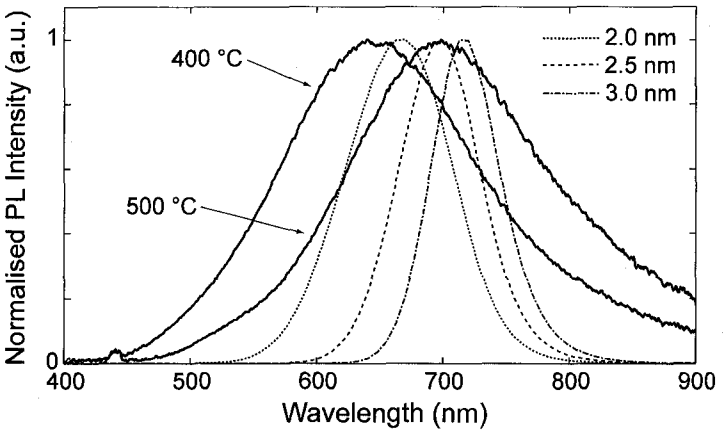

Fig. 5.3: PL data for the SiO films annealed at 400 and 500 °C (solid lines). Modelling results for three different sizes of amorphous silicon clusters are shown with dashed lines.

Using Eq. (5.1) with a mobility gap of $E_g = 1.7$ eV and the characteristic Urbach energies of the valence and conduction band tails of 46 and 23 meV, respectively, for bulk a-Si,[18] the calculated PL spectrum overlaps with the experimentally observed one, although it is considerably narrower (Fig. 5.3). The emission peak shifts to shorter wavelengths for smaller particles—not due to quantum confinement, but because of the spatial isolation of deep states. For the specific mean size observed in the energy-filtered TEM, the model results peak at slightly longer wavelength than the experimental results. By adjusting some of the parameters in the model such as the band tail and mobility gap energies, one can obtain a close fit to experiment, as will be shown in Chap. 6.[†] Other researchers have previously suggested that the PL from SiO_x films annealed at temperatures below 700 °C arises from amorphous silicon clusters (e.g., Refs.[21–23]), although without modelling the emission spectrum or directly observing the clusters.

The effects of incorporating rare-earth ions into this amorphous silicon nanocomposite are similar to the effects in erbium-doped silicon nanocrystals. For example, for amorphous Si nanoclusters annealed at 400 °C and doped with increasing concentrations of neodymium, it was found that the PL intensity from the a-Si nanoclusters decreased monotonically while the Nd bands first grew in intensity and subsequently decreased, presumably due to Nd–Nd interactions. As discussed in the previous chapter (see the inset to Fig. 4.3a), identical behaviour is observed in the case of erbium ions interacting with these a-Si clusters.[24] These observations show that the transfer mechanism from the amorphous clusters to the rare-earth ions is analogous to the much-debated silicon-nanocrystal-to-erbium transfer mechanism. Preliminary results of investigations with respect to the dynamics of the transfer process in Er- and Nd-doped films imply that the transfer occurs after the carriers are trapped in the band tails.[25] For a composition of SiO, the optimum annealing temperature for rare-earth luminescence is between 400 and 500 °C (temperatures between 300 and 1100 °C were tested).

In all cases, the addition of the rare earth either decreased or entirely quenched the nanocluster PL (Fig. 5.4). The standard $^4I_{11/2} \rightarrow {}^4I_{15/2}$ and $^4I_{13/2} \rightarrow {}^4I_{15/2}$ bands at 980

[†]This is not simply an *ad hoc* variation of free parameters: an increase in Urbach energies due to a widening of the mobility gap has been cited for nanostructured a-Si.[17] One may ask whether such an adjustment of the Urbach energies is necessary to simulate a PL spectrum of comparable width to that obtained experimentally, since only the mean particle size was used in the simulation. However, incorporating the (approximately lognormal) size distribution of the nanocluster ensemble into the simulation only produces an increase in peak width of ~40%.

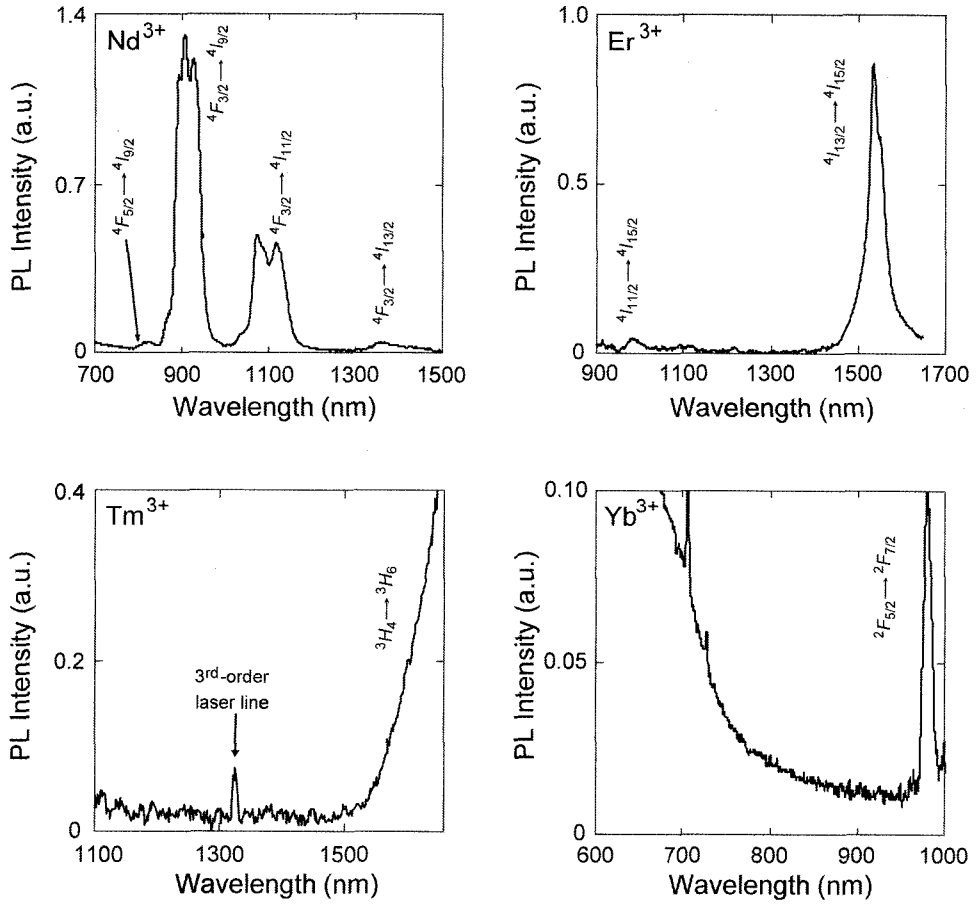

Fig. 5.4: Luminescence from the rare-earth $4f$-shell transitions in amorphous Si nanocomposite films doped with ~0.4 at.% Nd, ~0.2 at.% Er, ~0.1 at.% Tm, or ~0.5 at.% Yb. The latter two concentrations were estimated from the rate monitors and were not independently checked by electron microprobe. The PL was pumped at 325 nm in each case. The Yb, Tm and Er samples were annealed at 500 °C and the Nd-doped sample was annealed at 400 °C. The minor peaks in the Yb spectrum near 700 nm are artifacts due to the collection system. The term notation for the various optical transitions is given in each figure.

and 1535 nm were observed for Er-doped nanoclusters, and for the case of Nd-doping, the complete set of emission bands centred at ~800, 900, 1100, and 1350 nm were observed.[3,24] In the case of Yb, the $^2F_{5/2} \rightarrow ^2I_{7/2}$ transition occurs in the PL spectrum at a wavelength of 980 nm, on the long-wavelength side of the broad nanocluster luminescence band. For Tm, only one sample was prepared; the nanocluster emission was quenched and the short-wavelength edge of the $^3H_4 \rightarrow ^3H_6$ emission from Tm at 1600–1700 nm was observed. Finally, in the case of Dy and Tb, the nanocluster PL was quenched but no PL was found from the rare-earth ions. Dy^{3+} and Tb^{3+} have many closely-spaced levels in the $4f$ shell (see Fig. 1.20); therefore, decay can occur entirely via phonons in high-phonon-energy glass such as silica. The absence of nanocluster PL shows that the energy transfer process occurs for Dy and Tb, but relaxation takes place via phonons and not through luminescence.

Tb^{3+} has an energy gap between the $^5D_4$ and $^7F_0$ levels of approximately 1.8 eV; this is too large for pure phonon decay, even in silicate glasses. This transition would correspond to an emitted wavelength of ~700 nm. The fact that no luminescence is seen in the present specimens implies that, although energy transfer is occurring, the upper Tb^{3+} levels (i.e., $^5D_4$ and higher) are not populated by the energy transfer mechanism from the silicon

nanoclusters. The mobility gap of bulk amorphous silicon is typically expected to be at ~1.7–1.8 eV, although it can be shifted to higher energies due to surface effects in very small particles,[18] and quantisation of the gap should also result in higher energies. Since the nanoclusters are absorbing high-energy pump photons (3.8 eV), relaxation into the band tails must be fast compared to direct transfer to the rare-earth ions, consistent with a report that localisation in the band tails takes place over a sub-nanosecond timescale.[26] If the cluster-to-rare-earth transfer mechanism is on the order of a microsecond, as suggested for silicon nanocrystals interacting with erbium[27] (i.e., much longer than the nanocluster relaxation time), this would be consistent with the lack of upper level population of the Tb^{3+} ions.

Similar types of arguments can be made for the case of Yb: here, although PL from the $4f$-shell transition can be observed, it was found to always be weak. This implies that the transfer mechanism is less effective in Yb^{3+} than for the other rare-earth ions investigated. Nd, Dy, Er, Tb, and Tm all have $4f$-shell levels at energies that are within the emission band of the intrinsic nanocluster PL, but Yb has only a single (broad) excited energy level ~1.2 eV above the ground state. This is relatively far from the a-Si PL band, which is centred around 1.8 eV. Therefore, the PL from the Yb^{3+} ions is limited by an inefficient transfer mechanism that requires a coordinated many-phonon process for energy conservation. Finally, the fact that Yb^{3+} has no levels directly within the main nanocluster PL band appears difficult to reconcile with a resonant process such as dipole–dipole coupling (the Förster transfer), being more consistent with a non-resonant phonon-mediated process as often invoked for erbium-doped silicon nanocrystal composites.

5.4 Conclusions

Photoluminescence from rare-earth ions can be obtained via an energy transfer from the band tail states of amorphous silicon nanoclusters. The specimens can be prepared without the high-temperature thermal treatment that is generally necessary for silicon nanocrystal films—a fabrication process which is CMOS-compatible. Low-temperature processing and compatibility is an endorsement of the use of amorphous silicon clusters as sensitisers for Er, Nd, and other rare-earth ions. Steady-state PL evidence supports a non-resonant Auger excitation mechanism of the rare earths from states in the a-Si band tails.

Bibliography

[1] A. Meldrum, A. Hryciw, A. N. MacDonald, C. Blois, T. Clement, R. DeCorby, J. Wang, and Quan Li, "Interaction between rare-earth ions and amorphous silicon nanoclusters produced at low processing temperatures", *J. Luminesc.*, vol. 121, pp. 199–203, 2006.

[2] J. C. Pivin, A. Podhorodecki, R. Kudrawiec, and J. Misiewicz, "Study of neodymium photoluminescence and energy transfer in silicon-based gels", *Opt. Mater.*, vol. 27, no. 9, pp. 1467–1470, 2005.

[3] A. N. MacDonald, A. Hryciw, Q. Li, and A. Meldrum, "Luminescence of Nd-enriched silicon nanoparticle glasses", *Opt. Mater.*, vol. 28, no. 6–7, pp. 820–824, 2006.

[4] S.-Y. Seo, M. J. Kim, and J. H. Shin, "The Nd-nanocluster coupling strength and its effect in excitation/de-excitation of Nd^{3+} luminescence in Nd-doped silicon-rich silicon oxide", *Appl. Phys. Lett.*, vol. 83, no. 14, pp. 2778–2780, 2003.

[5] M. Fujii, S. Hayashi, and K. Yamamoto, "Excitation of intra-$4f$ shell luminescence of Yb^{3+} by energy transfer from Si nanocrystals", *Appl. Phys. Lett.*, vol. 73, no. 21, pp. 3108–3110, 1998.

[6] G. Franzò, V. Vinciguerra, and F. Priolo, "The excitation mechanism of rare-earth ions in silicon nanocrystals", *Appl. Phys. A*, vol. 69, no. 1, pp. 3–12, 1999.

[7] G. Franzò, V. Vinciguerra, and F. Priolo, "Room-temperature luminescence from rare-earth ions implanted into Si nanocrystals", *Philos. Mag. B*, vol. 80, no. 4, pp. 719–728, 2000.

[8] *MRS. Bull.*, vol. 24, no. 9, September 1999.

[9] S. Sedky, A. Witvrouw, H. Bender, and K. Baert, "Experimental determination of the maximum post-process annealing temperature for standard CMOS wafers", *IEEE Trans. Electr. Dev.*, vol. 48, no. 2, pp. 377–385, 2001.

[10] J. Wang, X.F. Wang, Q Li, A. Meldrum, and A. Hryciw, "The microstructure of SiO thin films: From nanoclusters to nanocrystals", *Philos. Mag.*, vol. 87, no. 1, pp. 11–27, 2007.

[11] S. P. Withrow, C. W. White, A. Meldrum, J. D. Budai, D. M. Hembree, and J. C. Barbour, "Effects of hydrogen in the annealing environment on photoluminescence from Si nanoparticles in SiO_2", *J. Appl. Phys.*, vol. 86, no. 1, pp. 396–401, 1999.

[12] S. Cheylan and R. G. Elliman, "The effect of ion dose and annealing ambient on room temperature photoluminescence from Si nanocrystals in SiO_2", *Nucl. Instr. Meth. B*, vol. 148, no. 1–4, pp. 986–990, 1999.

[13] S. Ambros, R. Carius, and H. Wagner, "Lifetime distribution in a-Si:H: geminate-, nongeminate- and Auger-processes", *J. Non-Cryst. Sol.*, vol. 137–138, pp. 555–558, 1991.

[14] T. Muschik and R. Schwarz, "Temperature dependence of radiative and non-radiative lifetimes in hydrogenated amorphous silicon", *J. Non-Cryst. Sol.*, vol. 164–166, pp. 619–622, 1993.

[15] A. Meldrum, A. Hryciw, A. N. MacDonald, C. Blois, K. Marsh, J. Wang, and Q. Li, "Photoluminescence in the silicon-oxygen system", *J. Vac. Sci. Tech. A*, vol. 24, no. 3, pp. 713–717, 2006.

[16] R. W. Collins, M. A. Paesler, and W. Paul, "The temperature dependence of photoluminescence in a-Si:H alloys", *Solid State Commun.*, vol. 34, no. 10, pp. 833–836, 1980.

[17] R. B. Wehrspohn, J.-N. Chazalviel, F. Ozanam, and I. Solomon, "Spatial versus quantum confinement in porous amorphous silicon nanostructures", *Euro. Phys. J. B*, vol. 8, no. 2, pp. 179–193, 1999.

[18] M. J. Estes and G. Moddel, "Luminescence from amorphous silicon nanostructures", *Phys. Rev. B*, vol. 54, no. 20, pp. 14633–14642, 1996.

[19] D. J. Dunstan and F. Boulitrop, "Photoluminescence in hydrogenated amorphous silicon", *Phys. Rev. B*, vol. 30, no. 10, pp. 5945–5957.

[20] N. F. Mott, "The random-phase model in non-crystalline systems", *Philos. Mag. B*, vol. 43, no. 5, pp. 941–942, 1981.

[21] M. Molinari, H. Rinnert, and M. Vergnat, "Visible photoluminescence in amorphous SiO_x thin films prepared by silicon evaporation under a molecular oxygen atmosphere", *Appl. Phys. Lett.*, vol. 82, no. 22, pp. 3877–3879, 2003.

[22] H. Rinnert, M. Vergnat, and A. Burneau, "Evidence of light-emitting amorphous silicon clusters confined in a silicon oxide matrix", *J. Appl. Phys.*, vol. 89, no. 1, pp. 237–243, 2001.

[23] L. B. Ma, A. L. Ji, C. Liu, Y. Q. Wang, and Z. X. Cao, "Low temperature growth of amorphous si nanoparticles in oxide matrix for efficient visible, photoluminescence", *J. Vac. Sci. Tech. B*, vol. 22, no. 6, pp. 2654–2657, 2004.

[24] A. Hryciw, C. Blois, A. Meldrum, T. Clement, R. DeCorby, and Q. Li, "Photoluminescence from Er-doped silicon oxide microcavities", *Opt. Mater.*, vol. 28, no. 6–7, pp. 873–878, 2006.

[25] A. N. MacDonald, A. Hryciw, F. Lenz, and A. Meldrum, "Interaction between amorphous silicon nanoclusters and neodymium ions", *Appl. Phys. Lett.*, vol. 89, Art. no. 173132, 2006.

[26] W. B. Jackson, C. Doland, and C. C. Tsai, "Systematic investigation of picosecond photoinduced absorption in hydrogenated amorphous silicon", *Phys. Rev. B*, vol. 34, no. 4, pp. 3023–3026, 1986.

[27] M. Fujii, K. Imakita, K. Watanabe, and S. Hayashi, "Coexistence of two different energy transfer processes in SiO_2 films containing Si nanocrystals and Er", *J. Appl. Phys.*, vol. 95, no. 1, pp. 272–280, 2004.

CHAPTER 6

Luminescence and tunnelling simulations for ensembles of a-Si nanoclusters

6.1 Introduction

The ease in which the electronic and optical properties of nanoscale crystalline semiconductor structures can be modified via quantum confinement effects has led to the prodigious growth of this field of research since its nascency in the early 1980s.[1] In particular, the tunability of the emission energy from direct-gap quantum dots by widening the bandgap ($\Delta E \propto \frac{1}{a^2}$ for nanocrystals of radius a in the strong confinement limit[1]) has arguably already passed from novelty to commodity.† For indirect-gap semiconductors such as Si, the influence of quantum confinement on nanocrystal emission is still somewhat controversial, with competing theories as regards the relative importance of interfacial trap sites as luminescent centres versus radiative recombination of electron–hole pairs across a bandgap which has been widened by quantum size effects (see Chap. 2 and references therein). In both cases, however, the general trends of a blueshift in emission and an increase in quantum efficiency with decreasing nanostructure size are observed.[1]

Similar effects have been observed in nanoscale a-Si, notably from a-Si:H/a-SiN$_x$:H multilayers[2] and porous a-Si,[3] which has sometimes been attributed to quantum confinement of electrons in the nanometre-sized structures.[2] However, while extended electron states in a-Si could be expected to display confinement effects, the wavefunctions of carriers in band-tail states, which result from the large degree of topological disorder in the material (see §1.2.2), are localised to within a few atomic distances (~6–7 Å).[4] Since tail-to-tail transitions represent the dominant contribution to photoluminescence, due to the rapid (~ps) thermalisation of carriers into the tails,[5] it is doubtful that quantum confinement plays the dominant role in determining the emission energy.[3,6] The need to reconcile carrier localisation, which should be insensitive to changes in the relatively large nanostructures, with an apparent size effect as regards the emission peak and intensity, can be satisfied with arguments concerning *spatial*—rather than quantum—confinement.

While spatial confinement has previously been cited to explain the PL behaviour of

†One need only refer to the diverse commercial applications of CdSe quantum dots—white-light LEDs, photovoltaic devices, and anti-counterfeiting inks, to name a few—manufactured by companies such as Evident Technologies (www.evidenttech.com). The emission from such CdSe nanocrystals is tunable across the visible spectrum.

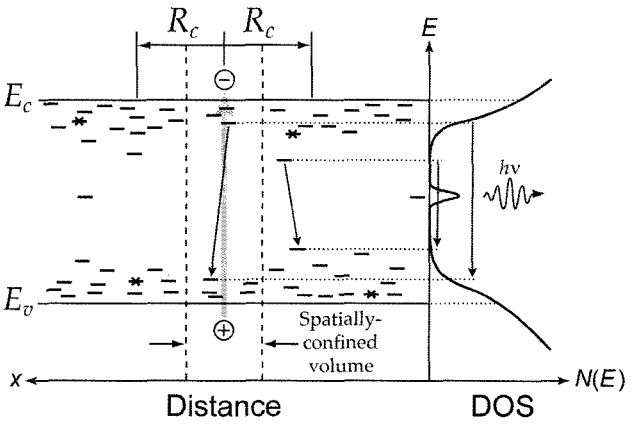

Fig. 6.1: The effect of spatial confinement on emission from a-Si. The localised band-tail states corresponding to the density of states function shown on the right are represented by the short horizontal lines in the left-hand region of the figure. Non-radiative quenching centres are denoted by a cross on such a state. A photogenerated e–h pair thermalises down to the deepest accessible states within a capture radius R_c. If no quenching centre is encountered, radiative recombination occurs from these deepest states. Restricting the volume accessible to the carriers decreases the probability of finding a quenching centre, and increases the mean energy separation between the lowest-lying accessible states. (After Ref.[6])

low-dimensional a-Si structures,[3,6,7] such treatments typically consider the effect of emission averaged geometrically over a *single* nanostructure. In particular, the possibility of carrier tunnelling between nanoclusters in a densely-packed ensemble of a-Si NCs is not considered. It has recently been shown[8] that such tunnelling effects in Si nanocrystals are capable of explaining many of the features of the spectral shape and luminescence lifetime in such nanocomposites; as such, this phenomenon should be investigated for the a-Si-NC system.

This chapter presents luminescence simulations incorporating spatial confinement effects for a-Si NCs, using both the one-particle treatment used by Estes and Moddel[6] and a Monte Carlo approach, for ensembles of NCs with size distributions corresponding to thin-film nanocomposite specimens. The versatility of the latter method allows an investigation of the effect of tunnelling between NCs on the luminescence. The simulation results will be compared with experimental PL spectra, with a discussion of the effect of non-radiative defect density on the emission.

6.2 Luminescence simulations

6.2.1 Model

The basic principles of the spatial-confinement model are shown schematically in Fig. 6.1. In bulk a-Si, an electron–hole (e–h) pair, initially excited to extended band states by the absorption of a photon, rapidly thermalises to the lowest-energy states accessible within a capture sphere of radius R_c. *Thermalisation*, the process by which excitation energy is lost to phonons, generally takes place in two steps: 1) emission of single phonons as the carriers scatter downward from extended state to extended state within the band, followed by 2) transitions between tail states via either tunnelling or multiple trapping (re-excitation to the mobility edge and subsequent capture at a different localised state).[5] Upon reaching the deepest accessible states within R_c, the carriers recombine radiatively. If, however, a carrier diffuses to a quenching centre (denoted by a cross in the figure), *non*-radiative recombination will occur. In this description, it has been implicitly assumed that the diffusion of electrons and holes is uncorrelated; this should be reasonable for a first-order approximation, particularly at low temperatures, where diffusion is limited.[6]

The effect of spatial confinement is illustrated by the vertical dashed lines in Fig. 6.1: the capture sphere is truncated by the surfaces of the spatially-confined volume, prevent-

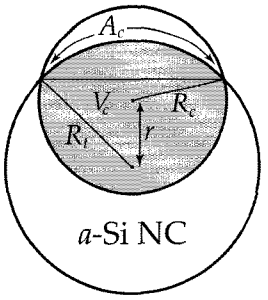

Fig. 6.2: Capture volume and surface area for an e–h pair generated a distance r from the centre of a spherical a-Si NC, shown for the case $R_c < R_t$. V_c is the volume formed by the intersection of the capture sphere (of radius R_c) and the NC (of radius Rt). A_c is the surface area of the NC lying inside the capture sphere. For $R_c < R_t$, V_c and A_c are functions of r.

ing the carriers from accessing deeper tail states, and yielding a blueshift in emission. This "statistical blueshift"[3] occurs even if the density of states is independent of the nanostructure size; since the DOS is largely determined by nearest-neighbour bonding, as mentioned in §1.2.2, this assumption should be valid for NCs larger than ~1 nm in diameter.[6] Also illustrated in Fig. 6.1 is the expectation that the quantum efficiency for spatially-confined e–h pairs will be statistically higher than in bulk: by restricting the volume accessible to the carriers, the probability of encountering a quenching centre decreases. In this model, non-radiative defects existing both within the volume and on the surface of the a-Si NCs will be considered.

The quantum efficiency η_i of a given a-Si NC is therefore the probability that no quenching centres are accessible to the carriers. The capture volume V_c and capture surface area A_c resulting from the intersection of the capture sphere, of radius R_c, and the nanocluster, of radius R_t. The relationship between these quantities for an e–h pair created at a distance r from the centre of the NC is illustrated in Fig. 6.2, where V_c and A_c are the volume and surface area of the NC *within* the capture sphere, respectively. As such, the quantum efficiency may be written as[6]

$$\eta_i(r) = e^{-V_c(r)N_{\rm nr} - A_c(r)N_{\rm snr}} \tag{6.1}$$

where $N_{\rm nr}$ (in $\rm cm^{-3}$) is the non-radiative defect volume density and $N_{\rm snr}$ (in $\rm cm^{-2}$) is the non-radiative defect surface density. The functional forms of $V_c(r)$ and $A_c(r)$ are given in §D.2. Averaging η_i over the entire nanocluster gives the mean quantum efficiency for a given NC:[6]

$$\eta_{\rm NC} = \frac{1}{\frac{4}{3}\pi R_t^3} 4\pi \int_0^{R_t} r^2 \eta_i(r)\, {\rm d}r = \frac{3}{R_t^3}\int_0^{R_t} r^2 \eta_i(r)\, {\rm d}r \tag{6.2}$$

Clearly, $\eta_{\rm NC} = \eta_i$ if η_i is independent of r; such is the case when $R_c \geq 2R_t$.

As the temperature increases, the additional thermal energy available to the carriers allows them to diffuse farther before being trapped, increasing the probability of encountering a non-radiative quenching centre; this mechanism has been used to explain the PL temperature quenching of bulk a-Si, which was empirically found to follow the expression[9]

$$\eta = \frac{1}{1 + \left(\frac{1}{\eta_0} - 1\right)\exp\left(\frac{T}{T_0}\right)} \tag{6.3}$$

The temperature dependence of R_c may therefore be found[6] by equating Eqs. (6.3) and (6.1), using expressions for V_c and A_c appropriate to the bulk case, viz. $A_c = 0$ and $V_c = \frac{4}{3}\pi R_c^3$:

$$R_c(T) = \left\{\frac{3}{4\pi N_{\rm nr}} \ln\left[1 + \left(\frac{1}{\eta_0} - 1\right)\exp\left(\frac{T}{T_0}\right)\right]\right\}^{1/3} \tag{6.4}$$

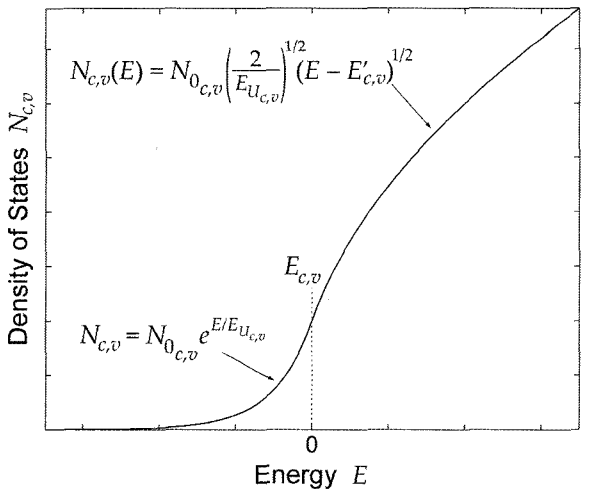

Fig. 6.3: A sketch of the density of states function used in the model. This plot applies to both the valence (N_v) and conduction (N_c) band. In both cases, the mobility edge $E_{c,v}$ is defined as zero, with negative energies corresponding to the band tails and positive energies corresponding to extended states.

From the work of Collins and coworkers,[9] the maximum quantum yield and characteristic quenching temperature for bulk a-Si are given by $\eta_0 \approx 0.998$ and $T_0 \approx 23$ K. In a simple model, the temperature quenching may be explained by assuming that any carrier which escapes a trap recombines non-radiatively, such that all carriers for which the thermal re-emission rate exceeds the radiative recombination rate do not contribute to the PL.[3] As such, T_0 can be shown to be related to the radiative lifetime τ_r and the band tail Urbach energy E_U via

$$T_0 = \frac{E_U}{k_B \ln(\omega_0 \tau_r)} \tag{6.5}$$

where k_B is Boltzmann's constant and $\omega_0 \approx 10^{12}$ s^{-1} is a characteristic attempt frequency for escape from localised band-tail states.

To calculate the PL spectra, the method put forward by Dunstan and Boulitrop will be used,[10] as extended by Estes and Moddel[6] to include the DOS for band as well as tail states. The DOS function for the conduction band of an amorphous semiconductor, as a function of E relative to the mobility conduction band mobility edge E_c, may be written as[6]

$$N_c(E) = \begin{cases} N_{0_c} e^{E/E_{U_c}} & \text{for } E \leq E_c \equiv 0 \\ N_{0_c} \left(\frac{2}{E_{U_c}}\right)^{\frac{1}{2}} (E - E'_c)^{\frac{1}{2}} & \text{for } E > E_c \end{cases} \tag{6.6}$$

where E_{U_c} is the conduction band-tail Urbach energy, N_{0_c} is the effective density of states at the mobility edge (in cm^{-3}eV^{-1}), and $E'_c = E_c - \frac{1}{2}E_{U_c}$ ensures smoothness at $E = E_c = 0$. A sketch of a general DOS function of this type is given in Fig. 6.3. The expression for the valence band, $N_v(E)$, may be written as Eq. (6.6) with $c \to v$; in such forms, E is not a global variable,[6] but instead must be considered with respect to E_c or E_v, as appropriate to the equation. The following two equations for the conduction band will have valence-band equivalents in an identical manner.

For an e–h pair photogenerated by a photon of energy $h\nu_{\text{ex}}$ in an amorphous semiconductor with a mobility gap of $E_g = E_c - E_v$, the electron (hole) is excited beyond the mobility edge by an energy ΔE_c (ΔE_v). These are related via $E_g + \Delta E_c + \Delta E_v = h\nu_{\text{ex}}$; for simplicity, we will assume symmetric carrier injection, such that $\Delta E_c = \Delta E_v = \frac{1}{2}(h\nu_{\text{ex}} - E_g)$. The total number of states available to such an electron in a volume V_c is therefore given

by

$$n_c = V_c \int_{-\infty}^{\Delta E_c} N_c(E)\,\mathrm{d}E \tag{6.7}$$

If we assume that these states may be considered independently, the probability that the lowest-energy state in the conduction band (accessible to an electron confined to a volume V_c) lies between E and $E + \mathrm{d}E$ is given by the product of the probability that a state exists between E and $E + \mathrm{d}E$ and the probability that the $n_c - 1$ remaining states lie *above* it. The corresponding probability density function we denote by $p_c(E)$; it may be written as[6]

$$p_c(E) = V_c N_c(E) \left[\frac{\int_E^{\Delta E_c} N_c(E')\,\mathrm{d}E'}{\int_{-\infty}^{\Delta E_c} N_c(E')\,\mathrm{d}E'} \right]^{n_c - 1} \tag{6.8}$$

Writing out an equivalent expression for the valence band, the normalised† probability $P(h\nu)$ that the lowest-lying energy states differ by an energy $h\nu$ in absolute terms is given by the convolution of $p_c(E)$ and $p_v(E)$. Here we must take into account the differing energy reference frames of the conduction- and valence-band expressions. $P(h\nu)$ is therefore[6]

$$P(h\nu) = p_c(E) * p_v(E) \tag{6.12}$$

$$= \int_{h\nu - \Delta E_v - E_g}^{\Delta E_c} p_c(E) p_v(h\nu - E_g - E)\,\mathrm{d}E \tag{6.13}$$

---

†It is not immediately obvious that Eq. (6.8) is in fact normalised, that is, that $\int_{-\infty}^{\Delta E_c} p_c(E)\,\mathrm{d}E = 1$. We therefore present the following proof. First, we write an equivalent condition for the normalisation of $p_c(E)$: we wish to prove that, for a function $f(x)$ which is integrable on $[a, b]$,

$$\int_a^b p(x)\,\mathrm{d}x = \int_a^b f(x) \left[\frac{\int_x^b f(x')\,\mathrm{d}x'}{\int_a^b f(x')\,\mathrm{d}x'} \right]^{\int_a^b f(x')\,\mathrm{d}x' - 1} \mathrm{d}x = 1 \tag{6.9}$$

We define $m = \int_a^b f(x')\,\mathrm{d}x'$, rewriting the integral in Eq. (6.9) as

$$\int_a^b p(x)\,\mathrm{d}x = \frac{1}{m^{m-1}} \int_a^b f(x) \left[\int_x^b f(x')\,\mathrm{d}x' \right]^{m-1} \mathrm{d}x \tag{6.10}$$

Defining $F(x)$ such that $\frac{\mathrm{d}}{\mathrm{d}x} F(x) = f(x)$, we have

$$\begin{aligned} \int_a^b p(x)\,\mathrm{d}x &= \frac{1}{m^{m-1}} \int_a^b f(x) \left[F(b) - F(x) \right]^{m-1} \mathrm{d}x \\ &= \frac{1}{m^{m-1}} \left\{ -\frac{1}{m} \left[F(b) - F(x) \right]^m \right\} \Bigg|_a^b \\ &= -\frac{1}{m^m} \left\{ \left[F(b) - F(b) \right]^m - \left[F(b) - F(a) \right]^m \right\} \\ &= \frac{1}{m^m} \left[F(b) - F(a) \right]^m \end{aligned} \tag{6.11}$$

Since $F(b) - F(a) = m$, by definition of m, we have $\int_a^b p(x)\,\mathrm{d}x = 1$. *Q.E.D.*

Finally, to obtain the emission intensity spectrum, we multiply $P(h\nu)$ by the photon energy $h\nu$, noting that $P(h\nu) = P(h\nu, r)$ through the r-dependence of V_c, and take the spatial average over the NC with a weight given by the quantum efficiency $\eta_i(r)$:[6]

$$I_{\mathrm{NC}}(h\nu) = \frac{3h\nu}{R_t^3} \int_0^{R_t} r^2 \eta_i(r) P(h\nu, r)\, \mathrm{d}r \tag{6.14}$$

Note that Eq. (6.14) gives an *energy*-dispersive PL spectrum; that is, the intensity of photons with energies lying between E and $E + \mathrm{d}E$ (equivalently, between $h\nu$ and $h\nu + h\mathrm{d}\nu$). To correctly compare a simulated spectrum calculated in this way to an experimentally-measured spectrum using a *wavelength*-dispersive technique, such as a monochromator or CCD array using a prism or diffraction grating, the intensity values must be multiplied by C/λ^2, where C is a constant. This is due to the change in variables from energy to wavelength:

$$\begin{aligned} p(E)\,\mathrm{d}E &= p\left(\frac{hc}{\lambda}\right)\left|\frac{\mathrm{d}E}{\mathrm{d}\lambda}\right|\mathrm{d}\lambda \\ &= p\left(\frac{hc}{\lambda}\right)\frac{hc}{\lambda^2}\,\mathrm{d}\lambda. \end{aligned} \tag{6.15}$$

For narrow spectra, the error resulting from a neglect of this conversion is small; broad spectra, however, can significantly shift their shape (the classic example is the wavelength- and energy-dependent forms of Planck's blackbody radiation density equation, with two corresponding versions of Wein's displacement law[11]).

6.2.2 Comparison of model with experiment

A selection of experimental PL spectra from a-Si-NC specimens with different size distributions is shown in Fig. 6.4. These samples were ~200 nm thick, grown by thermal evaporation of SiO under high vacuum and subsequently annealed for one hour in a flowing forming gas atmosphere (95% N_2+5% H_2) at the temperatures indicated. For annealing temperatures less than 800 °C, the films were found to be fully amorphous, as determined by TEM-related techniques (see, e.g., Chap. 5 and Refs.[12,13]). These specimens are characterised by a-Si NCs with a lognormal size distribution (see §C.3 for details). On going from 400 to 800 °C, the mean particle radii increase from ~13.4 Å to ~16.9 Å; complete values are listed in Table C.2.

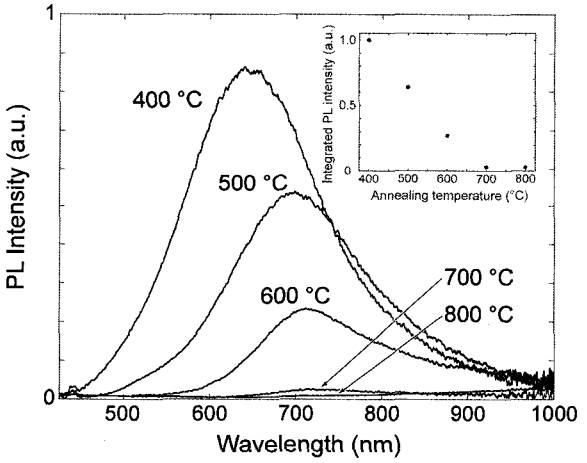

Fig. 6.4: Room-temperature photoluminescence spectra from a-Si-NC thin films. The measurements were taken with a fibre-optic CCD spectrometer, corrected for spectral response with a standard blackbody light source. Excitation was at 325 nm (~20 mW, ~4 mm^2 spot size). The specimens were nominally 200 nm thick, and were annealed in forming gas for one hour at the temperatures indicated. **Inset:** Integrated intensities for the five specimens as a function of annealing temperature. The PL spectra were integrated from 450 nm to 950 nm, and normalised to the 400-°C value.

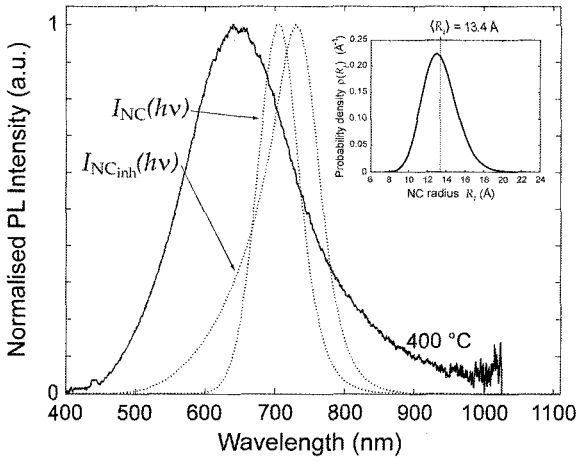

Fig. 6.5: Effect of inhomogeneous broadening on simulated PL spectra. All other parameters are as used for the simulation shown in Fig. 5.3. $I_{NC}(h\nu)$ was calculated using Eq. (6.14) with R_t = 13.4 Å, the mean radius for the 400-°C film. The inhomogeneously-broadened spectrum, $I_{NC_{inh}}(h\nu)$ was calculated using Eq. (6.16) with the size distribution $\rho(R_t)$ corresponding to a 400-°C-annealed specimen; the position of the mean radius $\langle R_t \rangle$ is marked on the upper axis of the inset. The experimental PL spectrum from the 400-°C-annealed specimen is shown as a solid line.

The simulated spectra shown in Fig. 5.3 for comparison with experimental 400-°C and 500-°C spectra were calculated using the same values for the various model parameters used by Estes and Moddel, which are ostensibly for bulk a-Si.[6] These values are: $E_g = 1.7$ eV, $E_{U_C} = 26$ meV, $E_{U_v} = 43$ meV, $N_{nr} = 1 \times 10^{16}$ cm^{-3}, $N_{snr} = 1 \times 10^{11}$ cm^{-2}, and $N_{c_0} = N_{v_0} = 1 \times 10^{16}$ cm^{-3}eV^{-1}. Excitation was ~20 mW from the 325-nm line of a HeCd laser, yielding $\Delta E_c = \Delta E_v = 1.06$ eV.

The peak centre wavelength and full-width at half-maximum (FWHM) of the experimental PL spectra, which we denote by λ_{peak} and $\Delta\lambda_{\frac{1}{2}}$, are 640 nm (699 nm) and 186 nm (190 nm), respectively, for the film annealed at 400 °C (500 °C). It is clear that while the simulated spectra lie within the correct general spectral range, the agreement with the experimental spectra is not particularly good: not only are the simulated peaks too narrow (by ~60% for the 400-°C specimen), but the size dependence of the peak wavelength shift is too weak. This last deficiency is apparent because a change in NC radius from 2.0 nm (which is smaller than the mean 400-°C NC size) to 3.0 nm (which is larger than the mean 500-°C NC size) only yields a peak shift of ~50 nm, whereas the experimentally-observed shift is ~60 nm. We will first consider the discrepancy in $\Delta\lambda_{\frac{1}{2}}$.

With respect to the model calculations, spectral broadening can have both homogeneous and inhomogeneous contributions. Since the model effectively returns the average emission from a monodisperse ensemble of a-Si NCs, inhomogeneous broadening can be introduced by incorporating a size distribution $\rho(R_t)$ similar to that which has been determined experimentally (see §C.3). That is, the inhomogeneously-broadened PL spectra can be calculated via

$$I_{NC_{inh}}(h\nu) = \int_0^\infty \rho(R_t) I_{NC}(h\nu, R_t)\, dR_t \qquad (6.16)$$

An example of such a procedure are shown in Fig. 6.5 for size parameters corresponding to a 400-°C film. While a broadening effect is observed, the peak width only increases from ~70 nm to ~95 nm, still almost a factor of two narrower than the experimental spectrum. The simulated spectrum also acquires a negative skewness (resulting from the greater average quantum efficiency of the smaller NCs) which disagrees with the experimental spectrum. This suggests that the broadening cannot be strictly inhomogeneous: an *ad hoc* size distribution constructed to return a simulated spectrum of the correct size and width would likely bear little resemblance to the experimentally-observed $\rho(R_t)$.

Considering *homogeneous* broadening, the simulation parameters most intimately con-

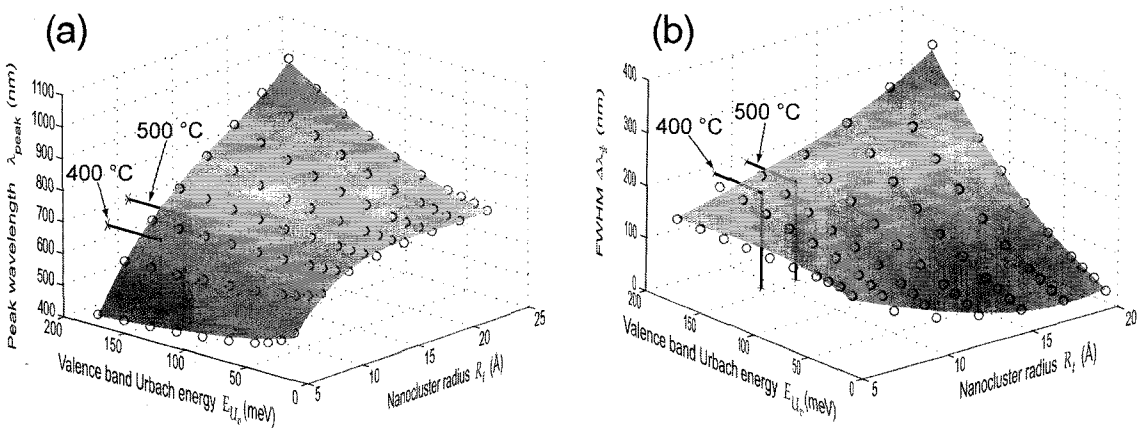

Fig. 6.6: Behaviour of (a) the peak wavelength (λ_{peak}) and (b) the FWHM ($\Delta\lambda_{\frac{1}{2}}$) of $I_{\text{NC}}(h\nu)$ as functions of NC radius (R_t) and valence-band Urbach energy (E_{U_v}). E_{U_c} was varied with E_{U_v} to maintain the same ratio as in bulk ($E_{U_c}/E_{U_v} = 26/43$).[6] The results from the simulation are shown as open circles, with the shaded surfaces corresponding to fits to these data using third-degree bivariate polynomials (in R_t and E_{U_v}). The solutions to these polynomial fits which yield the correct peak wavelength and FWHM for the experimental spectra from the 400-°C and 500-°C specimens are marked with bold lines.

nected with the width of the resulting spectra are the Urbach energies, E_{U_c} and E_{U_v}: larger values of these parameters result in DOS functions with broader band tails; since $P(h\nu)$ is determined by convolving two functions whose widths are essentially determined by the extent of the tail-state density below the mobility gap, viz., $p_c(E)$ and $p_v(E)$, an increase in the E_U values will broaden $I_{\text{NC}}(h\nu)$. Since the behaviour of the numerical model as a function of its many input parameters is not immediately quantitatively obvious, λ_{peak} and $\Delta\lambda_{\frac{1}{2}}$ cannot be directly varied independently. As such, the behaviour of $I_{\text{NC}}(h\nu)$ was investigated numerically, as a function of the nanocluster radius and the Urbach energies. The rationale for focusing on these two parameters is, first, that there exists some experimental error in determining the size distribution of the NCs, and second, adjusting the band-tail slopes is the most obvious method of increasing the FWHM of the simulated spectra.

Fig. 6.6 illustrates the dependence of λ_{peak} and $\Delta\lambda_{\frac{1}{2}}$ on R_t and E_{U_v}, where the open circles denote the results of the simulations, and the shaded surface represent third-degree bivariate polynomial fits to the simulation data, that is, polynomial functions for $\lambda_{\text{peak}}(R_t, E_{U_v})$ and $\Delta\lambda_{\frac{1}{2}}(R_t, E_{U_v})$. In the simulations, E_{U_c} was varied to maintain the same E_{U_c}/E_{U_v} ratio as in bulk a-Si, viz., 26/43.[6] Equating these functions to the experimental values for peak wavelength and FWHM for the 400-°C and 500-°C specimens and solving yields values for R_t and E_{U_v} of $R_t^{400\,^\circ\text{C}} = 9.0$ Å, $E_{U_v}^{400\,^\circ\text{C}} = 156.3$ meV, $R_t^{500\,^\circ\text{C}} = 10.9$ Å, and $E_{U_v}^{500\,^\circ\text{C}} = 154.1$ meV. The normalised spectra calculated using these values, and the corresponding normalised experimental spectra, are shown in Fig. 6.7. The simulated and experimental spectra match remarkably well overall; the steeper relative decay of the blue side of the simulated spectra could be due to inhomogeneous broadening resulting from a distribution in R_t, which was not included here.

From the relevant NC size distribution functions shown in Fig. C.2, it is seen that $R_t^{400\,^\circ\text{C}}$ and $R_t^{500\,^\circ\text{C}}$ are about 30% smaller than the actual mean values; in particular, for the 400-°C specimen, the probability density at this value is only ~0.03. Similarly, the values for the valence-band Urbach energies are somewhat smaller than—though still of

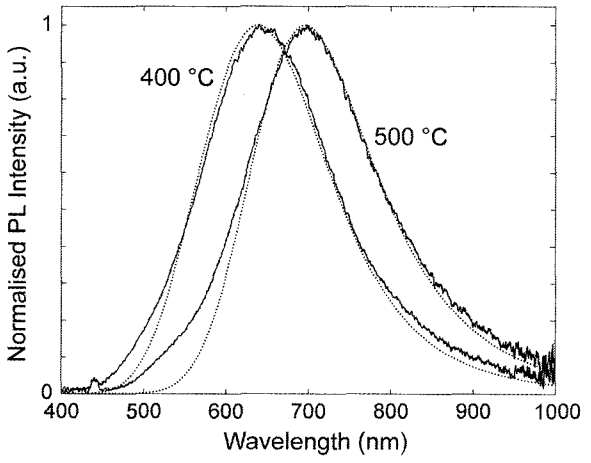

Fig. 6.7: Comparison of normalised experimental PL spectra from specimens annealed at 400 and 500 °C (solid lines) and best-fit simulated spectra with respect to R_t and E_{U_v} (dotted lines). All other model parameters (e.g, E_g, N_{nr}, N_{snr}, $\Delta E_{c,v}$, etc.) are as given in the paragraph following Fig. 6.4.

the same order of magnitude as—the ~200-meV values found for the films via transmission measurements (see §B.1.4); since the absolute error in the experimentally-determined Urbach energies is not well known, however, the values of $E_{U_v}^{400\,^\circ\text{C}}$ and $E_{U_v}^{500\,^\circ\text{C}}$ may still be reasonably taken to suggest that a broadening of the band tails is in fact responsible for the (homogeneous) broadening of the PL spectra.[14] An increase in E_U for nanoscale a-Si with respect to bulk has been attributed to a widening of the mobility gap, with the lowest-lying states remaining essentially unaffected.[3] It is important to realise that the simulated spectra shown in Fig. 6.7 do not necessarily represent the global best-fit in the complete parameter space of the model. For instance, the mobility gap E_g was left fixed at 1.7 eV; an increase in E_g would have the general effect of blueshifting the spectrum, and could therefore possibly result in best-fit values for $R_t^{\text{X00}\,^\circ\text{C}}$ which correspond better to the experimental NC sizes. In any event, since the large number of input parameters makes the existence of a unique best-fit solution unlikely, we will not explore the parameter space further in this manner.

It has been shown that, by varying only the (single) particle size and Urbach energies, the model presented is able to return simulated spectra which correspond very well to experimental results from a-Si-NC films. Note, however, that so far the primary concern has been the *shape* of the spectra (i.e., their centre wavelength and FWHM); normalised spectra have therefore been used to perform the fits. A look at Fig. 6.4, however, shows that another obvious characteristic of the photoluminescence from the experimental specimens is a strong *quenching* effect with an increase in average particle size (with increasing annealing temperature). Before investigating the quenching behaviour, however, the model will be reformulated in a manner which more realistically describes an ensemble of nanoclusters. This reworked model will also allow one to consider the effect of tunnelling between nanoclusters on the emission.

6.2.3 Monte Carlo approach to model

As stated in §6.2.1, for situations in which $R_c \geq 2R_t$, the spatial averaging of the luminescence given in Eq. (6.14) is redundant: $V_c = \frac{4}{3}\pi R_t^3$, irrespective of the value of r. Using the "typical" values of η_0 and T_0 as in Estes and Moddel,[6] the room-temperature capture radius corresponding to a volume defect density of $N_{\text{nr}} = 1 \times 10^{16}$ cm^{-3} is $R_c \approx 550$ Å—over an order of magnitude larger than R_t for our largest experimental a-Si NCs. As such, since the probability density functions for the lowest-lying carrier states, $p_c(E)$ and $p_v(E)$,

are determined only by the nanocluster sizes, an equivalent approach to the one-particle model as given in §6.2.1 would be to consider the radiative recombination from a large *ensemble* of NCs whose lowest-energy e–h pair states are determined stochastically. Before explaining the operation of such a Monte Carlo procedure, we will briefly review the method of generating random numbers obeying an arbitrary probability density function.

Transforming a set of uniformly-distributed random numbers into a set of random numbers distributed according to some other probability density function may be accomplished by the following technique. Given a continuous probability density distribution $P(x)$ normalised on $[a, b]$, we define the corresponding cumulative density function $D(x)$ as the probability that a random variate X obeying $P(x)$ is equal to or less than x:

$$D(x) = \int_a^x P(x')\,\mathrm{d}x' \tag{6.17}$$

Since $P(x)$ is normalised, the range of $D(x)$ is [0,1]. As such, if Y_k are *uniformly*-distributed variates on [0,1], then mapping each y-value to its corresponding x-value via $D(x)$ generates a set of variates X_k obeying $P(x)$. If $Y_k = D(X_k)$ cannot be inverted analytically, it may be done numerically instead. An illustration of this procedure is shown in Fig. 6.8.

The Monte Carlo (MC) formulation of the model is executed as follows. To simulate an a-Si-NC specimen, a large number of nanocluster radii are generated as in the foregoing explanation, using the lognormal probability density functions $\rho(a)$ as fit to the experimental histograms shown in §C.3. Each NC is then assigned lowest-lying electron and hole energies (E_e and E_h, respectively) based on its size, using the energy probability density functions $p_c(E)$ and $p_v(E)$ given by Eq. (6.8) and its corresponding valence-band form. For the emission process, nanocluster j is then assumed to emit a photon of energy $E_{\mathrm{lum}_j} = E_g + E_{e_j} + E_{h_j}$ with probability $\eta_i(R_{t_j})$. The luminescence spectrum is then given by the weighted energy (or wavelength) histogram of E_{lum_j}, where the weights are given by η_j. That is, the intensity for a narrow wavelength band between λ and $\lambda + \delta\lambda$ is proportional to the sum of the η_j of all NCs emitting photons within this range.

That this approach and the original statement of the model yield equivalent results can be seen by the good agreement of the spectra in Fig. 6.9; the parameters used are the same as those in the paragraph following Fig. 6.4, with $R_t = 15.1$ Å. The MC spectrum shown used an ensemble of 10^4 NCs.

The model may now be used to investigate the quenching effect exhibited by the speci-

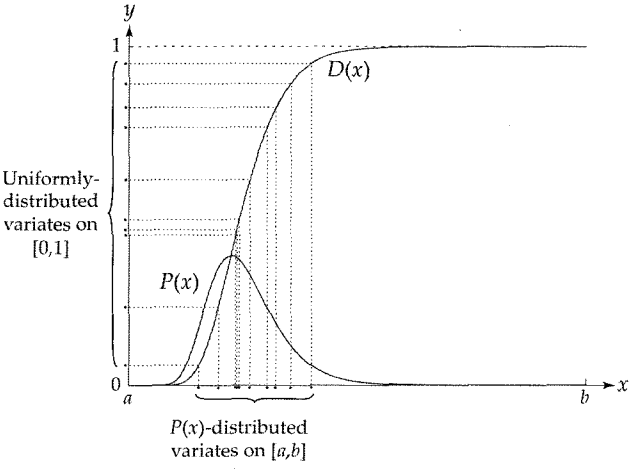

Fig. 6.8: Generating random numbers obeying an arbitrary probability distribution from uniformly-distributed random numbers. $P(x)$ is a probability density function normalised on $[a, b]$ and $D(x)$ is its corresponding cumulative density function. Uniformly-distributed numbers on [0,1] are mapped onto $[a, b]$ via $D(x)$.

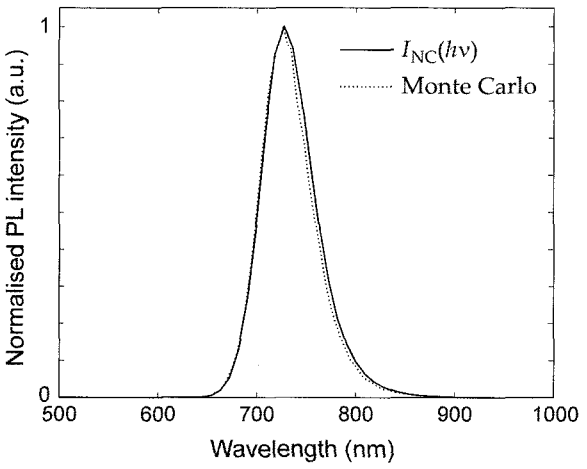

Fig. 6.9: Illustration of the equivalence of the PL spectra calculated using Eq. (6.14) (solid line) and using the Monte Carlo NC ensemble approach (dotted line), with the input parameters as given in the paragraph following Fig. 6.4, and $R_t = 15.1$ Å. For the Monte Carlo calculation, a monodisperse ensemble of 10 000 NCs was considered.

mens whose PL spectra are shown in Fig. 6.4. To quantify this quenching, we will consider the integrated PL intensity from 450 nm to 950 nm, as plotted in the inset. In particular, we will focus on the behaviour of the 400-, 500-, and 700-°C specimen PL with respect to the MC simulation. The TEM image for the specimen annealed at 600 °C exhibited poor contrast, such that only 60 NCs were able to be counted, as opposed to 100 for the other specimens; we therefore regard the 600-°C size distribution histogram and associated log-normal fit with some suspicion and will not use it in our simulations. As for the 800-°C specimen, its PL peak is very weak, broad, and ill-defined; it too will not be considered.

Fig. 6.10 portrays the effect of varying $N_{\rm nr}$ on the MC simulation spectra: the integrated intensities are shown in the insets, with the spectra themselves in the main axes. The size distributions used in the simulations are lognormal distributions with S and M values as given in Table C.2 for the specimens annealed at 400, 500, and 700 °C . 10^6 NC radii were generated using these size distributions, and assigned lowest electron and hole energies as explained previously. E_{U_v} was set to 200 meV in all simulations, corresponding to the values obtained from an analysis of the absorption coefficient α (see §B.1.4). As well, to provide a better qualitative agreement with the experimental spectra for the lower values of $N_{\rm nr}$, we use $E_g = 2.0$ eV (this adjustment compensates for the larger mean NC size with respect to the best-fit values of R_t determined in the previous section; the principal effect of altering E_g is to blueshift the spectrum, with little change in spectral shape).

We see that the "typical" value of $N_{\rm nr} = 10^{16}$ cm^{-3} used by Estes and Moddel[6] cannot adequately account for the experimental strong quenching (Fig. 6.10b). That is, for this value of $N_{\rm nr}$, the average increase in volume due to the difference in size distribution between the 400 -°C and 700-°C specimens is insufficient to cause $\eta_i(V_c)$ to display the experimentally-observed behaviour. Indeed, for such a small defect density, the quantum efficiency of each nanocluster is very nearly unity, as can be seen by comparing Fig. 6.10a and b. However, by increasing $N_{\rm nr}$ to 10^{20} cm^{-3}, the quenching begins more closely to approach that of the experimental spectra. A nonlinear least-squares fit yields $N_{\rm nr} = 2.18 \times 10^{20}$ cm^{-3}, the spectra for which are shown in Fig. 6.10e. Note that a blueshift occurs with increasing $N_{\rm nr}$ due to the greater quantum yield of the smaller particles, which possess (on average) higher lowest-lying electron and hole energies than the larger NCs; as such, the resulting simulated spectra become blueshifted by approximately 100 nm with respect to the experimental spectra. By adjusting E_g to 1.67 eV, the qualitative agreement of the spectra is reestablished, without sacrificing the quenching behaviour, as seen in

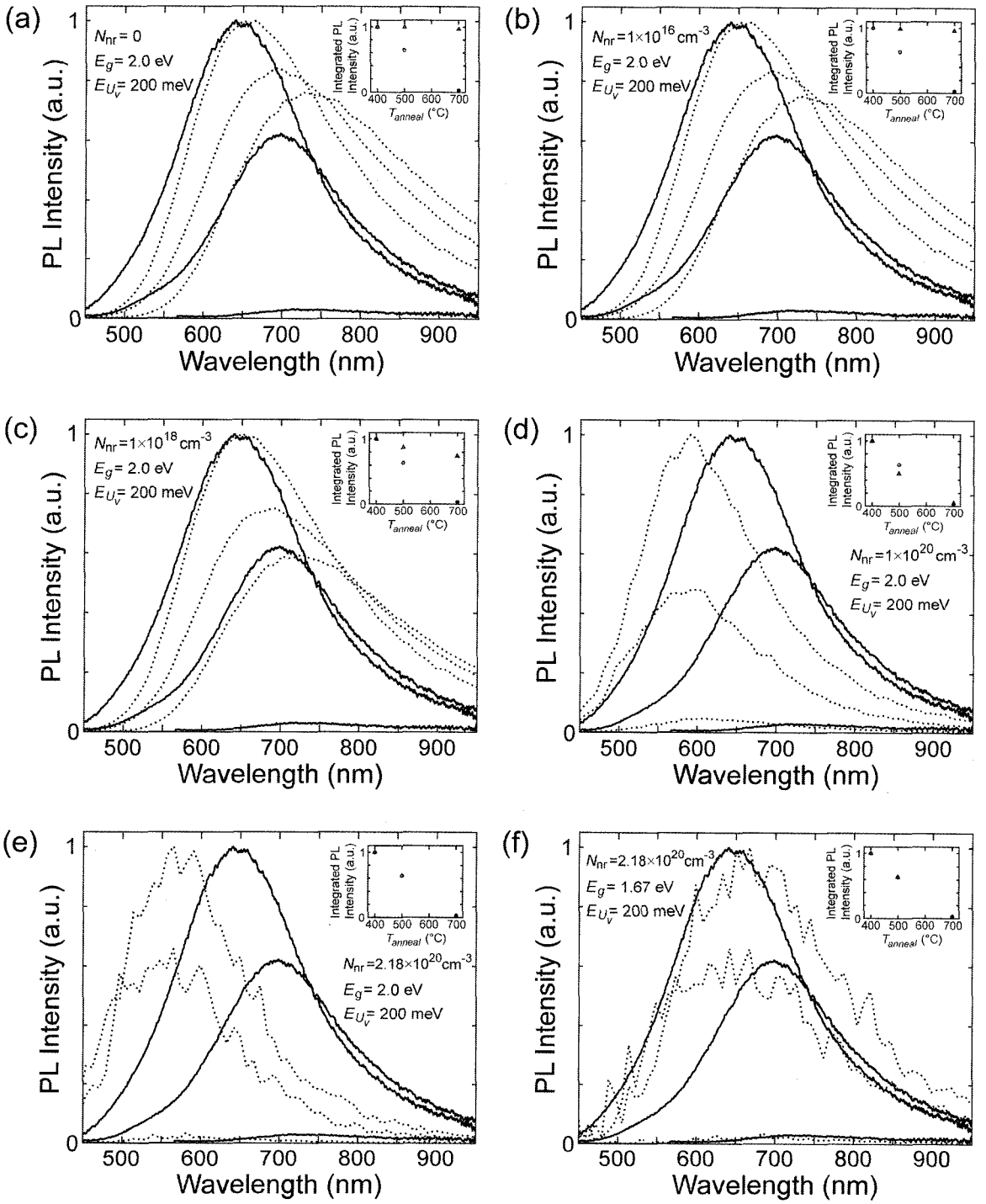

Fig. 6.10: Quenching of Monte Carlo simulation spectra as a function of N_{nr}. 10^6 NC radii were generated using the appropriate lognormal size distributions given in Table C.2. The values used for N_{nr}, E_g, and E_{U_v} are indicated for each plot. The experimental spectra are shown as solid lines, with the simulations as dotted lines, normlalised to the 400-°C spectra. **Insets:** Comparison of integrated PL for experimental specimens (open circles) and simulated spectra (open triangles), normalised to the 400-°C values.

the inset to Fig. 6.10f. The value of 1.67 eV for E_g was chosen "by eye" purely to provide a better qualitative visual fit; it is significantly smaller than the optical gaps extracted from Tauc plots of the specimen absorption ($E_g \approx 2.4$ eV). It is known that the non-radiative defect density of a-Si:H fabricated via glow discharge deposition can vary widely (from $\sim 10^{15}$ to $\sim 10^{18}$ cm^{-3}) depending on the processing parameters (RF power, pressure, precursor gas concentrations and flow rates, etc.).[5] Although the best-fit value of N_{nr} lies outside this typical range, it is conceivable that particulars of the fabrication technique of these specimens—thermal evaporation onto a cool substrate and a much lower hydrogen content (since it is introduced into the material only by diffusion during annealing), for instance—could result in such a high defect density.

One potential complication to this analysis is the fact that R_c assumes a value of ~ 20 Å for $N_{\mathrm{nr}} = 2.18 \times 10^{20}$ cm^{-3}. For NCs with $R_t > \frac{1}{2} R_c$, the assumption that $V_c = \frac{4}{3}\pi R_t^3$ breaks down, yielding larger values for η_i. This would have the general effect of requiring a greater defect density than the best-fit value given above, since the larger nanoclusters would have a greater quantum yield than suggested by the simulations shown in Fig. 6.10. A such, an obvious—although more computationally-intensive—future refinement to this simulation would be to calculate η_{NC} using Eq. (6.2) for each of the 10^6 nanoclusters, recalculating E_e and E_h for each tested value of N_{nr}; for this thesis, however, this procedure has not been considered.

The exponential dependence of $\eta_i(R_t)$ on V_c and A_c indicates that, for large values of N_{nr}, the quantum efficiency is very sensitive to changes in R_t; as much is suggested by Fig. 6.10. One means by which the effective capture volume and surface area can be increased for carriers in an ensemble of NCs with edge-to-edge space on the order of nanometres is by tunnelling from NC to NC. It has recently been shown that many aspects of the spectral behaviour of PL from densely-packed ensembles of *crystalline* Si NCs can be accounted for in the context of inter-NC tunnelling.[8] In light of the success of this tunnelling model for c-Si NCs, this possibility will now be considered for a-Si NC specimens.

6.3 Tunnelling: simulation

Tunnelling of carriers between closely-spaced low-dimensional structures is a well-known effect. For non-resonant tunnelling between GaAs quantum wells of slightly different widths through $\sim$nm-thick $Al_xGa_{1-x}As$ barriers, the theory for the textbook case of *resonant* tunnelling through a potential barrier (see §D.1) has been shown to provide an adequate description,[15,16] despite the fact that the plane-wave solutions for the incident, reflected, and transmitted wavefunctions is clearly a significant oversimplification for carriers confined in a quantum well, wire, or dot. The tunnelling transmission coefficient through a rectangular barrier of height V and width d for a carrier with energy E is given by[†]

$$T = \frac{4\left(\frac{m_p}{m_b}\right) E(V-E)}{4\left(\frac{m_p}{m_b}\right) E(V-E) + \left[\left(\frac{m_p}{m_b} - 1\right) E + V\right]^2 \sinh^2 \frac{d}{\lambda}} \tag{6.18}$$

[†]See §D.1 and references therein for a derivation of this expression and corrections to the corresponding relations used in Refs.[15,16].

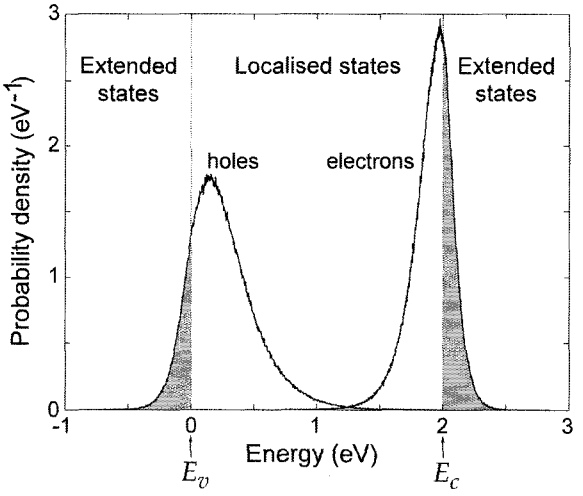

Fig. 6.11: Probability density functions for the lowest-lying electron and hole energies, as calculated for the size distribution corresponding to a specimen annealed at 400 °C . The energy scale is relative to the valence-band mobility edge, E_v. The shaded portions of the curves denote extended carrier states (i.e., those lying outside the mobility gap); they constitute 15.2% and 30.7% of the total holes and electrons, respectively. For this simulation, as in the simulations shown in Fig. 6.10a–e, $E_g = 2.0$ eV and $E_{U_v} = 200$ meV.

where m_p and m_b are the effective carrier masses outside and inside the barrier, respectively, and $\lambda = \frac{\hbar}{\sqrt{2m_b(V-E)}}$ is the wavefunction penetration depth in the barrier.

One might doubt even further the applicability of such a model to the case of a collection of amorphous semiconductor quantum dots, since the wavefunctions of localised carriers resemble the plane waves assumed in Eq. (6.18) even less than do the extended Bloch waves of carriers in a crystalline semiconductor. It is therefore instructive to consider the nature of the lowest-lying states (i.e., whether localised or extended) in the simulated ensembles of nanoclusters considered in this chapter. Fig. 6.11 illustrates the probability density of the lowest-lying electron and hole energies for the simulation of the 400-°C specimen, relative to the valence-band mobility edge E_v. The shaded portions of the plot correspond to extended states, that is, states with energies outside the mobility gap: for this simulation, ~15% of holes and ~31% of electrons exist in extended states. Since the size distribution for this specimen yields smaller particles, on average, than found in the other specimens, it should represent an upper bound with respect to the proportion of extended carriers.

Although the majority of the states are localised, it is useful to investigate a simplified tunnelling process for heuristic purposes. As such, we will treat all carriers equally, making no distinction between localised or extended states. In this limit, we are effectively allowing a greater possibility for tunnelling of carriers residing deep in the mobility gap than is present in reality. The tunnelling rate is then given by $w_{\text{tunn}} = \nu_0 T$, where T is the barrier transparency given in Eq. (6.18), and ν_0 is the tunnelling attempt frequency; for a carrier initially confined in a 1D well of width L, ν_0 may be approximated classically as

$$\nu_0 = \frac{v}{2L} = \frac{1}{2L}\left(\frac{2E}{m_p}\right)^{1/2} \tag{6.19}$$

To evaluate this expression, a shift is made in the carrier energies, separately, defining the zero of energy as that of the lowest-lying electron or hole, as appropriate. While this results in a zero probability of tunnelling from the two NCs in the ensemble with the (global) lowest-energy carrier states, this effect should be small overall; this is also suggested from the WKB limit of Eq. (6.18), which, for a rectangular barrier, is a function only of the difference $V - E$.[17] It is a further approximation to use Eq. (6.19) for a carrier confined in a

spherical quantum dot. However, since the tunnelling probability is expected to be dominated by T rather than ν_0, this should be acceptable within the heuristic context of this example.

The tunnelling simulation is implemented as follows. First, simulated ensembles of a-Si NCs corresponding to the 400-, 500-, and 700-°C specimens are constructed which mirror the size distribution and packing fraction resulting from each annealing temperature. 10^4 NC radii are generated as before, and randomly placed in a spherical box with a radius chosen to provide the correct NC packing fraction for the specimen to be considered. This packing fraction is defined as the fraction of material existing in an Si phase, $x_{\text{Si phase}}$, which may be determined experimentally by EELS measurements (see Table C.1). An electron and a hole are then placed in a NC and allowed to tunnel independently to NCs with lower energy states until such time as they "recombine" or become "stuck." During each timestep of Δt =100 fs, 101 possible events are considered for each carrier: the carrier can "recombine" with probability $1 - e^{\Delta t/\tau_r}$, where $\tau_r = 0.5$ μs is the characteristic lifetime of the PL from the a-Si specimens, or tunnel to one of the 100-closest particles, with probability $1 - e^{w_{\text{tunn}}\Delta t}$; the order of checking for each of these possibilities was random, different for each timestep. If no tunnelling events occur for 10 timesteps, the carrier is considered to be "stuck," having found a local minimum in the energy landscape. The effective accessible volume V_{acc} for this electron-hole pair is then taken to be the maximum of the sum of the NC volumes visited by each carrier. To avoid edge effects, only the 8000 centremost NCs were used as starting points. The values of the parameters used in this simulation are summarised in Table 6.1.

Table 6.1: Values for the parameters used in the tunnelling simulation.

Parameter name	Symbol	Value	Note
Electron effective mass in a-Si	m_{p_e}	$0.40m_0$	From Ref.[5], pg. 144
Hole effective mass in a-Si	m_{p_h}	$0.17m_0$	Inferred from Refs.[5,18]
Electron effective mass in SiO_2	m_{b_e}	$0.42m_0$	From Ref.[8]
Hole effective mass in SiO_2	m_{b_h}	$0.33m_0$	From Ref.[8]
Bandgap of a-Si	$E_{g_{a\text{-Si}}}$	2.0 eV	From simulations in §6.2.3
Bandgap of SiO_2	$E_{g_{\text{SiO}_2}}$	8.9 eV	From Ref.[19]
CB mobility edge–Fermi level separation in a-Si	$(E_c - E_F)_{a\text{-Si}}$	1.0 eV	Assume E_F lies mid-gap
CB edge–Fermi level separation in SiO_2	$(E_c - E_F)_{\text{SiO}_2}$	4.21 eV	Inferred from Ref.[20]
Electron barrier height	V_e	3.21 eV	Inferred from above values
Hole barrier height	V_h	3.69 eV	Inferred from above values

The results of the tunnelling simulations for the 400-, 500-, and 700-°C specimens are shown in Fig. 6.12. The average accessible NC volume, $\overline{V}_{\text{acc}}$, is indicated by an arrow in each plot. For comparison, the average average nanocluster volume $\overline{V}$ is also displayed. For convenience, we may therefore define the average number of NCs visited by carriers as $\overline{n}_{\text{acc}} = \overline{V}_{\text{acc}}/\overline{V}$; $\overline{n}_{\text{acc}}$ is 2.4, 3.2, and 3.1, for the 400-, 500-, and 700-°C specimens, respectively. To examine the effect this tunnelling has on the quenching behaviour of the MC luminescence model in a first-order approximation, we may simply adjust the values of $\eta_i(V_c, A_c)$ for each NC to reflect the increase in effective capture volume. That is to say, we assume that the emission energy for a given NC remains the same, but with a reduced probability of radiative recombination:

$$\eta_i^{\text{eff}} = e^{-N_{\text{nr}}V_{\text{acc}_i}^{\text{eff}} - N_{\text{snr}}A_{\text{acc}_i}^{\text{eff}}} \tag{6.20}$$

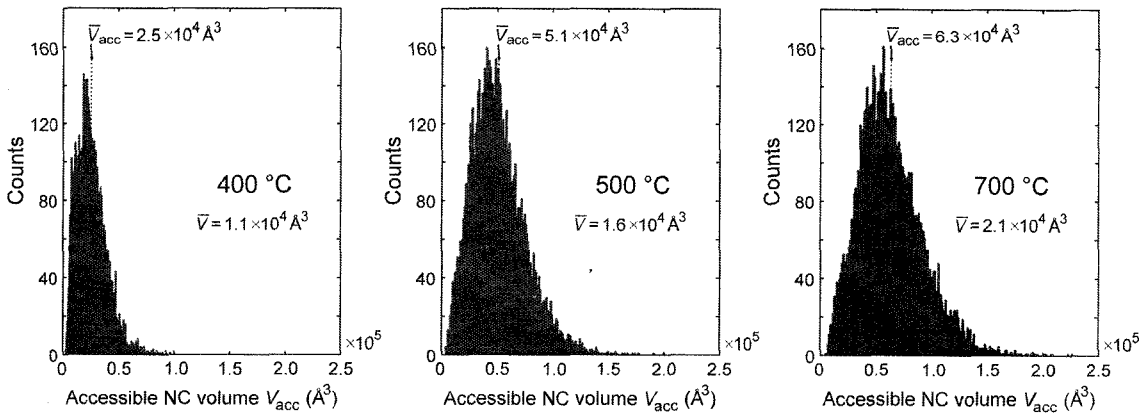

Fig. 6.12: Histograms of the accessible NC volume, V_{acc}, for 400-, 500-, and 700-°C specimen tunnelling simulations. The positions of the mean accessible volumes are indicated by arrows.

where

$$V_{acc_i}^{eff} = \frac{4}{3}\pi R_{t_i}^3 + (\overline{n}_{acc} - 1)\overline{V}_{acc} \tag{6.21}$$

and

$$A_{acc_i}^{eff} = 4\pi R_{t_i}^2 + (\overline{n}_{acc} - 1)\left[4\pi\left(\frac{3}{4\pi}\overline{V}_{acc}\right)^{\frac{2}{3}}\right] \tag{6.22}$$

for nanocluster i.

Incorporating the tunnelling results thus into the Monte Carlo luminescence simulation, the quenching of the PL is modified to the situation shown in Fig. 6.13. In this figure, we see that the ability of the model to reproduce the experimentally-observed quenching behaviour has been lost: no value of N_{nr} can produce the good qualitative fits shown in Fig. 6.10e and f. The shift in the ratios of the effective accessible volumes for the three specimens, that is, the change in $\overline{V}_{acc_{400\,°C}} : \overline{V}_{acc_{500\,°C}} : \overline{V}_{acc_{700\,°C}}$ from ~1.0:1.5:1.9 (no tunnelling) to ~1.0:2.0:2.5 (tunnelling), is responsible for the results in Fig. 6.13. Although it is imprudent to draw many firm conclusions from the results of such a simplified tunnelling model, they suggest, as expected from the much larger proportion of localised states and lower overall extended-state energies relative to carriers in Si nanocrystals,[8] that inter-

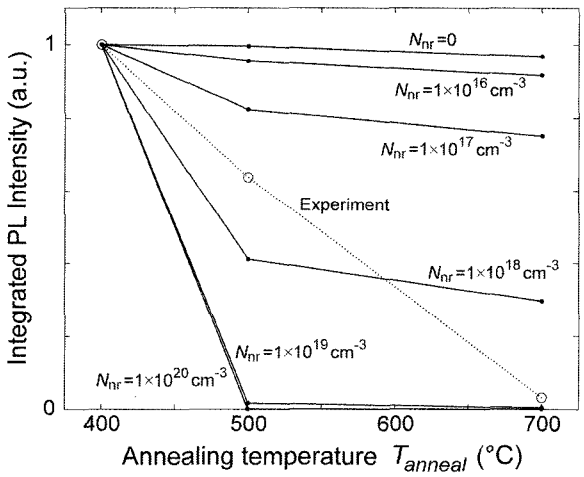

Fig. 6.13: Comparison of experiment and Monte Carlo luminescence simulations for integrated intensity PL quenching, including the effect of tunnelling, for 400-, 500-, and 700-°C specimens. The experimental quenching is denoted by open circles, with the MC simulation results including the effect of V_{acc}^{eff} indicated by closed circles; the values of N_{nr} are indicated for each simulation. The lines are a guide to the eye. Note the lack of qualitative agreement for the quenching behaviour.

nanocluster tunnelling plays a limited role in the luminescence from a-Si-NC-containing nanocomposite thin films.

6.4 Conclusions

The photoluminescence from ensembles of a-Si NCs has been simulated using a model developed for bulk a-Si:H,[6,10] in which radiative recombination occurs between the lowest-lying electron and hole states for a given nanocluster size; the probability density functions for these e–h pair energies are calculated using density of states functions including both the quadratic (extended) bands and the exponential (localised) band tails. This model was implemented using numerically-averaged single-NC simulations, as well as a Monte Carlo approach for an ensemble of NCs. The width of the experimentally-observed PL spectra from a-Si-NC-containing thin films is mostly likely dominated by homogeneous broadening, characterised by an increase in the valence- and conduction-band Urbach energies, although inhomogeneous broadening due to a distribution in NC radii may also contribute. The strong quenching behaviour of the PL can be well-described by considering an ensemble of isolated NCs with a non-radiative volume defect density on the order of 10^{20} cm^{-3}. Increasing the effective volume accessible to carriers using a simplified inter-NC tunnelling model did not yield luminescence quenching behaviour which could be fit to the experimental data; the increase in V_{acc} found by this tunnelling model, however, likely constitutes an upper limit, since by its simplified construction, the simulated tunnelling probabilities of localised states are likely much higher than in reality. Future refinements to these simulations include a detailed treatment of the quantum efficiency of each nanocluster for defect density concentration regimes yielding capture radii smaller than the nanocluster diameters, and considering the tunnelling process between a-Si NCs with more rigour.

Bibliography

[1] S. V. Gaponenko, *Optical properties of semiconductor nanocrystals*, Cambridge University Press, Cambridge, 1998, ISBN: 0-521-58241-5.

[2] B. Abeles and T. Tiedje, "Amorphous semiconductor superlattices", *Phys. Rev. Lett.*, vol. 51, no. 21, pp. 2003–2006, 1983.

[3] R. B. Wehrspohn, J.-N. Chazalviel, F. Ozanam, and I. Solomon, "Spatial versus quantum confinement in porous amorphous silicon nanostructures", *Euro. Phys. J. B*, vol. 8, no. 2, pp. 179–193, 1999.

[4] N. F. Mott and E. A. Davis, *Electronic processes in non-crystalline materials*, Oxford University Press, London, 1971, ISBN: 0-198-51259-7.

[5] R. A. Street, *Hydrogenated amorphous silicon*, Cambridge University Press, Cambridge, 1991, ISBN: 0-521-37156-2.

[6] M. J. Estes and G. Moddel, "Luminescence from amorphous silicon nanostructures", *Phys. Rev. B*, vol. 54, no. 20, pp. 14633–14642, 1996.

[7] T. Tiedje, B. Abeles, and B. G. Brooks, "Energy transport and size effects in the photoluminescence of amorphous-germanium/amorphous-silicon multilayer structures", *Phys. Rev. Lett.*, vol. 54, no. 23, pp. 2545–2548, 1985.

[8] R. Lockwood, A. Hryciw, and A. Meldrum, "Nonresonant carrier tunneling in arrays of silicon nanocrystals", *Appl. Phys. Lett.*, vol. 89, Art. no. 263112, 2006.

[9] R. W. Collins, M. A. Paesler, and W. Paul, "The temperature dependence of photoluminescence in a-Si:H alloys", *Solid State Commun.*, vol. 34, no. 10, pp. 833–836, 1980.

[10] D. J. Dunstan and F. Boulitrop, "Photoluminescence in hydrogenated amorphous silicon", *Phys. Rev. B*, vol. 30, no. 10, pp. 5945–5957.

[11] D. V. Schroeder, *Introduction to thermal physics*, Addison Wesley Longman, San Francisco, 2000, ISBN: 0-201-38027-7, pp. 292–293.

[12] J. Wang, X.F. Wang, Q Li, A. Meldrum, and A. Hryciw, "The microstructure of SiO thin films: From nanoclusters to nanocrystals", *Philos. Mag.*, vol. 87, no. 1, pp. 11–27, 2007.

[13] A. Meldrum, A. Hryciw, A. N. MacDonald, C. Blois, K. Marsh, J. Wang, and Q. Li, "Photoluminescence in the silicon-oxygen system", *J. Vac. Sci. Tech. A*, vol. 24, no. 3, pp. 713–717, 2006.

[14] Y. Kanemitsu, "Photoluminescence spectrum and dynamics in oxidized silicon nanocrystals: A nanoscopic disorder system", *Phys. Rev. B*, vol. 53, no. 20, pp. 13515–13520, 1996.

[15] T. Tada, A. Yamaguchi, T. Ninomiya, H. Uchiki, T. Kobayashi, and T. Yao, "Tunneling process in AlAs/GaAs double quantum wells studied by photoluminescence", *J. Appl. Phys.*, vol. 63, no. 11, pp. 5491–5494, 1988.

[16] M. Nido, M. G. W. Alexander, W. W. Rühle, T. Schweizer, and K. Köhler, "Nonresonant electron and hole tunneling times in GaAs/$Al_{0.35}Ga_{0.65}$As asymmetric double quantum wells", *Appl. Phys. Lett.*, vol. 58, no. 4, pp. 355–357, 1990.

[17] B. H. Brandsen and C. J. Joachain, *Quantum mechanics*, Prentice Hall, Harlow, England, second edition, 2000, ISBN: 0582-35691-1, pp. 417–420.

[18] A. Esser, K. Seibert, H. Kurz, G. N. Parsons, C. Wang, B. N. Davidson, G. Lucovsky, and R. J. Nemanich, "Ultrafast recombination and trapping in amorphous silicon", *Phys. Rev. B*, vol. 41, no. 5, pp. 2879–2884, 1990.

[19] R. B. Laughlin, "Optical absorption edge of SiO_2", *Phys. Rev. B*, vol. 22, no. 6, pp. 3021–3029, 1980.

[20] J. L. Alay and M. Hirose, "The valence band alignment at ultrathin SiO_2/Si interfaces", *J. Appl. Phys.*, vol. 81, no. 3, pp. 1606–1608, 1997.

CHAPTER 7

Energy transfer modelling in the a-Si–Er^{3+} system

The Si-NC–Er system is impossible to model.
A. Polman, E-MRS 2006 Spring Meeting

7.1 Introduction

Rare-earth-doped silicon nanocomposites have been the focus of widespread research interest, driven largely by their suitability for integrated photonics and opto-electronics. Strong emission from trivalent rare earth ions at technologically-significant wavelengths in the near infrared has been demonstrated from films containing crystalline[1,2] or amorphous[3] Si nanoclusters, due to the now well-established—at least in terms of observations, since the details of the mechanism are still not fully understood—sensitisation effect exhibited by NCs. In particular, Si nanocomposite films doped with erbium can emit strongly at 1.54 μm, corresponding to the third transparency window for minimum attenuation in conventional silica optical fibres, and therefore comprise an attractive class of materials for potential use in Er-doped waveguide amplifiers (EDWAs) (see, e.g., Refs.[4–6]).

A thorough understanding of the population dynamics in the Si-NC–Er system is essential for the development of viable EDWAs; in particular, the maximum output power is limited by the energy transfer rate between the Si-NC and the Er^{3+} ions. To this end, numerous phenomenological models have been proposed, of varying complexity, to investigate the relative importance of cooperative upconversion, excited-state excitation, confined carrier absorption, energy migration, and other gain-limiting processes.[7,8] In general, these models consist of several coupled nonlinear differential equations which must be solved numerically. While the model of Pacifici *et al.*[7] is thorough in terms of the processes considered, the large number of free parameters—ten in total—involved in fitting to experimental time-resolved PL data calls into question the uniqueness of the fit, as demonstrated by a discrepancy in the $^4I_{13/2} \rightarrow {}^4S_{3/2}, {}^2H_{11/2}$ Si-NC–Er excited-state excitation energy transfer coefficient, C_{b2}: the values obtained by Pacifici[7] and Loh[8] differ by over four orders of magnitude.

Also of dubious validity is the common practice of modelling Si NCs as effective two-level systems: whether due to a distribution in sizes in the ensemble, interactions between NCs, variation in the local density of states due to a distribution in proximity to a high-

index substrate,[9] or some other phenomenon, investigations of PL dynamics from undoped Si-NC films often exhibit markedly non-exponential behaviour;[10,11] this underlying distribution in NC lifetimes should be considered for an accurate description of the Si-NC–Er interaction.

In this chapter, a simple model is proposed which comprises the most important levels in the Si-NC–Er system, valid for optical pumping conditions in which the ground-state levels of the nanoclusters and Er^{3+} ions can be treated as approximately constant; in such an excitation regime, analytical solutions to the system of rate equations exist (see Appendix A). In addition to providing simple functions to fit to time-resolved PL data, the lucidity afforded by an analytical description of the population dynamics can provide a useful starting-point in the interpretation of more complex models.

7.2 Experimental

200-nm-thick Si-NC:Er films were deposited on fused quartz wafers by co-evaporation of SiO (electron-beam) and metallic Er (thermal), the deposition rates being measured by two independent quartz crystal monitors; the nominal SiO:Er rates varied from ~1000:1 to 25:1. A compositional analysis of the films was carried out via EMPA using a 3-kV beam energy; results are shown in Table 7.1. The films were annealed in 96% N_2+4% H_2 at 500 °C for one hour to precipitate amorphous nanoclusters, the presence of hydrogen increasing the PL intensity due to the passivation of non-radiative traps on nanocrystal surfaces.[12,13] The microstructure of the Si NCs produced by this method have been previously investigated by our group.[14,15] For visible PL, time- and frequency-resolved photoluminescence dynamics were measured using a photomultiplier tube with a ~300 ps response time interfaced to a multichannel analyser with 250 ns time bins; near-infrared PL dynamics were measured using a thermoelectrically-cooled InGaAs photodiode interfaced to a digital storage oscilloscope. The 514- or 476-nm lines of an Ar^+ ion laser were used as the excitation source (spot size ~4 mm^2), the amplitude of which was controlled via an acousto-optic modulator (AOM).

Table 7.1: Compositional analysis of SiO:Er films obtained using EMPA. All data are normalised to 100%. Specimen ST5 had a very low Er concentration, nearing the detection limit of the EMPA system, and yielded aberrant Si and O results (note that the values correspond very closely to pure silica), since the film should be nearly stoichiometric SiO; as such, we take the measured Er concentration as an upper limit in this specimen. The calculation for Er concentration in cm^{-3} is shown in §C.4.

Specimen	Nominal SiO:Er ratio	Si (at.%)	O (at.%)	Er (at.%)	Er(cm^{-3})
ST1	25:1	47.8±0.4	50.1±0.3	2.13±0.04	1.2×10^{21}
ST2	50:1	49.2±0.7	49.8±0.7	0.95±0.02	5.5×10^{20}
ST3	100:1	48.1±0.2	51.3±0.2	0.59±0.01	3.4×10^{20}
ST4	200:1	47.9±0.1	51.9±0.1	0.222±0.008	1.3×10^{20}
ST5	~1000:1	32.1±0.2	67.9±0.2	~0.03	1.9×10^{19}

7.3 Model

In a rate equation analysis of two coupled systems (Si NCs and Er^{3+} ions, for instance), the interaction is introduced via coupling coefficients, C_{ij}, resulting in a transfer of energy from level i in one system to level j in the other. If there are a total of n_k levels in the system,

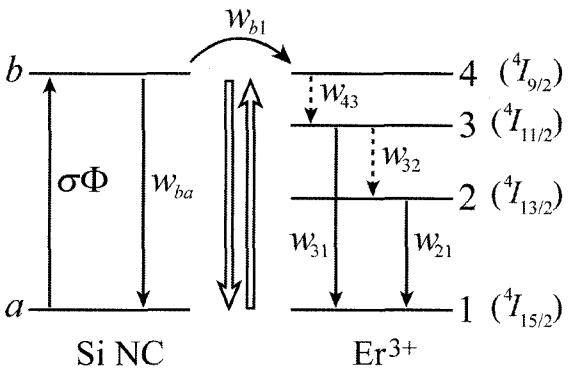

Fig. 7.1: Schematic of the interaction between a two-level Si NC and a four-level Er^{3+} ion in the small excitation regime. Radiative (non-radiative) transitions are denoted by solid (dashed) lines.

this results in a set of n_k nonlinear rate equations involving $C_{ij}N_iN_j$ terms, where N_i is the population of level i, which in general must be solved numerically. However, if the optical excitation of the nanoclusters is small, such that the fraction of excited NCs and Er^{3+} ions is small, we may make the approximation that $N_a(t)$ and $N_1(t)$, the respective populations of the NC and Er^{3+} ground states, remain constant. In this *small excitation regime*, the coupling coefficient C_{b1}, governing the energy transfer between the NC and the Er^{3+} may be replaced by a simple transfer rate $w_{b1} = C_{b1}\mathcal{N}_1$, where $\mathcal{N}_1$ is the concentration of Er^{3+} ions, and the total system may be described by $(n_k - 2)$ linear differential equations. This is in contrast to the pumping regime described by Loh and Kenyon,[8] in which the Er^{3+} are driven into saturation and $N_1 \approx 0$.

For simplicity, an effective two-level nanocluster is assumed, with a recombination rate of w_{ba}; a distribution in NC lifetimes can be incorporated later by approximating the real NC system by several two-level systems in the model with appropriate weights. For the energy transfer pathway between NC and Er^{3+}, a transfer from the ~700 nm broad NC PL band to the $^4I_{9/2}$ level in the ion is assumed, as in Pacifici *et al.*[7] As such, backtransfer to the NC should be negligible, as the $^4I_{9/2}$ level is quickly depopulated to $^4I_{11/2}$ via a very fast non-radiative relaxation (w_{43}).[7] In the small excitation regime, excited-state excitation should be also relatively unimportant, as the fraction of excited ions is small, and the effect of cooperative upconversion and energy migration may be neglected for a suitably low Er concentration. In this way, the set of differential equations describing the system (diagrammed in Fig. 7.1) is:

$$\frac{dN_b}{dt} = \sigma\Phi\mathcal{N}_a - (w_{ba} + w_{b1})N_b \tag{7.1a}$$

$$\frac{dN_2}{dt} = w_{32}N_3 - w_{21}N_2 \tag{7.1b}$$

$$\frac{dN_3}{dt} = w_{43}N_4 - (w_{31} + w_{32})N_3 \tag{7.1c}$$

$$\frac{dN_4}{dt} = w_{b1}N_b - w_{43}N_4 \tag{7.1d}$$

where Φ is the excitation photon flux, σ is the NC absorption cross-section, and $\mathcal{N}_a$ is the concentration of the NCs. We will consider the response of this system subject to initial conditions of zero for all excited states, under square-wave excitation (i.e. for $t \geq t_{off}$, we set $\Phi = 0$ in Eq. (7.1a)).

The evolution of levels b, 2, and 3 are directly accessible experimentally via time-resolved measurements of the nanocluster, 1535-nm, and 980-nm PL, respectively, in that $I_i(t) \propto w_{ij_{rad}} N_i(t)$, where $w_{ij_{rad}}$ is the radiative part of the transition rate from level i to level j. Thus, for these levels, we have, for $0 \leq t < t_{off}$:

$$N_b(t) = \frac{\sigma \Phi \mathcal{N}_a}{w_{ba} + w_{b1}} \left[1 - e^{-(w_{ba}+w_{b1})t}\right] \tag{7.2a}$$

$$\begin{aligned} N_2(t) = \sigma \Phi w_{b1} w_{32} \mathcal{N}_a \Bigg[& \frac{1}{w_{21}(w_{31}+w_{32})(w_{ba}+w_{b1})} \\ & + \frac{w_{43}}{w_{21}(w_{31}+w_{32}-w_{21})(w_{ba}+w_{b1}-w_{21})(w_{21}-w_{43})} e^{-w_{21}t} \\ & + \frac{w_{43}}{(w_{31}+w_{32})(w_{43}-w_{31}-w_{32})(w_{ba}+w_{b1}-w_{31}-w_{32})(w_{31}+w_{32}-w_{21})} e^{-(w_{31}+w_{32})t} \\ & + \frac{1}{(w_{21}-w_{43})(w_{43}-w_{31}-w_{32})(w_{ba}+w_{b1}-w_{43})} e^{-w_{43}t} \\ & + \frac{w_{43}}{(w_{ba}+w_{b1})(w_{ba}+w_{b1}-w_{21})(w_{ba}+w_{b1}-w_{43})(w_{ba}+w_{b1}-w_{31}-w_{32})} e^{-(w_{ba}+w_{b1})t} \Bigg] \end{aligned} \tag{7.2b}$$

$$\begin{aligned} N_3(t) = \sigma \Phi w_{b1} \mathcal{N}_a \Bigg[& \frac{1}{(w_{31}+w_{32})(w_{ba}+w_{b1})} \\ & + \frac{w_{43}}{(w_{31}+w_{32})(w_{43}-w_{31}-w_{32})(w_{31}+w_{32}-w_{ba}-w_{b1})} e^{-(w_{31}+w_{32})t} \\ & + \frac{1}{(w_{43}-w_{31}-w_{32})(w_{ba}+w_{b1}-w_{43})} e^{-w_{43}t} \\ & + \frac{w_{43}}{(w_{ba}+w_{b1})(w_{ba}+w_{b1}-w_{43})(w_{31}+w_{32}-w_{ba}-w_{b1})} e^{-(w_{ba}+w_{b1})t} \Bigg] \end{aligned} \tag{7.2c}$$

and for $t \geq t_{off}$:

$$N_b(t) = \eta_b e^{-(w_{ba}+w_{b1})(t-t_{off})} \tag{7.3a}$$

$$\begin{aligned} N_2(t) = & \left[\frac{w_{43} w_{32} w_{b1} \eta_b}{(w_{31}+w_{32}-w_{21})(w_{ba}+w_{b1}-w_{21})(w_{43}-w_{21})} \right. \\ & \left. + \frac{w_{43} w_{32} \eta_4}{(w_{31}+w_{32}-w_{21})(w_{43}-w_{21})} + \frac{w_{32}\eta_3}{w_{31}+w_{32}-w_{21}} + \eta_2 \right] e^{-w_{21}(t-t_{off})} \\ & + \left[\frac{w_{43} w_{32} w_{b1} \eta_b}{(w_{ba}+w_{b1}-w_{31}-w_{32})(w_{43}-w_{31}-w_{32})(w_{21}-w_{31}-w_{32})} \right. \\ & \left. + \frac{w_{43} w_{32} \eta_4}{(w_{43}-w_{31}-w_{32})(w_{21}-w_{31}-w_{32})} + \frac{w_{32}\eta_3}{w_{21}-w_{31}-w_{32}} \right] e^{-(w_{31}+w_{32})(t-t_{off})} \\ & + \left[\frac{w_{43} w_{32} \eta_4}{(w_{43}-w_{31}-w_{32})(w_{43}-w_{21})} \right. \\ & \left. + \frac{w_{43} w_{32} w_{b1} \eta_b}{(w_{ba}+w_{b1}-w_{43})(w_{43}-w_{31}-w_{32})(w_{43}-w_{21})} \right] e^{-w_{43}(t-t_{off})} \\ & + \frac{w_{43} w_{32} w_{b1} \eta_b}{(w_{ba}+w_{b1}-w_{31}-w_{32})(w_{ba}+w_{b1}-w_{43})(w_{21}-w_{ba}-w_{b1})} e^{-(w_{ba}+w_{b1})(t-t_{off})} \end{aligned} \tag{7.3b}$$

$$N_3(t) = \left[\frac{w_{43}w_{b1}\eta_b}{(w_{43}-w_{31}-w_{32})(w_{ba}+w_{b1}-w_{31}-w_{32})} + \frac{w_{43}\eta_4}{w_{43}-w_{31}-w_{32}} + \eta_3\right] e^{-(w_{31}+w_{32})(t-t_{off})} + \left[\frac{w_{43}\eta_4}{w_{31}+w_{32}-w_{43}} + \frac{w_{43}w_{b1}\eta_b}{(w_{31}+w_{32}-w_{43})(w_{ba}+w_{b1}-w_{43})}\right] e^{-w_{43}(t-t_{off})} + \frac{w_{43}w_{b1}\eta_b}{(w_{ba}+w_{b1}-w_{43})(w_{ba}+w_{b1}-w_{31}-w_{32})} e^{-(w_{ba}+w_{b1})(t-t_{off})} \quad (7.3c)$$

where $\eta_i = N_i(t_{off})$.[†] Note that, in the small excitation regime, the steady-state values of all level populations are linear with Φ.

Applying a fit to equations (7.3b) and (7.3c) to time-resolved PL decay data for the $^4I_{11/2} \rightarrow {}^4I_{15/2}$ emission at 980 nm or the $^4I_{13/2} \rightarrow {}^4I_{15/2}$ at 1.54 μm to extract values for the various lifetimes, however, can be problematic. Even in this simple model, both $N_3(t)$ and $N_4(t)$ are multi-exponential, with lifetimes for the component single exponentials which may be comparable (cf. $w_{31} + w_{32} \approx 4.2 \times 10^5$ s^{-1} and $w_{b1} \approx 10^6$ s^{-1} in Pacifici *et al.*,[7] since $\tau_{tr} \approx 1$ μs) and thus difficult to obtain uniquely. Furthermore, any fit to experimental data must include a multiplicative factor to account for the collection efficiency of the PL, adding yet another parameter to the fit.

Recourse to an *ad hoc* fit of time-resolved Er^{3+} PL data to a bi-exponential for the $^4I_{13/2} \rightarrow {}^4I_{15/2}$ transition at 1.54 μm has been employed by some authors, several of whom have gone so far as to postulate two different optically-active sites in Er^{3+}, obtaining two lifetimes and their relative contributions to the total PL from such a fit.[16,17] However, not only is there no reputable method, in general, of discriminating between goodness of bi-, tri-, or stretched exponential fits of data with experimental noise, but even a biexponential in which all four parameters (the lifetimes and the amplitudes) are to be fitted is very ill-conditioned, viz. it may not yield a unique fit.[18] As such, the number of free parameters must be reduced to have confidence in the uniqueness of a fit.

7.3.1 Determining w_{21}: 1535 nm PL

By considering the decay of the $^4I_{13/2}$ state in Er^{3+}, we may both fix the value of w_{21} as well as determine the upper limit of the small excitation regime with respect to the pump photon flux Φ. Selecting the 1535-nm PL with a band-pass filter, the decay of the PL was measured with a cooled InGaAs photodiode for square-wave 476-nm excitation chopped at 9.5 Hz. The incident power during illumination was varied between 0.10 and 6.30 mW (corresponding to photon fluxes of $\sim 1.3 \times 10^{16}$ and $\sim 4.0 \times 10^{17}$ cm^{-2}s^{-1}), and 10 000 sweeps were averaged for each incident power. The data shown in Fig. 7.2a is from specimen ST5 (0.03 at.% Er).

From the plot of steady-state PL values as a function of Φ (inset of Fig. 7.2a), a clear saturation effect is visible for the higher incident powers. For $\Phi \leq 10^{17}$ cm^{-2}s^{-1}, however, the steady-state value is, to a good approximation, linear with Φ. This provides a working definition of the small excitation regime for the specimens considered in this chapter.

Examining Eq. (7.3b), we see that the 1535-nm PL should be described by a sum of four exponentials, with rates of w_{21}, $w_{31}+w_{32}$, $w_{ba}+w_{b1}$, and w_{43}. For Er-doped nanocrystalline

[†]Please refer to §A.3.3 for the solutions to $N_4(t)$.

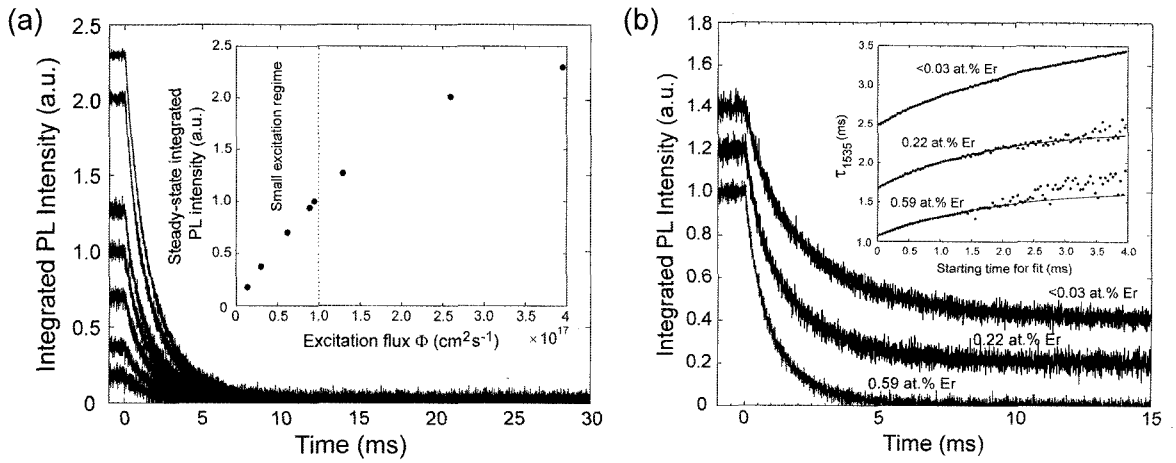

Fig. 7.2: Analysis of 1535-nm PL. In (a), 1535-nm PL decays from specimen ST5 (0.03 at.% Er.) is plotted for several different excitation fluxes, with the steady-state values plotted vs. Φ in the inset (note the linear trend for $\Phi \leq 10^{17}$ cm^{-2}s^{-1}). A means of estimating the $^4I_{13/2} \rightarrow {}^4I_{15/2}$ radiative recombination lifetime $\tau_{1535_{rad}}$ is shown in (b) for ST3, ST4, and ST5 (the decays have been arbitrarily displaced vertically for clarity). Using sequentially later starting points for single-exponential fits, the lifetime for the lowest-concentration sample, ST5, appears to saturate to a value of ~3.8 ms. The solid lines give the fit of these data to Eq. (7.4).

Si samples, Pacifici *et al.*[7] give values of $w_{32} + w_{31} \approx 4.2 \times 10^5$ s^{-1}, $w_{43} \approx 1 \times 10^7$ s^{-1}, and $w_{b1} = 1/\tau_{tr} \approx 1 \times 10^6$ s^{-1}. Since the ~700-nm *a*-Si-NC PL from the specimens considered here has a fast component on the order of 0.2 μs (see §7.3.2), w_{21}, the $^4I_{13/2} \rightarrow {}^4I_{15/2}$ radiative recombination rate, is expected to be the smallest of the four rates in Eq. (7.3b); the lifetime $\tau_{1535_{rad}} = 1/w_{21}$ can be as large as ~15 ms in SiO_2 and other silicate glass hosts.[19]

This provides a means of estimating the intrinsic (radiative) value of $w_{21_{rad}}$ for these specimens: if single-exponential fits are applied from progressively later and later starting points in the 1535-nm PL data after the excitation has been switched off, the faster components of the decay will contribute progressively less and less to the overall signal, and the single-exponential lifetime obtained from the fit (τ_{1535}) should become larger and tend to saturation. The inset to Fig. 7.2b shows the results of such a procedure, for specimens ST3, ST4, and ST5, with $\Phi \approx 10^{17}$ cm^{2}s^{-1}. Since the signal-to-noise ratio (SNR) of an exponentially-decaying signal becomes smaller as time advances, we cannot continue this fitting procedure indefinitely, and therefore cannot directly measure the value toward which τ_{1535} is saturating. As such, to estimate $\tau_{1535_{rad}}$, τ_{1535} may be fit to a function of the form:†

$$\tau_{1535} = \tau_{1535_{rad}} \left(1 - e^{-\frac{t_s - t_0}{t_n}}\right) \tag{7.4}$$

where t_s is the starting time (i.e., the temporal origin used for each fit), and t_0, t_n, and $\tau_{1535_{rad}}$ are free parameters. The results of fitting the τ_{1535} data for the three specimens are shown as solid lines in the inset to Fig. 7.2b. For the lowest-concentration specimen (ST5, 0.03 at.% Er), the value of $\tau_{1535_{rad}}$ obtained from a fit to Eq. (7.4) is ~3.8 ms. This a factor of ~3 smaller than the PL lifetime from Er-doped silicate glasses with a similar Er concentration,[20] but much larger than the values reported from bulk amorphous silicon (~200–400 μs for LPCVD *a*-Si:O,H).[21]

In the concentration quenching effect,[22] an excited Er^{3+} ion transfers its energy resonantly to unexcited Er^{3+} ions, the energy migration being favoured for smaller Er–Er

†This function is purely phenomenological, chosen simply because it provides a means of quantifying the value to which τ_{1535} is saturating.

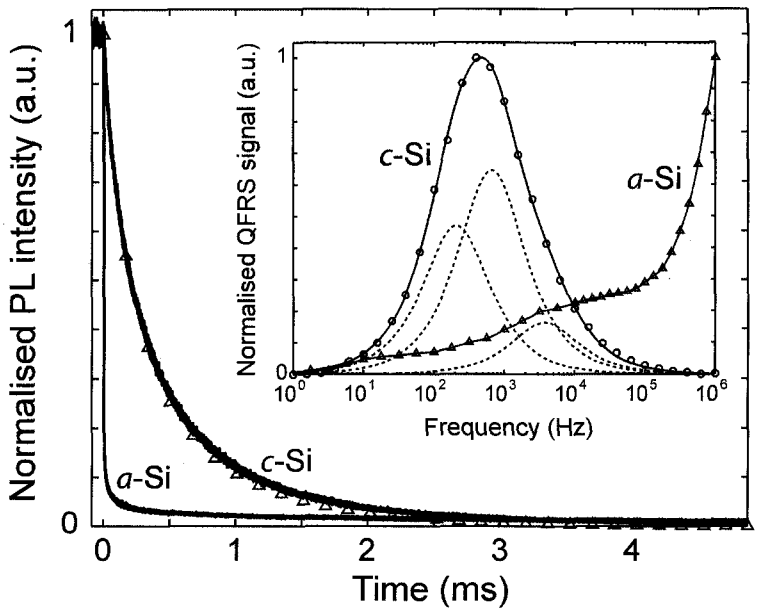

Fig. 7.3: Time-resolved PL spectra of the visible-NIR emission from amorphous and crystalline Si-NC films, with 514 nm and 476 nm excitation, respectively. A fit to the c-Si-NC decay using values for lifetimes obtained via QFRS is shown in open triangles. **Inset:** QFRS spectra of c-Si-NC (open circles) and a-Si-NC (open triangles) films. A fit of the c-Si-NC spectrum to three single exponential QFRS peaks is shown as a solid line, with the individual peaks shown shown as dotted lines. The line through the a-Si-NC data is a guide to the eye.

distances (higher concentrations), until a quenching centre such as a hydroxyl group[23] is encountered. This energy migration increases the total decay rate as the Er concentration is increased. We can see evidence for concentration quenching in the smaller saturation values for $\tau_{1535_{rad}}$ as the Er concentration is increased (refer to the 0.22 and 0.59 at.% Er curves in the inset to Fig. 7.2). Therefore, in this model, since concentration quenching processes have been neglected, specimen ST5 will be used for the remainder of the analysis, since its low level of Er doping should result in a fairly accurate description by Eqs. (7.3).

7.3.2 Determining w_{ba}: undoped a-Si-NC PL

If the "strong coupling" model[24] for the Si-NC–Er^{3+} energy transfer is strictly valid, the only measurable Si-NC PL would originate from nanoclusters which are isolated from the erbium ions; as such, one could use the dynamics of the ~700 nm PL band from a lightly-doped Si-NC:Er film to extract values for w_{ba}, the intrinsic a-Si-NC recombination rate. However, the transfer rate is much more likely to be a strong function of nanocluster–Er distance, of which there is necessarily a distribution. For instance, as explained in §1.3.2, $w_{b1} \propto r_{ij}^{-S}$ for electric multipole interactions, in which $S = 2$ for dipole–dipole (Förster) interactions,[25] $S = 8$ for dipole–quadrupole interactions and $S = 10$ for quadrupole–quadrupole interactions,[26] and $w_{b1} \propto e^{-r_{ij}/r_c}$ for exchange (Dexter) transfer.[26] To avoid such complications, an undoped a-Si-NC film will be used in the investigation of the distribution in w_{ba}.

If the two-level assumption is valid to describe the PL from a thin-film specimen typically containing ~10^{13} NCs in the excitation volume, the decay should be single exponential, with intensity varying as $I(t) = I_0 e^{-w_{ba}t}$ from the time when the excitation is switched off (see Appendix A.2.1). This assumption may be tested using time- and frequency-resolved measurements.

Fig. 7.3 compares the dynamics of PL from films containing a- and c-Si NCs via standard time-resolved PL decays from steady state as well as frequency-resolved spectra (inset). From the time-resolved data, it is clear that the PL from the a-Si-NC films is strongly non-exponential; while less obvious to the eye, the emission from the c-Si NCs is also not

well-described by a single exponential. Given the aforementioned difficulty in discriminating between the validity of bi- tri- or stretched-exponential fits from time-resolved data, however, it is useful to compare the response of the films in the frequency domain.

Quadrature frequency-resolved spectroscopy (QFRS) is a method which can be used to extract information about the distribution of PL lifetime components in a material, and is described in detail in Appendix B.2. Briefly, in QFRS, the excitation consists of both DC and sinusoidally-modulated components, the frequency of which, ω, is scanned over several decades. The resultant PL is recorded in terms of its amplitude and phase with respect to the excitation signal, and may then be fit by a number of single-exponential QFRS peaks, $S(\omega;\tau)$, given by Eq. (B.21).

The inset to Fig. 7.3 shows QFRS spectra for undoped crystalline and amorphous Si-NC films, corresponding to excitation rates of $\sigma\Phi \approx 50$ and 30 s^{-1}, respectively. The c-Si-NC spectrum fits well to a sum of three $S(\omega;\tau)$ peaks (lifetimes of 42.2 μs, 242.8 μs, and 763.1 μs, with relative weights of 0.127, 0.505, and 0.367, respectively); applying these lifetimes to the associated time-resolved PL decay data results in a fit with $R^2 = 0.997$. As the same fit parameter values (τ_i and weights) are returned for a wide range of initial guesses in the nonlinear least-squares fit, it is reasonable to have confidence in their uniqueness. The QFRS spectrum of the a-Si-NC specimen, however, is very broad, tending toward a high-frequency peak beyond the ~1-MHz detection limit of our system, as expected from the associated time-resolved behaviour shown in Fig. 7.3. For the frequency range given, a successful fit of the QFRS data well to three or four $S(\omega;\tau)$ peaks was not achieved, though this is most likely because we only have data for the low-frequency side of the main peak. Thus, although a quantitative analysis of the lifetime distribution of a-Si-NC samples is not possible from these data, it is evident that a wide distribution of lifetimes exists in both the crystalline and amorphous NC emission, suggesting that an accurate description of the Si-NC-Er system should include several lifetime components.

For the purposes of the a-Si-Nc–Er^{3+} rate equation model, however, if one is primarily interested in obtaining the energy transfer rate w_{b1}, so long as the population of the undoped nanocluster level N_b may be phenomenologically described by some weighted sum of exponentials with weights c_i and recombination rates w_{ba_i}, the response of the Er^{3+} may be modelled by appropriately-weighted sums of Eqs. (7.3b) and (7.3b) for the 1535- and 980-nm PL, respectively.

As such, if one does not wish to draw any conclusions with respect to the underlying physical processes governing the a-Si-NC PL, one is free to choose the number of recombination rates w_{ba_i} to include in the description. Since a tri-exponential fit provides three widely-spaced values for w_{ba_i} and fits the experimental data reasonably well ($R^2 \approx 0.92$; cf. $R^2 \approx 0.75$ for a bi-exponential), while the addition of a fourth exponential function only provides a marginal improvement in the goodness of fit ($R^2 \approx 0.98$), a tri-exponential function will be used here.

Time-resolved PL from a thick (>1 μm) SiO film annealed at 500 °C in forming gas was collected for 476-nm square-wave excitation in the small excitation regime (as determined in §7.3.1). Given the low repetition rate of 9.5 Hz, decay is essentially from steady-state values. Four such decays were fit to tri-exponentials; the results are summarised in Table 7.2. For comparison, values for τ and β for stretched exponential fits of the data are also given. Note that if one is only interested in providing a *description* of the dynamics of the a-Si-NC PL in terms of sums of exponentials, for use in the NC–Er coupled system model, it is of no consequence that the "best-fit" parameters for the tri-exponential are not unique:[18] as far as the Er^{3+} ions are concerned, their excitation source will be described accurately.

Table 7.2: Tri- and stretched-exponential fitting parameters for a-Si-NC PL. The measurements yielded steady-state PL values which are linear with Φ, confirming that pumping is still in the small excitation regime. The R^2 values are used as the weights for the averaging shown in the last column.

Φ ($\times 10^{16}$ cm^{-2}s^{-1})		1.3	3.2	6.2	9.7	Weighted average
Tri-exponential	c_1	0.846	0.849	0.848	0.851	0.848
	c_2	0.103	0.101	0.848	0.103	0.102
	c_3	0.052	0.050	0.049	0.046	0.049
	τ_1	0.190 μs	0.183 μs	0.218 μs	0.197 μs	0.197 μs
	τ_2	0.132 ms	0.133 ms	0.135 ms	0.131 ms	0.133 ms
	τ_3	8.30 ms	8.39 ms	8.17 ms	7.95 ms	8.20 ms
	R^2	0.853	0.919	0.943	0.950	
Stretched exponential	τ	31.1 ns	26.0 ns	29.5 ns	27.6 ns	28.5 ns
	β	0.108	0.107	0.109	0.110	0.109
	R^2	0.972	0.989	0.994	0.996	

7.3.3 The futility of fitting: properties of Eqs. (7.3)

It may seem that, having determined values for w_{ba} and w_{21}, it will now be possible to begin fitting experimental ${}^4I_{13/2} \rightarrow {}^4I_{15/2}$ and ${}^4I_{11/2} \rightarrow {}^4I_{15/2}$ decay data using Eqns. (7.3b) and (7.3c). As a first approximation, one might choose only the fast component of the a-Si NC decay (viz., τ_1 in Table 7.2), and let $w_{43} \rightarrow \infty$, as it is expected that the non-radiative transition from $4 \rightarrow 3$ is very fast.[7] The equations to be fit would be of the form $I_j(t) = a'_{j1} w_{j1} N_j(t)$, where j is 2 or 3 and a'_{j1} is a constant describing the collection efficiency of the PL from the $j \rightarrow 1$ transition. Since a'_{j1} is unknown, and must be left as a free parameter during the fit, there is nothing to be gained by having w_{j1} as part of the proportionality constant; thus, we may simply fit to $I_j(t) = a_{j1} N_j(t)$, where $a_{j1} = a'_{j1} w_{j1}$. As such, for a given fit, no information is lost by normalising the decay to unity at $t = 0$.

However, there now enters a subtlety with respect to the form of Eqns. (7.3b) and (7.3c) which essentially precludes the extraction of a meaningful value of w_{b1} from a fit to these equations. Let us consider typical values for the various rates in the system: $w_{21} \approx 263\ \text{s}^{-1}$ (§7.3.1), $w_{ba} \approx 5 \times 10^6\ \text{s}^{-1}$ (§7.3.2), and $w_{43} \approx 10^7\ \text{s}^{-1}$, $w_{32} \approx 4.2 \times 10^5\ \text{s}^{-1}$, and $w_{31} \approx 1400\ \text{s}^{-1}$ (from Ref.[7]). In the event that a fit does not yield a unique value for w_{b1}, one might hope at least to establish lower and upper limits for this rate. To this end, Eqs. (7.3b) and (7.3c) will now be considered, decaying from steady state, and normalised to unity at $t = 0$ (i.e., dividing by η_j for $t_{off} \rightarrow \infty$), for the extreme cases of $w_{b1} \rightarrow 0$ and $w_{b1} \rightarrow \infty$. The following expressions are obtained:

$$
\begin{aligned}
N_2(t)\Big|_{w_{b1}\rightarrow 0} = {} & \frac{w_{43}(w_{31}+w_{32})w_{ba}}{(w_{31}+w_{32}-w_{21})(w_{ba}-w_{21})(w_{43}-w_{21})} e^{-w_{21}t} \\
& + \frac{w_{21}w_{43}w_{ba}}{(w_{31}+w_{32}-w_{21})(w_{ba}-w_{31}-w_{32})(w_{31}+w_{32}-w_{43})} e^{-(w_{31}+w_{32})t} \\
& + \frac{(w_{31}+w_{32})w_{21}w_{ba}}{(w_{43}-w_{21})(w_{43}-w_{31}-w_{32})(w_{ba}-w_{43})} e^{-w_{43}t} \\
& + \frac{w_{43}w_{21}(w_{31}+w_{32})}{(w_{ba}-w_{31}-w_{32})(w_{ba}-w_{43})(w_{21}-w_{ba})} e^{-w_{ba}t} \qquad (7.5a)
\end{aligned}
$$

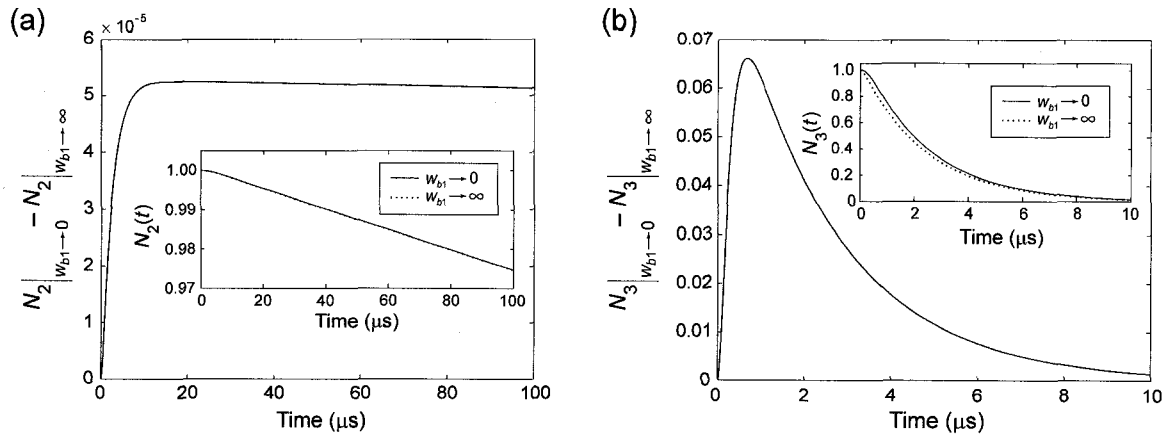

Fig. 7.4: Decay curves for $N_2(t)$ and $N_3(t)$ in the limits of $w_{b1} \to 0$ and $w_{b1} \to \infty$ are shown in the insets of (a) and (b), respectively, using typical values for the other rates as indicated in the text. The difference between the $w_{b1} \to 0$ and $w_{b1} \to \infty$ cases are shown in the main figures.

$$N_2(t)\Big|_{w_{b1}\to\infty} = \frac{w_{43}(w_{31}+w_{32})}{(w_{31}+w_{32}-w_{21})(w_{43}-w_{21})}e^{-w_{21}t} + \frac{w_{21}w_{43}}{(w_{31}+w_{32}-w_{21})(w_{31}+w_{32}-w_{43})}e^{-(w_{31}+w_{32})t} + \frac{(w_{31}+w_{32})w_{21}}{(w_{43}-w_{21})(w_{43}-w_{31}-w_{32})}e^{-w_{43}t} \tag{7.5b}$$

and

$$N_3(t)\Big|_{w_{b1}\to 0} = \frac{w_{43}w_{ba}}{(w_{43}-w_{31}-w_{32})(w_{ba}-w_{31}-w_{32})}e^{-(w_{31}+w_{32})t} + \frac{w_{ba}(w_{31}+w_{32})}{(w_{ba}-w_{43})(w_{31}+w_{32}-w_{43})}e^{-w_{43}t} + \frac{w_{43}(w_{31}+w_{32})}{(w_{ba}-w_{43})(w_{ba}-w_{31}-w_{32})}e^{-w_{ba}t} \tag{7.6a}$$

$$N_3(t)\Big|_{w_{b1}\to\infty} = \frac{w_{43}}{w_{43}-w_{31}-w_{32}}e^{-(w_{31}+w_{32})t} + \frac{w_{31}+w_{32}}{w_{31}+w_{32}-w_{43}}e^{-w_{43}t} \tag{7.6b}$$

These four equations should therefore comprise the most widely-differing behaviour of Eqs. (7.3b) and (7.3c) with respect to w_{b1}; they are plotted in the insets to Fig. 7.4. Also shown are the difference between Eqs. (7.5a) and (7.5b) (Fig. 7.4a), and between Eqs. (7.6a) and (7.6b) (Fig. 7.4b), which indicate the magnitude and position in time in which the largest difference in decays occurs due to the largest possible variation in w_{b1}. For the typical values for the rates used in this analysis, the maximum difference is less than 10^{-4} for the 1535-nm PL and less than 0.07 for the 980-nm PL. Given that the noise level for the normalised experimental ${}^4I_{13/2} \to {}^4I_{15/2}$ and ${}^4I_{11/2} \to {}^4I_{15/2}$ decay curves is ~0.01 and ~0.04, respectively, it is a practical impossibility even to bracket w_{b1} within any reasonable limits using this technique, let alone obtain a meaningful value in which one may have confidence.

The situation is not improved significantly even if time-resolved PL data from both the 1535-nm and 980-nm bands are fit simultaneously, since both Eqs. (7.3b) and (7.3c) suffer from the same weak dependence on w_{b1}. To determine a value for w_{b1} from an analysis of the Er^{3+} PL, one is therefore obliged to consider the system's response to another experimental parameter: the temperature.

7.3.4 Temperature dependence of a-Si-NC and Er^{3+} PL

Thus far in this chapter, we have considered the recombination of electron-hole pairs in the a-Si NCs to be characterised by a single rate w_{ba}. However, there are in fact two contributions to the recombination rate: a radiative component, w_{ba_r}, and a non-radiative component, $w_{ba_{nr}}$, such that $w_{ba} = w_{ba_r} + w_{ba_{nr}}$. In bulk amorphous hydrogenated Si (a-Si:H), the weak band tail recombination probability yields an average radiative rate of $w_{ba_r} \approx 10^3\ s^{-1}$, which is much smaller than the phonon-assisted non-radiative recombination rate at a defect, $w_{ba_{nr}} \approx 10^{13}\ s^{-1}$.[27] In the a-Si-NC specimens considered here, however, the fast component of the PL decay is on the order of $10^6\ s^{-1}$.[28] Thermal quenching of luminescence in a-Si is generally explained by the competition between these radiative and non-radiative recombination rates, such that as the temperature increases, increased carrier mobility allows more defects to become accessible, increasing $w_{ba_{nr}}$, and decreasing the luminescence quantum efficiency, y_L.[27] In terms of the recombination rates, the quantum efficiency, which is proportional to the PL intensity, is defined as

$$y_L = \frac{w_{ba_r}}{w_{ba_r} + w_{ba_{nr}}} \tag{7.7}$$

The emission from films containing a-Si NCs is strikingly different than that from bulk a-Si:H, as illustrated in Fig. 7.5. In bulk a-Si:H, the luminescence nominally has a distribution in lifetimes extending from $\sim 10^{-7}$ to $\sim 10^{-2}$ s, decaying quickly to 90% of its initial value in a few μs, and somewhat more slowly thereafter, decreasing by a factor of 10^3 less than its initial value by $\sim$140 μs (values taken from Ref.[29], for a specimen at 81 K). In contrast, a-Si-NC emission, while still exhibiting a fast initial decay, only drops by a factor of $\sim$2–4 before decaying much more slowly, such that a significant fraction of the PL exists even after 10 ms (specimen at 77 K). The slow component is non-exponential, and may be fit by stretched exponential[30] or Becquerel[31] decay functions, characteristic of systems possessing a wide distribution in recombination rates; in the case of a-Si, this distribution may be explained by a distribution in the distance separating the sites where electrons and holes are localised (see Eq. (8.34) in Ref.[27]). However, it is difficult to reconcile the behaviour of the a-Si NC emission as seen in Fig. 7.5 by this single mechanism, given the sharpness of the divide between fast and slow (stretched) components. As explained below, it is suggested that this behaviour may be explained by a twofold origin of the luminescence: from NCs containing non-radiative defects, and from defect-free NCs.

Consider an ensemble of a-Si NCs, of total number $\mathcal{N}$. Of these $\mathcal{N}$ NCs, assume that $\mathcal{N}_{df}$ of them to not contain any accessible non-radiative defects, and that the remainder, $\mathcal{N}_d = \mathcal{N} - \mathcal{N}_{df}$, do. It should be noted that $\mathcal{N}_{df}$ and $\mathcal{N}_d$ may be functions of temperature: the increase in number of accessible defects with temperature could increase $\mathcal{N}_d$ and decrease $\mathcal{N}_{df}$. Neglecting tunnelling between NCs, at steady state, the PL intensity will therefore be comprised of a component from the defect-free NCs (weighted by $\mathcal{N}_{df}$), with near-unity quantum efficiency and a distribution in w_{ba_r}, yielding stretched decay, and a component from NCs containing accessible defects (weighted by $\mathcal{N}_d$), with quantum efficiency given by Eq. (7.7) and a recombination rate of $w_{ba_{nr}} + w_{ba_r} \approx w_{ba_{nr}}$.

It is vital to note that the proportion of the steady-state PL originating from the fast process is *not* necessarily many times greater than that of the slow process, as may be intuitively thought by analogy to the explanation of blueshift with increasing PL intensity for ensembles of Si nanocrystals (see §2.4.1). We may see this by considering the solution to the two-level NC model, described in detail in §A.2.1. For square-wave excitation, the

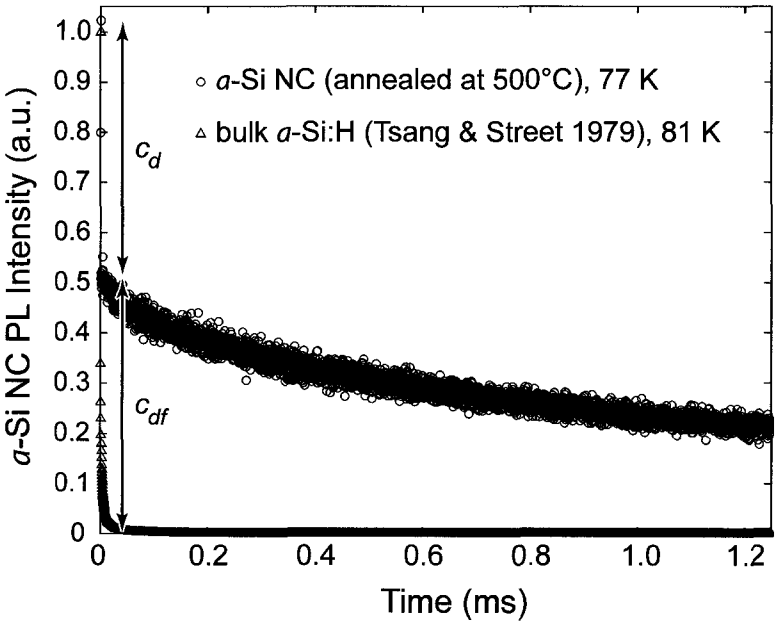

Fig. 7.5: Comparison of PL decay from a-Si in bulk and nanocluster form. The bulk data has been extracted from Ref.[29].

solution to level b is

$$N_b(t) = \begin{cases} \frac{R\mathcal{N}}{w_{ba_{nr}}+w_{ba_r}+R}\left[1 - e^{-(w_{ba_{nr}}+w_{ba_r}+R)t}\right] & \text{for } 0 \leq t < t_{off} \\ \eta_b\, e^{-(w_{ba_{nr}}+w_{ba_r})(t-t_{off})} & \text{for } t \geq t_{off} \end{cases} \tag{7.8}$$

where $R = \sigma\Phi$ is the pumping rate, $\mathcal{N}$ is the total concentration of particles described by the two-level model and $\eta_b = N_b(t_{off})$. From Eq. (7.8), $t < t_{off}$, we see that the steady state intensity is proportional to $Rw_{ba_r}/(w_{ba_{nr}} + w_{ba_r} + R)$. The usual explanation for explaining the blueshift with increased pumping power notes that the luminescence at shorter wavelengths have higher recombination rates than those at longer wavelengths (cf. §2.4.1). As such, for a given R, the contribution to the steady-state intensity from a blue-emitting NC will be greater than that from a red-emitting NC, and as R increases, the fractional increase in the denominator will be less for the blue-emitting NC, blueshifting the PL. However, this argument hinges on the fact that the two processes have different *radiative* rates. If we now consider the combined emission from a NC containing a defect and one containing none, since w_{ba_r} is the same for both clusters and $w_{ba_{nr}} \gg w_{ba_r}$, we see that the contribution from the NC with the defect is $\sim w_{ba_{nr}}/w_{ba_r}$ times *smaller* than that from the defect-free NC.

For a PL decay at a given temperature T, we denote the contribution to the steady-state intensity I_{ss} from the $\mathcal{N}_{df}$ defect-free NCs as c_{df}, and that of the $\mathcal{N}_d$ NCs containing defects as c_d, as shown in Fig. 7.5. In general, $c_i = c_i(T)$, as illustrated by Fig. 7.6. The total steady-state intensity is therefore

$$\begin{aligned} I_{ss} &\propto w_{ba_r}\left[\frac{\mathcal{N}_d}{w_{ba_r}+w_{ba_{nr}}} + \frac{\mathcal{N}_{df}}{w_{ba_r}}\right] \\ &\propto \frac{\mathcal{N}_d w_{ba_r}}{w_{ba_r}+w_{ba_{nr}}} + \mathcal{N}_{df} \\ &\propto c_d + c_{df} \end{aligned} \tag{7.9}$$

Thus, we have

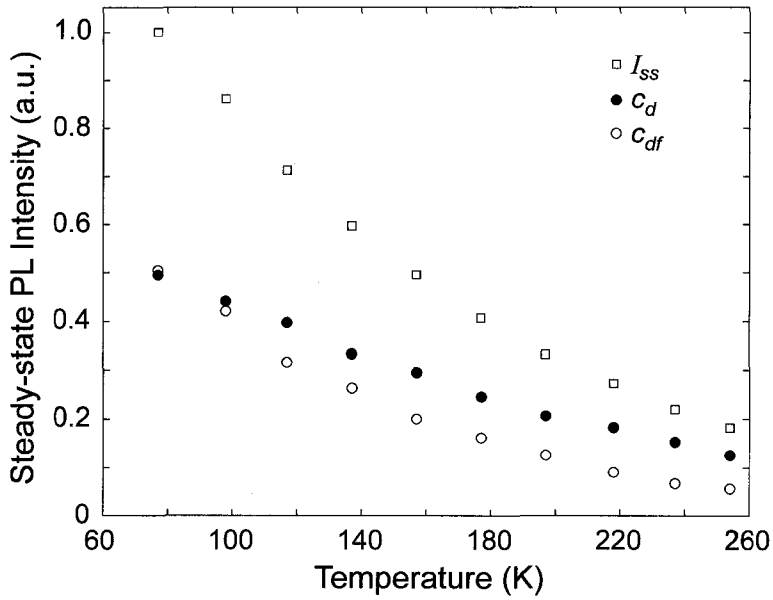

Fig. 7.6: Values for the total steady-state PL intensity (I_{ss}) from a 500-°C-annealed a-Si NC sample vs. temperature, as well as the contributions from NCs which contain defects (c_d), and those which are defect-free (c_{df}). Since the fast component of the decay takes place over the first three data points, c_{df} was determined by averaging data points 3 to 10.

$$\frac{\mathcal{N}_d}{\mathcal{N}_{df}}\frac{w_{ba_r}}{w_{ba_r}+w_{ba_{nr}}} = \frac{c_d}{c_{df}}$$

$$\mathcal{N}_{df} = \frac{\mathcal{N}_d w_{ba_r}}{w_{ba_r}+w_{ba_{nr}}}\frac{c_{df}}{c_d}$$

$$\mathcal{N}_{df} = \frac{(\mathcal{N}-\mathcal{N}_{df})w_{ba_r}}{w_{ba_r}+w_{ba_{nr}}}\frac{c_{df}}{c_d} \tag{7.10}$$

yielding

$$\mathcal{N}_{df} = \frac{1}{1+\frac{c_d}{c_{df}}\frac{w_{ba_r}+w_{ba_{nr}}}{w_{ba_r}}}\mathcal{N} \tag{7.11}$$

$$\mathcal{N}_d = \frac{1}{1+\frac{c_{df}}{c_d}\frac{w_{ba_r}}{w_{ba_r}+w_{ba_{nr}}}}\mathcal{N} \tag{7.12}$$

(7.13)

Since $w_{ba_r} \ll w_{ba_{nr}}$, one may see that $\mathcal{N}_d \approx \mathcal{N}$ and $\mathcal{N}_{df} \approx \frac{c_{df}}{c_d}\frac{w_{ba_r}}{w_{ba_r}+w_{ba_{nr}}}\mathcal{N}$. Using the value for NC density of $\sim 10^{19}$ cm^{-3} obtained via TEM and EELS measurements and typical values for w_{ba_r} and $w_{ba_{nr}}$ of 10^3 and 10^6 s^{-1}, respectively, $\mathcal{N}_{df}$ is plotted as a function of temperature in Fig. 7.7a.

Given a non-radiative defect density of $N_{\rm nr}$, the probability that there are *no* accessible defects in a volume V is given by the expression[32] $P = e^{-V_c N_{\rm nr} - A_c N_{\rm snr}}$. Thus, the number of particles in the ensemble which are defect-free is given by $\mathcal{N}_{df} = P\mathcal{N}$. If it is assumed, as in §6.2.3, that $N_{\rm snr}$ varies as $N_{\rm nr}^{2/3}$, then, using the previous approximation for $\mathcal{N}_{df}$, the result is

$$V_c N_{\rm nr} + A_c N_{{\rm snr}_0}\left(\frac{N_{\rm nr}}{N_{{\rm nr}_0}}\right)^{\frac{2}{3}} \approx \ln\left[\frac{w_{ba_r}}{w_{ba_r}+w_{ba_{nr}}}\frac{c_{df}}{c_d}\right] \tag{7.14}$$

Using the 77-K value of $\frac{c_{df}}{c_d} \approx 1$, the typical values for w_{ba_r} and $w_{ba_{nr}}$ of 10^3 and 10^6 s^{-1}, respectively, an average nanocluster volume for a 500-°C-annealed a-Si NC specimen of $\sim 1.6\times10^{-20}$ cm^3, for V_c, and the corresponding surface area for such an NC

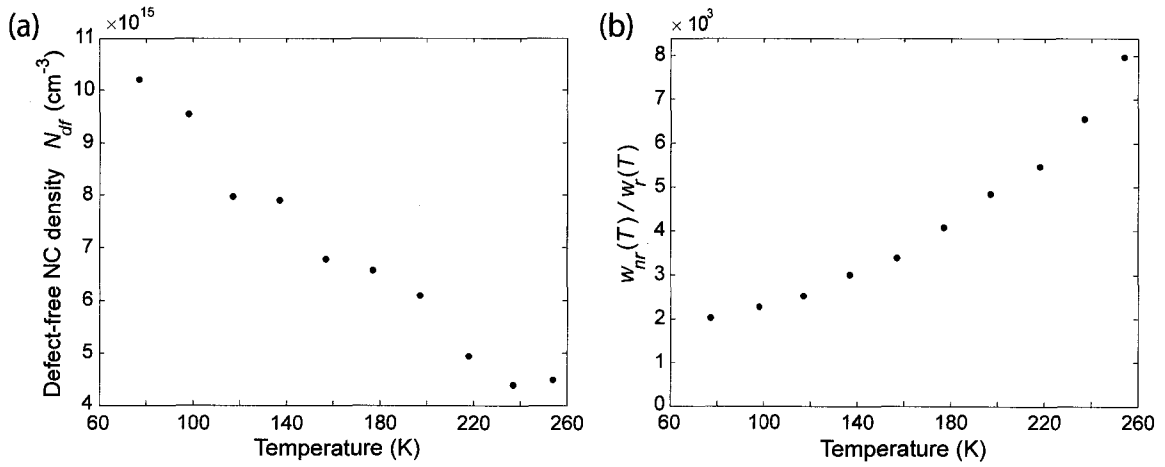

Fig. 7.7: (a) Defect-free NC density, $\mathcal{N}_{df}$, as a function of temperature, using $\mathcal{N} = 10^{19}$ cm^{-3}, $w_{ba_r} = 10^3$ s^{-1} and $w_{ba_{nr}} 10^6$ s^{-1}. (b) Behaviour of the ratio of non-radiative to radiative recombination rates, as a function of temperature. Since $w_{ba_{nr}}/w_{ba_r} \approx 10^3$, $q'\mathcal{N}$ was set to this value.

(i.e., $A_c = 4\pi\left(\frac{3}{4\pi}V_c\right)^{\frac{2}{3}}$), we obtain $N_{\rm nr} \approx 3.1 \times 10^{19}$ cm^{-3}. This is somewhat larger than the characteristic defect densities in bulk a-Si:H prepared by glow discharge of silane, typically in the 10^{15}–10^{18} cm^{-3} range,[27] although it is conceivable that since the specimens considered in this chapter were prepared via thermal evaporation of SiO onto a room-temperature substrate, a higher defect concentration may be possible. It is also suggestive to note that this value of $N_{\rm nr}$ agrees reasonably well (within a factor of ~7) with the non-radiative defect density yielded by the simulated fit to the PL quenching behaviour shown in §6.2.3.

Using the expressions (7.11) and (7.12) for $\mathcal{N}_{df}$ and $\mathcal{N}_d$ and Eq. (7.9), I_{ss} may be rewritten as

$$I_{ss} = q'\mathcal{N}\left[\frac{1}{1+\frac{c_{df}}{c_d}\frac{w_{ba_r}}{w_{ba_r}+w_{ba_{nr}}}}\frac{w_{ba_r}}{w_{ba_r}+w_{ba_{nr}}} + \frac{1}{1+\frac{c_d}{c_{df}}\frac{w_{ba_r}+w_{ba_{nr}}}{w_{ba_r}}}\right]$$

$$I_{ss} = \frac{q'\mathcal{N}}{1+\frac{c_d}{c_d+c_{df}}\frac{w_{ba_{nr}}}{w_{ba_r}}} = \frac{q'\mathcal{N}}{1+\frac{c_d}{I_{ss}}\frac{w_{ba_{nr}}}{w_{ba_r}}}$$

$$I_{ss}(T) = q'\mathcal{N} - c_d(T)\frac{w_{ba_{nr}}(T)}{w_{ba_r}(T)} \tag{7.15}$$

Thus,

$$\frac{w_{ba_{nr}}(T)}{w_{ba_r}(T)} = \frac{q'\mathcal{N} - I_{ss}(T)}{c_d(T)} \approx \frac{q'\mathcal{N}}{c_d(T)} \tag{7.16}$$

Although the exact behaviour of $w_{ba_r}(T)$ and $w_{ba_{nr}}(T)$ is not known, the ratio should be on the order of 10^3 for the specimens considered here; setting $q'\mathcal{N}$ to this value therefore allows the variation of $\frac{w_{ba_{nr}}}{w_{ba_r}}$ with T to be seen qualitatively (Fig. 7.7b).

Turning now to the case of the Er-doped films, Fig. 7.8 compares the temperature dependence of the 1535-nm Er^{3+} emission from specimen ST5 and an a-Si-NC specimen (as in Fig. 7.6), both annealed at 500 °C; the Er^{3+} PL was collected through a 1550-nm BPF via optical fibre, and measured with a cooled InGaAs photodiode. Note the surprising *increase* in the Er^{3+} PL with temperature; this result was reproduced several times with

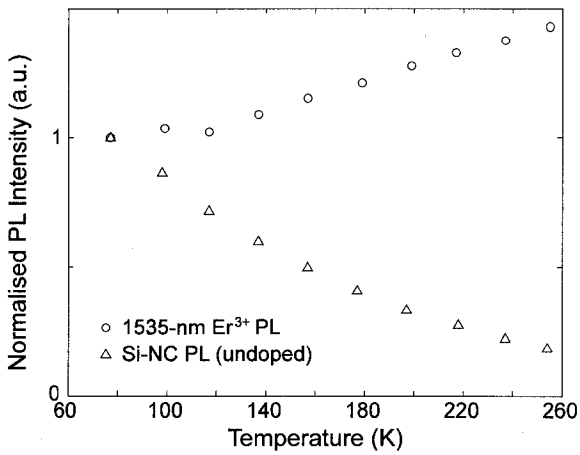

Fig. 7.8: Comparison of steady-state PL intensity vs. temperature for an a-Si-NC film and specimen ST5, both annealed at 500 °C. The Er^{3+} PL was measured with a cooled InGaAs photodiode, through a 1550-nm BPF.

different measurement techniques and using specimens with different [Er]. This behaviour is, however, unusual: Er^{3+} luminescence from a-Si NCs in silicon nitride films has been previously reported as exhibiting weak (factor of ~2) *quenching* with temperature.[33] The repeatability of the measurement, however, suggests that the results shown in Fig. 7.8 are not simply experimental artifacts.

The steady-state ${}^4I_{13/2} \rightarrow {}^4I_{15/2}$ intensity (proportional to N_2) could be written by analogy to Eq. (7.9) in the form

$$I_{ss_2} \propto w_{b1} \left[\frac{\mathcal{N}_d}{w_{ba_r} + w_{ba_{nr}} + w_{b1}} + \frac{\mathcal{N}_{df}}{w_{ba_r} + w_{b1}} \right] \tag{7.17}$$

If it is assumed that the behaviour of $\frac{w_{ba_{nr}}}{w_{ba_r}}$ is primarily determined by changes in $w_{ba_{nr}}$, as one would expect from the aforementioned interpretation of increased diffusion of carriers for higher temperatures, and furthermore, that w_{ba_r} is fairly constant in this temperature range, then an increase in $I_{ss_2}(T)$ with increasing T would have to be the result of a temperature dependence of w_{b1}. In particular, it is required that $w_{b1}(T)$ increases sufficiently quickly with increasing T to overcome the increase in $w_{ba_{nr}}$. A process whose probability increases with temperatures is *phonon-assisted* energy transfer (see §1.3.2). The phonon-assisted transfer rate for a N-photon process can be written in the form[34]

$$w_{b1}(T) = w_{b1}(0) \left[1 - \exp\left(\frac{-\hbar\omega}{k_B T} \right) \right]^{-N} \tag{7.18}$$

where $\hbar\omega$ is the energy of the dominant phonon contributing to the transfer. Since there is good overlap between the a-Si PL spectrum and the ${}^4I_{15/2} \rightarrow {}^4I_{9/2}$ absorption transition, it is reasonable to assume that a $N = 1$ process dominates. Unfortunately, a simple substitution of Eq. (7.18) into Eq. (7.17) was unable to yield results which matched the observed Er^{3+} PL temperature dependence for reasonable values of $w_{b1}(0)$ and $\hbar\omega$. A more sophisticated treatment of phonon-assisted energy transfer, perhaps including higher-order multiphonon processes to several different Er^{3+} levels, would almost certainly be a fruitful future line of inquiry.

7.4 Conclusions

In this chapter, the luminescence from Er-doped a-Si-NC films via a phenomenological rate equation model was investigated. In particular, to avoid complications due to cooperative

effects, the situation was considered in which optical pumping is such that it is a good approximation to treat the ground-state populations of the NCs and Er^{3+} as constant (small excitation regime); this model assumes an effective two-level NC and a four-level Er^{3+} ion. In this regime, the rate equations may be solved analytically, providing a particularly lucid portrayal of the behaviour of the PL dynamics on the various system parameters. However, experimental time-resolved PL measurements of undoped a-Si-NC films show clear non-exponential behaviour, challenging the "two-level nanocluster" assumption widely used in rate modelling for this system. The temperature dependence of the ratio of fast and slow (stretched exponential) components of the undoped a-Si NC PL suggests that the origin of the slow component is from NCs which do not contain any non-radiative defects; the estimated volume defect density agrees reasonably well with the estimate in the previous chapter from luminescence quenching simulations. For Er-doped films, however, a measurement of the temperature dependence of the steady-state $^4I_{13/2} \rightarrow ^4I_{15/2}$ transition yielded the surprising behaviour of *increasing* with increasing temperature. While a qualitative fit to this data was not achieved, a possible mechanism for this phenomenon could be phonon-assisted energy transfer from the NCs to the Er^{3+} ions, the transfer probability for which, as required, increases concomitantly with temperature. Although the possibility of modelling a-Si-NC–Er films is perhaps not so bleak as stated by Albert Polman, it must be conceded that the complexity of the system does present a considerable obstacle to achieving a confident, quantitative interpretation of experimental photoluminescence results.

Bibliography

[1] G. Franzò, V. Vinciguerra, and F. Priolo, "Room-temperature luminescence from rare-earth ions implanted into Si nanocrystals", *Philos. Mag. B*, vol. 80, no. 4, pp. 719–728, 2000.

[2] G. Franzò, V. Vinciguerra, and F. Priolo, "The excitation mechanism of rare-earth ions in silicon nanocrystals", *Appl. Phys. A*, vol. 69, no. 1, pp. 3–12, 1999.

[3] A. Meldrum, A. Hryciw, A. N. MacDonald, C. Blois, T. Clement, R. DeCorby, J. Wang, and Quan Li, "Interaction between rare-earth ions and amorphous silicon nanoclusters produced at low processing temperatures", *J. Luminesc.*, vol. 121, pp. 199–203, 2006.

[4] P. G. Kik and A. Polman, "Gain limiting processes in Er-doped Si nanocrystal waveguides in SiO_2", *J. Appl. Phys.*, vol. 91, no. 1, pp. 534–536, 2002.

[5] J. Lee, J. H. Shin, and N. Park, "Optical gain at 1.5 μm in nanocrystal Si-sensitized Er-doped silica waveguide using top-pumping 470 nm LEDs", *J. Lightwave Tech.*, vol. 23, no. 1, pp. 19–25, 2005.

[6] J.H. Shin, H.-S. Han, and S.-Y. Seo, "Optical gain using nanocrystal sensitized erbium", in *Towards the first silicon laser*, L. Pavesi, S. Gaponenko, and L. Dal Negro, Eds., vol. 93 of *NATO Science Series II*, pp. 401–420. Kluwer Academic Publishers, Norwell, Massachusetts, 2003, ISBN: 1-402-01193-8.

[7] D. Pacifici, G. Franzò, F. Priolo, F. Iacona, and L. Dal Negro, "Modeling and perspectives of the Si nanocrystals–Er interaction for optical amplification", *Phys. Rev. B*, vol. 67, no. 24, Art. no. 245301, 2003.

[8] W. H. Loh and A. J. Kenyon, "Excited state absorption in the Si nanocluster-Er material system", *IEEE Phot. Tech. Lett.*, vol. 18, no. 1, pp. 289–291.

[9] M. J. A. de Dood, J. Knoester, A. Tip, and A. Polman, "Förster transfer and the local optical density of states in erbium-doped silica", *Phys. Rev. B*, vol. 71, no. 11, Art. no. 115102, 2005.

[10] J. Linnros, N. Lalic, A. Galeckas, and V. Grivickas, "Analysis of the stretched exponential photoluminescence decay from nanometer-sized silicon crystals in SiO_2", *J. Appl. Phys.*, vol. 86, no. 11, pp. 6128–6134, 1999.

[11] M. Dovrat, Y. Goshen, J. Jedrzejewski, I. Balberg, and A. Sa'ar, "Radiative versus nonradiative decay processes in silicon nanocrystals probed by time-resolved photoluminescence spectroscopy", *Phys. Rev. B*, vol. 69, no. 15, Art. no. 155311, 2004.

[12] S. P. Withrow, C. W. White, A. Meldrum, J. D. Budai, D. M. Hembree, and J. C. Barbour, "Effects of hydrogen in the annealing environment on photoluminescence from Si nanoparticles in SiO_2", *J. Appl. Phys.*, vol. 86, no. 1, pp. 396–401, 1999.

[13] S. Cheylan and R. G. Elliman, "The effect of ion dose and annealing ambient on room temperature photoluminescence from Si nanocrystals in SiO_2", *Nucl. Instr. Meth. B*, vol. 148, no. 1–4, pp. 986–990, 1999.

[14] J. Wang, X.F. Wang, Q Li, A. Meldrum, and A. Hryciw, "The microstructure of SiO thin films: From nanoclusters to nanocrystals", *Philos. Mag.*, vol. 87, no. 1, pp. 11–27, 2007.

[15] A. Meldrum, A. Hryciw, A. N. MacDonald, C. Blois, K. Marsh, J. Wang, and Q. Li, "Photoluminescence in the silicon-oxygen system", *J. Vac. Sci. Tech. A*, vol. 24, no. 3, pp. 713–717, 2006.

[16] S. W. Roberts, G. J. Parker, and M. Hempstead, "The photoluminescence of erbium-doped silicon monoxide", *Opt. Mater.*, vol. 6, no. 1–2, pp. 99–102, 1996.

[17] M. Fujii, K. Imakita, K. Watanabe, and S. Hayashi, "Coexistence of two different energy transfer processes in SiO_2 films containing Si nanocrystals and Er", *J. Appl. Phys.*, vol. 95, no. 1, pp. 272–280, 2004.

[18] F. S. Acton, *Numerical methods that work*, Mathematical Association of America, Washington D.C., second edition, 1990.

[19] A. Polman, "Erbium implanted thin film photonic materials", *J. Appl. Phys.*, vol. 82, no. 1, pp. 1–39, 1997.

[20] E. Snoeks, G. N. van den Hoven, and A. Polman, "Optical doping of soda-lime silicate glass with erbium by ion implantation", *J. Appl. Phys.*, vol. 73, no. 12, pp. 8179–8183, 1993.

[21] G. N. van den Hoven, J. H. Shin, A. Polman, S. Lombardo, and S. U. Campisano, "Erbium in oxygen-doped silicon: Optical excitation", *J. Appl. Phys.*, vol. 78, no. 4, pp. 2642–2650, 1995.

[22] W. J. Miniscalco, "Erbium-doped glasses for fiber amplifiers at 1500 nm", *J. Lightwave Tech.*, vol. 9, no. 2, pp. 234–250, 1991.

[23] Y. C. Yan, A. J. Faber, and H. de Waal, "Luminescence quenching by OH groups in highly Er-doped phosphate glasses", *J. Non-Cryst. Sol.*, vol. 181, no. 3, pp. 283–290, 1995.

[24] P. G. Kik, M. L. Brongersma, and A. Polman, "Strong exciton-erbium coupling in Si nanocrystal-doped SiO_2", *Appl. Phys. Lett.*, vol. 76, no. 17, pp. 2325–2327, 2000.

[25] T. Förster, "10th Spiers Memorial Lecture: Transfer mechanisms of electronic excitation", *Discuss. Faraday Soc.*, vol. 27, no. 7, pp. 7–17, 1959.

[26] D. L. Dexter, "A theory of sensitized luminescence in solids", *J. Chem. Phys.*, vol. 21, no. 5, pp. 836–850, 1953.

[27] R. A. Street, *Hydrogenated amorphous silicon*, Cambridge University Press, Cambridge, 1991, ISBN: 0-521-37156-2.

[28] A. N. MacDonald, A. Hryciw, F. Lenz, and A. Meldrum, "Interaction between amorphous silicon nanoclusters and neodymium ions", *Appl. Phys. Lett.*, vol. 89, Art. no. 173132, 2006.

[29] C. Tsang and R. A. Street, "Recombination in plasma-deposited amorphous Si:H, Luminescence decay", *Phys. Rev. B*, vol. 19, no. 6, pp. 3027–3040, 1979.

[30] M. N. Berberan-Santos, E. N. Bodunov, and B. Valeur, "Mathematical functions for the analysis of luminescence decays with underlying distributions 1. Kohlrausch decay function (stretched exponential)", *Chem. Phys.*, vol. 315, no. 1–2, pp. 171–182, 2005.

[31] M. N. Berberan-Santos, E. N. Bodunov, and B. Valeur, "Mathematical functions for the analysis of luminescence decays with underlying distributions: 2. Becquerel (compressed hyperbola) and related decay functions", *Chem. Phys.*, vol. 317, no. 1, pp. 57–62, 2005.

[32] M. J. Estes and G. Moddel, "Luminescence from amorphous silicon nanostructures", *Phys. Rev. B*, vol. 54, no. 20, pp. 14633–14642, 1996.

[33] N. M. Park, T. Y. Kim, S. H. Kim, G. Y. Sung, K. S. Cho, J. H. Shin, B. H. Kim, S. J. Park, J. K. Lee, and M. Nastasi, "Luminescence of Er-doped amorphous silicon quantum dots", *Thin Solid Films*, vol. 475, no. 1–2, pp. 231–234, 2005.

[34] N. Yamada, S. Shionoya, and T. Kushida, "Phonon-assisted energy transfer between trivalent rare-earth ions", *J. Phys. Soc. Japan*, vol. 32, no. 6, pp. 1577–1586, 1972.

CHAPTER 8

Afterword: summary and future directions

The characterisation of new light-emitting materials is important for the continued development of the still-nascent field of integrated photonics. A silicon-based light emitter in particular would allow novel optoelectronic devices to take advantage of the mature state of IC processing technology, facilitating monolithic integration of photonic components with existing CMOS electrical architectures. Although bulk Si is a poor light emitter, being an indirect-gap semiconductor, nanoscale silicon can exhibit intense emission in the visible and near infrared. Comparable increases in the quantum efficiency of both amorphous and crystalline NCs have been observed, with several extant competing theories to explain the details of the emission mechanism. By doping such nanocomposite films with rare-earth elements, a non-radiative energy transfer can take place between the NCs and the RE ions. Of particular technological interest for communications is Er^{3+}, since its first-excited-state to ground-state transition corresponds to 1.5 μm, a wavelength within the so-called "third transparency window" for minimum attenuation in conventional silica optical fibres. This well-known sensitisation process can yield effective excitation cross-sections for the RE luminescence in the NIR which can exceed those of RE-doped silica by some five orders of magnitude. Furthermore, by taking advantage of the broad NC absorption spectrum, the REs can be indirectly excited by photons that are not resonant with any of their characteristic intra-$4f$ transitions. This property makes Er-doped Si nanocomposites an attractive class of materials for cost-effective optical amplifiers, since they could be pumped with inexpensive, efficient LEDs instead of the costly solid-state lasers required in the operation of conventional erbium-doped fibre amplifiers. Keeping such device applications in mind, this thesis has investigated silicon nanocomposite thin films, both in intrinsic form and doped with rare earths.

Si-NC-containing films were fabricated via physical vapour deposition of Si-based suboxides (Si, SiO, and SiO_2 used as source materials). Subsequent thermal processing induces phase separation of the thermodynamically-metastable SiO_x films, causing nucleation of Si-rich regions within a more oxygen-rich matrix. Energy-filtered TEM and EELS measurements have revealed that SiO thin films annealed for one hour at temperatures less than 800 °C are fully amorphous; annealing at temperatures exceeding 900 °C results in c-Si NCs. The characteristic photoluminescence of such films fabricated via thermal evaporation of SiO is a broad PL band centred at ~600–800 nm, the peak position of which is dependent on the annealing temperature. To incorporate RE elements into the nanocom-

posite films, electron-beam or thermal evaporation of REs in oxide or metallic form, respectively, was used. Evidence of efficient energy transfer from the NCs to trivalent Nd, Tb, Dy, Er, Tm, and Yb ions was inferred by the strong quenching of the NC luminescence with increasing RE concentration. For Tb- and Dy-doped films, however, no RE emission was observed, as these ions have closely-spaced energy levels for which non-radiative phonon-based de-excitation is dominant.

As a demonstration of the potential for *a*-Si nanocomposites to be used in photonics applications, they were incorporated into simple trial devices consisting of optical microcavities. By varying the thicknesses of the active layer at metal mirrors, control over the width and centre wavelength of the luminescence can be achieved. The 475-nm-to-875-nm range of tunability for undoped *a*-Si films is remarkable for a single material; Er-doped microcavities are capable of extending tunable, sharpened emission to 1630 nm. The thin-film metal mirrors used in these optical resonator structures could naturally serve as electrodes in electroluminescence experiments; such a prospect is currently under investigation in our research group. Another obvious photonic device application using RE-doped Si nanocomposites is that of waveguide amplifiers; in a collaborative effort,[†] our research group is currently investigating the use of Er-doped *a*-Si-NC films into waveguide structures, evaluating them for the prospect of achieving gain.

In addition to the more device-based experiments, we have also modelled the luminescence from *a*-Si NCs (undoped and RE-doped), comparing results of the simulations with experimental PL data. For undoped *a*-Si-NC films, a strong quenching of the luminescence with increased annealing temperature was observed. Using experimentally-determined size distributions for these specimens, good agreement with this quenching behaviour was found for the simulations in which the non-radiative defect density was $\sim 10^{20}$ cm^{-3}. An increase in effective NC volume calculated using a simplified treatment of inter-NC tunnelling, however, could not reproduce the observed quenching qualitatively. Since the majority of lowest-energy carriers in nanoclusters of these sizes were calculated to be localised, rather than extended, the tunnelling probabilities used likely represent an overestimate of the true situation.

The photoluminescence dynamics of the coupled NC–Er^{3+} system were investigated using a coupled rate equation model. Many such models exist in the literature, but the uniqueness of the values obtained for the transition rates is in certain cases rather doubtful. This is especially the case for numerical models including many parameters. The analysis was simplified by considering the system in the small excitation regime, in which optical pumping is of low enough intensity that the approximation of constant ground-state populations is valid for both the NCs and the Er^{3+} ions. In such a situation, analytical solutions to the set of rate equations exist. However, we have shown that, even in this simplified situation in which cooperative effects resulting from an appreciable excited Er^{3+} population do not have to be considered, obtaining a unique value for the NC–Er^{3+} transfer rate by fitting experimental time-resolved PL data to the rate-equation solutions is extremely improbable. From the temperature dependence of the *a*-Si-NC and Er^{3+} PL, a phonon-assisted energy transfer process seems likely; a more detailed study of this process is another suggested direction for future work.

[†]Our collaborators for this project are the members of Dr. Ray DeCorby's research group in the University of Alberta Department of Electrical and Computer Engineering and TRLabs.

APPENDIX A

Analytical photoluminescence dynamics modelling of Si nanocluster–rare-earth interactions

A.1 Introduction

Rare-earth-doped silicon nanocomposite thin films are very interesting from an integrated photonics perspective due to the so-called sensitisation effect of rare-earth ions by neighbouring silicon nanoclusters. In particular, the increase in excitation cross-section of Er^{3+} in Si nanocomposites by several orders of magnitude[1] over that of Er-doped SiO_2 via non-resonant nanocluster-mediated pumping suggests the fabrication of efficient broadband-pumped optical amplifiers.

To gain a better understanding of the interaction between amorphous or crystalline Si NCs and RE ions, we may consider the photoluminescence dynamics of the material, modelling the level populations phenomenologically via a system of coupled rate equations. In the literature, although such coupled rate-equation models abound, analytically-soluble results are infrequently derived, and the leap is generally made directly to numerical solutions to *nonlinear* sets of differential equations (DEs). This is unfortunate, as the lucidity offered by analytical solutions often provides an intuitive starting-point before considering more complex models. Also, for low-power pumping regimes or short excitation times, the effect of nonlinear terms in the DEs can be negligible; in such circumstances, the analytical solutions can accurately describe the evolution of the system directly. It is the purpose of this Appendix to derive analytical solutions to several sets of rate equations are often encountered when considering the transfer of energy between two coupled systems.

A.2 General simplified systems

We may begin by considering a general two- or three-level system, without assigning a particular physical identity to any of the levels. In this way, the model could represent a single Si NC or a single RE ion. By concatenating several levels into one, such a model could also represent a coupled Si-NC:RE system; such an approach is widely used to obtain initial estimates of effective excitation cross-sections for a particular transition in the RE (e.g., Refs.[2–4]).

Once we solve for a given level population $N_i(t)$, the PL intensity corresponding to a

radiative transition from the ith to the jth level will be given by:

$$I_{ij}(t) \propto w_{ij_{rad}} N_i(t) \tag{A.1}$$

where $w_{ij_{rad}}$ is the radiative component of the decay rate from level i to j.

A.2.1 Two-level system

We begin by examining a simple two-level system (Fig. A.1). For excitation via a rectangular pulse, the pumping rate is R for $0 \leq t < t_{off}$ and zero for $t \geq t'_{off}$. Clearly, as $t_{off} \to 0$, we will obtain the result for δ-function excitation.

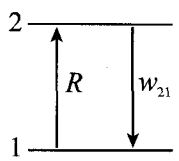

Fig. A.1: Schematic of a two-level system

The time evolution of this system is described by the following set of first-order rate equations:

$$\frac{\mathrm{d}N_1}{\mathrm{d}t} = -RN_1 + w_{21}N_2 \tag{A.2a}$$

$$\frac{\mathrm{d}N_2}{\mathrm{d}t} = RN_1 - w_{21}N_2 \tag{A.2b}$$

where we substitute $R = 0$ for $t \geq t_{off}$. For initial conditions of $N_1(0) = N_{1_o}$ and $N_2(0) = 0$, the solutions to equations (A.2) are:

$$N_1(t) = \begin{cases} \frac{N_{1_o}}{w_{21}+R}\left[w_{21} + R\,e^{-(w_{21}+R)t}\right] & \text{for } 0 \leq t < t_{off} \\ \eta_1 + \eta_2\left[1 - e^{-w_{21}(t-t_{off})}\right] & \text{for } t \geq t_{off} \end{cases} \tag{A.3a}$$

$$N_2(t) = \begin{cases} \frac{RN_{1_o}}{w_{21}+R}\left[1 - e^{-(w_{21}+R)t}\right] & \text{for } 0 \leq t < t_{off} \\ \eta_2\, e^{-w_{21}(t-t_{off})} & \text{for } t \geq t_{off} \end{cases} \tag{A.3b}$$

where N_{1_o} is the total concentration of particles described by the two-level model and $\eta_i = N_i(t_{off})$.

Since the pumping rate is related to the excitation photon flux Φ via $R = \sigma_{12}\Phi$, the excitation cross-section σ_{12} may be obtained by measuring the rise- and decay-times of the PL. From (A.3b), the $(1 - e^{-1})$ rise-time may therefore be written as:

$$\frac{1}{\tau_r} = \frac{1}{\tau_d} + \sigma_{12}\Phi \tag{A.4}$$

where $\tau_d = 1/w_{21}$ is the $1/e$ PL decay-time. If the excitation transition from $1 \to 2$ describes the true physical situation, viz. $1 \to 2$ does *not* represent a concatenation of several transitions leading from 1 to 2, then σ_{12} is the absorption cross-section of the transition. Otherwise, σ_{12} would represent an *effective* excitation cross-section; this is the approach used to quote effective excitation cross-sections for the 1.54 μm PL from the $^4I_{13/2} \to {}^4I_{15/2}$ transition in Er^{3+} (see, e.g., Ref.[2]).

If R and/or t_{off} are sufficiently small (the so-called *small excitation regime*), then we may approximate that $N_1(t)$ does not appreciably change during the excitation. We may therefore replace $N_1(t)$ by the constant $\mathcal{N}_1$, and simplify (A.2) to a single rate equation:

$$\frac{dN_2'}{dt} = R\mathcal{N}_1 - w_{21}N_2' \tag{A.5}$$

where the primes refer to the ground state being held constant. Solving (A.5) yields:

$$N_2'(t) = \begin{cases} \frac{R\mathcal{N}_1}{w_{21}}\left[1 - e^{-w_{21}t}\right] & \text{for } 0 \leq t < t_{off} \\ \eta_2' \, e^{-w_{21}(t-t_{off})} & \text{for } t \geq t_{off} \end{cases} \tag{A.6}$$

As $R \to 0$ and/or $t_{off} \to 0$, $\eta_2 \to \eta_2'$, and $N_2(t) \to N_2'(t)$, showing the equivalence of the two methods for the small excitation regime. From equations (A.3), it is clear that N_2 reaches its maximum at $t = t_{off}$ and exhibits single exponential decay thereafter.

A.2.2 Three-level system

Although the two-level model has the benefit of simplicity, justifying its use for initial investigations and estimates of effective excitation cross-sections, a much more realistic model for most physical situations is the three-level system (Fig. A.2). For example, in the luminescent centre model for the mechanism of PL from Si NC,[5–8] a quantum-confined exciton is created in the nanocluster, becomes trapped at a luminescent trap site (often a defect on the NC surface), then radiatively recombines. Thus, even in this simplified model, three rates are required: a pump rate R, a trapping rate w_{tr}, and a radiative recombination rate w_{rad}. As we shall see, for the case of very fast trapping, this situation reduces to the two-level system mentioned in §A.2.1.

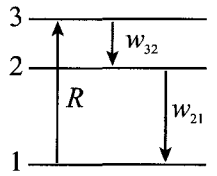

Fig. A.2: Schematic of a three-level system

This three-level system evolves according to:

$$\frac{dN_1}{dt} = -RN_1 + w_{21}N_2 \tag{A.7a}$$

$$\frac{dN_2}{dt} = w_{32}N_3 - w_{21}N_2 \tag{A.7b}$$

$$\frac{dN_3}{dt} = RN_1 - w_{32}N_3 \tag{A.7c}$$

As before, we substitute $R = 0$ for $t \geq t_{off}$. The initial conditions are $N_3(0) = N_2(0) = 0$

and $N_1(0) = N_{1_o}$. For $0 \leq t < t_{off}$, the solutions are:

$$N_1(t) = \frac{N_{1_o} w_{32} w_{21}}{R w_{21} + R w_{32} + w_{21} w_{32}} \left[1 - \frac{R\left(-\frac{R}{w_{21}} - \frac{R}{w_{32}} + \frac{w_{21}}{w_{32}} + \frac{w_{32}}{w_{21}} - \left\{\frac{1}{w_{32}} + \frac{1}{w_{21}}\right\}\Delta\right)}{2\Delta} e^{-w_+ t} \right.$$
$$\left. - \frac{R\left(\frac{R}{w_{21}} + \frac{R}{w_{32}} - \frac{w_{21}}{w_{32}} - \frac{w_{32}}{w_{21}} - \left\{\frac{1}{w_{32}} + \frac{1}{w_{21}}\right\}\Delta\right)}{2\Delta} e^{-w_- t} \right] \quad \text{(A.8a)}$$

$$N_2(t) = \frac{R N_{1_o} w_{32}}{R w_{21} + R w_{32} + w_{21} w_{32}} \left[1 + \frac{R + w_{21} + w_{32} - \Delta}{2\Delta} e^{-w_+ t} - \frac{R + w_{21} + w_{32} + \Delta}{2\Delta} e^{-w_- t} \right] \quad \text{(A.8b)}$$

$$N_3(t) = \frac{R N_{1_o} w_{21}}{R w_{21} + R w_{32} + w_{21} w_{32}} \left[1 + \frac{-2R\frac{w_{32}}{w_{21}} - R - w_{32} + w_{21} - \Delta}{2\Delta} e^{-w_+ t} \right.$$
$$\left. + \frac{2R\frac{w_{32}}{w_{21}} + R + w_{32} - w_{21} - \Delta}{2\Delta} e^{-w_- t} \right] \quad \text{(A.8c)}$$

where $\Delta = \sqrt{R^2 - 2R(w_{32} + w_{21}) + (w_{32} - w_{21})^2}$ and $w_\pm = \frac{1}{2}\left[R + w_{32} + w_{21} \pm \Delta\right]$. Defining $\eta_i = N_i(t_{off})$ as before, the solutions for $t \geq t_{off}$ are:

$$N_1(t) = (\eta_1 + \eta_2 + \eta_3) - \left[\eta_2 + \frac{\eta_3}{1 - \frac{w_{21}}{w_{32}}} \right] e^{-w_{21}(t - t_{off})} - \frac{\eta_3}{1 - \frac{w_{32}}{w_{21}}} e^{-w_{32}(t - t_{off})} \quad \text{(A.9a)}$$

$$N_2(t) = \frac{1}{1 - \frac{w_{21}}{w_{32}}} \left[\left\{ \eta_2 \left(1 - \frac{w_{21}}{w_{32}}\right) + \eta_3 \right\} e^{-w_{21}(t - t_{off})} - \eta_3 \, e^{-w_{32}(t - t_{off})} \right] \quad \text{(A.9b)}$$

$$N_3(t) = \eta_3 \, e^{-w_{32}(t - t_{off})} \quad \text{(A.9c)}$$

Before examining the physical significance of these solutions, it is worth considering the simpler case of the small excitation regime, viz. $N_1(t) = \mathcal{N}_1$ being held constant. Similarly to §A.2.1, the rate equations simplify to:

$$\frac{\mathrm{d}N_2'}{\mathrm{d}t} = w_{32} N_3' - w_{21} N_2' \quad \text{(A.10a)}$$

$$\frac{\mathrm{d}N_3'}{\mathrm{d}t} = R\mathcal{N}_1 - w_{32} N_3' \quad \text{(A.10b)}$$

yielding

$$N_2'(t) = \begin{cases} \frac{R\mathcal{N}_1}{w_{21}} \left[1 - \frac{1}{1 - \frac{w_{21}}{w_{32}}} e^{-w_{21} t} - \frac{1}{1 - \frac{w_{32}}{w_{21}}} e^{-w_{32} t} \right] & \text{for } 0 \leq t < t_{off} \\ \frac{1}{1 - \frac{w_{21}}{w_{32}}} \left[\left\{ \eta_2' \left(1 - \frac{w_{21}}{w_{32}}\right) + \eta_3' \right\} e^{-w_{21}(t - t_{off})} - \eta_3' e^{-w_{32}(t - t_{off})} \right] & \text{for } t \geq t_{off} \end{cases} \quad \text{(A.11a)}$$

$$N_3'(t) = \begin{cases} \frac{RN_1}{w_{32}}\left[1 - e^{-w_{32}t}\right] & \text{for } 0 \leq t < t_{off} \\ \eta_3' \, e^{-w_{32}(t-t_{off})} & \text{for } t \geq t_{off} \end{cases} \tag{A.11b}$$

To show that the solutions (A.8) and (A.9) reduce to equations (A.11) for the small excitation regime, we must consider both situations in which the approximation that $N_1(t)$ remains constant: first, when R is small compared to w_{32} and w_{21}, and second, when t_{off} is sufficiently small such that, regardless of the magnitude of R, few particles in level 1 have time to be excited to level 3.

For the first case, consider the situation where $R \to 0$ and $w_{32} > w_{21}$, which is justified under low-power pumping of nanoclusters with fast trapping sites. In this case, $\Delta \to (w_{32} - w_{21})$, $w_+ \to w_{32}$, and $w_- \to w_{21}$. Thus, $\eta_2 \to \eta_2'$ and $\eta_3 \to \eta_3'$, so (A.8) and (A.9) become equivalent to (A.11).

For short excitation pulses, since equations (A.9b) and (A.9c) have the same form as equations (A.11a) and (A.11b) for $t \geq t_{off}$, it suffices to show that they demonstrate the same behaviour for $0 \leq t < t_{off}$ when $t_{off} \to 0$. Expanding equations (A.8a) and (A.9a) to first order and (A.8b) and (A.9b) to second order about $t = 0$, we obtain:

$$N_2(t) = N_2'(t) \approx \frac{Rw_{32}N_{1_o}}{2}t^2 \tag{A.12a}$$

$$N_3(t) = N_3'(t) \approx RN_{1_o}t \tag{A.12b}$$

Since both $N_i(t)$ and $N_i'(t)$ have the same functional form for short times, (A.9) and (A.11) are equivalent.

For qualitative comparisons with experimental PL data, it is worth noting a few characteristics with respect to the behaviour of the solutions to the three-level system, (A.8), (A.9) and (A.11). For $t_{off} > 0$, $\frac{dN_2}{dt} = 0$ at $t = 0$, and is concave up until an inflection point at a time given by:

$$t_{infl} = \frac{1}{\Delta}\ln\left[\left(\frac{R + w_{21} + w_{32} - \Delta}{R + w_{21} + w_{32} + \Delta}\right)\frac{w_+^2}{w_-^2}\right] \tag{A.13}$$

Physically, this result is due to N_2 being filled via decay from N_3, and not directly by the pump rate R, which has been assumed to turn on instantaneously (cf. §A.2.1, where $\frac{dN_2}{dt} > 0$ at $t = 0$). Thus, the presence of an inflection point in the rising portion of the PL signal precludes the possibility of describing the nanocluster by an effective two-level system. However, for any short pulsed excitation for which t_{infl} is significantly smaller than the time resolution of the PL collection system, the change in concavity will be lost due to an insufficient data sampling rate.

The condition for the change of concavity to be lost from a discrete-time-sampled function $f(t)$ is that the slope between the first two data points is greater than or equal to that of the slope between the second and third data points. Assuming a constant data sampling time of t', this corresponds to the condition

$$2f(t') \geq f(2t'). \tag{A.14}$$

For long values of t_{off} with respect to t', we may Taylor-series-expand (A.11a) for $0 \leq t < t_{off}$ about $t \to 0$ to third order to obtain an approximate solution to condition (A.14), yielding

$$N_2(t) \approx \frac{1}{2}Rw_{32}N_{1_o}t^2 - \frac{1}{6}(w_{21} + w_{32})w_{32}RN_{1_o}t^3. \tag{A.15}$$

Using this approximation, the condition $2N_2(\tilde{t}') \geq N_2(2\tilde{t}')$ yields $\tilde{t}' \geq (w_{21} + w_{32})^{-1}$. As this result was derived using only the lowest-order expansion of $N_2(t)$ yielding non-trivial solutions to (A.14), only if $t' \gg \tilde{t}'$ is it certain that the loss of inflection will be observed.

For $t_{off} \ll t'$, it is possible to have effective δ-function excitation with respect to the time response of the PL detection system. This situation can be described by the rate equations (A.10) with $R = 0$ and initial conditions $N_2(0) = 0$ and $N_3(0) = N_{3_o}$, with solutions:

$$N_2(t) = \frac{N_{3_o} w_{32}}{w_{32} - w_{21}} \left[e^{-w_{21}t} - e^{-w_{32}t}\right] \tag{A.16a}$$

$$N_3(t) = N_{3_o} e^{-w_{32}t} \tag{A.16b}$$

where $N_{3_o} = R\mathcal{N}_1 t_{off}$. For Q-switched and mode-locked excitation lasers with photodiode PL detection, this is the usual experimental situation. Note that these solutions may also be obtained by Taylor-expanding equations (A.11) for $t \geq t_{off}$ about $t_{off} = 0$.

For δ-function excitation, the restriction on t' required to satisfy condition (A.14) may be found, as in the previous example, by expanding (A.16a) about $t = 0$ to third order. Substitution into condition (A.14) yields $\tilde{t}' \geq \frac{w_{32}+w_{21}}{w_{32}^2+w_{21}w_{32}+w_{21}^2}$. As before, only for $t' \gg \tilde{t}'$ will the inflection point certainly fail to be resolved.

A.3 Two coupled systems

We may now turn to the more complex situation where two of the systems described in §A.2 interact via a coupling coefficient C_{ij}, resulting in a transfer of energy from level i in system A to level j in system B. For systems with n_k levels, this results in $n_A + n_B$ nonlinear rate equations involving $C_{ij}N_iN_j$ terms, which in general must be solved numerically. However, if we make the small excitation regime approximation, keeping the ground states of systems A and B constant, the coupling coefficients C_{ij} may be replaced by a transfer rate $w_{ij} = C_{ij}\mathcal{N}_j$, where $\mathcal{N}_j$ are the ground state concentrations, and we may describe the total system with $n_A + n_B - 2$ *linear* differential equations. We will therefore use this approach to investigate the interaction between Si-NC and rare-earth elements.

The validity of approximating a RE ion by a three-level system will depend on the energy levels of the particular RE being considered. For the Si-NC–Er interaction, if we are only interested in the $^4I_{9/2}$, $^4I_{11/2}$, and $^4I_{15/2}$ levels, we may treat the Er^{3+} ions as three-level systems provided that there is negligible concentration quenching, cooperative upconversion, and backtransfer. These conditions should be satisfied given a sufficiently low Er concentration in the film, small excitation rates, and low temperature.

A.3.1 Two-level nanocluster coupled to a three-level rare earth

The first coupling situation we will consider is the two-level nanocluster, with energy levels a and b, interacting with a three-level rare earth ion, with energy levels 1, 2, and 3 (Fig. A.3). An effective two-level NC is an approximation which has been frequently used in the literature (e.g., Refs.[2,9]), even if the modelling of the rare-earth energy levels is considerably more complex.

Identifying each level in the three-level system depends on the choice of RE being modelled, as well as which transition is being measured experimentally. The RE is being excited via a transfer of energy from the nanocluster, but the details of the transition affect

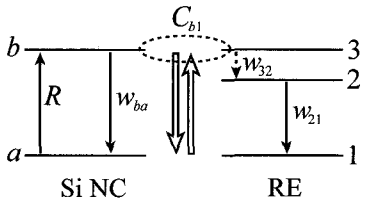

Fig. A.3: Schematic of the interaction between a two- and a three-level system

the physical identity of level 3. Assuming that the exciton migrates first to a luminescent trap site, from which it may either radiatively recombine or non-radiatively transfer its energy to the RE, level 3 should be associated with the level(s) most closely match the peak energy of Si-NC PL emission (~600–900 nm, depending on composition and annealing conditions).[10] For Er^{3+}, this corresponds to the $^4I_{9/2}$ level; for Nd^{3+}, the $^4F_{7/2}$, $^4S_{3/2}$, and $^4F_{9/2}$ levels all lie within this range (see Fig. A.4). Level 2 in this model is then the first level which can be filled by level 3 after the energy transfer from the Si-NC. Whereas this corresponds unambiguously to the $^4I_{11/2}$ level in Er^{3+}, for Nd^{3+}, the applicability of this model becomes somewhat more suspect. It has been assumed[11] that after pumping to one of the three levels mentioned above, the Nd^{3+} drops to the $^2H_{9/2}$ or $^4F_{5/2}$ levels, whereupon it may decay radiatively to the $^4I_{9/2}$ ground state, or nonradiavely to the $^4F_{3/2}$ state. However, as the rate for the latter process is much larger than for the former, for the purposes of this model one could effectively treat a concatenation of levels $^4F_{9/2}$, $^4S_{3/2}$, $^4F_{7/2}$, $^2H_{9/2}$ and $^4F_{5/2}$ as level 3, and $^4F_{3/2}$ as level 2. Level 1, being the ground state of the ion, is unambiguous for both rare earths: $^4I_{15/2}$ and $^4I_{9/2}$ for Er^{3+} and Nd^{3+}, respectively.

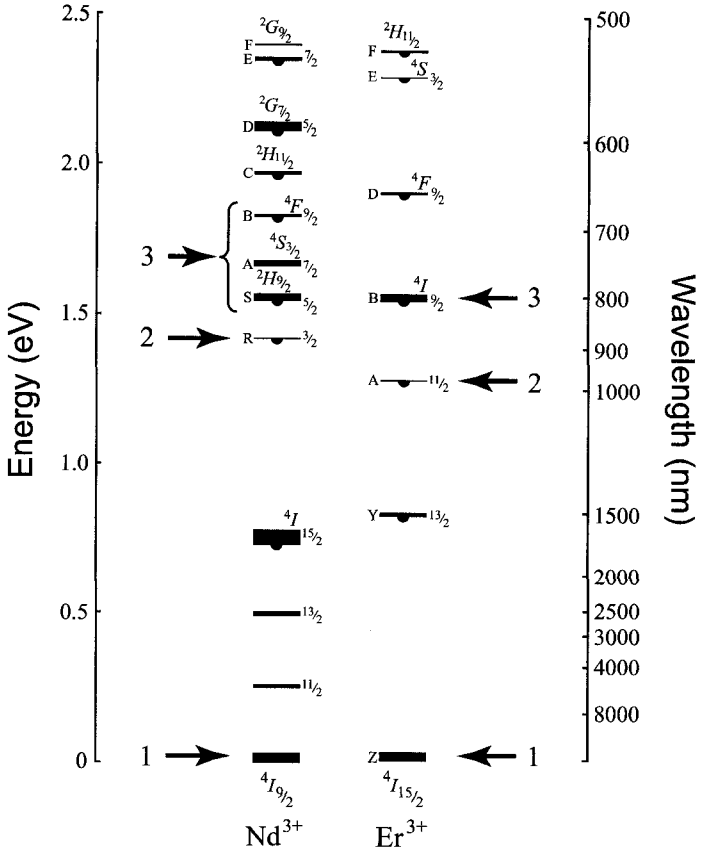

Fig. A.4: Diagram of energy levels for Nd^{3+} and Er^{3+}, after Dieke.[12] The RE levels corresponding to levels 1, 2, and 3 as defined for a simplified three-level model are marked with arrows.

In the small excitation regime, we hold $N_a(t) = \mathcal{N}_a$ and $N_1(t) = \mathcal{N}_1$ constant, yielding rate equations:

$$\frac{\mathrm{d}N_b}{\mathrm{d}t} = R\mathcal{N}_a - (w_{ba} + w_{b1})\, N_b \tag{A.17a}$$

$$\frac{\mathrm{d}N_3}{\mathrm{d}t} = w_{b1}N_b - w_{32}N_3 \tag{A.17b}$$

$$\frac{\mathrm{d}N_2}{\mathrm{d}t} = w_{32}N_3 - w_{21}N_2 \tag{A.17c}$$

where $w_{b1} = C_{b1}\mathcal{N}_1$. The usual initial conditions of $N_b(0) = N_3(0) = N_2(0) = 0$ produce the following solutions for $0 \le t < t_{off}$:

$$N_b(t) = \frac{R\mathcal{N}_a}{w_{ba} + w_{b1}}\left[1 - e^{-(w_{ba}+w_{b1})t}\right] \tag{A.18a}$$

$$\begin{aligned} N_2(t) = w_{b1}R\mathcal{N}_a \Bigg[& \frac{1}{(w_{32} - w_{21})(w_{ba} + w_{b1} - w_{32})}\, e^{-w_{32}t} \\ & + \frac{w_{32}}{w_{21}(w_{32} - w_{21})(w_{21} - w_{ba} - w_{b1})}\, e^{-w_{21}t} \\ & + \frac{w_{32}}{(w_{ba} + w_{b1})(w_{21} - w_{ba} - w_{b1})(w_{ba} + w_{b1} - w_{32})}\, e^{-(w_{ba}+w_{b1})t} + \frac{1}{w_{21}(w_{ba} + w_{b1})}\Bigg] \end{aligned} \tag{A.18b}$$

$$\begin{aligned} N_3(t) = w_{b1}R\mathcal{N}_a \Bigg[& \frac{1}{w_{32}(w_{32} - w_{ba} - w_{b1})}\, e^{-w_{32}t} \\ & - \frac{1}{(w_{ba} + w_{b1})(w_{32} - w_{ba} - w_{b1})}\, e^{-(w_{ba}+w_{b1})t} + \frac{1}{w_{32}(w_{ba} + w_{b1})}\Bigg] \end{aligned} \tag{A.18c}$$

and, for $t \ge t_{off}$, where $R = 0$:

$$N_b(t) = \eta_b\, e^{-(w_{ba}+w_{b1})(t-t_{off})} \tag{A.19a}$$

$$\begin{aligned} N_2(t) = & \frac{w_{32}}{w_{21} - w_{32}}\left[\eta_3 + \frac{w_{b1}}{w_{ba} + w_{b1} + w_{32}}\eta_b\right] e^{-w_{32}(t-t_{off})} \\ & + \left[\eta_2 + \frac{w_{b1}w_{32}}{(w_{21} - w_{ba} - w_{b1})(w_{21} - w_{32})}\eta_b - \frac{w_{32}}{w_{21} - w_{32}}\eta_3\right] e^{-w_{21}(t-t_{off})} \\ & + \frac{w_{32}w_{b1}}{(w_{32} - w_{ba} - w_{b1})(w_{21} - w_{ba} - w_{b1})}\eta_b\, e^{-(w_{ba}+w_{b1})(t-t_{off})} \end{aligned} \tag{A.19b}$$

$$N_3(t) = \left[\frac{w_{b1}}{w_{ba} + w_{b1} - w_{32}}\eta_b + \eta_3\right] e^{-w_{32}(t-t_{off})} - \frac{w_{b1}}{w_{ba} + w_{b1} - w_{32}}\eta_b\, e^{-(w_{ba}+w_{b1})(t-t_{off})} \tag{A.19c}$$

The form of (A.19a) suggests that the transfer rate $\tau_{b1} = 1/w_{b1}$ may be obtained by measuring the difference in Si-NC PL decay lifetime between doped and undoped specimens; in practice, however, this cannot be easily accomplished exactly, as such a procedure implicitly assumes that in the RE-doped film, *all* nanoclusters from which Si-NC PL is measured are equally coupled to surrounding RE ions. Indeed, according to the "strong coupling" model for the interaction between nanoclusters and RE ions (see, e.g., Ref.[13]), it is assumed that all measurable Si-nc PL from RE-doped specimens originates from nanoclusters which are *not* coupled to a RE, as any nanoclusters that are have their intrinsic PL quenched. One might expect a distribution in w_{b1} to exist, due to varying proximity of RE ions to the nanoclusters. For such a relaxation of the strong coupling condition, viz. that w_{b1}/w_{ba} varies from cluster to cluster such that some excitons may radiatively recombine before transferring their energy to the RE, fitting the above equations to data would yield, at best, a "mean" τ_{b1}.

A.3.2 Three-level nanocluster coupled to a three-level rare earth

By means of improving the model with respect to the Si-NC, we assume a three-level nanocluster, as in §A.2.2 (Fig. A.5). As a straightforward elaboration of the system described in §A.3.1, we again use the small excitation regime, holding $N_a(t) = \mathcal{N}_a$ and $N_1(t) = \mathcal{N}_1$ constant.

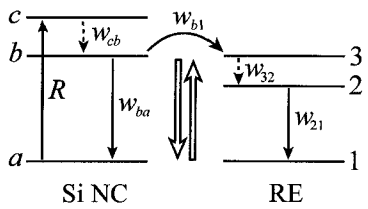

Fig. A.5: Schematic of the interaction between two three-level systems in the small excitation regime

The system of rate equations is:

$$\frac{\mathrm{d}N_b}{\mathrm{d}t} = w_{cb}N_c - (w_{ba} + w_{b1})N_b \tag{A.20a}$$

$$\frac{\mathrm{d}N_c}{\mathrm{d}t} = R\mathcal{N}_a - w_{cb}N_c \tag{A.20b}$$

$$\frac{\mathrm{d}N_2}{\mathrm{d}t} = w_{32}N_3 - w_{21}N_2 \tag{A.20c}$$

$$\frac{\mathrm{d}N_3}{\mathrm{d}t} = w_{32}N_3 - w_{21}N_2 \tag{A.20d}$$

which, given the initial conditions $N_b(0) = N_c(0) = N_2(0) = N_3(0) = 0$, has the following solutions. For $0 \leq t < t_{off}$:

$$N_b(t) = R\mathcal{N}_a \left[\frac{1}{w_{ba} + w_{b1}} - \frac{1}{w_{ba} + w_{b1} - w_{cb}} e^{-w_{cb}t} - \frac{w_{cb}}{(w_{ba} + w_{b1})(w_{cb} - w_{ba} - w_{b1})} e^{-(w_{ba}+w_{b1})t} \right] \tag{A.21a}$$

$$N_c(t) = \frac{R\mathcal{N}_a}{w_{cb}}\left(1 - e^{-w_{cb}t}\right) \tag{A.21b}$$

$$\begin{aligned} N_2(t) = R\mathcal{N}_a w_{b1}\Bigg[&\frac{1}{w_{21}(w_{ba}+w_{b1})} - \frac{w_{cb}w_{32}}{w_{21}(w_{32}-w_{21})(w_{cb}-w_{21})(w_{ba}+w_{b1}-w_{21})}e^{-w_{21}t} \\ &- \frac{w_{cb}}{(w_{cb}-w_{32})(w_{21}-w_{32})(w_{ba}+w_{b1}-w_{32})}e^{-w_{32}t} \\ &- \frac{w_{32}}{(w_{cb}-w_{32})(w_{21}-w_{cb})(w_{cb}-w_{ba}-w_{b1})}e^{-w_{cb}t} \\ &- \frac{w_{32}w_{cb}}{(w_{ba}+w_{b1})(w_{ba}+w_{b1}-w_{32})(w_{ba}+w_{b1}-w_{21})(w_{cb}-w_{ba}-w_{b1})}e^{-(w_{ba}+w_{b1})t}\Bigg] \end{aligned} \tag{A.21c}$$

$$\begin{aligned} N_3(t) = R\mathcal{N}_a w_{b1}\Bigg[&\frac{1}{w_{32}(w_{ba}+w_{b1})} - \frac{1}{(w_{cb}-w_{32})(w_{cb}-w_{ba}-w_{b1})}e^{-w_{cb}t} \\ &- \frac{w_{cb}}{w_{32}(w_{cb}-w_{32})(w_{ba}+w_{b1}-w_{32})}e^{-w_{32}t} \\ &- \frac{w_{cb}}{(w_{ba}+w_{b1})(w_{cb}-w_{ba}-w_{b1})(w_{32}-w_{ba}-w_{b1})}e^{-(w_{ba}+w_{b1})t}\Bigg] \end{aligned} \tag{A.21d}$$

Setting $R = 0$ for $t \geq t_{off}$, we obtain:

$$N_b(t) = \left[\frac{w_{cb}\eta_c}{w_{cb}-w_{ba}-w_{b1}} + \eta_b\right]e^{-(w_{ba}+w_{b1})(t-t_{off})} - \frac{w_{cb}\eta_c}{w_{cb}-w_{ba}-w_{b1}}e^{-w_{cb}(t-t_{off})} \tag{A.22a}$$

$$N_c(t) = \eta_c\, e^{w_{cb}(t-t_{off})} \tag{A.22b}$$

$$\begin{aligned} N_2(t) = &\frac{w_{b1}w_{32}w_{cb}\eta_c}{(w_{cb}-w_{ba}-w_{b1})(w_{cb}-w_{32})(w_{21}-w_{cb})}e^{-w_{cb}(t-t_{off})} \\ &- \left[\frac{w_{32}\eta_3}{w_{32}-w_{21}} + \frac{w_{b1}w_{32}\eta_b}{(w_{32}-w_{21})(w_{ba}+w_{b1}-w_{32})} \right. \\ &\left. + \frac{w_{b1}w_{32}w_{cb}\eta_c}{(w_{32}-w_{21})(w_{cb}-w_{32})(w_{ba}+w_{b1}-w_{32})}\right]e^{-w32(t-t_{off})} \\ &- \left[\frac{w_{b1}w_{32}w_{cb}\eta_c}{(w_{21}-w_{ba}-w_{b1})(w_{ba}+w_{b1}-w_{32})(w_{cb}-w_{ba}-w_{b1})} \right. \\ &\left. + \frac{w_{b1}w_{32}\eta_b}{(w_{21}-w_{ba}-w_{b1})(w_{ba}+w_{b1}-w_{32})}\right]e^{-(w_{ba}+w_{b1})(t-t_{off})} \\ &+ \left[\eta_2 + \frac{w_{32}\eta_3}{w_{32}-w_{21}} + \frac{w_{b1}w_{32}\eta_b}{(w_{ba}+w_{b1}-w_{21})(w_{32}-w_{21})} \right. \\ &\left. + \frac{w_{b1}w_{32}w_{cb}\eta_c}{(w_{ba}+w_{b1}-w_{21})(w_{32}-w_{21})(w_{cb}-w_{21})}\right]e^{-w_{21}(t-t_{off})} \end{aligned} \tag{A.22c}$$

$$N_3(t) = \frac{w_{b1}w_{cb}\eta_c}{(w_{cb} - w_{ba} - w_{b1})(w_{cb} - w_{32})} e^{-w_{cb}(t-t_{off})} + \left[\eta_3 + \frac{w_{b1}\eta_b}{w_{ba} + w_{b1} - w_{32}} + \frac{w_{b1}w_{cb}\eta_c}{(w_{ba} + w_{b1} - w_{32})(w_{cb} - w_{32})}\right] e^{-w_{32}(t-t_{off})} + \left[\frac{w_{b1}w_{cb}\eta_c}{(w_{ba} + w_{b1} - w_{32})(w_{cb} - w_{ba} - w_{b1})} + \frac{w_{b1}\eta_b}{w_{ba} + w_{b1} - w_{32}}\right] e^{-(w_{ba}+w_{b1})(t-t_{off})} \quad \text{(A.22d)}$$

The pumping conditions for which these analytical solutions are valid, that is, those for which the assumption of keeping $N_1(t) = \mathcal{N}_1$ and $N_a(t) = \mathcal{N}_a$ constant is justified, may be checked via a comparison with numerical solutions to the (nonlinear) model with no restrictions on $N_1(t)$ and $N_a(t)$ (see introduction to §A.3). For Er^{3+}, since the three-level RE model used in §A.3.1 and §A.3.2 subsumes all depopulation pathways from $^4I_{11/2}$ and the ground state (predominantly the radiative $^4I_{11/2} \rightarrow {}^4I_{15/2}$ and non-radiative $^4I_{11/2} \rightarrow {}^4I_{13/2}$ transitions) into one effective rate, w_{21}, a potential concern with the small excitation regime approximation could arise if one considers that the lifetime of the $^4I_{13/2} \rightarrow {}^4I_{15/2}$ transition is on the order of several ms, whereas the nanocluster recombination time is ~100 μs. As such, the ions can easily be pushed into saturation, with nearly all Er^{3+} excited to the $^4I_{13/2}$ level and $N_1(t) \approx 0$, even at low pump powers;[14] relaxation to this metastable configuration is clearly not included in the small excitation regime. With the more accurate description afforded by a four-level RE model, the small excitation pumping condition may be determined with more certainty.

A.3.3 Two-level nanocluster coupled to a four-level rare earth

We may proceed as in §A.3.1 and §A.3.2, the only difference being that, with respect to identifying the four RE levels with an actual state in Er^{3+}, level 2 is now $^4I_{13/2}$, level 3 is $^4I_{11/2}$, and level 4 is $^4I_{9/2}$. Thus, the model may be given in schematic form as shown in Fig. A.6, with two depopulation pathways from level 3 ($^4I_{11/2}$).

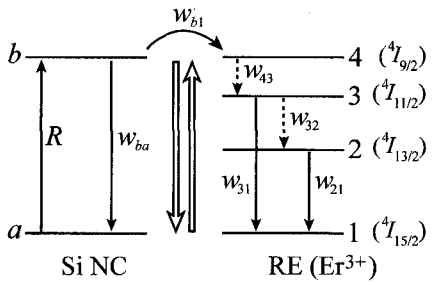

Fig. A.6: Schematic of the interaction between a two-level NC and a four-level RE in the small excitation regime

Again adopting the small excitation regime approximation, we describe this model via:

$$\frac{dN_b}{dt} = R\mathcal{N}_a - (w_{ba} + w_{b1})N_b \quad \text{(A.23a)}$$

$$\frac{dN_2}{dt} = w_{32}N_3 - w_{21}N_2 \quad \text{(A.23b)}$$

$$\frac{dN_3}{dt} = w_{43}N_4 - (w_{31} + w_{32})N_3 \quad \text{(A.23c)}$$

$$\frac{dN_4}{dt} = w_{b1}N_b - w_{43}N_4 \tag{A.23d}$$

We use the usual initial conditions of zero for all excited states to obtain the following solutions for $0 \leq t < t_{off}$:

$$N_b(t) = \frac{R\mathcal{N}_a}{w_{ba}+w_{b1}}\left(1 - e^{-(w_{ba}+w_{b1})t}\right) \tag{A.24a}$$

$$\begin{aligned} N_2(t) = Rw_{b1}w_{32}\mathcal{N}_a \Bigg[& \frac{1}{w_{21}(w_{31}+w_{32})(w_{ba}+w_{b1})} \\ & + \frac{w_{43}}{w_{21}(w_{31}+w_{32}-w_{21})(w_{ba}+w_{b1}-w_{21})(w_{21}-w_{43})} e^{-w_{21}t} \\ & + \frac{w_{43}}{(w_{31}+w_{32})(w_{43}-w_{31}-w_{32})(w_{ba}+w_{b1}-w_{31}-w_{32})(w_{31}+w_{32}-w_{21})} e^{-(w_{31}+w_{32})t} \\ & + \frac{1}{(w_{21}-w_{43})(w_{43}-w_{31}-w_{32})(w_{ba}+w_{b1}-w_{43})} e^{-w_{43}t} \\ & + \frac{w_{43}}{(w_{ba}+w_{b1})(w_{ba}+w_{b1}-w_{21})(w_{ba}+w_{b1}-w_{43})(w_{ba}+w_{b1}-w_{31}-w_{32})} e^{-(w_{ba}+w_{b1})t} \Bigg] \end{aligned} \tag{A.24b}$$

$$\begin{aligned} N_3(t) = Rw_{b1}\mathcal{N}_a \Bigg[& \frac{1}{(w_{31}+w_{32})(w_{ba}+w_{b1})} \\ & + \frac{w_{43}}{(w_{31}+w_{32})(w_{43}-w_{31}-w_{32})(w_{31}+w_{32}-w_{ba}-w_{b1})} e^{-(w_{31}+w_{32})t} \\ & + \frac{1}{(w_{43}-w_{31}-w_{32})(w_{ba}+w_{b1}-w_{43})} e^{-w_{43}t} \\ & + \frac{w_{43}}{(w_{ba}+w_{b1})(w_{ba}+w_{b1}-w_{43})(w_{31}+w_{32}-w_{ba}-w_{b1})} e^{-(w_{ba}+w_{b1})t} \Bigg] \end{aligned} \tag{A.24c}$$

$$\begin{aligned} N_4(t) = Rw_{b1}\mathcal{N}_a \Bigg[& \frac{1}{w_{ba}+w_{b1}} \left\{ \frac{1}{w_{43}} + \frac{1}{w_{ba}+w_{b1}-w_{43}} e^{-(w_{ba}+w_{b1})t} \right\} \\ & + \frac{1}{w_{43}(w_{43}-w_{ba}-w_{b1})} e^{-w_{43}t} \Bigg] \end{aligned} \tag{A.24d}$$

and for $t \geq t_{off}$:

$$N_b(t) = \eta_b e^{-(w_{ba}+w_{b1})(t-t_{off})} \tag{A.25a}$$

$$N_2(t) = \left[\frac{w_{43}w_{32}w_{b1}\eta_b}{(w_{31}+w_{32}-w_{21})(w_{ba}+w_{b1}-w_{21})(w_{43}-w_{21})} + \frac{w_{43}w_{32}\eta_4}{(w_{31}+w_{32}-w_{21})(w_{43}-w_{21})} + \frac{w_{32}\eta_3}{w_{31}+w_{32}-w_{21}} + \eta_2\right] e^{-w_{21}(t-t_{off})} + \left[\frac{w_{43}w_{32}w_{b1}\eta_b}{(w_{ba}+w_{b1}-w_{31}-w_{32})(w_{43}-w_{31}-w_{32})(w_{21}-w_{31}-w_{32})} + \frac{w_{43}w_{32}\eta_4}{(w_{43}-w_{31}-w_{32})(w_{21}-w_{31}-w_{32})} + \frac{w_{32}\eta_3}{w_{21}-w_{31}-w_{32}}\right] e^{-(w_{31}+w_{32})(t-t_{off})} + \left[\frac{w_{43}w_{32}\eta_4}{(w_{43}-w_{31}-w_{32})(w_{43}-w_{21})} + \frac{w_{43}w_{32}w_{b1}\eta_b}{(w_{ba}+w_{b1}-w_{43})(w_{43}-w_{31}-w_{32})(w_{43}-w_{21})}\right] e^{-w_{43}(t-t_{off})} + \frac{w_{43}w_{32}w_{b1}\eta_b}{(w_{ba}+w_{b1}-w_{31}-w_{32})(w_{ba}+w_{b1}-w_{43})(w_{21}-w_{ba}-w_{b1})} e^{-(w_{ba}+w_{b1})(t-t_{off})} \quad \text{(A.25b)}$$

$$N_3(t) = \left[\frac{w_{43}w_{b1}\eta_b}{(w_{43}-w_{31}-w_{32})(w_{ba}+w_{b1}-w_{31}-w_{32})} + \frac{w_{43}\eta_4}{w_{43}-w_{31}-w_{32}} + \eta_3\right] e^{-(w_{31}+w_{32})(t-t_{off})} + \left[\frac{w_{43}\eta_4}{w_{31}+w_{32}-w_{43}} + \frac{w_{43}w_{b1}\eta_b}{(w_{31}+w_{32}-w_{43})(w_{ba}+w_{b1}-w_{43})}\right] e^{-w_{43}(t-t_{off})} + \frac{w_{43}w_{b1}\eta_b}{(w_{ba}+w_{b1}-w_{43})(w_{ba}+w_{b1}-w_{31}-w_{32})} e^{-(w_{ba}+w_{b1})(t-t_{off})} \quad \text{(A.25c)}$$

$$N_4(t) = \left[\frac{w_{b1}\eta_b}{w_{ba}+w_{b1}-w_{43}} + \eta_4\right] e^{-w_{43}(t-t_{off})} + \frac{w_{b1}\eta_b}{w_{43}-w_{ba}-w_{b1}} e^{-(w_{ba}+w_{b1})(t-t_{off})} \quad \text{(A.25d)}$$

In practice, however, obtaining values for the various rate constants by fitting experimental time-resolved PL data to the solutions of any of these models may be difficult, especially if any of the rates w_i are comparable.

It should be noted that for the analysis thus far in this Appendix, there is an implicit assumption that the nanoclusters to not interact with each other, leading to dynamics consisting of sums of simple exponentials for all levels. Given the size distribution of the nanoclusters, and the possibility of energy transfer between nanoclusters before excitation of the RE, it is to be expected that the radiative transition in the Si-NC (i.e., from $b \rightarrow a$) may be better described by *stretched* exponential relaxation.

A.4 Stretched exponential relaxation

A system in which the experimental PL dynamics are characterised by a continuous distribution of lifetimes may be described in terms of a stretched exponential (StrExp) function. For stretched exponential decay, this is given by:

$$N(t) = N_0 e^{-\left(\frac{t}{\tau}\right)^{\beta}} \quad \text{(A.26)}$$

where $0 < \beta < 1$ is a parameter determining the "degree of stretching" and τ is the characteristic lifetime of the decay process. Such a system may arise when the recombination rate depends on the size, local environment, or some other parameter of the nanocluster, such that the cluster size distribution intrinsic to most nanocomposite fabrication methods will in turn yield a distribution in lifetimes, or when migration of excitons between nanoclusters result in quenching by progressively-depleted, randomly-distributed non-radiative trap sites.[15] Due to the continuous nature of the lifetime distribution, (A.26) may equivalently be written as:

$$N(t) = \int_0^\infty e^{\left(-\frac{t}{\tau}\right)} \rho(\tau) \mathrm{d}\tau \tag{A.27}$$

where $\rho(\tau)$ is the distribution function of the recombination lifetimes.[16]

The differential equation giving rise to the StrExp solution shown in (A.26) is:

$$\frac{\mathrm{d}N}{\mathrm{d}t} = -\frac{\beta}{\tau^\beta t^{1-\beta}} N \tag{A.28}$$

Given the form of (A.28), one may interpret such a decay process as having a decay rate which decreases with time rather than remaining constant.

Unfortunately, the effect of introducing a NC recombination as shown in (A.28) to a model such as A.23 is to prevent the solutions from being expressed in a closed form for arbitrary β. If one is primarily interested in the dynamics of the RE, however, one could in principle proceed by approximating the stretched exponential decay of the NC by a bi- or tri-exponential and use the results of A.24 and A.25 with appropriate weights. Clearly, much caution must be given when attempting to fit experimental data to such a model.

Bibliography

[1] F. Priolo, G. Franzò, D. Pacifici, V. Vinciguerra, F. Iacona, and A. Irrera, "Role of the energy transfer in the optical properties of undoped and Er-doped interacting Si nanocrystals", *J. Appl. Phys.*, vol. 89, no. 1, pp. 264–272, 2001.

[2] D. Pacifici, G. Franzò, F. Priolo, F. Iacona, and L. Dal Negro, "Modeling and perspectives of the Si nanocrystals–Er interaction for optical amplification", *Phys. Rev. B*, vol. 67, no. 24, Art. no. 245301, 2003.

[3] A. Hryciw, C. Blois, A. Meldrum, T. Clement, R. DeCorby, and Q. Li, "Photoluminescence from Er-doped silicon oxide microcavities", *Opt. Mater.*, vol. 28, no. 6–7, pp. 873–878, 2006.

[4] P. G. Kik and A. Polman, "Exciton-erbium interactions in Si nanocrystal-doped SiO_2", *J. Appl. Phys.*, vol. 88, no. 4, pp. 1992–1998, 2000.

[5] K. S. Zhuravlev, A. M. Gilinsky, and A. Y. Kobitsky, "Mechanism of photoluminescence of Si nanocrystals fabricated in a SiO_2 matrix", *Appl. Phys. Lett.*, vol. 73, no. 20, pp. 2962–2964, 1998.

[6] G. Allan, C. Delerue, and M. Lannoo, "Nature of luminescent surface states of semiconductor nanocrystallites", *Phys. Rev. Lett.*, vol. 76, no. 16, pp. 2961–2964, 1996.

[7] I. Vasiliev, J. R. Chelikowsky, and R. M. Martin, "Surface oxidation effects on the optical properties of silicon nanocrystals", *Phys. Rev. B*, vol. 65, no. 12, Art. no. 121302, 2002.

[8] D. Kovalev, J. Diener, H. Heckler, G. Polisski, N. Künzner, and F. Koch, "Optical absorption cross sections of Si nanocrystals", *Phys. Rev. B*, vol. 61, no. 7, pp. 4485–4487, 2000.

[9] P. G. Kik and A. Polman, "Towards an Er-doped Si nanocrystal sensitized waveguide laser – the thin line between gain and loss", in *Towards the first silicon laser*, L. Pavesi, S. Gaponenko, and L. Dal Negro, Eds., vol. 93 of *NATO Science Series II*, pp. 383–400. Kluwer Academic Publishers, Norwell, Massachusetts, 2003, ISBN: 1-402-01193-8.

[10] A. Meldrum, A. Hryciw, A. N. MacDonald, C. Blois, K. Marsh, J. Wang, and Q. Li, "Photoluminescence in the silicon-oxygen system", *J. Vac. Sci. Tech. A*, vol. 24, no. 3, pp. 713–717, 2006.

[11] J. Świderski, A. Zajak, M. Skórczakowski, Z. Jankiewicz, and P." Konieczny, "Rare-earth-doped high-power fiber lasers generating in near infrared range", *Optoelec. Rev.*, vol. 12, no. 2, pp. 169–173.

[12] G. H. Dieke, *Spectra and energy levels of rare earth ions in crystals*, Interscience Publishers, 1968, ISBN: 0-470-21390-6.

[13] P. G. Kik, M. L. Brongersma, and A. Polman, "Strong exciton-erbium coupling in Si nanocrystal-doped SiO_2", *Appl. Phys. Lett.*, vol. 76, no. 17, pp. 2325–2327, 2000.

[14] W. H. Loh and A. J. Kenyon, "Excited state absorption in the Si nanocluster-Er material system", *IEEE Phot. Tech. Lett.*, vol. 18, no. 1, pp. 289–291.

[15] J. C. Phillips, "Stretched exponential relaxation in molecular and electronic glasses", *Rep. Prog. Phys.*, vol. 59, pp. 1133, 1996.

[16] K. C. Benny Lee, J. Seigel, S. E. D. Webb, S. Lévêque-Fort, M. J. Cole, R. Jones, K. Dowling, M. J. Lever, and P. M. W. French, "Application of the stretched exponential function to fluorescence lifetime imaging", *Biophys. J.*, vol. 81, no. 3, pp. 1265–1274.

APPENDIX B

Miscellaneous optical characterisation techniques

B.1 Determining the optical constants from a-Si nanocomposite films: Swanepoel's method

B.1.1 Introduction

Silicon nanocomposite films, both intrinsic and doped with rare earths, comprise an attractive class of materials for advanced photonics applications, including waveguide structures,[1–6] microcavities,[7–9] and electroluminescent devices.[10–13] It is therefore crucial to determine the optical constants (the index of refraction n and extinction coefficient k) as a function of wavelength, to allow for accurate modelling of the optical properties of devices incorporating Si NCs.

Possessing values for the optical constants in turn allows the calculation of important parameters required for rate equation modelling and gain calculations, such as the NC absorption cross-section, σ: if the NC number density (n_{NC})[†] and the film absorption coefficient (α) are known, σ may be calculated by

$$\sigma = \frac{\alpha}{n_{\mathrm{NC}}} \tag{B.1}$$

For amorphous nanoclusters, it is also of interest to determine the Urbach energy, E_U, of the band tails: a plot of the natural logarithm of the absorption coefficient vs. photon energy (below the mobility gap) will have a slope of E_U. An estimate of the optical gap may also be extracted from absorption coefficient data via a Tauc plot ($(\alpha h\nu)^{1/2}$ vs. $h\nu$), as mentioned in §1.2.3.

One method of determining the optical constants and thickness of the material is spectroscopic ellipsometry;[14–16] other methods, such as cavity ringdown spectroscopy[7,17,18] and photothermal deflection,[19] only measure the absorption, albeit to great precision. All of these techniques require relatively elaborate apparatus. However, there exists another approach, pioneered by Swanepoel,[20] building on ideas proposed by Manifacier,[21] which allows the optical constants and the thickness of a thin film to be determined though an analysis of one simple measurement: the transmission spectrum, T. In

[†] See §C.2

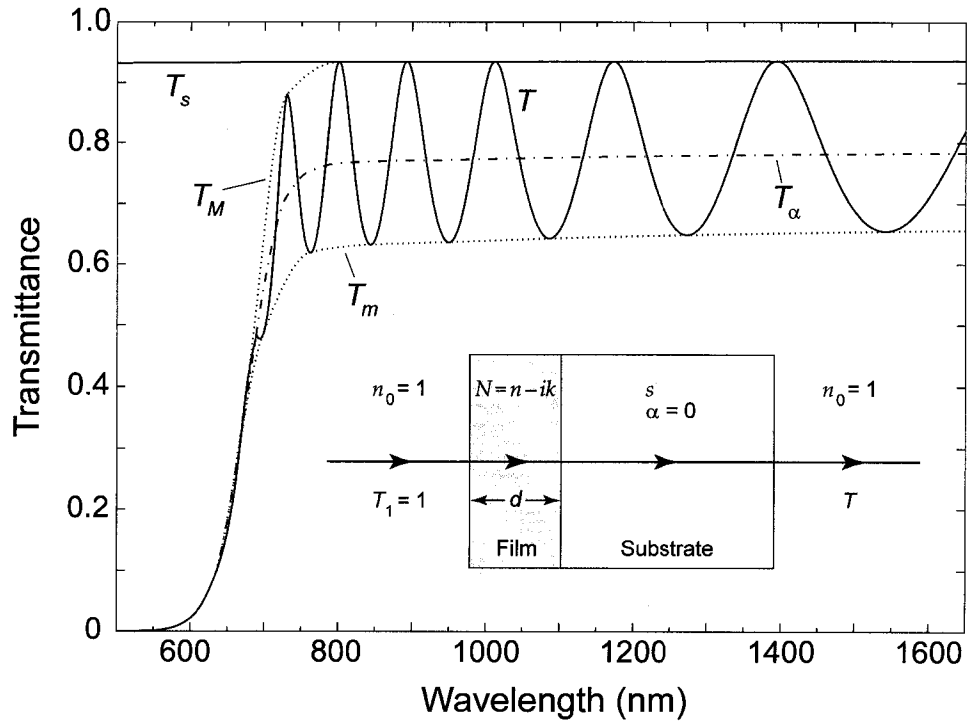

Fig. B.1: Simulated normal-incidence transmission spectra for a 1.5-μm-thick SiO film on a SiO_2 substrate:[‡] full transmission spectrum (T), maxima and minima envelope functions (T_M and T_m, respectively), interference-free transmission (T_α), and substrate-only transmission (T_s). These spectra were calculated using Eqs. (A1), (6), (7), and (17) from Ref.[20], respectively. **Inset:** Schematic of film–substrate system considered in this analysis.

this section of this Appendix, we briefly explain the technique and apply it to Si-NC films annealed at temperatures between 400 and 1000 °C.

B.1.2 Theory

The specimen considered by this technique is a thin film with complex refractive index $N = n - ik$ and thickness d on a thick[†] transparent substrate of refractive index s, as shown in the inset to Fig. B.1. If the film thickness is uniform, interference effects involving multiple reflections at the air–film, film–substrate, and substrate–air interfaces will give rise to a fringed transmission spectrum as shown in Fig. B.1. For this entire analysis, we will assume that all transmission spectra are taken at normal incidence.

Determining n and k

From a transmission measurement of the substrate alone, without a film (T_s), the substrate index of refraction s may be determined from the expression for transmittance through a

[†]Here, "thick" is defined as thick enough that interference effects between waves reflected off the front and back surfaces of the substrate are not observed, due to the small coherence length of the light, variations in parallelism of the substrate faces, lack of collimation of the incident light, etc. In such a scenario, the waves will add incoherently rather than coherently.[22] It should be noted, however, that Swanepoel's technique does not assume an infinite substrate, as does Manifacier's, and thus yields more accurate results for n, k, and d.

[‡]Optical constants for SiO and SiO_2 were taken from the SOPRA database (http://www.sopra-sa.com/more/database.asp).

thick slab:

$$T_s = \frac{(1-R)^2}{1-R^2} = \frac{2s}{s^2+1} \tag{B.2}$$

where $R = [(s-1)/(s+1)]^2$ is the reflectance at an air–substrate interface, yielding

$$s = \frac{1}{T_s} + \left(\frac{1}{T_s^2} - 1\right)^{1/2} \tag{B.3}$$

In the presence of a film of sufficient thickness, numerous interference fringes appear in T, their position governed by

$$2nd = m\lambda \tag{B.4}$$

where m is either an integer (maxima) or half-integer (minima). A rigorous analysis of the film-plus-substrate system yields a transmission spectrum T of the form

$$T = \frac{A'x}{B' - C'x + D'x^2} \tag{B.5}$$

where

$$A' = 16s(n^2+k^2) \tag{B.6a}$$

$$B' = [(n+1)^2+k^2][(n+1)(n+s^2)+k^2] \tag{B.6b}$$

$$\begin{aligned} C' =& [(n^2-1+k^2)(n^2-s^2+k^2) - 2k^2(s^2+1)]2\cos\varphi \\ & - k[2(n^2-s^2+k^2) + (s^2+1)(n^2-1+k^2)]2\sin\varphi \end{aligned} \tag{B.6c}$$

$$D' = [(n-1)^2+k^2][(n-1)(n-s^2)+k^2] \tag{B.6d}$$

and

$$\varphi = \frac{4\pi nd}{\lambda} \tag{B.7a}$$

$$x = e^{-\alpha d} \tag{B.7b}$$

$$\alpha = \frac{4\pi k}{\lambda} \tag{B.7c}$$

For regions in which absorption is not so strong that the interference fringes disappear (e.g., $\lambda \gtrsim 675$ nm in Fig. B.1), we may make the approximation that $k = 0$. Eq. (B.5) is then simplified to

$$T = \frac{Ax}{B - Cx\cos\varphi + Dx^2} \tag{B.8}$$

where

$$A = 16n^2s \tag{B.9a}$$

$$B = (n+1)^3(n+s^2) \tag{B.9b}$$

$$C = 2(n^2-1)(n^2-s^2) \tag{B.9c}$$

$$D = (n-1)^3(n-s^2) \tag{B.9d}$$

From Eq. (B.8), we see that the extrema of the interference fringes are given by

$$T_M = \frac{Ax}{B - Cx + Dx^2} \tag{B.10}$$

$$T_m = \frac{Ax}{B + Cx + Dx^2} \tag{B.11}$$

As we are interested in calculating $n(\lambda)$ and $k(\lambda)$ throughout some continuous wavelength range, we now consider T_M and T_m to be continuous functions of λ,[21] such that they correspond to the *envelopes* of the extrema, as shown in Fig. B.1.

Combining Eqs. (B.10), (B.11), (B.9a), and (B.9c), we may solve for n, yielding

$$n = \left[N + \left(N^2 - s^2\right)^{1/2}\right]^{1/2} \tag{B.12}$$

where

$$N = 2s\frac{T_M - T_m}{T_M T_m} + \frac{s^2 + 1}{2} \tag{B.13}$$

Knowing $n(\lambda)$, we may now solve for x via Eq. (B.10):

$$x = \frac{E_M - \left[E_M^2 - (n^2 - 1)^3(n^2 - s^4)\right]^{1/2}}{(n - 1)^3(n - s^2)} \tag{B.14}$$

where

$$E_M = \frac{8n^2 s}{T_M} + (n^2 - 1)(n^2 - s^2) \tag{B.15}$$

If the film thickness d is known, $k(\lambda)$ can then be obtained from x using Eqs. (B.7b) and (B.7c).

Determining d

Once $n(\lambda)$ has been calculated, the film thickness d may be obtained from Eq. (B.4). If n_1 and n_2 are the refractive indices at two adjacent extrema (found at λ_1 and λ_2), we may solve for d to yield

$$d = \frac{\lambda_1 \lambda_2}{2(\lambda_1 n_2 - \lambda_2 n_1)} \tag{B.16}$$

This equation is sensitive to errors in n;[20] however, Swanepoel uses the following method to increase the accuracy of both n and d.

Values for d are calculated using Eq. (B.16) for all pairs of extrema visible in the spectrum of T, and obvious outliers are discarded; the average of these values is denoted $\bar{d}_1$. Next, Eq. (B.4) is used to determine the order numbers m corresponding to each extremum. Rounding these order numbers to the nearest integer or half-integer, values for d are recalculated using Eq. (B.4), the average of which we denote $\bar{d}_2$. Finally, again using Eq. (B.4) and $\bar{d}_2$, values for n are recalculated. These corrected values for n can then be used to recalculate x via Eq. (B.14), yielding corrected values for k. We now apply this approach to experimental transmission spectra obtained for our SiO films.

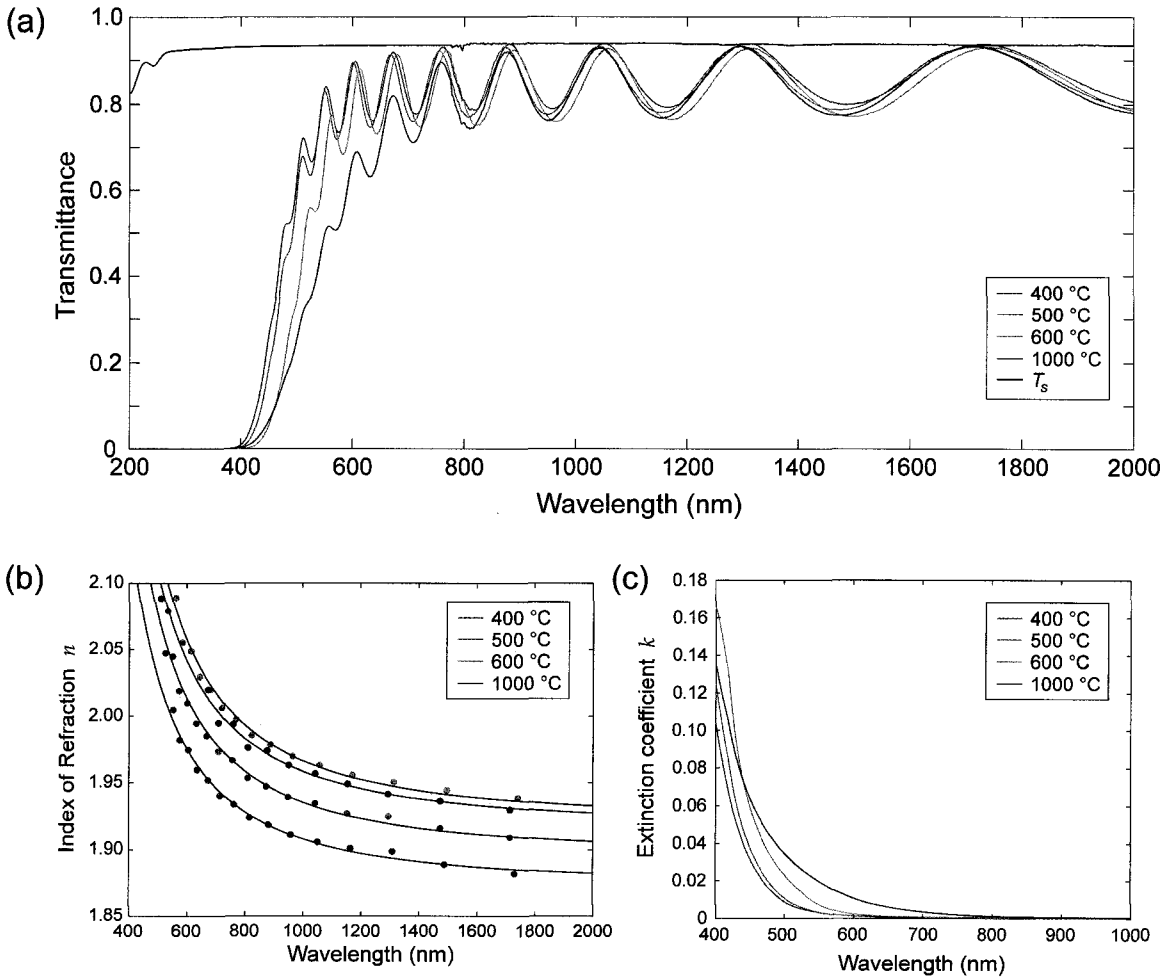

Fig. B.2: Swanepoel analysis of SiO films annealed at 400, 500, 600, and 1000 °C. In (a), the transmission spectra for the four specimens and a blank SiO_2 substrate (T_s) are shown. Following the Swanepoel analysis explained in §B.1.2, the refractive index n and extinction coefficient k were extracted, shown in (b) and (c), respectively. The solid lines in (b) indicate Wemple-DiDomenico fits for n.

B.1.3 Swanepoel analysis of a-Si-NC and c-Si-NC films

Transmission spectra were obtained from $\sim$ 1.5-μm-thick SiO films annealed for 1 h at 400, 500, 600 and 1000 °C in 95% N_2+5% H_2 (forming gas), using a Perkin-Elmer NIR–UV spectrophotometer, for the wavelength range $\lambda \in [200, 2000]$ nm; a reference transmission spectrum from a blank SiO_2 substrate was also measured (Fig. B.2a). In performing the Swanepoel analysis on these data, the values of the fringe extrema, T_M and T_m, were corrected for the finite spectral bandwidth of the spectrophotometer (2 nm for $\lambda \leq 800$ nm and 4 nm for $\lambda > 800$ nm), as explained in §5 of Swanepoel's paper;[20] the effect was minimal ($< 0.4\%$ difference for all extrema).

The index of diffraction n and extinction coefficient k obtained from the analysis are shown in Fig. B.2b and B.2c, respectively. The index of refraction data has been fit using the Wemple-DiDomenico dispersion equation for a single oscillator:[23]

$$n^2(\omega) - 1 = \frac{E_d E_0}{E_0^2 - (\hbar\omega)^2} \tag{B.17}$$

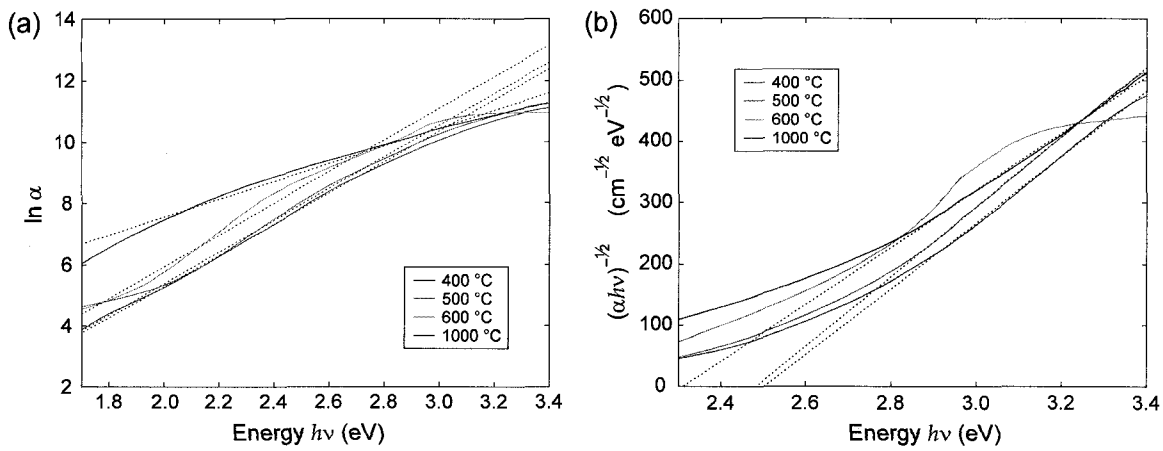

Fig. B.3: Analysis of the absorption coefficient α for the four SiO films studied in §B.1.3: (a) Urbach plot ($\ln\alpha$ vs. $h\nu$), to determine E_U, and (b) Tauc plot ($(\alpha h\nu)^{1/2}$ vs. $h\nu$), to determine E_g. The α data from 600-°C-annealed film did not exhibit good linearity in the same energy range used for the three other films, so no fit was calculated for that specimen.

where E_0 is the effective oscillator energy for band-to-band transitions,[†] and E_d is the dispersion energy. This simple expression is remarkably accurate for a wide range of solids, crystalline and amorphous alike.[23] The E_0 and E_d values determined from the fitting is summarised in Table B.1. Substituting the calculated values for n, k, and d back into Eq. (B.5) yields transmission spectra which match the experimental T curves extremely well throughout the entire wavelength range.

B.1.4 Analysis of α: determining E_U, E_g, and σ

We may now use the values for the absorption coefficient α obtained from the Swanepoel analysis to calculate several other useful parameters characterising the Si-NC films, namely the Urbach energy for the band tails (E_U), the optical band gap (E_g), and the absorption cross-section (σ). σ is particularly useful in rate modelling, where it is required to calculate the excitation rate (see Appendix A).

Due to the exponential band tail density of states, transitions between band tails yield an absorption edge proportional to $e^{-h\nu/E_U}$, where E_U, the Urbach energy, is an empirical parameter describing the distribution of states.[24] As such, a semilogarithmic plot of α vs. $h\nu$ will yield a value for E_U from the slope. In Fig. B.3a, we plot a linear fit of $\ln\alpha$ for the energy range $h\nu \in [1.9, 2.9]$ eV, to avoid the deviation from linearity near the mobility gap; values for E_U are summarised in Table B.1. For the three a-Si-NC films, we obtain $E_U \approx 200$ meV, significantly higher than the ~30–50 meV quoted for bulk a-Si.[25] Such a broadening of the band tails for nanoscale a-Si structures has been attributed to a widening of the mobility gap with respect to bulk, the lowest-lying band tail states remaining essentially unaltered.[26,27]

Determining the optical Tauc band gap via a plot of $(\alpha h\nu)^{1/2}$ vs. $h\nu$ is a well-known optical characterisation technique.[28] For amorphous materials, absorption can take place via gap-to-tail, tail-to-band, and band-to-band state transitions. As this last process occurs at higher energies and with greater probability, Tauc plots considering energies for which $\alpha \gtrsim 10^4$ cm^{-1} are often used;[29] as mentioned in §1.2.3, however, generating an op-

[†]Empirically, $E_0 \approx 2E_g$, where E_g is the optical band gap.

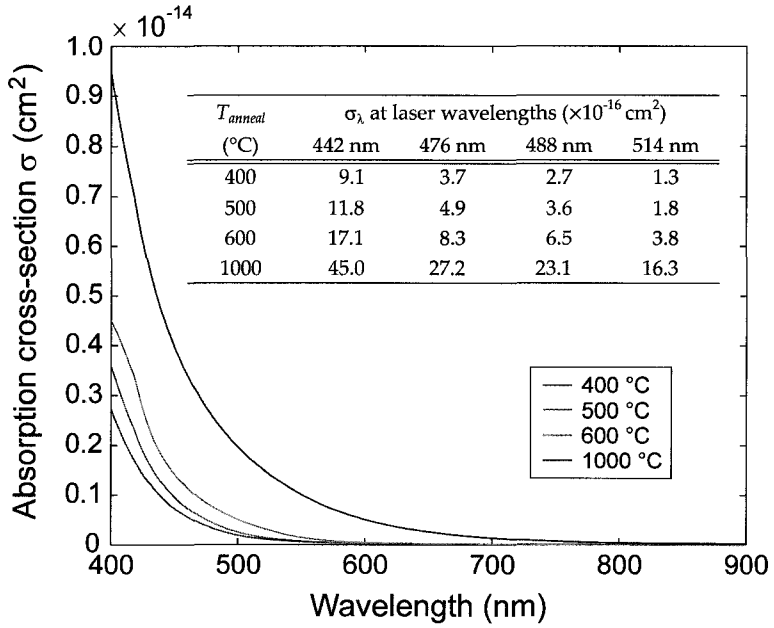

T_{anneal}	σ_λ at laser wavelengths ($\times 10^{-16}$ cm^2)			
(°C)	442 nm	476 nm	488 nm	514 nm
400	9.1	3.7	2.7	1.3
500	11.8	4.9	3.6	1.8
600	17.1	8.3	6.5	3.8
1000	45.0	27.2	23.1	16.3

Fig. B.4: Si-NC absorption cross-sections for the four films studied in §B.1.3, calculated using Eq. (B.4). The table in the inset summarises values of σ at important laser wavelengths.

tical gap from a Tauc plot may not be a true representation of the mobility gap. Fig. B.3b shows Tauc plots for the four SiO films. The best-fit lines were calculated using the energy range $h\nu \in [2.8, 3.4]$ eV, corresponding to $\alpha \gtrsim 1.2 \times 10^4$ cm^{-1}. For the 600-°C-annealed film, the data was insufficiently linear to provide a meaningful fit, so the linear regression was not performed. Values for the Tauc optical band gap are given in Table B.1. Being approximately 2.2 times larger than the corresponding effective oscillator energies E_0 obtained from the Wemple-DiDomenico fits of n, the Tauc gaps are in fair agreement with the empirical $E_0 \approx 2E_g$ law. Note that the a-Si-NC nanocomposite films are significantly larger than the mobility gaps for bulk or even continuous thin film a-Si, typically in the 1.7–1.9 eV range.[29–31] This is attributed to quantum confinement effects: a shift in optical gap by ~0.5 eV has been reported for ~1-nm-thick a-Si:H superlattices (periodic quantum wells).[32]

Finally, from the α spectra for the four films, along with the nanocluster number density n_{NC} values calculated in §C.2, we use Eq. (B.4) to determine the NC absorption cross-section, σ, shown in Fig. B.4.

Table B.1: Summary of parameters obtained via the Swanepoel analysis of SiO films annealed at 400, 500, 600, and 1000 °C. $\bar{d}$ is the thickness of the film, E_d and E_0 are the Wemple-DiDomenico fitting parameters for the index of refraction, E_U is the band tail Urbach energy, and E_g is the Tauc optical gap.

T_{anneal} (°C)	$\bar{d} \pm \delta\bar{d}$ (nm)	E_d (eV)	E_0 (eV)	E_U (meV)	E_g (eV)
400	1378±3	14.18	5.64	197	2.50
500	1346±3	13.92	5.36	194	2.49
600	1350±20	13.67	5.07	194	—
1000	1330±30	14.09	5.26	346	2.31

B.2 Quadrature frequency-resolved spectroscopy (QFRS)

B.2.1 Introduction

In quadrature frequency-resolved spectroscopy, the excitation consists of continuous-wave (CW) and sinusoidal components, with detection set in quadrature (i.e., the resultant PL signal is multiplied by a sinusoid phase-shifted by $\pi/2$ to the excitation modulation and averaged over one period). As a method of determining the distribution of luminescence lifetimes, QFRS possesses several advantages over time-resolved spectroscopy (TRS). TRS suffers if the system includes lifetime components which are longer than the pulse repetition time: in this case TRS probes the relaxation of the system to a metastable excited state rather than its ground state, and the resultant lifetimes appear proportional to the excitation pulse widths.[33] Also, QFRS is not limited by the signal-to-noise ratio for long lifetime components,[34] and is insensitive to DC offsets in the detector.[33]

B.2.2 Theory

The photoluminescence from a typical experimental system consisting of a large number of emitting species is in general characterised by a distribution in lifetimes, $P(\tau)$. We first consider the component of the PL with a single lifetime τ. Such a component will have a normalised impulse response function (i.e., response to δ-function excitation) of the form

$$h(t;\tau) = \frac{1}{\tau} e^{-\frac{t}{\tau}} \tag{B.18}$$

The excitation used for QFRS, modulated at an angular frequency of ω, may be written as

$$G(t) = G_0 + g\sin(\omega t) \qquad g < G_0 \tag{B.19}$$

For times much longer than τ after the excitation is switched on, the resultant PL is given by the convolution of $h(t;\tau)$ and $G(t)$:

$$\begin{aligned} I(t;\tau) &= h(t;\tau) * G(t) \\ &= \int_{-\infty}^{t} \frac{1}{\tau} \exp\left[\frac{-(t-u)}{\tau}\right] [G_0 + g\sin(\omega u)]\ du \\ &= G_0 + \frac{g}{1+\omega^2\tau^2} [\sin(\omega t) - \omega\tau\cos(\omega t)] \\ &= G_0 + g\cos\phi\sin(\omega t - \phi) \end{aligned} \tag{B.20}$$

where we have made the substitution $\tan\phi = \omega\tau$.

For detection in quadrature, we multiply $I(t;\tau)$ by $-\cos(\omega t)$ and average over one period, yielding a QFRS signal of the form

$$\begin{aligned} S(\omega;\tau) &= \frac{\omega}{2\pi} \int_0^{\frac{2\pi}{\omega}} -[G_0 + g\cos\phi\sin(\omega t - \phi)]\cos(\omega t) \\ &= \frac{g}{2\left[(\omega\tau)^{-1} + \omega\tau\right]} \end{aligned} \tag{B.21}$$

Setting $g = 4$ in this expression normalises the peak value of $S(\omega;\tau)$, found at $\omega\tau = 1$, to unity. From Fig. B.5a, we see that a semilogarithmic plot of $S(\omega;\tau)$ is a symmetric line

with a full-width at half-maximum of ~1.15 decades. For a system with a distribution of lifetimes, the resultant QFRS signal is given by

$$S(\omega) = \int_0^\infty P(\tau) S(\omega;\tau)\, d\tau \tag{B.22}$$

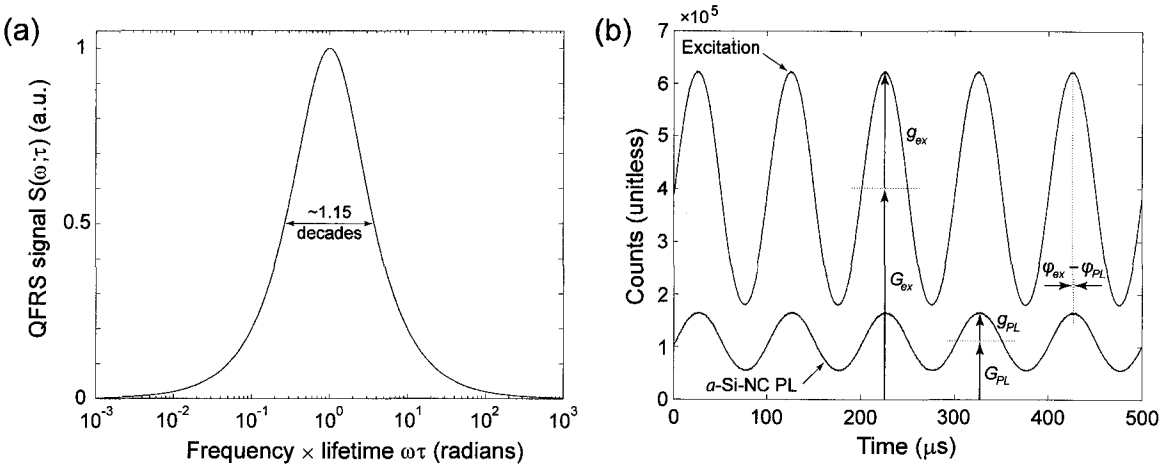

Fig. B.5: (a) Normalised single lifetime QFRS peak, $S(\omega;\tau)$. (b) Time-domain realisation of QFRS signal from a ~200-nm-thick SiO film annealed at 500 °C (f=10 kHz, 514 nm excitation, $\sigma\overline{\Phi} \approx 16\ \mathrm{cm^{-2}s^{-1}}$), as measured with a PMT.

Although QFRS is usually executed using a lock-in amplifier (LIA), which measures the in-phase and out-of-phase (quadrature) components of a signal with respect to a reference sinusoid, it is also possible to perform the measurement by fitting *time*-domain data to sinusoids, circumventing the need for a LIA. For each frequency f, the scattered laser light and PL signals are fit to the form $I_i(t) = G_i + g_i \sin(2\pi f t + \varphi_i)$. Dividing the PL signal by its DC component, G_{PL}, effectively removes errors due to small fluctuations in averaged laser intensity between measurements; dividing further by the normalised excitation modulation amplitude, g_{ex}/G_{ex}, corrects the PL signal for any changes in AOM performance as a function of frequency. Multiplying the normalised PL signal by a sinusoid phase-shifted by $\pi/2$ to the excitation and averaging over one period yields a QFRS signal of the form

$$S(\omega) = \frac{g_{PL} G_{ex}}{g_{ex} G_{PL}} \sin(\varphi_{ex} - \varphi_{PL}) \tag{B.23}$$

where all variables are potentially functions of ω. An example of such a fit is shown in Fig. B.5b, for 514-nm excitation ($\sigma\overline{\Phi} \approx 16\ \mathrm{cm^{-2}s^{-1}}$) with a modulation frequency of $f = 10$ kHz. By scanning over a range of frequencies, the resultant QFRS spectrum $S(\omega)$ may be obtained; such a process was used for the inset to Fig. 7.3.

For a given $S(\omega)$ spectrum, the inverse problem of determining $P(\tau)$ is in general ill-posed, as it is with time-resolved PL data. When fitting an experimentally-observed QFRS spectrum to a number of single-exponential $S(\omega;\tau)$ peaks, it can be easier to discriminate between bi-, tri-, or higher-order exponentials than in TRS, since each $S(\omega;\tau)$ has a set width which is independent of its amplitude; in some cases, unfortunately, difficulties of this sort do still remain. Ultimately, however, the advantages of QFRS, as stated in §B.2.1, make it a valuable, complementary technique to investigate a material system's PL dynamics.

Bibliography

[1] P. G. Kik, M. L. Brongersma, and A. Polman, "Strong exciton-erbium coupling in Si nanocrystal-doped SiO_2", *Appl. Phys. Lett.*, vol. 76, no. 17, pp. 2325–2327, 2000.

[2] H. S. Han, S. Y. Seo, J. H. Shin, and D. S. Kim, "1.54 μm Er^{3+} photoluminescent and waveguiding properties of erbium-doped silicon-rich silicon oxide", *J. Appl. Phys.*, vol. 88, no. 4, pp. 2160–2162, 2000.

[3] H. S. Han, S. Y. Seo, and J. H. Shin, "Optical gain at 1.54 μm in erbium-doped silicon nanocluster sensitized waveguide", *Appl. Phys. Lett.*, vol. 79, no. 27, pp. 4568–4570, 2001.

[4] H. S. Han, S. Y. Seo, J. H. Shin, and N. Park, "Coefficient determination related to optical gain in erbium-doped silicon-rich silicon oxide waveguide amplifier", *Appl. Phys. Lett.*, vol. 81, no. 20, pp. 3720–3722, 2002.

[5] N. Daldosso, D. Navarro-Urrios, M. Melchiorri, L. Pavesi, F. Gourbilleau, M. Carrada, R. Rizk, C. Garcia, P. Pellegrino, B. Garrido, and L. Cognolato, "Absorption cross section and signal enhancement in Er-doped Si nanocluster rib-loaded waveguides", *Appl. Phys. Lett.*, vol. 86, no. 26, Art. no. 261103, 2005.

[6] P. G. Kik and A. Polman, "Towards an Er-doped Si nanocrystal sensitized waveguide laser – the thin line between gain and loss", in *Towards the first silicon laser*, L. Pavesi, S. Gaponenko, and L. Dal Negro, Eds., vol. 93 of *NATO Science Series II*, pp. 383–400. Kluwer Academic Publishers, Norwell, Massachusetts, 2003, ISBN: 1-402-01193-8.

[7] D. Amans, S. Callard, A. Gagnaire, J. Joseph, F. Huisken, and G. Ledoux, "Spectral and spatial narrowing of the emission of silicon nanocrystals in a microcavity", *J. Appl. Phys.*, vol. 95, no. 9, pp. 5010–5013, 2004.

[8] F. Iacona, G. Franzò, E. C. Moreira, and F. Priolo, "Silicon nanocrystals and Er^{3+} ions in an optical microcavity", *J. Appl. Phys.*, vol. 89, no. 12, pp. 8354–8356, 2001.

[9] F. Iacona, G. Franzò, E. C. Moreira, D. Pacifici, A. Irrera, and F. Priolo, "Luminescence properties of Si nanocrystals embedded in optical microcavities", *Mater. Sci. Eng. C*, vol. 19, no. 1–2, pp. 377–381, 2002.

[10] S. Chan and P. M. Fauchet, "Silicon microcavity light emitting devices", *Opt. Mater.*, vol. 17, no. 1–2, pp. 31–34, 2001.

[11] A. Irrera, M. Miritello, D. Pacifici, G. Franzò, F. Priolo, F. Iacona, D. Sanfilippo, G. Di Stefano, and P. G. Fallica, "Electroluminescence properties of SiO_x layers implanted with rare earth ions", *Nucl. Instr. Meth. B*, vol. 216, pp. 222–227, 2004.

[12] D. Pacifici, A. Irrera, G. Franzò, M. Miritello, F. Iacona, and F. Priolo, "Erbium-doped Si nanocrystals: optical properties and electroluminescent devices", *Physica E*, vol. 16, no. 3–4, pp. 331–340, 2003.

[13] M. Sopinskyy and V. Khomchenko, "Electroluminescence in SiO_x films and SiO_x-film-based systems", *Curr. Opin. Sol. State Mater. Sci.*, vol. 7, no. 2, pp. 97–109, 2003.

[14] J. A. Woollam, B. Johs, C. M. Herzinger, J. Hilkiker, R. Synowicki, and C. L. Bungay, "Overview of variable angle spectroscopic ellipsometer (VASE), Part I: Basic theory and typical applications", in *Optical Metrology*, G. A. Al-Jumaily, Ed. Proc. SPIE, July 1999, vol. CR72 of *Critical reviews of optical science and technology*.

[15] B. Johs, J. A. Woollam, C. M. Herzinger, J. Hilkiker, R. Synowicki, and C. L. Bungay, "Overview of variable angle spectroscopic ellipsometer (VASE), Part II: Advanced applications", in *Optical Metrology*, G. A. Al-Jumaily, Ed. Proc. SPIE, July 1999, vol. CR72 of *Critical reviews of optical science and technology*.

[16] D. Amans, S. Callard, A. Gagnaire, J. Joseph, G. Ledoux, and F. Huisken, "Ellipsometric study of silicon nanocrystal optical constants", *J. Appl. Phys.*, vol. 93, no. 7, pp. 4173–4179, 2003.

[17] H. Mertens, A. Polman, I. M. P. Aarts, W. M. M. Kessels, and M. C. M. van de Sanden, "Absence of the enhanced intra-4f transition cross section at 1.5 μm of Er^{3+} in Si-rich SiO_2", *Appl. Phys. Lett.*, vol. 86, no. 24, Art. no. 241109, 2005.

[18] I. M. P. Aarts, B. Hoex, A. H. M. Smets, R. Engeln, W. M. M. Kessels, and M. C. M. van de Sanden, "Direct and highly sensitive measurement of defect-related absorption in amorphous silicon thin films by cavity ringdown spectroscopy", *Appl. Phys. Lett.*, vol. 84, no. 16, pp. 3079–3081, 2004.

[19] A. C. Boccara, D. Fournier, W. Jackson, and N. M. Amer, "Sensitive photothermal deflection technique for measuring absorption in optically thin media", *Opt. Lett.*, vol. 5, no. 9, pp. 377–379, 1980.

[20] R. Swanepoel, "Determination of the thickness and optical constants of amorphous silicon", *J. Phys. E*, vol. 16, no. 12, pp. 1214–1222, 1983.

[21] J. C. Manifacier, J. Gasiot, and J. P. Fillard, "Simple method for determination of optical constants n, k and thickness of a weakly absorbing thin film", *J. Phys. E*, vol. 9, no. 11, pp. 1002–1004, 1976.

[22] H. A. Macleod, *Thin-film optical filters*, Institute of Physics Publishing, Bristol, third edition, 2001, ISBN: 0-750-30688-2, p. 67.

[23] S. H. Wemple and M. DiDomenico, "Behavior of the electronic dielectric constant in covalent and ionic materials", *Phys. Rev. B*, vol. 3, no. 4, pp. 1338–1351, 1971.

[24] J. I. Pankove, *Optical processes in semiconductors*, Dover, Mineola, 1971, ISBN: 0-486-60275-3.

[25] M. J. Estes and G. Moddel, "Luminescence from amorphous silicon nanostructures", *Phys. Rev. B*, vol. 54, no. 20, pp. 14633–14642, 1996.

[26] S. Miyazaki, K. Yamada, and M. Hirose, "Optical and electrical properties of a-si$_3$n$_4$:h/a-si:h superlattices prepared by plasma-enhanced nitridation technique", *J. Non-Cryst. Sol.*, vol. 137–138, pp. 1119–1122, 1992.

[27] F. Yonezawa and F. Satoh, "Optical absorption spectra of bulk and multilayer amorphous semiconductors", *Philos. Mag. B*, vol. 60, no. 1, pp. 109–117, 1989.

[28] J. Tauc, "Optical properties of amorphous semiconductors", in *Amorphous and liquid semiconductors*, J. Tauc, Ed., pp. 159–220. Plenum Publishing Company Ltd, New York, 1974, ISBN: 0-306-30777-4.

[29] G. Tamizhmani, M. Cocivera, R. T. Oakley, C. Fischer, and M. Fujimoto, "Physical characterization of a-Si thin films deposited by thermal decomposition of iodosilanes", *J. Phys. D*, vol. 24, no. 6, pp. 1015–1021, 1991.

[30] R. A. Street, *Hydrogenated amorphous silicon*, Cambridge University Press, Cambridge, 1991, ISBN: 0-521-37156-2.

[31] J. Bullot, P. Cordier, and M. Gauthier, "Photoconductivity in hydrogenated amorphous silicon: I. Thermal emission and hopping of trapped charges", *Philos. Mag. B*, vol. 67, no. 6, pp. 751–762, 1993.

[32] B. Abeles and T. Tiedje, "Amorphous semiconductor superlattices", *Phys. Rev. Lett.*, vol. 51, no. 21, pp. 2003–2006, 1983.

[33] S. P. Depinna and D. J. Dunstan, "Frequency-resolved spectroscopy and its application to the analysis of recombination in semiconductors", *Philos. Mag. B*, vol. 50, no. 5, pp. 579–597, 1984.

[34] L. R. Tessler and D. Biggemann, "Temperature independent Er^{3+} photoluminescence lifetime in a-Si:H⟨Er⟩ and a-SiO_x:H⟨Er⟩", *Mater. Sci. Eng. B*, vol. 105, no. 1–3, pp. 165–168, 2003.

APPENDIX C

Miscellaneous calculations

C.1 Reflectance, transmittance, and absorptance of a thin-film stack

The reflectance modelling of the microcavities discussed in Chap. 3 (Fig. 3.2b) was performed using a MATLAB implementation of the characteristic matrix approach to calculating the reflectance of an assembly of thin films. By this technique, the reflectance, transmittance, and absorptance of an arbitrary number of thin films deposited on a thick substrate can be calculated so long as the complex index of refraction ($N = n - ik$) and thickness of each layer, and N of the substrate, are known. We summarise the main results of this analysis here.[1]

Consider an assembly of q thin films, each with thickness d_r and with complex index of refraction N_r (Fig. C.1). The ratio of the magnetic and electric fields of a light wave travelling through vacuum is the free-space optical admittance, $\mathcal{Y} = 2.6544 \times 10^{-3}$ S. In a medium, the optical admittance is $y = N\mathcal{Y}$, which is in general complex.

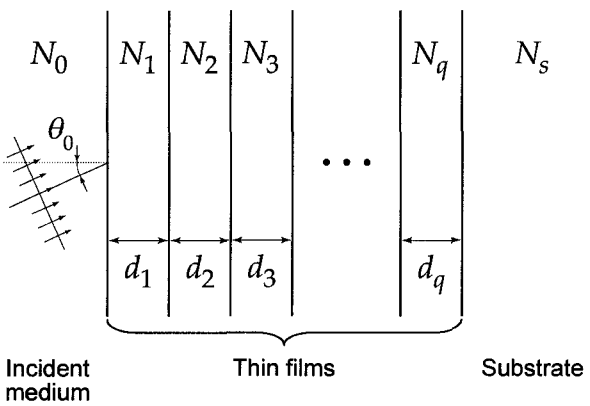

Fig. C.1: Notation for an assembly of q thin films on a thick substrate. In general, we allow N of the incident medium and the substrate to be complex, as well as that of the films. θ_0 is the angle of incidence.

We introduce a tilted optical admittance, η, which is different for p-polarised (TM) and

s-polarised (TE) waves.

$$\eta_p = \frac{N\mathcal{Y}}{\cos\theta} \tag{C.1}$$

$$\eta_s = N\mathcal{Y}\cos\theta \tag{C.2}$$

where θ is the angle from the normal within the layer. For normal incidence, these two polarisation states are not well-defined, and $\eta_p = \eta_s$.

We now consider the thin-film assembly as a single layer, defining a total admittance $Y = C/B$, where

$$\begin{bmatrix} B \\ C \end{bmatrix} = \left\{ \prod_{r=1}^{q} \begin{bmatrix} \cos\delta_r & \frac{i}{\eta_r}\sin\delta_r \\ i\eta_r \sin\delta_r & cos\delta_r \end{bmatrix} \right\} \begin{bmatrix} 1 \\ \eta_s \end{bmatrix} \tag{C.3}$$

where $\delta_r = \frac{2\pi N d_r \cos\theta_r}{\lambda}$. θ_r may be found by Snell's law:

$$N_0 \sin\theta_0 = N_r \sin\theta_r \tag{C.4}$$

For reflectance and transmittance to be well-defined, η_0 must be real. Once B and C are known, the reflectance, transmittance, and absorptance at a given wavelength λ may be calculated via

$$R' = \left(\frac{\eta_0 B - C}{\eta_0 B + C}\right)\left(\frac{\eta_0 B - C}{\eta_0 B + C}\right)^* \tag{C.5a}$$

$$T' = \frac{4\eta_0\, \Re(\eta_m)}{(\eta_0 B + C)(\eta_0 B + C)^*} \tag{C.5b}$$

$$A' = \frac{4\eta_0\, \Re(BC^* - \eta_m)}{(\eta_0 B + C)(\eta_0 B + C)^*} = 1 - R - T \tag{C.5c}$$

Eqns. (C.5) give results for the so-called *infinite substrate* approximation, as the effect of incoherent addition of multiple reflections between the surfaces of the substrate has not been considered.† For the reflectance of a typical microcavity structure with a thick, essentially opaque bottom mirror, this effect is negligible. However, when considering transparent films on a transparent substrate, as is often the case when performing Swanepoel's analysis (see §B.1), the infinite substrate approximation can yield unphysical results, such as transmittance maxima which exceed the maximum transmission through an air–substrate boundary.[3] The correct expressions for reflectance and transmittance are then[4]

$$R = \frac{R' + R_s - 2R'R_s}{1 - R'R_s} \tag{C.6}$$

$$T = \left(\frac{1}{T'} + \frac{1}{T_s} - 1\right)^{-1} \tag{C.7}$$

where $R_s = \left(\frac{s-1}{s+1}\right)^2$ and $T_s = \frac{4s}{(s+1)^2}$ are the reflectance and transmittance at the substrate–air boundary, respectively.

†This was the situation considered by Manifacier[2] in his algorithm to determine the optical constants from a single transmittance measurement (see B.1).

C.2 Nanocluster number density

The number density of nanoclusters in a Si nanocomposite film (n_{NC}, in cm^{-3}) is an important parameter characterising the material, as it is used in the determination of the NC absorption cross-section σ (see §B.1), and is useful for comparison to ensembles of c- or a-Si NCs used in simulations (see Chap. 6). From electron energy-loss spectroscopy (EELS) and TEM measurements on our SiO films annealed at different temperatures, we may estimate an average value for n_{NC}.

By fitting EEL spectra from our films to linear combinations of spectra obtained from pure SiO_2, Si, and bulk SiO, the fraction of the Si atoms in the film existing in an Si phase, $x_{\text{Si phase}}$, may be extracted.[5] Assuming a monodisperse ensemble of NCs, the number density of the NCs in the film may therefore be expressed as

$$\begin{aligned} n_{NC} &= \left(\frac{\#\text{ Si atoms per NC}}{\text{cm}^3}\right)\left(\frac{\#\text{ Si atoms}}{\text{NC}}\right)^{-1} \\ &= \left(\frac{\rho_{SiO} N_A x_{\text{Si phase}}}{M_{Si} + M_O}\right)\left(\frac{4}{3}\pi \left\langle a^3 \right\rangle \frac{\rho_{Si} N_A}{M_{Si}}\right)^{-1} \\ &= \frac{\rho_{SiO}}{\rho_{Si}} \frac{M_{Si}}{M_{Si} + M_O} \frac{3}{4\pi \left\langle a^3 \right\rangle} x_{\text{Si phase}} \end{aligned} \tag{C.8}$$

where N_A is Avogadro's number (6.02×10^{23} mol^{-1}), ρ_{SiO}=2.13 g/cm^3, ρ_{Si}=2.32 g/cm^3, M_i is the molar mass of element i, and $\langle a^3 \rangle$ is the cube of the radius of a nanocluster with the mean NC volume.

Using the EELS data and values for $\langle a^3 \rangle$ as determined from TEM for SiO films annealed for 1 hr in 95% N_2 + 5% H_2 forming gas at temperatures ranging from 400 to 1100 °C, the calculation for n_{NC} yields results summarised in Table C.1.

Table C.1: Calculation of the Si-NC number density n_{NC} for SiO films.

T_{anneal} (°C)	$x_{\text{Si phase}}$ †	$\langle a^3 \rangle^{1/3}$ (nm)	n_{NC} (cm^{-3})
400	0.16	1.23	1.20×10^{19}
500	0.26	1.49	1.09×10^{19}
600	0.26	1.46	1.16×10^{19}
700	0.28	1.54	1.08×10^{19}
800	0.29	1.59	1.00×10^{19}
900	0.31	1.73	8.37×10^{18}
1000	0.35	2.22	4.49×10^{18}
1100	0.43	3.19	1.85×10^{18}

†The values of $x_{\text{Si phase}}$ for T_{anneal} = 700, 800, and 900 °C are unpublished (Quan Li, 2006); all other values are taken from Ref.[5]

C.3 Nanocluster size distributions

Preparing a practically-monodisperse ensemble of particles is extremely difficult. Instead, many fabrication processes result in particle size distributions with significant widths. In particular, particles formed via nucleation and growth—such as a phase-separation process in a supersaturated solid solution—typically follow a *lognormal* distribution.[6–8]

TEM images of NC-containing thin films† can yield rough histograms of the NC sizes after careful scrutiny, which may then be fit to lognormal distribution functions. Such a fit (with two free parameters) can be useful for describing the specimen sizes in a systematic manner, since the properties of the lognormal distribution are well-known; also, it may help to suggest the existence of smaller particles which are not well-resolved by TEM techniques.

The lognormal distribution is a continuous distribution with the property, as befits its name, that the logarithm of its variable is described by a normal (Gaussian) distribution.[10] The probability density of the lognormal distribution may be written in the following form:[10]

$$\rho(x) = \frac{1}{S\sqrt{2\pi}x} e^{-\frac{(\ln x - M)^2}{2S^2}} \tag{C.9}$$

Where S and M are real parameters. This distribution has the following properties:

- First raw moment (population mean): $\mu_1' = \mu = \langle x \rangle = e^{M+\frac{S^2}{2}}$
- Second raw moment: $\mu_2' = \langle x^2 \rangle = e^{2(M+S^2)}$
- Third raw moment: $\mu_3' = \langle x^3 \rangle = e^{3M+\frac{9S^2}{2}}$
- Variance: $\sigma^2 = \langle (x-\mu)^2 \rangle = e^{S^2+2M}\left(e^{S^2}-1\right)$
- Skewness: $\gamma_1 = \sqrt{e^{S^2}-1}\left(2+e^{S^2}\right)$ [N.B. $\gamma_1 > 0 \,\forall\, S$]
- Position of maximum: $x_{\text{peak}} = e^{-s^2+M}$
- Maximum value: $\rho(x_{\text{peak}}) = \frac{1}{\sqrt{2\pi}S} e^{\frac{s^2}{2}-M}$

Histograms of NC population sizes were determined by counting ~100 particles on plan-view TEM micrographs[11] and fit to Eq. (C.9), as shown in Fig. C.2; the numerical results of this fitting is summarised in Table C.2.

Table C.2: Summary of fitting parameters and useful properties of lognormal Si-NC size distribution fits to the histograms shown in Fig. C.2. The S and M parameters yield lognormal distributions for the NC diameter d. The mean radius $\langle a \rangle$ in Å as well as the mean diameter $\langle d \rangle$ in nm is both given for easy comparison with values discussed in Chap. 6.

T_{anneal} (°C)	S	M	$\langle d \rangle$ (nm)	$\langle a \rangle$ (Å)	σ^2 (nm^2)
400	0.136	0.974	2.67	13.4	2.68
500	0.171	1.092	3.02	15.1	3.46
600	0.128	1.137	3.14	15.7	3.69
700	0.149	1.193	3.33	16.7	4.18
800	0.123	1.211	3.38	16.9	4.27
900	0.132	1.300	3.70	18.5	5.13
1000	0.196	1.490	4.52	22.6	7.82
1100	0.158	1.874	6.60	33.0	16.41

†See, for example, Fig. 4.1 and Refs.[5,9].

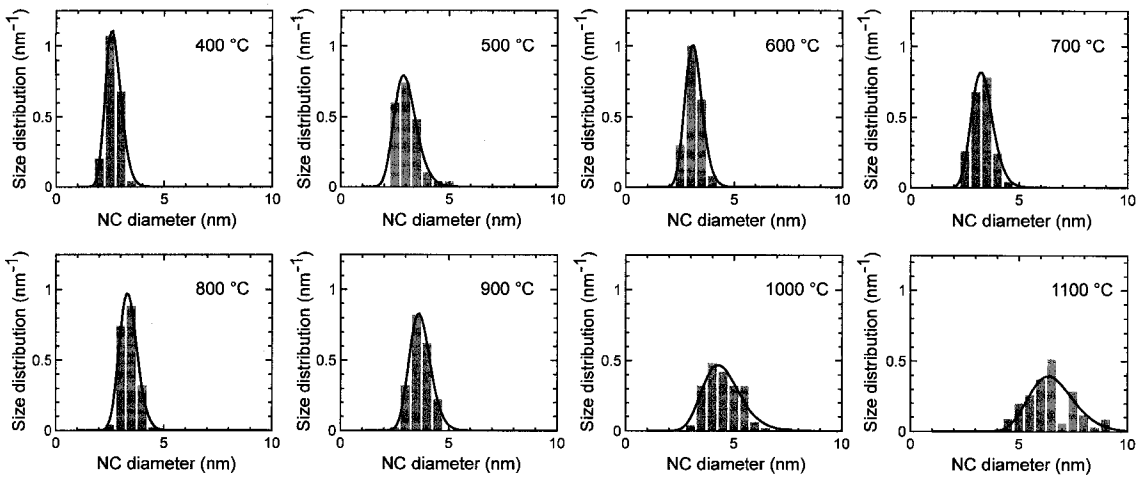

Fig. C.2: Normalised histograms and lognormal distibution fits of NC diameters, for specimens annealed between 400 and 1100 °C. The histograms were determined experimentally from TEM images of the specimens.[11] 60 particles were counted for the 600-°C specimen and 70 for the 1100-°C specimen; for all other specimens, 100 particles were considered.

C.4 Erbium concentration in SiO:Er and SiO:Er_2O_3 films

The electron microprobe analysis (EMPA) of the Er-doped SiO films yields the composition in weight percent or weight fraction ($x_{i_{\mathrm{wt}}}$), which may easily be converted to atomic percent or atomic fraction ($x_{i_{\mathrm{at}}}$) via the following expression:

$$x_{i_{\mathrm{at}}} = \frac{x_{i_{\mathrm{wt}}}}{M_i} \cdot \frac{1}{\sum_i \frac{x_{i_{\mathrm{wt}}}}{M_i}} \tag{C.10}$$

where M_i is the molar mass of element i. However, it is often of interest to know the concentration of the erbium, [Er], in atoms/cm^3. There are a number of ways to calculate this value from EMPA results.

The simplest approach is to assume that the presence of Er does not change the atomic number density of the film appreciably from that of bulk SiO,† which should be valid for low Er concentrations. In this case, [Er] may be found by:

$$[\mathrm{Er}] = \frac{N_A \rho_{\mathrm{SiO}} x_{\mathrm{Er_{at}}}}{\overline{M}_{\mathrm{SiO}}} \tag{C.11}$$

where N_A is Avogadro's number (6.02×10^{23} mol^{-1}), ρ_{SiO} is the density of SiO (2.13 g/cm^3), and $\overline{M}_{\mathrm{SiO}} = \frac{1}{2}(M_{\mathrm{Si}} + M_{\mathrm{O}})$ is the average molar mass of the atoms in the SiO film (22.04 g/mol).

For films grown via electron-beam evaporation of SiO and thermal evaporation of metallic Er, we may use Eq. (C.11), since the Er vapour flux should be in the form of single Er atoms. Using the EMPA data for the STX series of specimens (considered in Chap. 7), we may calculate [Er] in this way, the results of which are shown in Table C.3. Note that the weight fractions of Si and O for ST5 deviate significantly from what one would expect from a film with a very low Er concentration, and should therefore be the closest to

†We assume that the film density is similar to that of bulk SiO (i.e., zero porosity), as TEM of the films did not indicate the presence of any appreciable voids.

stoichiometric SiO; we therefore regard the EMPA results for specimen ST5 with some suspicion. For comparison, the last row in Table C.3 uses $x_{\mathrm{Si_{wt}}}$ and $x_{\mathrm{O_{wt}}}$ values for undoped SiO, and the $x_{\mathrm{Er_{wt}}}$ from the EMPA, yielding a value for [Er] which is nearly identical to that obtained previously. The last column of Table C.3 is reproduced in the last column of Table 7.1.

Table C.3: Calculation of [Er] for STX series (electron-beam SiO and thermal metallic Er) SiO:Er films, using EMPA data and Eq. (C.11). The calculation marked ST5* uses $x_{\mathrm{Si_{wt}}}$ and $x_{\mathrm{O_{wt}}}$ values for undoped SiO, and $x_{\mathrm{Er_{wt}}}$ from the EMPA.

Specimen	$x_{\mathrm{Si_{wt}}}$	$x_{\mathrm{O_{wt}}}$	$x_{\mathrm{Er_{wt}}}$	$x_{\mathrm{Si_{at}}}$	$x_{\mathrm{O_{at}}}$	$x_{\mathrm{Er_{at}}}$	[Er] ($\mathrm{cm^{-3}}$)
ST1	0.546	0.326	0.1451	0.478	0.501	0.0213	1.2×10^{21}
ST2	0.627	0.361	0.0722	0.492	0.498	0.0095	5.5×10^{20}
ST3	0.572	0.347	0.0415	0.481	0.513	0.0059	3.4×10^{20}
ST4	0.554	0.342	0.0153	0.479	0.519	0.0022	1.3×10^{20}
ST5	0.418	0.504	0.0026	0.321	0.679	0.0003	1.9×10^{19}
ST5*	0.637	0.363	0.0026	0.500	0.500	0.00003	2.0×10^{19}

For the SiO:Er films grown via thermal evaporation of SiO and electron-beam evaporation of Er_2O_3 (specimens A–E in Chap. 4), we may test a further refinement with respect to our calculation of [Er] by assuming that the atomic number density of the film is affected by the presence of Er, such that the mass density of film, $\overline{\rho}_{\mathrm{SiO:Er}}$, is the weighted average (by composition) of the densities of SiO and Er_2O_3:

$$\overline{\rho}_{\mathrm{SiO:Er}} = x_{\mathrm{Er_2O_{3wt}}}\rho_{\mathrm{Er_2O_3}} + (1 - x_{\mathrm{Er_2O_{3wt}}})\rho_{\mathrm{SiO}} \tag{C.12}$$

where

$$x_{\mathrm{Er_2O_{3wt}}} = x_{\mathrm{Er_{wt}}}\frac{M_{\mathrm{Er_2O_3}}}{2M_{\mathrm{Er}}} \tag{C.13}$$

is the weight fraction of Er_2O_3 in the film. We must consider the *weight* fraction of Er in Eq. (C.13) because we are considering the film's *mass* density. Defining the average molar mass of atoms in the film as $\overline{M}_{\mathrm{SiO:Er}} = x_{\mathrm{Si_{at}}}M_{\mathrm{Si}} + x_{\mathrm{O_{at}}}M_{\mathrm{O}} + x_{\mathrm{Er_{at}}}M_{\mathrm{Er}}$, the revised expression for [Er] is

$$[\mathrm{Er}] = \frac{N_A\overline{\rho}_{\mathrm{SiO:Er}}x_{\mathrm{Er_{at}}}}{\overline{M}_{\mathrm{SiO:Er}}} \tag{C.14}$$

Using the EMPA data for specimens A–E, the calculation for [Er] using this method is given in Table C.4.

Table C.4: Calculation of [Er] for A–E series (thermal SiO and electron-beam Er_2O_3) SiO:Er films, using EMPA data and Eq. (C.14).

Specimen	$x_{\mathrm{Si_{wt}}}$	$x_{\mathrm{O_{wt}}}$	$x_{\mathrm{Er_{wt}}}$	$x_{\mathrm{Si_{at}}}$	$x_{\mathrm{O_{at}}}$	$x_{\mathrm{Er_{at}}}$	$\overline{\rho}_{\mathrm{SiO:Er}}$ ($\mathrm{g/cm^3}$)	$\overline{M}_{\mathrm{SiO:Er}}$ (g/mol)	[Er] ($\mathrm{cm^{-3}}$)
A	0.631	0.366	0.0029	0.495	0.504	0.0004	2.15	22.042	2.3×10^{19}
B	0.627	0.367	0.0068	0.493	0.506	0.0009	2.18	22.093	5.3×10^{19}
C	0.623	0.362	0.0153	0.494	0.504	0.0020	2.24	22.274	1.2×10^{20}
D	0.567	0.337	0.0961	0.483	0.504	0.0137	2.85	22.909	9.8×10^{20}
E	0.522	0.316	0.1618	0.473	0.502	0.0246	3.33	25.441	1.9×10^{21}

For comparison, [Er] calculated using Eq. (C.11) yield values of 2.2×10^{19}, 5.2×10^{19}, 1.2×10^{20}, 8.0×10^{20}, and 1.4×10^{21} $\mathrm{cm^{-3}}$ for specimens A–E, respectively; these results

are very similar to the values produced from Eq. (C.14), deviating slightly for the larger Er concentrations. Given the error in the EMPA results and the assumptions with respect to density of the SiO:Er film used for Eq. (C.12), it is unlikely that Eq. (C.14) comprises a significant advantage over Eq. (C.11) in the calculation of [Er]. As such, we may use the latter, which has a slight benefit in simplicity.

Bibliography

[1] H. A. Macleod, *Thin-film optical filters*, Institute of Physics Publishing, Bristol, third edition, 2001, ISBN: 0-750-30688-2, Chap. 2.

[2] J. C. Manifacier, J. Gasiot, and J. P. Fillard, "Simple method for determination of optical constants n, k and thickness of a weakly absorbing thin film", *J. Phys. E*, vol. 9, no. 11, pp. 1002–1004, 1976.

[3] R. Swanepoel, "Determination of the thickness and optical constants of amorphous silicon", *J. Phys. E*, vol. 16, no. 12, pp. 1214–1222, 1983.

[4] H. A. Macleod, *Thin-film optical filters*, Institute of Physics Publishing, Bristol, third edition, 2001, ISBN: 0-750-30688-2, p. 67.

[5] J. Wang, X.F. Wang, Q Li, A. Meldrum, and A. Hryciw, "The microstructure of SiO thin films: From nanoclusters to nanocrystals", *Philos. Mag.*, vol. 87, no. 1, pp. 11–27, 2007.

[6] J. Söderlund, L. B. Kiss, G. A. Niklasson, and C. G. Granqvist, "Lognormal size distributions in particle growth processes without coagulation", *Phys. Rev. Lett.*, vol. 80, no. 11, pp. 2386–2388, 1998.

[7] I. M. Lifshitz and V. V. Slyozov, "The kinetics of precipitation from supersaturated solid solutions", *J. Phys. Chem. Sol.*, vol. 19, no. 1–2, pp. 35–50, 1961.

[8] C. G. Granqvist and R. A. Buhrman, "Ultrafine metal particles", *J. Appl. Phys.*, vol. 47, no. 5, pp. 2200–2219, 1976.

[9] A. Meldrum, A. Hryciw, A. N. MacDonald, C. Blois, K. Marsh, J. Wang, and Q. Li, "Photoluminescence in the silicon-oxygen system", *J. Vac. Sci. Tech. A*, vol. 24, no. 3, pp. 713–717, 2006.

[10] http://mathworld.wolfram.com/LogNormalDistribution.html.

[11] Si-NC diameter statistics were counted by A. Meldrum using energy-filtered TEM micrographs prepared by Quan Li and coworkers (unpublished).

APPENDIX D

Corrections to papers in the literature

During a review of the literature concerning emission from nanoscale a-Si and tunnelling rates in ensembles of quantum structures, three papers were found to possess a number of errata. In this Appendix, we present corrections to these papers.

D.1 Tunnelling through a square potential barrier: Errata in Tada *et al.* (1988) and Nido *et al.* (1990)

The papers by Tada *et al.*[1] and Nido *et al.*[2] concern "nonresonant"[†] tunnelling between asymmetric quantum well structures. Tada cites the exact equation (Tada Eq. (4)), whereas Nido rewrites it in a form valid when the carrier wavefunction penetration depth is much less than the barrier width.

We will begin by briefly deriving the exact relation and comparing it to Tada Eq. (4). We examine 1D resonant tunnelling of carriers of energy E from one particle to another through a square potential barrier of width d (Fig. D.1):

$$U(x) = \begin{cases} 0 & x > d \quad \text{(region I)} \\ U_0(>0) & 0 < x < d \quad \text{(region II)} \\ 0 & x < 0 \quad \text{(region III)} \end{cases} \tag{D.1}$$

where $U(x) = \frac{2}{\hbar^2}V(x)$. Defining $\epsilon = \frac{2}{\hbar^2}E$, the time-independent Schrödinger equation may be rewritten as:

$$\frac{-\hbar^2}{2m}\psi'' + V(x)\psi = E\psi \tag{D.2}$$

$$\psi'' + m[\epsilon - U(x)]\psi = 0 \tag{D.3}$$

We consider the situation where the carrier has different effective masses in the particle ($m = m_p$) and in the barrier ($m = m_b$), and $\epsilon < U_0$ (equivalent to $E < V_0$). We define

[†]Although the tunnelling is referred to as "nonresonant," since the quantum wells are asymmetric and therefore have different ground-state energies, the formula used by both authors does not actually take any non-resonant condition into account: it is simply the semiclassical tunnelling transparency relation for plane waves through a square potential barrier.

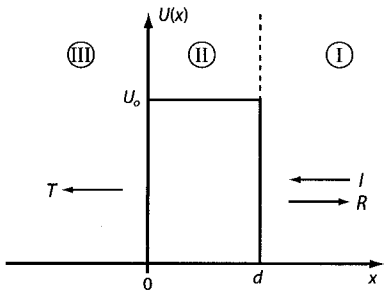

Fig. D.1: 1D tunnelling through a square potential barrier (I=incident, R=reflected, T=transmitted).

$k_1 = \sqrt{m_p \epsilon}$ and $\kappa_2 = \sqrt{m_b(U_0 - \epsilon)}$, yielding boundary conditions

$$\psi(x) = \begin{cases} e^{-ik_1 x} + Qe^{ik_1 x} & x > d \\ Ae^{-\kappa_2 x} + be^{\kappa_2 x} & 0 < x < d \\ Se^{-ik_1 x} & x < 0 \end{cases} \tag{D.4}$$

Continuity of ψ' and ψ at $x = 0$ yields

$$\kappa_2(B - A) = -ik_1 S \tag{D.5}$$

$$A + B = S \tag{D.6}$$

Continuity of ψ' and ψ at $x = d$ yields

$$\kappa_2 \left(Be^{\kappa_2 d} - Ae^{-\kappa_2 d} \right) = ik_1 \left(-e^{-ik_1 d} + Qe^{ik_1 d} \right) \tag{D.7}$$

$$Ae^{-\kappa_2 d} + Be^{\kappa_2 d} = e^{-ik_1 d} + Qe^{ik_1 d} \tag{D.8}$$

Solving Eqs. (D.5) and (D.5) for S, we obtain

$$S = \frac{2\kappa_2}{\kappa_2 + ik_1} A \tag{D.9}$$

Substituting Eqs. (D.8) and (D.6) into Eq. (D.7), and solving for A, we have

$$\begin{aligned} \kappa_2 \left(Be^{\kappa_2 d} - Ae^{-\kappa_2 d} \right) &= ik_1 \left(-2e^{-ik_1 d} + Ae^{-\kappa_2 d} + Be^{\kappa_2 d} \right) \\ A \left(-\kappa_2 e^{-\kappa_2 d} - ik_1 e^{-\kappa_2 d} \right) &= -\kappa_2 Be^{\kappa_2 d} - 2ik_1 e^{-ik_1 d} + ik_1 Be^{\kappa_2 d} \\ A \left(-\kappa_2 e^{-\kappa_2 d} - ik_1 e^{-\kappa_2 d} \right) &= (S - A)(ik_1 - \kappa_2) e^{\kappa_2 d} - 2ik_1 e^{-ik_1 d} \\ A \left[-\kappa_2 \left(e^{-\kappa_2 d} + e^{\kappa_2 d} \right) + ik_1 (e^{\kappa_2 d} - e^{-\kappa_2 d}) \right] &= Se^{\kappa_2 d}(ik_1 - \kappa_2) - 2ik_1 e^{-ik_1 d} \end{aligned}$$

$$A = \frac{Se^{\kappa_2 d}(ik_1 - \kappa_2) - 2ik_1 e^{-ik_1 d}}{ik_1 \left(e^{\kappa_2 d} - e^{-\kappa_2 d} \right) - \kappa_2 \left(e^{\kappa_2 d} + e^{-\kappa_2 d} \right)} \tag{D.10}$$

A substitution of Eq. (D.10) into Eq. (D.9) yields

$$S = \frac{2\kappa_2}{\kappa_2 + ik_1} \frac{Se^{\kappa_2 d}(ik_1 - \kappa_2) - 2ik_1 e^{-ik_1 d}}{ik_1 \left(e^{\kappa_2 d} - e^{-\kappa_2 d} \right) - \kappa_2 \left(e^{\kappa_2 d} + e^{-\kappa_2 d} \right)}$$

which may be solved for S to yield

$$\begin{aligned} S &= \frac{-4ik_1\kappa_2 e^{-ik_1 d}}{(\kappa_2^2 - k_1^2)\left(e^{\kappa_2 d} - e^{-\kappa_2 d}\right) - 2ik_1\kappa_2\left(e^{\kappa_2 d} + e^{-\kappa_2 d}\right)} \\ &= \frac{-4ik_1\kappa_2 e^{-ik_1 d}}{2(\kappa_2^2 - k_1^2)\sinh\kappa_2 d - 4ik_1\kappa_2\cosh\kappa_2 d} \end{aligned} \tag{D.11}$$

Thus, the transmission coefficient is

$$\begin{aligned} T = |S|^2 &= \frac{16k_1^2\kappa_2^2}{4(\kappa_2^2 - k_1^2)^2\sinh^2\kappa_2 d + 16k_1^2\kappa_2^2\cosh^2\kappa_2 d} \\ &= \frac{4k_1^2\kappa_2^2}{(\kappa_2^2 - k_1^2)^2\sinh^2\kappa_2 d + 4k_1^2\kappa_2^2(1 + \sinh^2\kappa_2 d)} \\ &= \frac{4k_1^2\kappa_2^2}{(\kappa_2^2 + k_1^2)^2\sinh^2\kappa_2 d + 4k_1^2\kappa_2^2} \\ &= \frac{4m_p m_b\epsilon(U_0 - \epsilon)}{4m_p m_b\epsilon(U_0 - \epsilon) + \left[m_b(U_0 - \epsilon) + m_p\epsilon\right]^2\sinh^2\kappa_2 d} \\ &= \frac{4\left(\frac{m_p}{m_b}\right)E(V - E)}{4\left(\frac{m_p}{m_b}\right)E(V - E) + \left[\left(\frac{m_p}{m_b} - 1\right)E + V\right]^2\sinh^2\frac{d}{\lambda}} \end{aligned} \tag{D.12}$$

where $\lambda = \kappa_2^{-1} = \frac{\hbar}{\sqrt{2m_b(V-E)}}$ is the $1/e$ wavefunction penetration depth in the barrier.

Eq. (D.12) is identical to the transmission coefficient in Tada Eq. (4),

$$T = \frac{4kE(V - E)}{4kE(V - E) + [(k - 1)E + V]^2\sinh^2\frac{d}{\lambda}} \tag{D.13}$$

if k is defined as m_p/m_b, as opposed to m_b/m_p, as indicated in the manuscript.

Unfortunately, this error is propagated in the manuscript of Nido *et al.*, where it is evaluated for the regime $d \gg \lambda$. For $x \gg 1$, $\sinh x \approx \frac{1}{2}e^x$, so

$$\begin{aligned} T &\approx \frac{4\left(\frac{m_p}{m_b}\right)E(V - E)}{\left[\left(\frac{m_p}{m_b} - 1\right)E + V\right]^2\frac{1}{4}e^{2\kappa_2 d}} \\ &\approx \frac{16\left(\frac{m_p}{m_b}\right)E(V - E)}{\left[\left(\frac{m_p}{m_b} - 1\right)E + V\right]^2}e^{-2\kappa_2 d} \end{aligned} \tag{D.14}$$

For a quantum well of width L, the classical attempt frequency is $\nu_0 = \left(\frac{1}{2L}\right)\left(\frac{2E}{m_p}\right)^{1/2}$, so the tunnelling time τ_T is given by the expression

$$\frac{1}{\tau_T} \approx \left(\frac{1}{2L}\right)\left(\frac{2E}{m_p}\right)^{1/2}\frac{16E(V - E)\left(\frac{m_p}{m_b}\right)}{\left[V + \left(\frac{m_p}{m_b} - 1\right)E\right]^2}\exp\left[-2d\left(\frac{2m_b}{\hbar^2}(V - E)\right)^{1/2}\right] \tag{D.15}$$

where m_p is the mass in the well and m_b is the mass in the barrier. This is the corrected version of Nido Eq. (1).

It is encouraging to note that, although the change is small, the corrected theoretical electron tunnelling times for barrier widths of 4, 6, and 8 nm, as shown in Fig. 3 of Nido *et al.*, match the experimental values better than those calculated with the incorrect formula used in the paper (Fig. D.2).

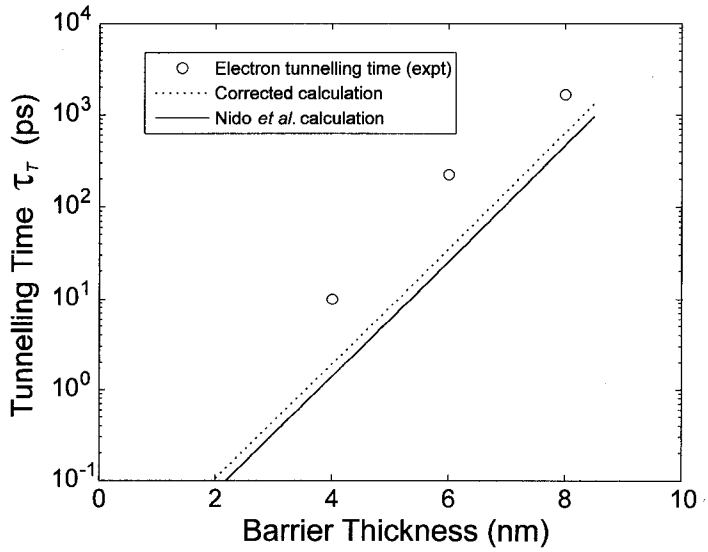

Fig. D.2: Comparison of values for experimental electron tunnelling times and theoretical values calculated using Eq. (D.15) and the incorrect Eq. (1) in Nido *et al.*, using $L = 5$ nm, $E = 80$ meV, $V = 289$ meV, $m_p = 0.067m_0$, and $m_b = 0.096m_0$.

D.2 Emission from a-Si nanostructures: Errata in Estes and Moddel (1996)

As explained in Chap. 6, the paper by Estes and Moddel[3] indicates a method of calculating the emission spectra from nanoscale a-Si (quantum wells, wires, and dots) based on a geometrical limitation of the accessible capture volume and area (V_c and A_c, respectively) due to the size and shape of the a-Si nanostructures. The precise form of $V_c(r)$ and $A_c(r)$ as functions of position within the quantum structures is integral to a correct calculation for the luminescence spectrum, especially for a-Si structures of comparable size to the capture radius; it is therefore unfortunate that the expressions given in the Appendix of the paper do not produce the correct result. Corrected expressions for $V_c(r)$ and $A_c(r)$ for 2D slabs and 0D spheres are given here (*with* derivation) for a capture radius of R_c, a nanocluster radius (or 2D slab half width) of R_t, and a centre-to-centre separation (or distance from left edge of 2D slab) of r.

First, however, we note an error in Eq. (3), an expression for the empirical quantum efficiency of bulk a-Si (from Ref.[4]). Eq. (3) should read

$$\eta = \frac{1}{1 + \left(\frac{1}{\eta_0} - 1\right) \exp\left(\frac{T}{T_0}\right)} \tag{D.16}$$

Fortuitously, this error is not propagated in ensuing equations. One other small error is that the effective density of states for the conduction band, N_{c0}, is given as having dimensions of [cm^{-3}], when from the form of Eq. (6), it clearly must be in [cm^{-3}eV^{-1}].

D.2.1 2D planar slabs

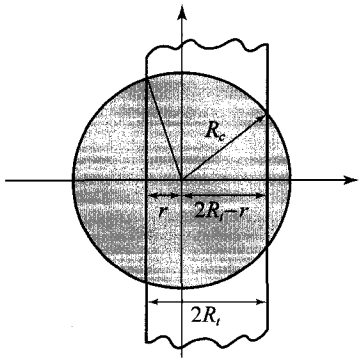

For both sides of sphere protruding,

$$\begin{aligned} A_c &= \pi\left\{(R_c^2 - r^2) + (R_c^2 - [2R_t - r]^2)\right\} \\ &= 2\pi(R_c^2 - r^2 - 2R_t^2 + 2R_t r) \end{aligned}$$

In general, for V_c,

$$V_c = \pi \int_{x_1}^{x_2} (R_c^2 - x^2)\, \mathrm{d}x = \pi \left[R_c^2(x_2 - x_1) + \frac{1}{3}(x_1^3 - x_1^3) \right]$$

For only the left side protruding, $x_1 = -r$ and $x_2 = R_c$:

$$V_c = \frac{\pi}{3}(2R_c^3 + 3R_c^2 r - r^3)$$

For both sides protruding, $x_1 = -r$ and $x_2 = 2R_t - r$:

$$V_c = \frac{2\pi}{3} R_t (3R_c^2 - 4R_t^2 + 6R_t r - 3r^2)$$

There are three cases with respect to R_t and R_c:

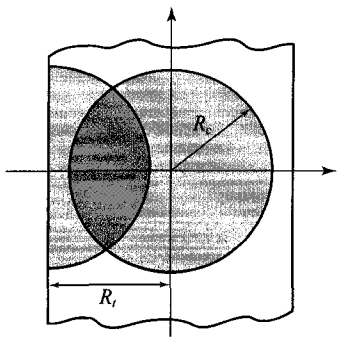

Case 1: $R_c \leq R_t$

Capture sphere is completely enclosed if $r > R_c$.

- $0 \leq r \leq R_c$

  $A_c = \pi(R_c^2 - r^2)$

  $V_c = \frac{\pi}{3}(2R_c^3 + 3R_c^2 r - r^3)$

- $R_c < r \leq R_t$

  $A_c = 0$

  $V_c = \frac{4\pi}{3} R_c^3$

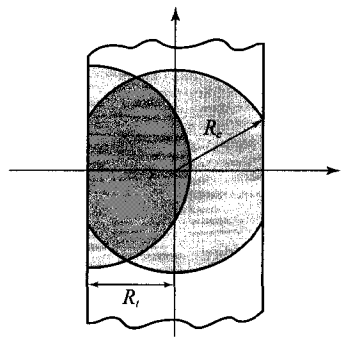

Case 2: $R_t < R_c \leq 2R_t$

Second side of capture sphere protrudes if $r > 2R_t - R_c$.

- $0 \leq r \leq 2R_t - R_c$

  $A_c = \pi(R_c^2 - r^2)$

  $V_c = \frac{\pi}{3}(2R_c^3 + 3R_c^2 r - r^3)$

- $2R_t - R_c < r \leq R_t$

  $A_c = 2\pi(R_c^2 - r^2 - 2R_t^2 + 2R_t r)$

  $V_c = \frac{2\pi}{3} R_t (3R_c^2 - 4R_t^2 + 6R_t r - 3r^2)$

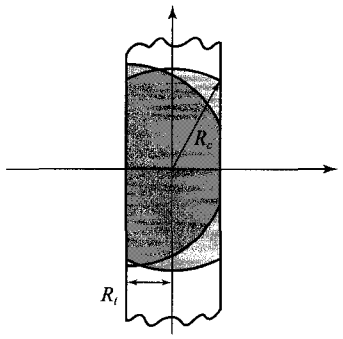

Case 3: $2R_t < R_c$

Both sides of capture sphere protrude for all r.

- $0 \leq r \leq R_t$

$$A_c = 2\pi(R_c^2 - r^2 - 2R_t^2 + 2R_t r)$$
$$V_c = \frac{2\pi}{3} R_t(3R_c^2 - 4R_t^2 + 6R_t r - 3r^2)$$

D.2.2 0D spheres

For spherical (0D) quantum dots, there are four cases with respect to R_t and R_c:

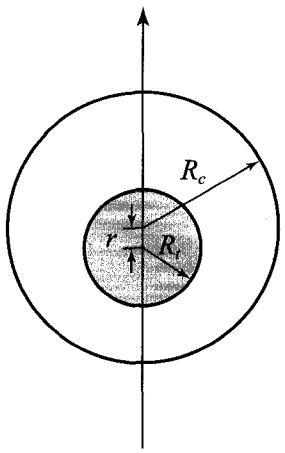

Case 1: $R_c \geq 2R_t$

The dot is completely enclosed by the capture sphere for all r.

$$V_c = \frac{4\pi}{3} R_t^3$$
$$A_c = 4\pi R_t^2$$

Case 2: $R_t < R_c < 2R_t$

For $r \leq R_c - R_t$, the dot is completely enclosed (A_c and V_c as in Case 1).

For $r > R_c - R_t$, we have:

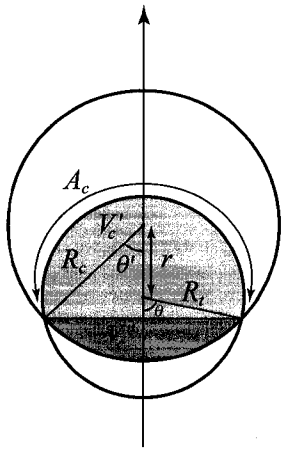

$$\cos\theta' = \frac{R_c^2 + r^2 - R_t^2}{2R_c r} \qquad \cos\theta = \frac{R_c\cos\theta' - r}{R_t}$$

$$V_c' = \pi \int_{-R_t}^{R_c\cos\theta' - r} (R_t^2 - x^2)\,\mathrm{d}x = \pi\left[R_t^2\left(R_t + \frac{R_c^2 - r^2 - R_t^2}{2r}\right) - \frac{1}{24}\left(\frac{R_c^2 - r^2 - R_t^2}{2r}\right)^3 - \frac{R_t^3}{3}\right]$$

$$V_c'' = \pi \int_{R_c\cos\theta'}^{R_c} (R_c^2 - x^2)\,\mathrm{d}x = \pi\left[R_c^2\left(R_c - \frac{R_c^2 + r^2 - R_t^2}{2r}\right) + \frac{1}{24}\left(\frac{R_c^2 + r^2 - R_t^2}{2r}\right)^3 - \frac{R_c^3}{3}\right]$$

$$\therefore V_c = V_c' + V_c'' = \frac{\pi}{12r}\left[r^4 - 6r^2(R_t^2 + R_c^2) + 8r(R_t^3 + R_c^3) - 3(R_t^4 + R_c^4) + 6R_t^2R_c^2\right]$$

$$A_c = 2\pi R_t^2 \int_\theta^\pi \sin\theta\,\mathrm{d}\theta = 2\pi R_t^2[\cos\theta + 1] = 2\pi R_t^2\left[\frac{R_c^2 - r^2 - R_t^2}{2R_t r} + 1\right]$$

Case 3: $R_t = R_c$

For $r = 0$, the capture sphere surface overlaps exactly with that of the dot, so $V_c = \frac{4\pi}{3}R_t^3$ and $A_c = 4\pi R_t^2$.

For $r > 0$, use results from Case 2, yielding $V_c = \frac{\pi}{12}(r^3 - 12R_t^2 r + 16R_t^3)$ and $A_c = 2\pi R_t^2\left(1 - \frac{r}{2R_t}\right)$.

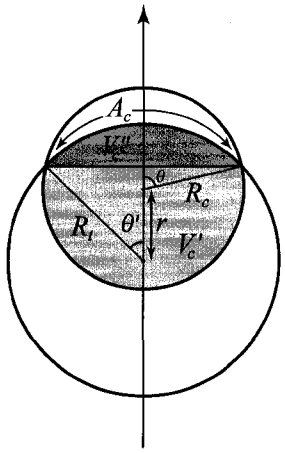

Case 4: $R_c < R_t$

For $r \leq R_t - R_c$, the capture sphere is completely enclosed by the dot:

$$V_c = \frac{4\pi}{3} R_c^3$$
$$A_c = 4\pi R_c^2$$

For $r > R_t - R_c$, we have:

$$\cos\theta' = \frac{R_t^2 + r^2 - R_c^2}{2R_t r} \qquad \cos\theta = \frac{R_t \cos\theta' - r}{R_c}$$

$$V_c' = \pi \int_{-R_c}^{R_t\cos\theta' - r} (R_c^2 - x^2)\, \mathrm{d}x \quad \text{and} \quad V_c'' = \pi \int_{R_t\cos\theta'}^{R_t} (R_t^2 - x^2)\, \mathrm{d}x$$

V_c is the same as for $r > R_c - R_t$ in Case 3:

$$V_c = V_c' + V_c'' = \frac{\pi}{12r}\left[r^4 - 6r^2(R_t^2 + R_c^2) + 8r(R_t^3 + R_c^3) - 3(R_t^4 + R_c^4) + 6R_t^2 R_c^2\right]$$

$$A_c = 2\pi R_t^2 \int_0^{\theta'} \sin\theta\, \mathrm{d}\theta = 2\pi R_t^2[1 - \cos\theta] = 2\pi R_t^2 \left[1 - \frac{R_t^2 + r^2 - R_c^2}{2R_t r}\right]$$

Bibliography

[1] T. Tada, A. Yamaguchi, T. Ninomiya, H. Uchiki, T. Kobayashi, and T. Yao, "Tunneling process in AlAs/GaAs double quantum wells studied by photoluminescence", *J. Appl. Phys.*, vol. 63, no. 11, pp. 5491–5494, 1988.

[2] M. Nido, M. G. W. Alexander, W. W. Rühle, T. Schweizer, and K. Köhler, "Nonresonant electron and hole tunneling times in GaAs/$Al_{0.35}Ga_{0.65}As$ asymmetric double quantum wells", *Appl. Phys. Lett.*, vol. 58, no. 4, pp. 355–357, 1990.

[3] M. J. Estes and G. Moddel, "Luminescence from amorphous silicon nanostructures", *Phys. Rev. B*, vol. 54, no. 20, pp. 14633–14642, 1996.

[4] R. W. Collins, M. A. Paesler, and W. Paul, "The temperature dependence of photoluminescence in a-Si:H alloys", *Solid State Commun.*, vol. 34, no. 10, pp. 833–836, 1980.